UNIVERSITY OF LIVERPOOL | STEPHENSON INSTITUTE FOR RENEWABLE ENERGY

Photocatalytic Oxidation of Glucose and Cellobiose Using TiO_2 Supported Bimetallic Nanoparticles.

Luigi Da Vià

Chemistry Department

This dissertation is submitted for the degree of

Doctor of Philosophy

February 2016

J. Blues: The band? The band.

Rev. C. James: DO YOU SEE THE LIGHT?

J. Blues: THE BAND!.

Rev. C. James: DO YOU SEE THE LIGHT?

E. Blues: [Confused] What light?

Rev. C. James: HAVE YOU SEEEEN THE LIGHT?

J. Blues: YES! YES! JESUS H. TAP-DANCING CHRIST... I HAVE SEEN THE LIGHT!

The Blues Brothers, 1980

Declaration

I hereby declare that except where specific reference is made to the work of others, the contents of this dissertation are original and have not been submitted in whole or in part for consideration for any other degree or qualification in this, or any other university. This dissertation is my own work and contains nothing which is the outcome of work done in collaboration with others except as specified in the text. This dissertation contains fewer than 73,000 words including appendices, bibliography, footnotes, tables and equations and has fewer than 130 figures.

Luigi Da Vià

February 2016

Acknowledgements

This PhD is not just mine. I mean, it is as I did most of the leg work, but all of this would not have been possible without the enormous amount of help I've received in these three and half years of the spectacularly emotional roller-coaster that a PhD is. I would like to thank all the technicians in the department for helping me setting up most of the equipment in the lab specially, Dave, Ken, Sandra and Gordon for the helping me scavenging anything I could put my hands on, the laughs, and the weird Friday afternoon requests.

I would like to thank all Mikko, Estevão, Thalita, Thiago, Stephanie all the people that came by to do some research here in Liverpool. Thank you for sharing fragments of your lives with me and becoming friends. I hope I will see you again in the future! I would like to thank all the people in our group, Joel for the quaffable drinks and the fat frogs (you evil!), Aldo for the patience and all the others for having to deal with me during some stressful times.

A special thank to all the people I've helped in the lab, thank you Erica for the patience and understanding of being my first student, Carlo for all the work in the lab and allowing me to use for the first time the depilatory strips, sta senz' pensieri e portami doje frittur!!

Thank you all for your patience!

Thank you Tom for the all the support, mentoring, drinking, supervision, friendship and so much more! This work is as much mine as it is yours!

Finally, last but not least, I would like to thank Tony for giving me the opportunity to embark myself upon a PhD and making me realize that, as Winston Churchill said, *"If you're going through hell keep going."*.

Vorrei ora ringraziare "the big Italian family", i papino e mammina per aver sempre creduto nel figlio che non vedeva l'ora di esplorare il mondo ed avermi sempre so(su)pportato

in tutto e per tutto. Grazie per avermi dato l'opportunità di diventare l'uomo che sono nonostante tutti i miei difetti.

Grazie a Roberto e Daniela, essere il fratellone maggiore a distanza é dura ogni tanto ma vedervi seguire le vostre strade con successo mi rende fiero di voi.

A special THANK YOU to my Canadian family. Without you this incredible adventure probably would have never started. Those 6 months changed my life I will be forever grateful to you guys. Uncle Ben, Aunt Maria, Annamaria and Richard thank you for being there even if time passes by and you are across the ocean! I will be back soon, I promise!

Ilaria, questi (quasi) 4 anni assieme sono stati intensi. Nostri. Grazie per avermi ascoltato quando agli inizi le cose non giravano, avermi sopportato nei giorni bui e aver riso con me nei tanti giorni felici. Spero di riuscire ad essere un punto di riferimento per te come lo sei stata per me. Adesso tocca a te! Una volta mi hai scritto "Che tu possa avere sempre il vento in poppa, che il sole ti risplenda in viso [..]", Luiz.

Ti auguro e ci auguro lo stesso per molto tempo a venire!

Come non ricordare i gladiatori di SSRC, La Sergia, Sgrillons, Emiliano-boldra-Poli ed Enzo. Abatjour mi ha causato notti insonni per le vivide immagini condivise, ma senza di voi, le cene, le risate, le bestemmie (tante), questo PhD sarebbe stato incolore. Grazie ed in bocca al lupo!

Vorrei ringraziare la "Banda del Mersey": Diego, Serafino, Luca, Sara, Giulia, Danilo, Diego, Michela e tutti gli italiani che ho conosciuto qui per avermi fatto sentire a casa distante da casa. Grazie regaz!

Thanks to all the members of "Neighbours making sense of the neighbourhood" for organising improbable hiking trips and random events!

Finally, I would like to thank all the people I've met through Volleyball, Andy, Maurizio aka Big Man, James, Ethan, James, Josue, Andy, Stoqn, Zach, Lucas for building a team, and learning the hard way what it means to win and lose together. I wish you guys all the best!

Abstract

There is a growing interest in developing new photocatalytic routes for biomass upgrade to chemicals and fuels, but despite of some recent progress this remains an area in infancy.

The ultimate aim is to convert hemicellulose, cellulose and lignin into valuable platform chemicals using green processes, there is a need to find model compounds to mimic their properties and obtain fundamental understanding of the chemistry. For this reason, cellobiose is used as model compound for cellulose because of its dimer structure, whilst glucose is cheap, easily sourced, and very abundant as the monomeric unit of cellulose, the most abundant polymer on earth, which presents great potential for commercial applications and its upgrade via selective oxidation reactions is highly desirable.

However, for oxidation processes, photocatalysis is typically associated with total mineralisation reactions. In this PhD thesis will be presented for the first time the visible light mediated selective photo-catalytic oxidation of glucose and cellobiose with +98% selectivity to partial oxidation products and a near total suppression of the mineralization pathway.

In this study three different experimental set-ups were used. A photoreactor equipped with UVA lamps for a total power of 112 W, a 300 and 1000 W Xenon lamps equipped with visible light filters with a cut-off wavelength of 420 nm. Typically, 40 mg of catalyst were suspended in H_2O and exposed to visible light for different reaction times from 2-24h at room temperature. TiO_2-P25 displayed significant activity under visible light when glucose and cellobiose were used as substrates. Nonetheless, the decoration of the surface of the support with the metal nanoparticles enhances the overall activity of the catalyst achieving 100% cellobiose conversion in under UVA light in under 2 hours at room temperature.

With the addition of the 1 wt% AuAg nanoparticles with different molar ratios to the surface of the TiO_2 support, cellobiose conversions of up to 30% were observed. Under UVA light the AuAg catalysts displayed a 100% cellobiose conversion with the presence of the partial oxidation products and the oxidation products coming from the hydrolysis of cellobiose. The reaction conditions were optimized by controlling the catalyst to substrate ratio, the light source power and the wavelength range. The catalysts were recycled 3 times with no significant loss of activity or changes in the product distribution values and were characterized with ICP, XRD, XPS, TEM and solid UV-Vis.

This study attempts to apply a systematic approach towards the understanding of photocatalytic reactions, specifically focusing on the possibility of upgrading glucose and cellobiose to valuable chemicals. The reactivity of sugars when exposed to UV light and metal supported catalysts has been reported in the literature, but for the first time, this work tries to combine the production of the gaseous products (H_2 and CO_2) along with the presence of partially oxidised products in the aqueous phase with a new global reaction mechanism which takes into account what are believed to be the two main competitive reaction pathways, the Ruff degradation, and the alpha scission of sugars.

This study can be transferred to other bio-derived molecules to get a better understanding on how to optimize and exploit photoactive materials to upgrade biomass under mild conditions and emphasises the crucial role of the Au and Ag metal nanoparticles present on the surface towards extending the activity range in the visible part of the spectrum.

Table of contents

List of figures

List of tables

Chapter 1

Introduction

The band? The band.

J. Blues

The unpredictable trends observed in recent years on the crude oil price along with profound environmental issues have deeply influenced our dependency on non-renewable energy sources. In the early seventies, after one of the major oil crises in history, the research on alternative energy sources observed an exponential growth due to necessity of exploiting cheaper alternatives by governments and industries informed by scientific evidence (Figure 1.1). Along with the development of more sustainable ways of harvesting the power of tides and winds for the production of electricity, the exploitation of solar irradiation to produce heat and electricity observed a phenomenal increment in government funds and research projects, and now many of the prototypes developed in the past 40 years are commercially available products with running costs sometimes even cheaper or at least as competitive as conventional processes. The use of solar irradiation is an appealing perspective as in 2000 the United Nations Development Programme assessed that the annual potential of solar energy ($\sim$50EJ) is several times lager than the world energy consumption which in 2012 was 559.8 exajoules.[1] In this new green economy, along with the development of sustainable

[1] Key World Energy Statistics report by the International Energy Agency (2014)

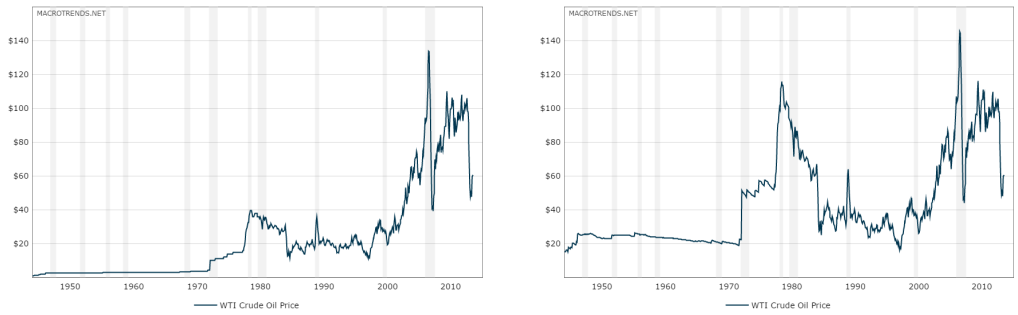

(a) **(b)**

Figure 1.1 Oil price trend since 1948 (1.1a) and the inflation corrected oil price (1.1b). The grey areas represent the economic recession during the last century.

energy sources technologies, the quest for alternative substrates not derived from crude oil is the challenge that the chemical industry as a whole is undertaking to keep up with the worldwide demand for bulk and fine chemicals. Biomass, is now considered a "green-oil", as it can provide many platform chemicals which are highly functionalized, but at the same time, because of the complex molecular structure and the presence of heteroatoms such as oxygen, nitrogen, the chemistry and the processing of such substrates are complex challenges that are currently being tackled worldwide. One of the first uses of biomass was in the production of bio-hydrogen via chemical and fermentative processes. Moreover, it has to be noted that the biomass used as feedstock should not be competing with food production in terms of land and resources, but on the other hand, should promote a valorisation of waste and of the non-edible parts of the plant, unlike what is happening for the production of bio-ethanol, bio-diesel and bio-oils in developing countries [12, 87, 56, 65, 111]. Biomass derivatives such as ethanol, glycerol and sugars are hydrogen-rich compounds and through hydrogenation processes the CO_2 produced can be reintroduced with photosynthetic reactions to the carbon cycle without contributing to the production of greenhouse gases. Despite the initial studies on the photo-reforming of biomass, it seems necessary to try to preserve the chemical functionalities present on the substrates and use them to produce high-value chemicals from bio-renewables. For this purpose, in the past 5 years, there has been an increasing amount of attention on the

possibility of performing selective photo-oxidation on sugars, glycerol and other substrates. In this short review, after introducing the common traits for various photocatalysts and illustrating some of the accepted reaction mechanisms responsible for the photoactivity, this work will briefly describe some of the reaction pathways for the H_2 production and oxidation of bio-derived substrates from biomass, and will then cover the most recent results on the photo-oxidative reaction conditions required to successfully convert sugars in platform chemicals.

1.1 Biomass Chemistry

Lignocellulosic biomass is typically made of three fractions: cellulose (35-55%), hemicellulose (20-40%) and lignin (10-20%). In addition to these macro polymers, there are two categories which account for the remaining fractions: ashes (mineral components) and extractives (fats, oils, steroids waxes and other phenolic compounds). The ratio between each of the fractions is determined by the type of plant, age, climate and several other factors, thus making it difficult to standardize chemical processes and reaction pathways [256, 107, 177]. Cellulose is a homopolymer consisting of $\beta(1\rightarrow4)$ linked glycosidic units and the geometry of the bond linking each of the D-glucose units is responsible for its physical-chemical properties. In fact, as each of the chain can be as big as 100.000 Da, there is a great interaction between the hydroxyl groups thus creating a strong intra and intermolecular hydrogen bond network which is responsible for the low cellulose solubility and its tensile strength [262, 133].

On the other hand, hemicellulose is a mixture of different monosaccharides with different carbon chain lengths, namely C_5 (xylose, arabinose) and C_6 (glucose, galactose, mannose) along with some sugar acids (glucuronic and galacturonic acid mainly); it is generally characterized by shorter chain lengths and due to the diverse structure of the polysaccharides, it is a heavily branched polymer unlike cellulose [83]. Finally, lignin is a highly branched

polymer made of aromatic alcohols, which impart to this biopolymer a very complex and poorly defined structure. Generally, from lignin four major components can be extracted via depolymerization reactions such as coumaryl alcohols, sinapyl alcohols, and coniferyl alcohols which are used in the production of organic compounds, flavouring agents and food preservatives [57, 177].

1.2 Conventional Processes for Biomass Utilization

Sourcing energy from biomass can be divided in four general categories, (i) crops (herbaceous, agricultural, industrial and aquatic), (ii) agricultural waste and residues including animal waste, (iii) paper industry residues (mill wood, shrubs, logging residues) and finally, from municipal waste, including sewage and industrial waste streams [182]. Within these four categories, two different process streams are available to produce energy from biomass: the thermochemical and the fermentative biological routes. Within the thermochemical approach, liquefaction, pyrolysis, gasification and combustion are the main approaches used, whilst for biological processes, the biological water-gas shift, the photo and dark fermentation processes, the direct and indirect bio-photolysis constitute the more common routes, but the reviewing in detail of these processes exceeds the purposes of the present work (Figure 1.2).

1.2.1 Thermochemical Processes

At high temperatures, biomass decomposes to produce liquid oils, solid residues, a mixture of gases containing CH_4, CO_2, H_2, CO and other products depending on the composition of the starting feedstock. During the flash pyrolysis, biomass is rapidly heated up to *ca.* 550°C under inert pressure to form a vapour and then condensed. This process, in addition to the gaseous products described above, also produces oils, tars and other chemicals such as acetic acid in addition to the solid carbonaceous and inert fractions. Generally, the main reaction

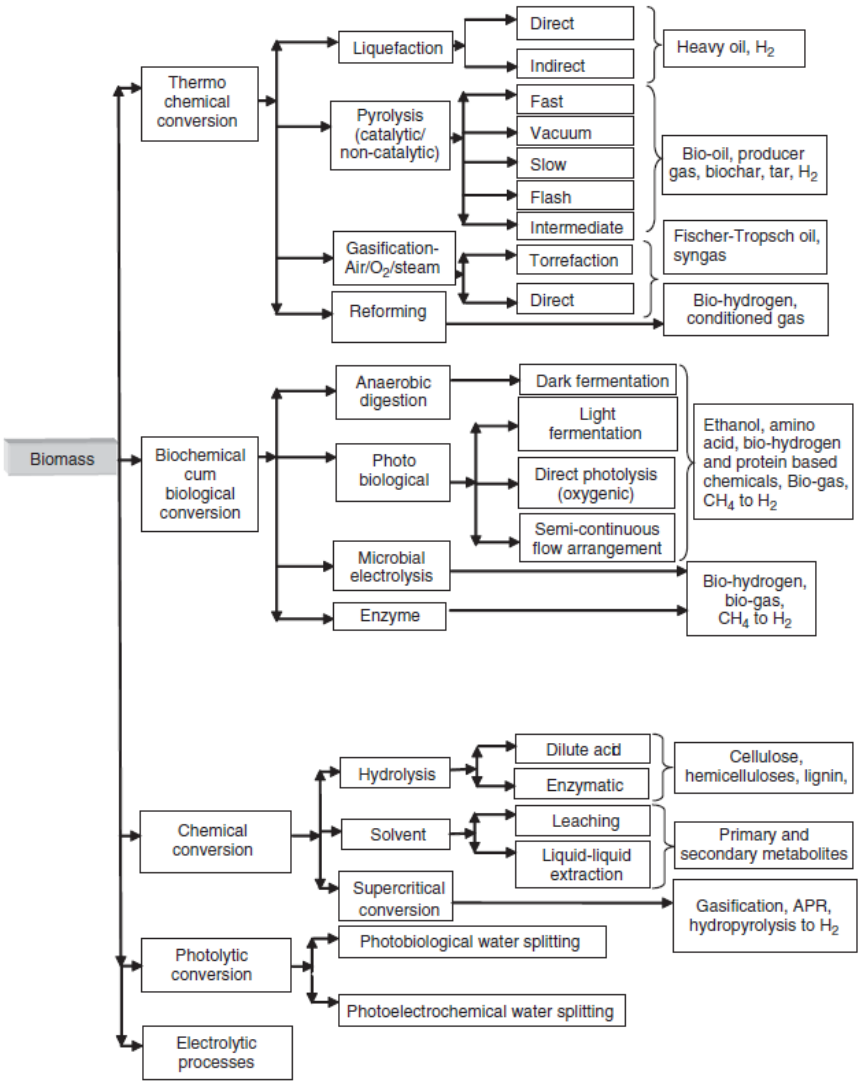

Figure 1.2 Different processes available for the conversion of biomass to biofuels [173].

schemes for the production of H_2 from biomass are the following:

$$Biomass + heat \rightarrow H_2 + CO + CH_4 + others \tag{1.1}$$

With the steam reforming, methane which is produced at low temperatures, can be converted to hydrogen:

$$CH_4 + H_2O \rightarrow CO + 3H_2 \tag{1.2}$$

Subsequently, the water-gas shift reaction can be used to convert CO to CO_2 as follows:

$$CO + H_2O \rightarrow CO_2 + H_2 \tag{1.3}$$

Due to the positive Gibbs energy value of the steam reforming, high temperatures (>1000°C) are required even in the presence of catalysts. When Ni-based catalysts are used, H_2 yields can reach values up to 90%. Due to the harsh conditions required, several reactor set-ups and catalysts have been investigated to improve the reaction rate. Inorganic salts and carbonates such as K_2CO_3, Na_2CO_3 and $CaCO_3$ [50], have been used as inexpensive materials along with Y-type zeolites, metal oxides (Al_2O_3, TiO_2, ZrO_2, SiO_2)[226] and noble metal based catalysts to improve the decomposition rate of the hydrocarbons produced [97]. When oxidizing gases such as O_2, air, and steam are used, the gasification of biomass can be described as follows:

$$Biomass + heat \rightarrow CO_2 + CO + H_2 + CH_4 + hydrocarbons + char \tag{1.4}$$

During the process, the partial oxidation of the biomass produces charcoal which is subsequently reduced do form the gases described in Eqn 1.4. The gaseous stream produced during the process can be converted to H_2 with the water-gas shift reaction as discussed previously to increase the efficiency of the process. It has to be noted that this approach can be used with fraction of biomass with low moisture content (<35%) because of the high water heat capacity value which makes the process energy demanding [72]. Additionally, one of the major drawback of these processes is the formation of tars which cause unwanted polymerization reactions along with the formation of ashes which diminish the overall process efficiency. In order to overcome the issue of having to process wet feedstock with a moisture content greater than 35%, in recent years extensive research has been made on the application of supercritical water for the gasification of biomass. Several examples on the gasification of

cellulose and glucose with supercritical water are available in the literature [246, 66], and the main advantage of this process is that the formation of tars and chars is suppressed. An overview of the experimental results using glucose was published in a recent review by Ni et al. [182] and the reader is encouraged to use it as a reference.

1.2.2 Biological Processes

The biological processes introduced at the beginning of this section, are generally found to be more sustainable and greener alternatives to the thermochemical ones as they require milder reaction conditions and therefore, much lower running costs. These processes generally rely on the biological or photo-biological production of hydrogen with the only two known enzymes which can catalyse this reaction biologically: hydrogenases and nitrogenases [105, 68, 121]. The conversion of the different saccharides in aqueous solutions is subject of intense research as it can be approached using homogeneous or heterogeneous systems. These approaches are aimed at the production of methane from the anaerobic fermentation in three major reaction steps, which can be summarized with the conversion of the macro polymers in smaller units such as amino acids, monosaccharides and fatty acids, acid lactic and ethanol, their conversion into methane and hydrogen by the bacteria and finally, into methane by the methanogenic bacteria. The biogas thus obtained can either be converted into hydrogen with by thermal decomposition or cracking reactions and to syngas with steam reforming or water-gas shift processes [42, 15, 134]. The main drawbacks of these fermentative techniques are the slow hydrogen production rate and the low concentration of the gaseous and the difficulty in designing efficient bio-reactors[145].

1.3 Chemical Conversion of Carbohydrates

As mentioned before, the conversion of biomass into useful chemicals, is one of the greatest challenges of this century as it can potentially reduce our dependency on oil-exporting countries and reduce the global footprint of chemical production. Specifically, during the past 50 years, the research has focused on the production of biofuels from renewable sources to integrate at first, and then maybe replace completely, the conventional petrochemical processes. From an economical perspective, carbohydrates are abundant and inexpensive as they account for 75 wt% of plant biomass and can be the ideal feedstock for both biofuels and platform chemicals. In fact, the conversion of these chemicals provide access to a wide range of "versatile chemicals" which can be incorporated in a wide range of applications as surfactants, bio-polymers, resins and pharmaceutical intermediates, and can be used for personal care, transportation and packaging to name but a few (Table 1.1).

It has to be pointed out, that the conversion of carbohydrates has a long history, but the practical applications of some selected reactions on a large scale is still at an infant stage as this field of research only started in the 1990s whilst petrochemical processes have been thoroughly studied and continuously developed since the early 1900s. The purpose of this short review is to give a brief overview of the main platform chemicals and their chemical synthetic routes, in order to set the basis for the comparison of what can be achieved with photochemical processes and if this new promising route can be practically viable and not just a mere academic curiosity.

1.3.1 Pretreatment of Carbohydrates from Biomass

The complex structure of the raw feedstock and the presence of multiple inter-penetrating layers make pretreatment processes necessary to be able to extract the various fractions (cellulose and hemicellulose) from lignin. Usually, the pretreatments involve the physical-chemical transformation of the raw material by ball milling, steam explosion, and acid or

Table 1.1 Some of the platform chemicals obtainable from biomass, their bio-derived chemicals and possible applications.
Adapted from Chatterjee et al. [49].

Platform chemical	**Bio-derived Chemical**	**Application**
C_5,C_6 sugar alcohols (sorbitol, xylitol, etc)	Ethylene and propylene glycol	Solvents, cosmetics, plastics, detergent
C_3 Acids (malonic, propionic)	Propionyl acrilate, pharmaceutical intermediates and reagents	Water and gas purification cleaning products, fertilizers, pesticides and preservatives
C_6 Acids (gluconic, glucaric)	Esters, lactones	Comestics, pharmaceuticals, preservatives, intermediates
Furfurals	Furan derivatives	Polymers, adhesives, fuels, resins, coatings, textiles
Levulinic Acid	Succinates, γ-valerolactone 2-methyltetrahydrofuran, 1-4,diols	Plastics, packaging, fuels insulator agents, coatings, textiles
C_1 and higher alcohols	Formaldehyde, carbonates, primary alcohols	Fuels, solvents, gas purification lubricants, detergents, flocculant, coatings
(α, ω) Diacids (succinic, malic, etc.)	THF, 1,4 butandiol esters γ-buyrolactone, diamines	Resins, crosslinkers, specialty chemicals, chelators water cleaners, disinfectants cosmetics, detergents

base treatment [107, 201]. The isolated fractions can then be further converted via enzymatic, chemical and thermochemical treatments. These steps are energy demanding and they are the main drawbacks in the large scale utilization of biomass as feedstock as, at the moment, they are not cost-effective [111].Some of the advantages and disadvantages of the downstream processing of biomass have been highlighted in a recent review by Chatterjee et al. [49] and an adapted extract is reported in Table 1.2.

It is then clear, how the conversion of carbohydrates in commodity chemicals must be tackled from a multidisciplinary perspective as the nature of the raw material requires new processes, new catalysts and different down-stream purification processes, but the analysis of these variables exceeds the scope of this discussion. What will be discussed

Table 1.2 General advantages and disadvantages of the most common routes for biomass transformations.
Adapted from Chatterjee et al. [49].

	Biomass Transformation Routes		
	Thermochemical	**Bio-processes**	**Chemical Conversion**
PROS	• Fast process • Hydrogenation and Hydrogenolysis can be performed unlike with bio-processes • Ideal for biofuels production	• Mild reaction conditions • High selectivity towards desired products • No need to protect functional groups • Processes are scalable	• Wide range of operating conditions • Catalysts can be easily modified • One-pot multistep reactions can be performed • Hydrogenation and Hydrogenolysis can be performed unlike with bio-processes
CONS	• Energy demanding • Limited choice of catalysts • Not used for synthesis • Pyrolysis requires dry feedstock	• Enzymes and starting materials are expensive • Narrow operating conditions • High volume of waste produced • Purification and work-up of the products are complex	• Toxicity of reagents used • Catalyst stability and recyclability • Protection of functional groups is necessary

instead, are some of the main reaction pathways investigated to convert the treated material (glucose, sucrose, cellobiose, etc.) and highlight the main oxidation reactions present in the literature for the production of the chemical intermediates shown in Table 1.1. It is possible to chemically convert carbohydrates in one-pot reactions such as oxidations, esterifications, and etherifications in which the -OH groups present on the carbon backbone are converted without altering the carbon chain. Degradation reactions are defined by the alteration of the polymerization degree or of the carbon structure of the monosaccharides and are often undesired side-reactions. One of the green strategies recently adopted is to try and introduce functional groups in the macropolymer without cracking them into fine chemicals, as this approach is typically a single-step process and does not require intensive purifications downstream processes. The so functionalized macropolymers have found applications in resins, paper, lubricants, packaging and surfactants. Nonetheless, the basic chemistry knowledge was developed studying the properties of simpler system by analysing probe molecules such as glucose, cellobiose, lactose *etc*. In fact, most of the recent literature still focuses both on the one-pot reactions using cellulose as a substrate and glucose and

cellobiose due to the variety of substrates available and the different composition of each feedstock.

Oxidation of Mono and Disaccharides

The oxidation of sugars is well known, and it is usually performed under mild conditions (T<100°C) using transition metal catalysts, mineral acids and organometallic complexes in a wide range of pH values (6-9) and using air or oxygen as oxidants (Figure 1.3). Detailed mechanistic and kinetic studies are now available to further tailor new catalysts. For homogeneous catalysis, NaClO and 2,2,6,6-tetramethylpiperidine-1-oxyl (TEMPO) is the most recent advance in the oxidation of carbohydrates and it allows the reaction to run at low temperature (0-15°C) with high yields towards the oxidised products (60-90%) as it allows for the generation *in situ* of the oxidant species [69] .The main drawback of this catalyst is that it has to be regenerated using secondary oxidising agents such as NaClO/NaBr or peracetic acid and the use of halogenated compounds limits the practical usage of this system [41, 40, 43]. As regards heterogeneous catalytic systems, supported metal catalysts (Pd, Pt,

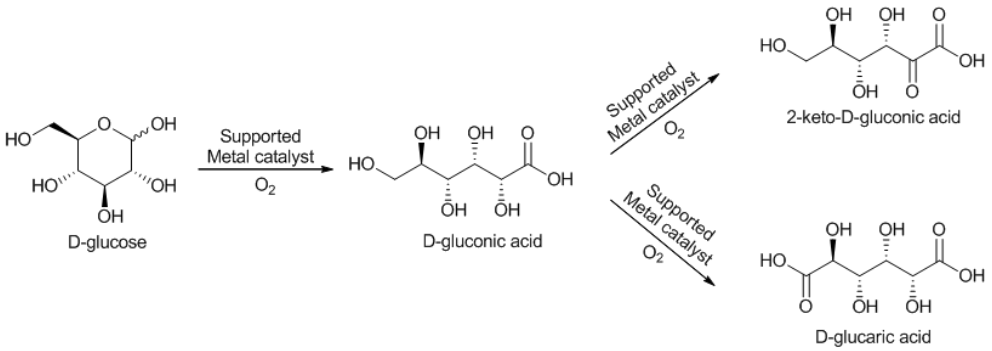

Figure 1.3 Glucose oxidation pathway to the corresponding C_6 acids with metal supported catalysts.

Au) on activated carbon, Al_2O_3, TiO_2 or SiO_2 are common catalysts as the regioselectivity of the oxidation process can be controlled as it is an important parameter for pharmaceutical intermediates (Table 1.3). Some drawbacks of these materials are due to the leaching of

the metal in solution with the subsequent loss of catalytic activity which directly affect the lifetime and the recyclability of these materials.

Table 1.3 Selected examples of the different heterogeneous catalysts used in the glucose oxidation reaction

Catalyst	Reaction Conditions	Glucose Conversion (%)	Gluconic Acid Selectivity (%)	Reference
Pd/C, 2 wt%	60°C, pH 9, 7 hrs	95	96	[71]
Pd/Al_2O_3	50°C, pH 9	100	95	[149]
Au/Al_2O_3 0.3 wt%	50°C, pH 9.5, 1 equiv H_2O_2	71	100	[195]
Pt-Au/TiO_2 4 wt%	119°C, 28 bar O_2	71	45	[178]
Au/activated C 0.9 wt%	100°C, pH 9.5	99	95	[29]

In addition to the oxidation of monosaccharides, the oxidation of disaccharides such as maltose, sucrose, cellobiose and lactose has been investigated [180, 27, 140].In two recent papers Amaniampong et al. [7],[8], investigated the oxidation of cellobiose using Au/TiO_2 and Au-based bimetallic catalysts. With the Ru-Au/TiO_2 catalyst 100% cellobiose conversion was obtained after 12 hours of reaction at 145°C with 10 bar of O_2 pressure. Interestingly, the main reaction product was not cellobionic acid but a wide range of smaller chain carbohydrates with a 86.7% selectivity towards gluconic acid. Scheme 1.1 shows the

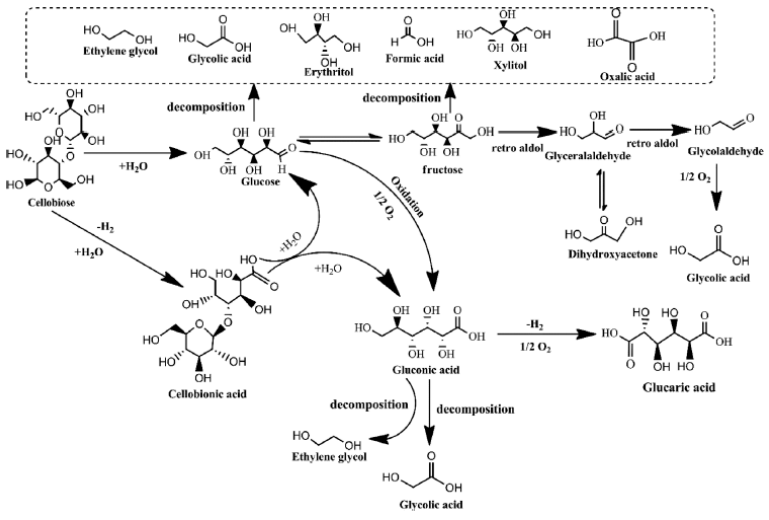

Scheme 1.1 Suggested reaction pathway of the cellobiose conversion to gluconic acid and other derivatives. Taken from Amaniampong et al. [7].

possible reaction pathway for the conversion of cellobiose to a wide range of smaller carbon

chain molecules. It is clear how the selectivity towards the formation of the corresponding acid is negligible as the hydrolysis and oxidation of the monosaccharides appear to be the prevalent reaction pathways. On the other hand, lactose is reported to successfully oxidise to the corresponding lactobionic and 2-ketolactobionic acid (similarly to what has been observed with glucose as a substrate) using a wide range of bimetallic catalysts (Pd-Bi, Pt-Bi, and Au-Pd) on various supports (SiO_2, CeO_2, activated carbon and Al_2O_3) with the Au supported catalysts on SiO_2, CeO_2[180, 27, 140] showing 100% selectivity to the lactobionic acid at 65°C and pH 9 [104, 160]. Overall, by analysing these results it appears clear how the structure and the three-dimensional conformation of the disaccharide deeply affects its reactivity and product distribution.

1.4 Photocatalysis

Photocatalytic processes differ from electrochemical transformations as the oxidised and reduced intermediates are generated *in situ* on the surface of the photoactive material. Additionally, they differ from conventional catalytic processes by their activation mechanism as the thermal energy required to activate these photoactive metal oxides, is replaced by the incident irradiation which lowers the activation energy of the processes and allows for milder reaction conditions, thus making this process more suitable for partial oxidation reactions in the liquid phase due to the possibility of controlling the selectivity and the production of the desired intermediates [194]. There are also some profound similarities between the surfaces properties of a photoactive material and a conventional catalyst. In fact, the nature of the semiconductor, its band gap value and the adsorption-desorption properties of the material determines whether or not the reaction will occur. The ideal photocatalyst or photoactive material should fit several criteria in order to be appealing for practical uses such as: it should be inert in biological and chemical environments, stable photochemically by avoiding photo-corrosion phenomena [58], cheap and easy to synthesise, activated efficiently by solar

light, versatile towards a plethora of reactions and present low risks for the environment or living organisms [47]. TiO_2-based materials are close to being ideal photocatalysts as they fulfil most of the necessary prerequisites, albeit being easily activated by solar light due to their band gap position. Therefore, several strategies have been applied to extend the activation of this material in the visible range of the electromagnetic spectrum and will be analysed in this chapter. Generally, photo-initiated reactions can be described as follows:

$$(Ox\ Species_1)_{ads} + (Red\ Species_2)_{ads} \xrightarrow[Semiconductor]{E_g \leq h\nu} Red\ Species_1 + Ox\ Species_2 \quad (1.5)$$

If the variation of the Gibbs free energy (ΔG_0) is positive the reaction might be an example of photosynthesis, if negative a photocatalytic process might be on going. Specifically, when TiO_2 is used as photocatalyst, the $\Delta G_0 < 0$ implies that most of the reactions are photocatalytic rather than photosynthetic [25]. Functional groups of organic substrates can undergo several chemical transformations in inert solvents. The prerequisite for an appreciable conversion of the substrate is the presence of non-bonded lone pair or π-orbitals which might display an oxidative reactivity when TiO_2 is used and might undergo several transformations such as deoxygenation, dehydrogenation, or oxidative cleavages.

On the other hand, it is possible to impart a reducing character to the system by removing oxygen and proton sources in the system, nonetheless, the efficiency of these process will be lower than the ones previously described for two reasons: (1) the reducing power of the electrons in the conduction band (e^-_{cb}) is generally lower than the one observed for the holes in the valence band (h^+_{vb}), and (2) many of the groups which can be reduced do not compete with oxygen in trapping the conduction band electrons. For these reasons, the research performed on photo-reduction reactions is mainly focused on the reduction of CO_2 [117, 144, 234, 176].

1.4.1 Semiconductors and Photocatalytic Activity

Semiconductors in general can be divided in two categories, n-type and p-type materials. In n-type semiconductors the concentration of the electrons is greater than the hole concentration, hence the electrons are the main energy carriers and this imparts a negative charge to the material. In an n-type semiconductor, the Fermi level is at a higher energy level than the one of an intrinsic semiconductor and lies closer to the conduction band than to the valence band. On the contrary, p-type semiconductors have holes as primary energy carriers and the Fermi level lies closer to the valence band rather than to the conduction band as for n-type materials. P-type semiconductors can be prepared by doping an intrinsic semiconductor with acceptors impurities. Due to the oxygen vacancies in the lattice structure, TiO_2 is an n-type

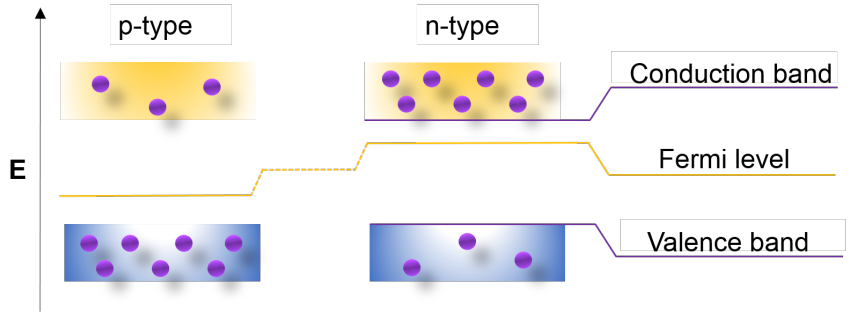

Figure 1.4 Typical n-type (left) and p-type (right) semiconductor schematic structure. The top band is the conduction band (cb), whilst the bottom one is the valence band (vb). The shift in the Fermi level value can also be observed if compared with an intrinsic semiconductor.

semiconductor, and the vacancies are formed according to the following reaction:

$$O_o^x \xrightarrow{TiO_2} V_o^{hh} + 2e^- + \frac{1}{2}O_2 \tag{1.6}$$

The representation of the defects with the Kröger-Vink notation explains that within the TiO_2 structure a positive oxygen vacancy (V_o^{hh} , +2 charge) is formed upon the subsequent release of molecular oxygen and two electrons, and this process is commonly achieved by heat treating the material in oxygen-poor environments.

Generally, photocatalysts can be characterized by their ability to adsorb multiple species simultaneously and these reactants can either be reduced or oxidized with the activation of the material through an efficient photonic absorption (E_g<hν). In Figure 1.5 several band gap values are represented along with some standard redox couples. To observe the photo-initiated electron transfer mechanism, the position of the redox couples value has to be within the band gap value of the semiconductor. The energy level at the bottom defines the reduction potential of the photoelectrons, whilst the value at the top of the conduction band depicts the oxidation properties of the holes, thus providing information on the capability of the material to promote oxidation or reduction reactions. The third important parameter is the

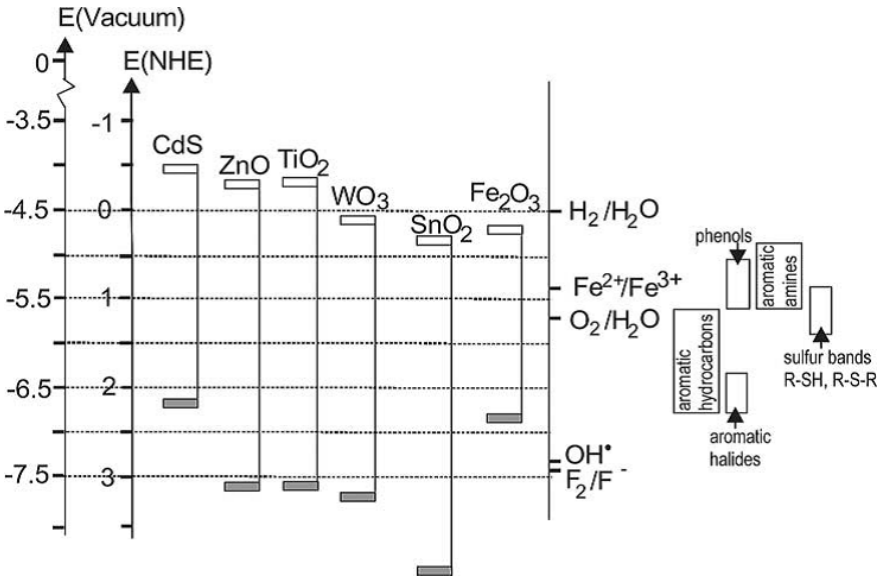

Figure 1.5 Band positions (top of valence band and bottom of conduction band) of several semiconductors [47].

flatband potential (V_{fb}) which locates the energy of the photo-generated electrons and holes on the surface of the material at the interface with an electrolyte solution. Different values can be found depending on the nature of the material, the presence of different electrolytes in solution and on the system equilibrium. It is clear then how molecules can be either reduced by the conduction band electrons if they possess redox potentials more positive than the V_{fb}

or oxidized by the positive holes on the valence band if they have redox potentials lower than the V_{fb}.

The flatband potential can also be influenced by the pH or the ionic strength of the reaction medium, and the variation of the V_{fb} value follows a Nernstian pH dependency with a -59mV decrease per pH unit. This pH dependency directly influences the properties and the ability of the photogenerated electron/hole pair to drive redox reactions. By simply looking at this representation it is then possible to predict if a reaction will occur photochemically, or to design and engineer new materials to satisfy the thermodynamic requirements [35, 36, 85, 197, 209].

Due to the lack of a continuum of intraband states, semiconductors have the peculiar property of assuring long lifetime of the electron/hole pair partially avoiding their recombination, allowing the diffusion of these reactive species towards the surface of the material.

Because TiO_2 exists in different polymorphs, the difference in the band gap values of 3.2 eV for anatase and 3.02 eV for rutile, can be explained with the different crystalline structure and this difference directly affects the absorption threshold values of 384 nm and 410 nm respectively for the two polymorphs. The absorption values are also influenced by the particle size, the amorphous content, and generally blue shifts (0.2 eV) are observed for nanosized TiO_2 materials in the range from 5-10 nm [139, 196].

1.5 Photochemical Processes

Photoactive materials have been used in several fields, from nanomedicine, water splitting reactions, to water streams purifications, and in organic synthesis. In this section, photoreforming of bio-derived molecules and the degradation of organic compounds, specifically dyes, will be discussed to point out the differences and the parameters to be tuned to obtain selective photochemical processes.

1.5.1 Photoreforming

Photoreforming processes are based on a series of consecutive steps, and they all start with the absorption of a photon by a semiconductor material with the subsequent promotion of an electron to the conduction band and the formation of a positive hole in the valence band. This charge separation is the driving force of all photochemical reactions, the longer the recombination time, the more efficient the material will be in harvesting light. The band gap is the energy barrier that photons have to at least to match in order to promote electrons and the values have to be between 1.23 eV (1008 nm) and 3 eV (414 nm) in order to harvest the solar light efficiently. At values lower than 1.23 eV the energy of the photons is not enough to drive chemical reactions further and IR harvesting materials are required [245, 161]. The general low efficiency of photochemical reactions is generally due to several factors such as inefficient illumination due to light scattering or reflection phenomena, poor absorption due to the material characteristics and to the fast electron/hole recombination rate. In order to overcome the recombination rate several strategies can be applied, such as the decoration of the semiconductor surface with metal nanoparticles. In fact, small amounts of metal act as co-catalysts and are able to harvest the electrons thus slowing down the recombination process. Additionally, protons can harvest these electrons to produce H_2 and sometimes this side reaction is not desired if photoreforming or water splitting are not the target reactions. For this reason, metals should have lower overpotential values than H_2; practically, if a metal has a lower overpotential than the half reaction thermodynamic reduction potential it will promote the production of H_2 from water (Table 1.4). In addition to the production of H_2, if the metal has the proper work function, the excited electrons will tend to migrate towards the metal itself until the two Fermi levels will be aligned and the strong metal support-interaction, or Schottky barrier, enhances the electron scavenging tendency of the metal thus decreasing the overall electron-hole recombination. In fact, it has to be noted that the synergistic effect of the metal-support heterojunction in ameliorating the properties of the material is also

Table 1.4 Overpotential values for several metallic electrodes for the hydrogen and oxygen semi-reactions.

Material of the electrode	**Hydrogen**	**Oxygen**
Platinum (platinized)	-0.07 V	+0.77 V
Palladium	-0.07 V	+0.93 V
Gold	-0.09 V	+1.02 V
Iron	-0.15 V	+0.75 V
Platinum (shiny)	-0.16 V	+0.95 V
Silver	-0.22 V	+0.91 V
Nickel	-0.28 V	+0.56 V
Graphite	-0.62 V	+0.95 V
Lead	-0.71 V	+0.81 V
Zinc	-0.77 V	
Mercury	-0.85 V	

influenced by the concentration and the proximity of the metal nanoparticles on the surface. Specifically, if the metal centres are too close to each other, the distance between the trapping sites is not enough to avoid the electron hole recombination [60, 101]. Therefore, it is necessary to find the optimum loading according to the surface are and the porosity of the material [147]. Finally, the conventional spill-over mechanism over metal nanoparticles also plays an important role in the photo-production of H_2. On the other hand, if electrons tend to move towards the surface of the semiconductor, so do the positive holes, and these species are responsible for the photo-oxidative processes of the adsorbed molecules on the catalyst surface. It becomes then clear how the ability of organic substrates to scavenge and adsorb on the catalyst surface are key factors in the electron/hole recombination and in the economy of the process [142]. On the surface of a semiconductor the oxidation and reduction processes can happen simultaneously, and the selectivity on one reaction mechanism over the other, is imparted with the choice of the substrate, the tuning of the reaction conditions, but most importantly by the different time-scale of the two steps; the photo-generation of the e^-/h^+ couple occurs within a few femtoseconds, whilst the recombination time is 6 order of magnitude greater (10-100 ns) [137, 95, 146, 128]. The kinetics of an electron-mediated oxidative reaction is in the order of milliseconds, whilst the hole-mediated reductive process

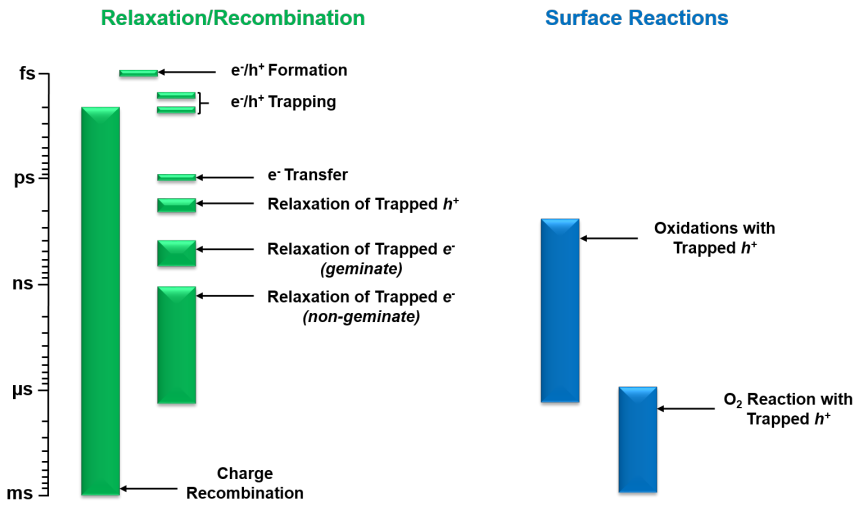

Figure 1.6 Time scales of fundamental steps occurring during a photocatalytic process. Taken from Kubacka et al. [137].

takes approximately 100 ns. It is clear that, in order to obtain selective oxidation processes, it is mandatory to increase the mobility of the electrons and their lifetime by trapping them around metal centers, or with a similar approach, adopt an appropriate hole scavenger to avoid the recombination [23, 208].

1.5.2 Photoreforming of Carbohydrates

The main application of photocatalytic processes is in the degradation of pollutants and contaminants and in water-splitting processes, and the latter, despite promising results, is still affected by low efficiency thus making it unappealing for practical applications given the current state of the art. Water is not the only green source of H_2 as many bio-derived molecules are hydrogen rich, albeit at a lesser extent than olefins or other saturated aliphatic compounds. Nonetheless, the possibility of extracting a combustible gas from green and renewable sources is an interesting perspective, specifically if one considers the huge amount of solid and liquid waste produced worldwide which has to be treated and disposed of nowadays mainly via biological and fermentative processes. In the early 1980s, Kawai and Sakata in a pioneering work a few years after the discovery of the TiO_2 photoactivity under

UV light, assessed the feasibility of the production of H_2 from sugars and soluble starch using a $RuO_2/TiO_2/Pt$ mixture, reporting for the first time a successful photoreforming process in aqueous solutions. Additionally, the activity of the substrates was reported as a function of the molecular size of the substrate (starch<sucrose<glucose) with glucose being the most reactive substrate [123]. It is known that the polyols hole scavenging efficiency can be correlated with the number of hydroxyl groups present in the molecular structure. With time-resolved transient spectroscopy, it was possible to monitor and assess the scavenging properties of C_2-C_6 polyols and it was found that carbohydrates could neutralize 50-60% of the holes generate on the TiO_2 surface in approximately 6 ns [34, 215–217]. The sacrificial action of these molecules allows for a more efficient combination between the valence band holes than water thus enhancing the H_2 production compared with the water splitting reactions. The abundance of hydroxyl groups in carbohydrates generally leads to an increase activity until the molecular structure reaches a critical mass and it becomes too bulky and the accessibility of the functional groups is limited by steric hindrance or by the formation of thick hydrogen bonds network. This intricate structure directly affects the solubility and the properties of polysaccharides, thus explaining why cellulose is such a recalcitrant substrate towards solubilisation, hydrolysis and conversion to valuable chemicals under mild conditions and conventional chemical processes. The exploitation of photoreforming processes on biomass derived compounds has been tested on several substrates such as alcohols, organic acids, carbohydrates (glucose, mannose, arabinose, fructose and ribose)[135, 37, 38], and generally, the ratio of H_2/CO_2 is in good agreement with the stoichiometry of the total mineralization of carbohydrates to produce CO_2 and H_2 (Eqn. 1.7):

$$C_xH_yO_z + (2x-z) \rightarrow xCO_2 + (2x-z+\frac{y}{2})H_2 \tag{1.7}$$

It has also been found that the H_2 production is strongly influenced by the concentration and the structure of the substrate and, to a lesser extent, by temperature and pH.

1.5.3 Selective Photocatalytic Processes

Selective oxidation reactions, if compared with the degradation of pollutants, are a much more interesting application of photoactive materials for the production of fine chemicals. Recently, Zhang et al. [254] reported the oxidation of alcohols to aldehydes using Au nanoparticles supported on zeolites at room temperature and under visible light, moreover, Ag/Al_2O_3 was used to catalyse the epoxidation of ethylene oxide, in addition to CO and NH_3 oxidation under visible light and these are just two cases of the well reported activity of metal supported nanoparticles [54]. It is clear how, despite the complexity of photochemical reactions, the difficulty in identifying the reactive species involved, and the challenges the design and tailoring of the properties of the material, there is a growing interest in applying the current know-how in the oxidation of probe molecules to the more complex bio-derived substrates. Lignocellulosic substrates can be transformed using conventional processes (see Section 1.2), but, additionally, under UV irradiation, they undergo oxidative degradation reactions. Early studies in 1944 by Stillings and Nostrand [223] showed the possible production of CO, CO_2 and some reducing sugars from cellulose , a few years later, the degradation of filter paper was reported to produce oxygenated hydrocarbons upon irradiation [103, 74] and more recently, in 2011 Fan et al. [86] reported the one-pot degradation of cellulose to hydroxymethylfurfural (HMF) under UV irradiation using a concentrated $ZnCl_2$ solution and a supported TiO_2 catalyst. The results are somewhat difficult to interpret due to the different experimental conditions used, but generally, show that it is possible to convert natural polymers to platform chemicals using photoactive materials. Specifically, the selective photo-oxidation of biomass, could potentially supply a wide range of high-value chemicals to the pharmaceutical, food and automotive industry, as most of the obtainable substrates can be found in the top 12 sugar derived platform chemicals identified by the U.S Department of Energy in 2004[243], and more recently this list has been revised by Bozell and Petersen [39]. Most importantly, the selective oxidation of alcohols to carbonyls is one of the most

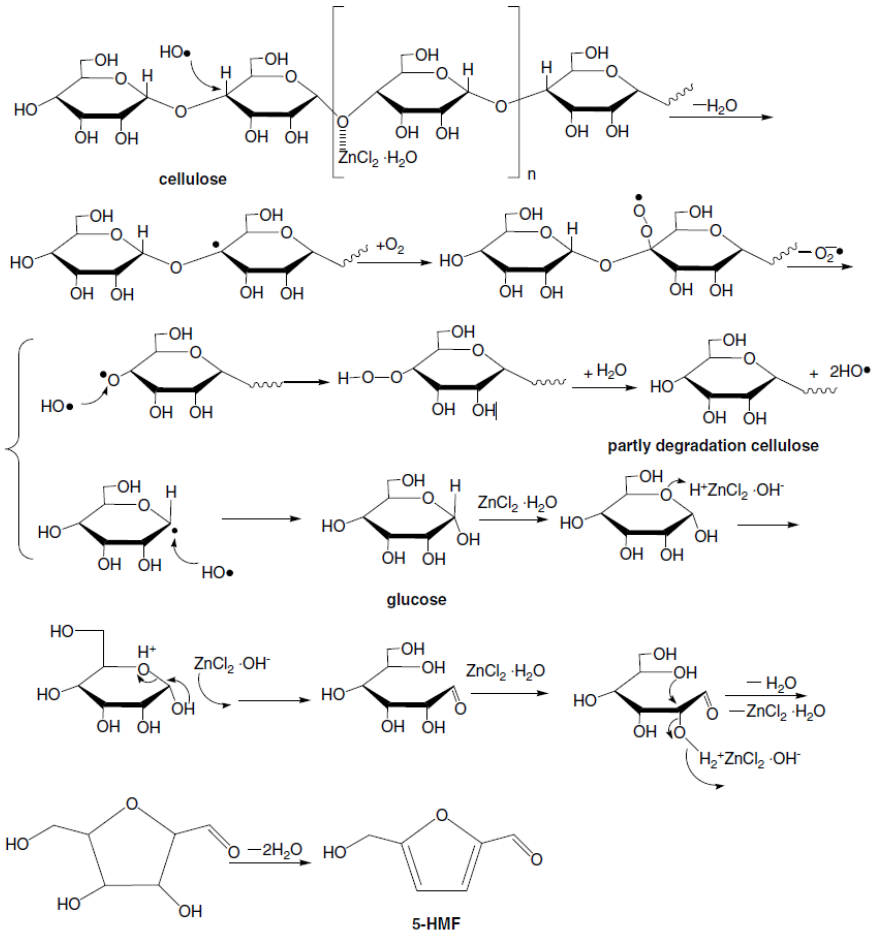

Figure 1.7 Suggested mechanism for the one-pot degradation of cellulose to HMF.[86].

important industrial processes in the chemical industry. In fact, ketones, aldehydes and carboxylic acids are precursors for many drugs, vitamins, food preservatives, fragrances, and other important organic intermediates [112, 240, 2]. Most of the industrial processes use strong mineral acids or toxic oxidants and require high temperature and pressure to overcome the thermodynamics of the reactions and guarantee high volume production rates [112, 55]. It also has to be noted that only the aldehydes and ketones that are stable under those conditions can be synthesised, whilst photocatalytic dehydrogenation occurs at room temperature and therefore, represents a really interesting alternative for the production of aldehydes. The photo-oxidation of C_1-C_4 alcohols in the liquid phase is well known specifically for the oxidation of 2-propanol, and it was found that in the presence of oxygen these molecules

can be oxidised to the corresponding aldehydes or ketones [16, 159, 158, 106]. Colmenares et al. [63][61] recently reported the oxidation of glucose to glucaric and gluconic acid under UV irradiation with good selectivity values using TiO_2 based photocatalysts (Figure 1.8). From the literature, it is clear how there is discontinuity in the choice of the substrate used,

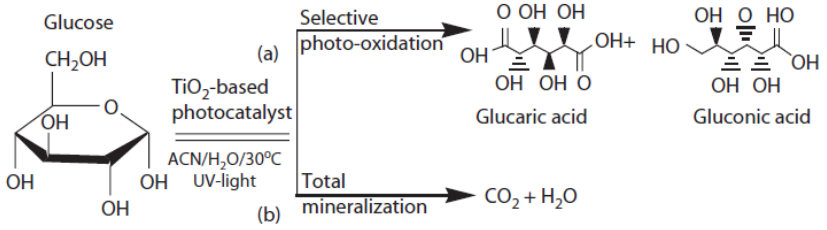

Figure 1.8 Reaction mechanism proposed by Colmenares et al. [61] for the photo oxidation of glucose to glucaric and gluconic acid.

as one would think to gradually increase the complexity of the substrate, but actually, the first results were obtained with cellulose, and research moved on to study, only recently, the simplest monosaccharide available from cellulose and hemicellulose, analyse its adsorption properties and the chemistry involved when this polyol is used. The use of probe molecules is common in conventional heterogeneous catalysis of bio-derived molecules, in fact, phenols are used instead of lignin, cellobiose is used instead of cellulose and other xylans are used to investigate hemicellulose. The limitations of this approach are clear as several properties are dramatically influenced by the size of the substrate, nonetheless, it is necessary to obtain a deep understanding of the reaction mechanisms of the single molecule, to try and predict, and design better performing catalysts.

1.6 Plasmonic Photocatalysis

As stated earlier on, photocatalysis is expected to play an important role in tackling energy challenges and the need to run chemical reactions under mild conditions, and in order to achieve these milestones, it is necessary to extend the range of activity of the most used semiconductors (TiO_2, ZnO) to the visible light part of the electromagnetic spectrum to effectively use the sunlight, as at ground level 43% of the solar irradiation is visible, and only the 4% currently harvested by TiO_2-based materials is due to UV light whilst the remaining 52% is infrared irradiation. Plasmonic photocatalysis is a recent technology and the term was first introduced by Awazu et al. [20] in 2008 and it has gained momentum as a promising route for "high-performance" photocatalysis [253]. Noble metal nanoparticles (i.e Pt, Au, Ag) strongly absorb visible light at different wavelengths due to the surface plasmon resonance (SPR), and this property can be tuned by varying the size, shape, and the physical-chemical environment surrounding the particles. It is well known since medieval times that gold can absorb visible light and this metal has been used to impart colour to stained glass in churches for centuries. The strong interaction between the metal centres and the incident visible radiation, is now being studied as a promising route to convert sunlight in chemical energy and to use it as the main driving force in chemical reactions. In fact, several examples are available in the literature on the application of plasmonic nanoparticles in several reactions, from various organic reactions (eg. oxidations [254] and hydroaminations [255]) and, most importantly, for the purification of water streams[100] from organic dyes [6] and other pollutants [242]. The deposition of metal nanoparticles on the semiconductor surface enhances several times the overall activity due to the beneficial effect of several factors as shown in Figure 1.9. The strong resonance of the free electrons in the metal nanoparticles (LSPR) is the most prominent feature of plasmonic photocatalysis for several reasons which can be summarised as follows [150, 206, 260, 225]:

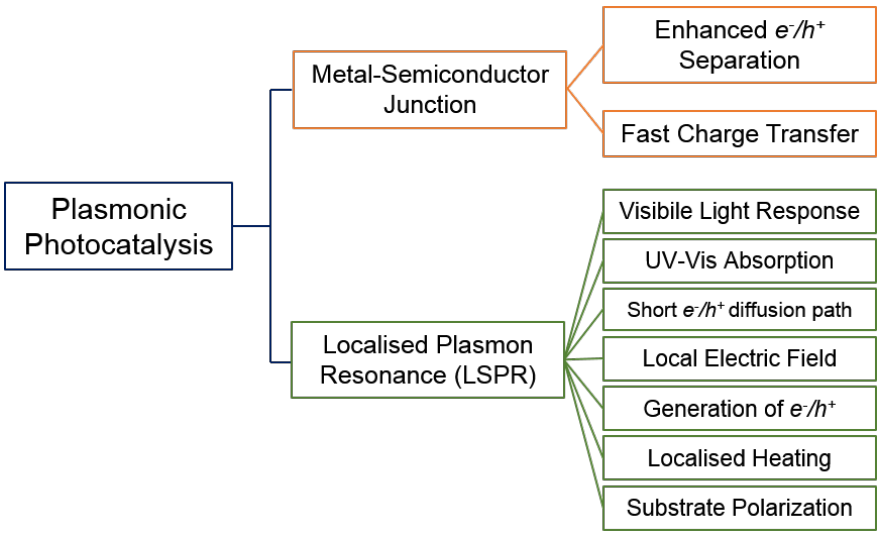

Figure 1.9 Beneficial contribution of several factors in plasmonic photocatalysis.Adapted from [253].

- Resonance frequency of Au and Ag can be tailored by varying the size, the shape and the environment surrounding the particles.

- The presence of LSPR enhances the adsorption of low band gap photocatalysts such as CdS and Fe_2O_3 under both UV and visible light.

- This process is characterized by the adsorption of light on a very thin layer below the surface of the material and this feature shortens the distance the charge carries have to cover to surface again thus reducing their recombination rate.

- The formation of a strong electric field during the LSPR, enhances the production of electrons and holes and prevents their recombination

- The overheating of the metal nanoparticles exposed to visible light irradiation favours the reaction rate of redox reactions along with the mass transfer properties.

- The electric field charges on the metal centres, impart polarizing properties to the nanoparticles this increasing the substrate adsorption affinity of the material.

The presence of metal nanoparticles does not automatically imply an enhancement of the material properties, and in some cases, the effects might be detrimental. In fact, if the metal centres are embedded too deep in the semiconductors surface, or if the loading of the metal is too high, the metal centres can actually act as charge recombination centres causing lower photocatalytic efficiency values.

1.6.1 Plasmonic Photocatalysis Mechanism

In detail, the SPR of a metal is the collective excitation of the free metal electrons due to the oscillating electric field of the electromagnetic radiation (Figure 1.10). When the oscillation

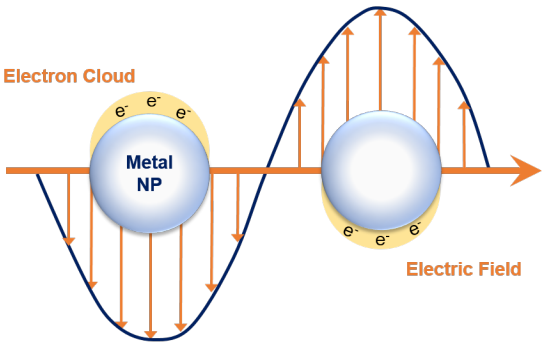

Figure 1.10 Schematic representation of the plasmon resonance due to the coupling of the oscillation frequency of the electromagnetic radiation with the free metal conduction electrons.

frequency satisfies the polarizability condition, which for a metallic sphere can be described as:

$$\alpha = 3V\varepsilon_0 \frac{\varepsilon - \varepsilon_m}{\varepsilon_m + 2\varepsilon_m} \tag{1.8}$$

In which V is the volume of the nanoparticle, ε_0 is the vacuum permittivity and ε_m is the dielectric constant of the medium surrounding the nanoparticle. The fascinating properties of the LSPR can be found taking a closer look to the denominator of equation 1.8. Without deriving the full expression which can be found elsewhere [126], when the frequency (ω) of the electromagnetic radiation reaches the value which satisfies the combination of the complex dielectric function of the metal $\varepsilon(\omega) = -2\varepsilon_m$ the resonance occurs. It is also clear,

how in addition to the direct dependency of the SPR to the electromagnetic frequency, the reaction medium properties also have dramatic effects on the intensity and the positioning of the LSPR band. The Mie theory just described, provides a rigorous description of the phenomenon for particles up to 100 nm as above this size, some of the approximations regarding the distribution of the charges on the metallic surface and the phase changes of the oscillation frequency over the volume of the particle are not valid [91, 203, 126]. If compared with the conventional semiconductor photocatalysis, there are two distinctive differences in plasmonic processes; the presence of a Schottky junction at the interface of the metal nanoparticle and the semiconductor surface, which allows for the build-up of an electrical field in the so called space-charge region in the bulk of the material but in close proximity to the metal/semiconductor interface (Figure 1.11). Additionally, the metal acts as charge-transfer centre by trapping charges on the metallic surface and creating active sites for photo-reactions. The coexistence of the space-charge region, the Schottky barrier and the charge-trap centre, impart different movements to the photo-generated electrons thus avoiding the electron-hole pair recombination and increasing the lifetime of the active species. As shown in Figure 1.5, semiconductors are described by their band gap position which determines the cut-off absorption wavelength and the energy of the conduction band electrons (E_{cb}) and the energy of the holes in the valence band (E_{vb}). When coupled with metal nanoparticles, this representation, needs to take into account the work function of the metal along with the electrochemical potentials of the redox couples (Figure 1.12). The band gap energy can be defined as $E_g = E_{cb}\text{-}E_{vb}$ and the e^-/h^+ pair is generated when the electromagnetic radiation energy is higher than the band gap than this value. As soon as these charge carrier species are generated they are available to be transferred to the other

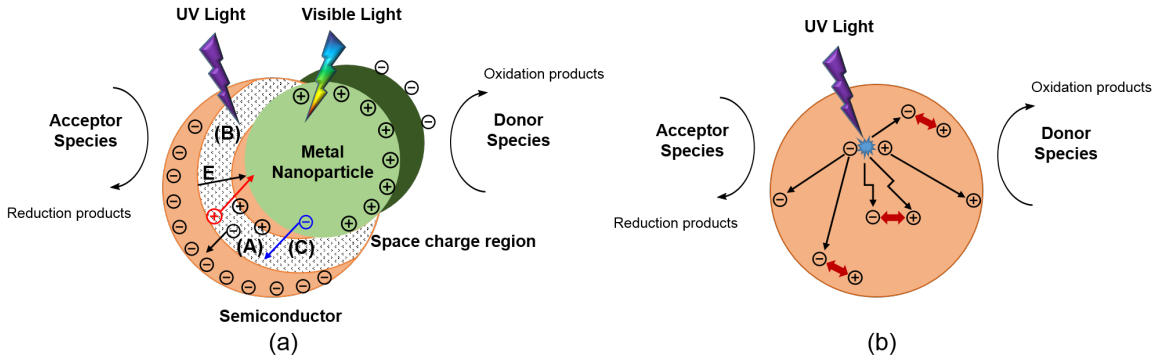

Figure 1.11 Representation of the main differences in plasmonic photocatalysis (a) compared with conventional semiconductors processes (b). The n-TiO_2 particle displayed (a) is used as an example in conjunction with a metal nanoparticle. The presence of the nanoparticle forms the space-charge zone (E) with the electrons moving from the particle to the semiconductor (A) (whilst the electric field generated has opposite direction); it has to be noted that for a p-TiO_2 particle, the movement of the electrons and the electric field generated would be in opposite directions. When n-TiO_2 is not decorated with metal nanoparticles (b) the recombination of the electron-hole pair is more severe causing a less efficient process.
Adapted from Zhang et al. [253].

molecules. The system can be described as follows:

$$A + e^-_{cb} \rightarrow A^- \tag{1.9a}$$

$$D + h^+_{vb} \rightarrow D^+ \tag{1.9b}$$

In which an acceptor molecule can be reduced by capturing the electron (Eqn. 1.9a) or can be oxidized by donating an electron to the photo-generated hole (Eqn. 1.9b). These two processes will occur spontaneously only if the redox potentials requirements are met. Specifically, for the electron reaction (Eqn. 1.9a) the $E_{cb} \gg E_{red}$ and for the hole $E_{vb} \gg E_{ox}$. The energy level of the electrons, is set with the vacuum energy level E = 0 at the top of the diagram, therefore, for the electrons the higher the potential the higher the energy, whilst for the holes, the lower the potential, the higher the oxidation power. Therefore, just by looking at the graphical representation of the band gap potential and of the redox couples given in standard hydrogen electrode (SHE) it is possible to choose the right material for the

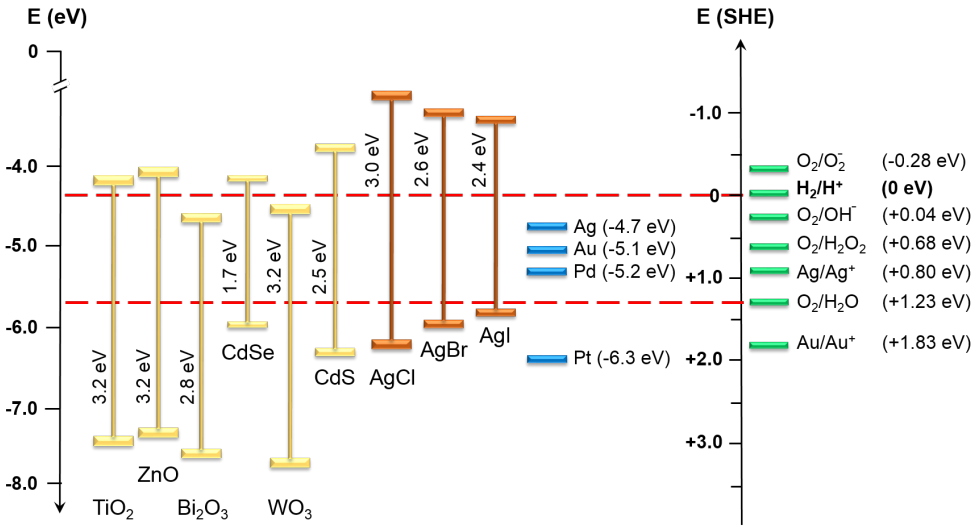

Figure 1.12 Semiconductors bandgap (left) noble metals work function (middle) and some redox couples potential values (right). Adapted from [253].

species one intends to make react. As the purpose of adding a noble metal on the catalyst surface is to enhance the reactivity, we are now going to investigate how the position and the work function values affects photochemical processes. If we consider in their original state, in a n-type semiconductor (TiO_2), the Fermi level E_f is closer to the E_{cb} and the E_{vb} is far below, a noble metal has a work function (W) and a redox couple D/D^+ is defined by its electrochemical potential E_{red}. If we consider these elements separately, E_f, W, and E_{red} could well have different values and therefore, not being aligned (Figure 1.13a). When these three components come into contact with each other, the electrons and the holes will flow to reach a new state of equilibrium at which, E_f, W, and E_{red} are aligned (Figure 1.13b). In a typical plasmonic photocatalytic process the redox potential E_{red} does not change significantly whereas the available energy of the metal and the semiconductor due to the small surface area available and the reduced number of energy states cause an alignment of the E_f and W to the redox potential. In this case, it was assumed that the E_f> E_{red}>W, and in this case the metal difference in the potential E_f>W allows the formation of the space-charge region separating the electrons and causing a upwards bending of the flatband potential (V_{fb}) thus incrementing the energy level of the conduction band E'_{cb}

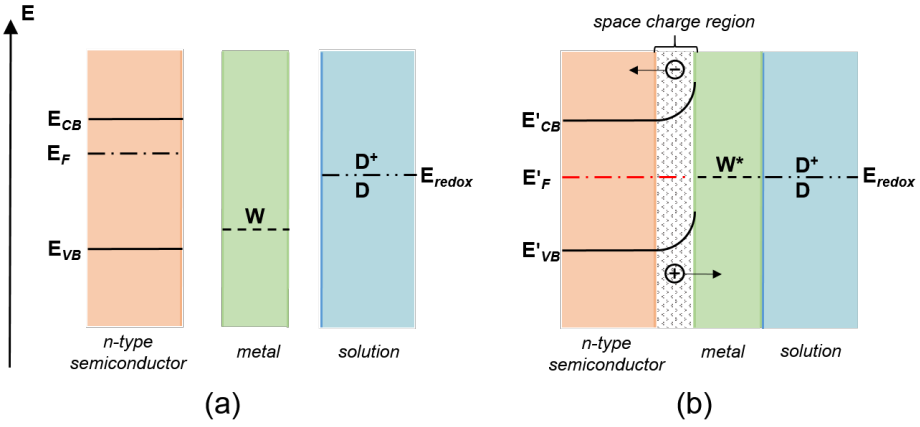

Figure 1.13 n-type semiconductor photocatalysis prior (a) and after contact (b) with the plasmonic noble metal nanoparticle. Adapted from [253].

thus incrementing the reducing potential of the electrons whilst the oxidation properties of the E'_{vb} are diminished. For a p-type semiconductor (not shown) the effect would be the opposite with the result of downwards bending of the E'_{cb} and the E'_{vb} with an increment of the oxidation properties of the holes and a diminished reducing potential for the electrons. In Figure 1.14 a typical photocatalytic process is shown in the absence of a metal, and the

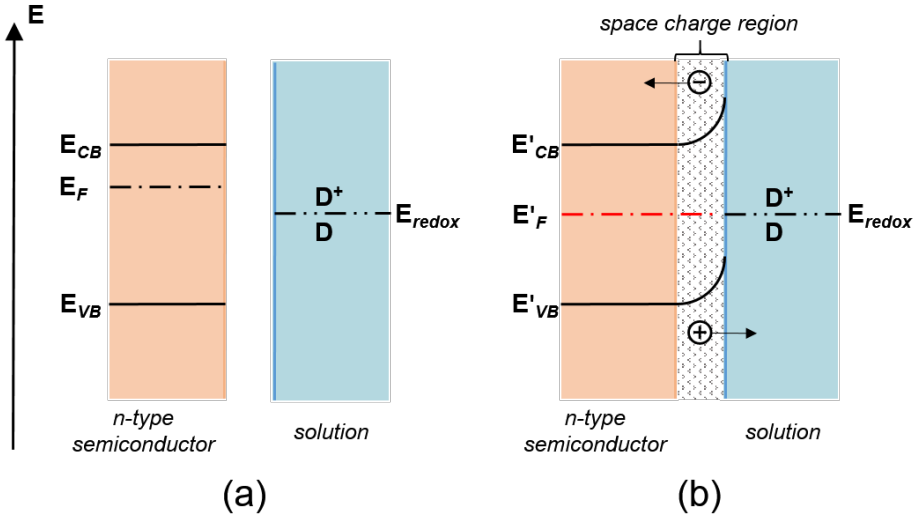

Figure 1.14 n-type photocatalysis in the absence of a noble metal before (a) and after contact with the solution (b). Adapted from [253].

semiconductor surface is in direct contact with the solution. It can be seen how the flat-band

potential is bent upwards in the space charge region if the E_f and the E_{red} do not have the same value and this bending of might have detrimental effect on the charge carrier transfer during photocatalytic processes. Variations of the flatband potential as a function of several parameters can be found in the work of Fitzmaurice et al. [35, 36, 85, 197] and Gratzel [102]. After having described the LSPR on a single nanoparticle supported on a n-type semiconductor with the formation of space charge region and the improved charge separation along variations on the potential of the E'_{cb} and E'_{vb} of a semiconductor in contact with a noble metal, it is possible to discuss the role of the metal as a nano-antennas to inject electrons in the semiconductor, also known as the LSPR sensitization effect, which plays a crucial role in plasmonic photocatalysis. In a clear representation taken from Zhang et al. [253] (Figure 1.15) in which an n-type semi-conductor is coupled with a metal nanoparticle, and shows in chronological order all the phenomena occurring upon excitation of the electrons on the metal nanoparticle. It is known that some dyes can extend the activity range of TiO_2 catalyst by injecting electrons in the conduction band of the semiconductor [52, 261] and, to a certain extent, the mechanism involving metal nanoparticles shows similar properties. In fact, when the electrons of the metal nanoparticles are exited upon irradiation, they possess higher energy than the conduction band and they can be transferred to the conduction band of the semiconductor (Figure 1.15a), once the electron redistribute themselves through relaxation mechanism, they follow the Fermi-Dirac distribution and the energy value can be higher than the Fermi level, therefore, making possible a further injection of electrons of the distribution tail with suitable energy values (Figure 1.15b). After all the available electrons have been transferred and the plasmonic energy has been dissipated, the system relaxes to its standard distribution value (Figure 1.15c). It has to be noted, that the incident photon energy $h\nu$ does not have to match the band gap of the semiconductor but, instead, it has to be greater than the difference between the flat band potential (E_{cb0}) and the Fermi level (E_f) (Eqn. 1.10).

$$h\nu \geq E_{cb0} - E_f \tag{1.10}$$

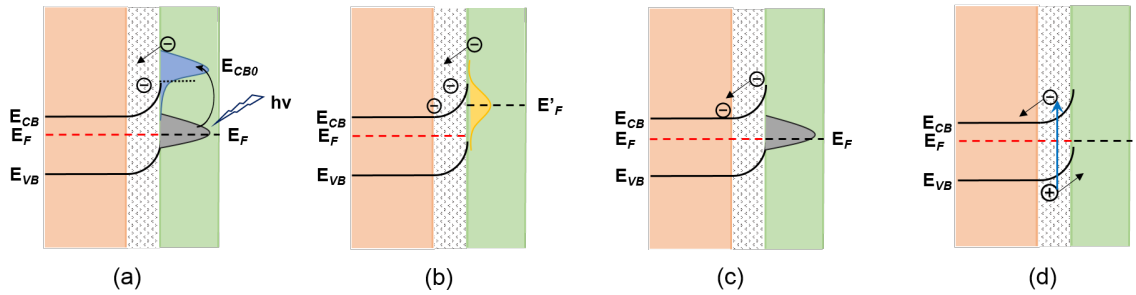

Figure 1.15 LSPR sensitization effect (a)–(c) and LSPR-powered LSPR sensitization effect (a)–(c) and LSPR-powered band gap breaking effect (d) due to the electron–electron relaxation in the course of the non-radiative decay of surface plasmon resonance. The net effect is the generation of more electrons in the semiconductor. (a) Excitation of the electrons from the thermal equilibrium to a high energy state upon absorbing the photons, which feeds the electrons to the conduction band of the semiconductor. (b) In the metal nanoparticle, the collision induced a redistribution of electron energy, forming a Fermi–Dirac distribution at a high-temperature Fermi level. (c) In the metal nanoparticle, the electrons go back to the standard distribution, and in the semiconductor electrons and holes flow to different regions. (d) In the semiconductor, the electron collision excites electrons to the conduction band (i.e. LSPR-powered band gap breaking effect). It is assumed that the semiconductor is n-type and has a direct contact with the metal nanoparticle.
Adapted from Zhang et al. [253].

In the literature there are several examples of this feature as it was possible to inject electrons from the metal nanoparticle to the TiO_2 conduction band with wavelength values from red light (600 nm) to the near infrared (1300 nm) [184]. If one considers the flatband potential before contact for TiO_2 is E_{cb0}= -0.3 eV (SHE) and the Au workfunction value (5.1 eV), by applying the methodology described above, the flatband potential will bend down in a n-type semiconductor and the Fermi level will be aligned with the work-function of the metal (Figure 1.13b). Therefore, if the hydrogen standard reduction potential is -4.44 eV, by applying Eqn. 1.10, we will have:

$$h\nu \geq E_{cb0} - E_f = (-4.44\,eV + 0.3\,eV) + 5.1\,eV = 0.96\,eV$$

It is then clear that the energy of the red irradiation at 600 nm of 2.1 eV is sufficient to activate the process, unlike what has been reported for violet irradiation at 450 nm when no photocurrent was observed. Interestingly, the near IR irradiation at 1300 nm, has an energy

of 0.95 eV which is really close to the necessary value to generate the photocurrent and also explains why at values greater than 1300 nm no photocurrent is observed [184]. It becomes than clear that during a photocatalytic process with incoherent light sources such as Xenon lamps it is possible to irradiate the material from the UV to the infrared, thus exciting the support under UV light and the metal (UV+ Vis+ Infrared). A clear graphical representation of the different possibilities is shown in Figure 1.16.

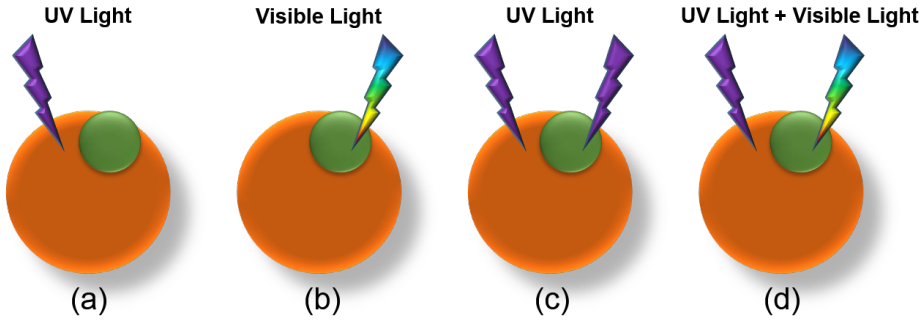

Figure 1.16 Different irradiation states of a plasmonic material (green) on a semiconductor surface (orange): (a) band gap irradiation, only the semiconductor is excited; (b) LSPR induced by visible light irradiation (c) dual state excitation, both the semiconductor and the nanoparticle are excited. (d) incoherent broadband light source excites both the support and the metal.
Adapted from Zhang et al. [253].

1.7 Operational Parameters in Photocatalysis

Photocatalytic processes are governed by several operational parameters very much like conventional heterogeneous catalytic reactions. Despite being substrate and solvent dependent, the effect of the temperature, pH, catalyst to substrate ratio (C/S), oxygen concentration, light intensity have shown to have sometimes dramatic effects on the degradation of organic substrates, and the tuning of the very same parameters, can promote more selective reactions, and enhance the reaction pathway towards selective oxidation processes rather than total mineralization ones. Each of the parameters introduced will be discussed in the following sections.

1.7.1 Solvents

When water is used as a solvent, due to the aggressive oxidising properties of the $^{\cdot}OH$ the partial oxidation or the total degradation of organic substrates are favourite against photosynthetic reactions. Generally, every mineralization reaction for the production of CO_2 and other inorganic species (nitrates, phosphates) starts with a partial oxidation reaction.

The ideal solvent in photocatalytic processes, should resist the strong oxidising power of heterogeneous photocatalysts and of the reactive species produced during such reactions. This is the main reason why, photocatalytic reactions in the presence of O_2 have been carried out in acetonitrile [16, 171, 172, 175, 214], as this polar and aprotic solvent is transparent to UV and visible light irradiation, and most importantly is chemically inert. Sometimes benzene [114] or alkenes [99] such as n-hexane or heptane were used albeit being less unreactive. Cyclohexane was also used and was found to a better solvent than 2-propanol in alcohol oxidation reactions [90]; however, it has to be noted that cyclohexane is oxidised over TiO_2 [46, 79] and therefore it is not a suitable solvent in the oxidation of weakly oxidisable compounds as it might alter the equilibria and the reactivity of the photocatalytic system.

It is then advisable to avoid the competition of the substrate with the adsorption properties and reactivity of the reaction medium, that is why neat liquids have been applied to maximise the substrate adsorption, but this approach is feasible only if the products can be easily separated from the reaction mixture and the process do not require complicated work-up conditions. For aromatic substrates correlations between the Hammett constant (σ) or the 1-octanol-water partition coefficient (K_{OW}) have been proposed for several phenolic and substituted phenolic compounds [192]. These correlations, might become useful in targeting special photocatalytic processes on the upgrading of the lignocellulose phenolic fraction.

1.7.2 Catalyst and Substrate Concentration

The decomposition rate of organics generally increases with the catalyst loading due to the higher amount of the photoactive material in solution. However, there is an optimum value above which further increments in the catalyst quantity are detrimental to the photocatalytic processes for a few very simple reasons, the first being the low light transmission due to the light scattering from the solid particles suspended in solution, whilst the second involves an increase rate of terminal reactions, which is a common phenomenon in radical chemistry and can be described with the equations (Eqn. 1.11a) and (Eqn. 1.11b):

$$H^{\cdot} + OH^{\cdot} \rightarrow H_2O_2 \tag{1.11a}$$

$$H_2O_2 + OH^{\cdot} \rightarrow H_2O + HO_2^{\cdot} \tag{1.11b}$$

The formation of the hydrogen peroxide initiates after the formation of hydroperoxyradicals which are less reactive than the $^{\cdot}$OH. The reactor design for slurry or stirred system is then fundamental, as the effective light penetration length is the key parameter for an efficient utilization of the photoreactor, and for this reason several dosage values are reported in the literature for slurry system from a few mg/L to several g/L [211, 210, 220].

Immobilised systems are an alternative configuration, and in this case the key parameter is the thickness of the film. In fact, the thicker the film, the higher the probability of incurring in slow transfers of the photo-generated electron/hole towards the surface with a subsequent lower turnover frequency of the adsorbed substrate, along with an increase possibility of the undesired electron/hole recombination.

It is generally agreed that, for an efficient photodegradation process, the adsorption of the substrate on the semiconductor material is one of the key prerequisites. Additionally, in some cases the adsorption of the substrate actually increases the reaction rate due to the formation of additional radical species, but it has to be noted that the high reactivity

of the ·OH radicals is such that they cannot diffuse far from and the reaction has to take place in close proximity to the catalyst surface [166]. The adsorption of the substrate plays then a crucial role, and it is influenced by the phenomena described earlier on such as the hydrophilicity of the surface, adsorption of solvent molecules, and it is subjected to Van der Waals forces along with hydrogen bonding, dipole-dipole interaction and outer sphere complexation equilibria. Nonetheless, many photo-mineralization reactions can be described with the Langmuir-Hinshelwood (LH) law, which explains the reactions kinetics occurring between two adsorbed species such as a free radical and the substrate or a free substrate with a surface bound radical species. Generally, the mechanism can be described as follows:

$$R_i = k\theta = -\frac{[S_i]}{dt} = \frac{kK[S_i]}{(1 + K[S_i])} \tag{1.12}$$

In equation 1.12, the initial degradation rate is a function of the surface coverage (θ); the [S_i] is the initial substrate concentration, t is the reaction time and k and K are the Langmuir adsorption constant and the adsorption equilibrium constant respectively. Specifically, K is a measurement of the intrinsic reactivity for a photoactive surface S. Therefore, different regimes can be identified according to the substrate concentration. According to Carp et al. [47] if the substrate concentration [S_i] is lower than 10^{-3}M the reaction kinetic is an apparent first order as the denominator in equation 3 is much lower than 1, whilst, if the [S_i] is higher than 5x10^{-3} M the numerator becomes much greater than 1 and the reaction kinetics has a zero order and maximum reaction rate. However, different kinetics values have been observed for the dehydrogenation of alcohols and for the degradation of pesticides and dyes [250, 232, 207]. Selective oxidation reactions are better described by the competitive adsorption mechanisms. Therefore, the 1.12 can be rewritten considering two species, namely A and B which compete for the same adsorption site on the catalysts surface. There are a few assumptions to apply:

- All sites are equivalent

- Each site can either hold A or B not both.

- There are no interactions between the adsorbate molecules and on adjacent sites.

The surface S of the catalyst can be described as follows:

$$S = [S_{free}] + A_{ads} + B_{ads} \tag{1.13}$$

In which S_{free}, A_{ads}, and B_{ads} represent the unoccupied active sites on the catalyst surface and the sites occupied by A and B respectively. Therefore, if we consider that each of the species has its own equilibrium constant $k_{A,B}$ and $K_{A,B}$, it is possible to define the surface coverage values for each of the species as follows:

$$\theta_A = \frac{k_A K_A}{1 + k_A K_A + k_b K_B} \tag{1.14}$$

$$\theta_B = \frac{k_B K_B}{1 + k_A K_A + k_b K_B} \tag{1.15}$$

The difficulty in the application of the competitive adsorption model in photocatalytic applications lies in the identification and quantification of the reactive species being produced. Therefore, several suggestions have been to include the oxygen content, catalyst amount and light intensity to improve the model and obtain better correlation with the experimental data [164, 165].

1.7.3 Temperature

Photocatalytic reactions are generally not affected by minor temperature variations. The variation of the activity as a function of the temperature is only 5-16 kJ mol^{-1} if compared with the conventional thermal reactions. In fact, at room temperature, the thermal energy value kT is only 0.026 eV and it has negligible contribution to the TiO_2 band gap [47].

Nonetheless, if the thermal energy does not have a direct impact on the TiO_2 E_g, this value is close to the activation energy for the formation of $^{\cdot}OH$ radicals, this is an indication that most photocatalytic processes are governed by the formation of these active species to the low activation energy. Moreover, changes in the temperature might affect the adsorption-desorption properties of certain substrates along with the desorption of the intermediates, thus freeing more surface area and increasing the activity of the material, as in most cases, at low temperatures, the desorption of the surface-bound species is the rate-limiting factor. Within wider temperature ranges, the variation of the Fermi level for TiO_2 from 21-75°C was only 0.04 eV but sufficient to increment the electron-transfer kinetics at the interface. On the other hand, for O_2 mediated reactions, an increase in temperature lowers the adsorption isotherms thus lowering the overall solubilised oxygen concentration [164, 165]. Therefore, it is important to monitor the reactions conditions, as usually the substrate concentration is much lower than the O_2 pressure and under these conditions, the effect of the temperature will be dominant on the reaction rate rather than on the oxygen isotherms. Vice versa, the effect of the temperature will be dominant on the electron transfer mechanism to oxygen [25].

1.7.4 pH Influence

The pH of the reaction medium can influence the photocatalytic properties of a semiconductor in various ways. The first one is related to the isoelectric point of the metal oxide, defined as the pH value at which the surface does not present any electric charges due to the presence of hydroxyl groups or protons. For TiO_2 this value is around pH 6, and at lower values the surface will be positively charge, and vice versa, at alkali pH values the surface will be negatively charged. This electrostatic charging directly affects the capability of a substrate in the adsorption of molecules with polar functional groups. For TiO_2 as previously mentioned, the flatband position affects the activity of the catalyst, and affects the rate of production

of the different radical species formed during the photo-initiated process. For rutile, it was found by Fujishima et al. [95] that the dependency of the flatband potential for rutile and anatase to follow a Nernstian trend due to the acid-base equilibria on the surface of the catalyst at 25°C and it was found to be at pH 0 +0.01 V for rutile and -0.02 V for anatase versus SHE (Eqn. 1.16).

$$TiO(O) + H^{+} = TiO(OH) \tag{1.16}$$

In Figure 1.17 the photoactivity of rutile and anatase are summarised at different pH levels. It can be seen how the energy conduction band (E_{cb}) is superimposed to the hydrogen potential at all pH values for rutile, whereas anatase has more negative potential. At low pH levels the E_{cb} for rutile is also coinciding with the O_2 reduction potential to generate hydroperoxyradicals ($HO_2^{\cdot}$). At higher pH values the reduction potential remains constant at -0.284 V [230] but the E_{cb} continues its negative trend. It can be assumed that this reaction is going to be preferred at alkali pH values. As regards anatase, the E_{cb} is negative enough to reduce O_2 to the superoxide anion (O_2^{-}) over a wide range of pH values and this is reflected by the higher activity of this polymorph. Both valence band energy levels (E_{vb}) for anatase and rutile are at the same potential value which is sufficient for the generation of $^{\cdot}OH$ radicals at lower pH, and $O^{\cdot -}$ at higher pH values. Therefore, by tuning the pH of the reaction medium it is possible to favour the adsorption of polar molecules on the catalyst surface and tailor the production of selected radical species.

1.7.5 Light Intensity

Mills et al. [164] suggested that the LH isotherm is also influenced by the light absorption. Specifically, the equilibrium constant K, is proportional to the I_a^{θ} in which I_a is the rate of the light absorption of the photoactive material and θ is a power term which is a function of the intensity of the lamp and can be equal to 0.5, 1 or 2 for low, medium and high intensity lamps respectively. They also reported that, in many of the kinetic studies, the light intensities were

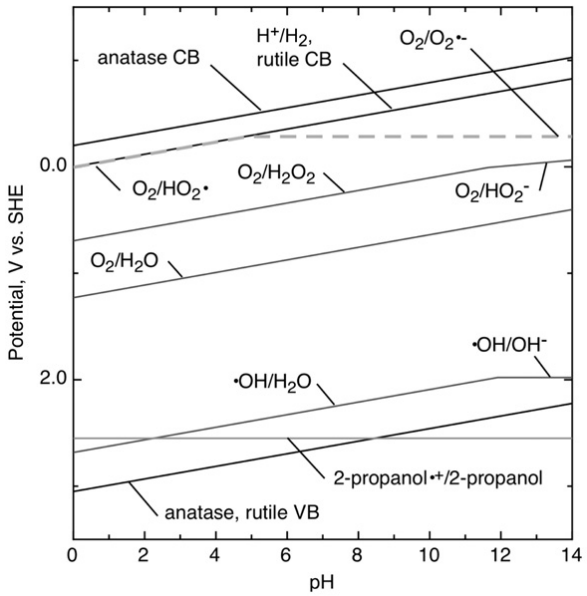

Figure 1.17 TiO_2 band gap value as a function of the pH of the reaction medium. To be noted the position of the rutile conduction band which is superimposed on the reversible H^+/H_2 at all pH values. Taken from Fujishima et al. [95].

so high, that the kinetic rate of the reactions was found to be proportional to I_a^2. Some research groups [207, 84, 19, 18, 205, 80, 239, 174, 186] also successfully correlated the dependence of the kinetic rate from first-order to half-order as the light intensity was increased from low to high. Carp et al. [47] reported that for UV regimes, up to 25 mW cm^{-2} reactions have first-order kinetics whilst they are characterized by half-order rates for higher intensities. They also state that processes defined by first order kinetics are characterized by the fast consumption of the electron/hole pair by the photocatalytic process rather than from the recombination rate, whereas in the latter, the recombination rate is the dominant factor. Additionally, the variation of the reaction rate as a function of the irradiation wavelength is matched by the adsorption spectrum of the photoactive material with the band gap value being its threshold value [191, 237, 118]. Nonetheless, despite this general trend, no specific values of the power lamp or the photon flux are available to be used as guidelines for visible irradiating sources.

1.7.6 Adsorption on Semiconductor Surfaces

Most metal oxides are hydroxylated under normal conditions as crystal structures are more stable as the electroneutrality principle is preserved, and this is achieved by covering the surface with monovalent ions which makes the whole ionic structure more stable than if the bivalent of multivalent ions were present. For anatase, approximately 40% of the surface is hydroxylated, whereas the hydroxylation of rutile is relatively weak, and because of this as it hard to distinguish between the chemical and the physical absorption of water and there is no agreement on the experimental data on the surface concentration of OH groups on rutile [219]. It was also proved that the level of hydroxylation on rutile, does not change the band-gap value, but on the other hand, the valence and conduction band show similar trends upon hydroxylation. In fact, the band edges shift due to the formation of dipoles on the surface thus increasing the conduction band edge. This increment directly influences the reducing power of rutile towards the water splitting reactions under illumination and the role of the Ti-OH groups in photocatalytic processes, was recently investigated [249]. Back in 1971, Boehm [33] identified two main types of surface-bound hydroxyl groups present in equal amounts on metal oxides surfaces: the bridging OH bound to a Ti^{4+} ion with a coordination number of 4 compared with the lattice structure and the terminal OH groups bound to Ti^{4+} with coordination number of 5 (Figure 1.18). In a recent paper, Li et al.

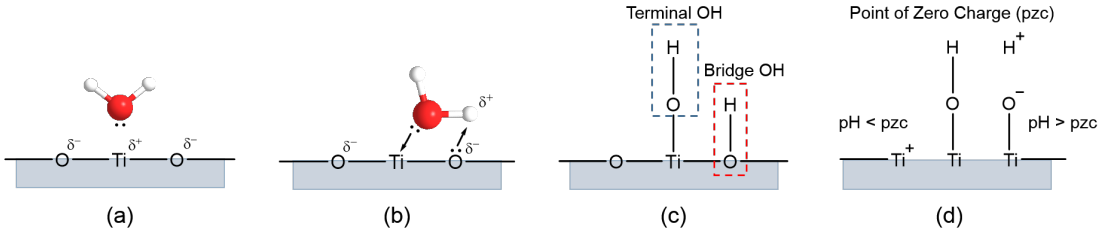

Figure 1.18 Water adsorption on a TiO_2 surface (a,b); formation of the terminal and bridge OH groups (c); Point of zero charge of TiO_2 (d)

[146] assessed the role of the bridging and terminal OH groups in photochemical processes, specifically in the degradation of Rhodamine B, methyl orange and p-chlorophenol. By

ion-exchange techniques with NaOH and HNO_3 it was possible to remove the bridging OH groups with acidic properties and the terminal ones characterized by a basic character. By treating the TiO_2-P25 it was possible to tune the activity of the material, and the amount of radicals produced was monitored with electron spin trapping (ESR) and it was found that the role of the acid OH groups was greater than the terminal ones. This experiment directly correlates the activity of the catalyst with the nature of the hydroxyl radical adsorbed on the semiconductor surface showing that the adsorbed OH groups are responsible for the *in situ* generation of the reactive $^{\cdot}OH$. The authors remark the importance of correlating the surface properties of semiconductors and photoactive materials with the identification of the reactive species involved. Additionally, it was found that the TiO_2 surface hydroxylation degree also influences the hole scavenging properties with the production of $^{\cdot}OH$, which are the main reactive species in photochemical reactions as they initiate a cascade of radical reactions and are known to react quickly with sugars [78]. Isopropanol, propylene glycol and glycerol were also tested in the photoreforming process with results in line with the correlation between the H_2 production and the amount of OH groups on the substrate. By comparison of the different activity values, it was found that uncoordinated Ti sites on the surface of the semiconductor, can be stabilized by several R-OH (R= water, alcohols, polyols, and carbohydrates), as the Ti binds the substrate (R-OH) forming a Ti-OH with a subsequent release of the proton, thus changing the titanium sites to an octahedral configuration, and this has been experimentally determined with XANES analysis observing the Ti K-edge spectra [215, 217, 78]. The pH of the reaction mixture influences the physical properties of the metal oxide, as the pKa of the different hydroxyl groups adsorbed on the surface imparts different charges to the support thus affecting the adsorption rate of different substrates Shin et al. [212]. The photoinduced superhydrophilicity discovered by Wang et al. [238] and Fujishima et al. [94] might also influence the activity of the material (Figure 1.19). In fact, upon illumination, the electron/hole pair reacts in a different way, and the electrons migrate

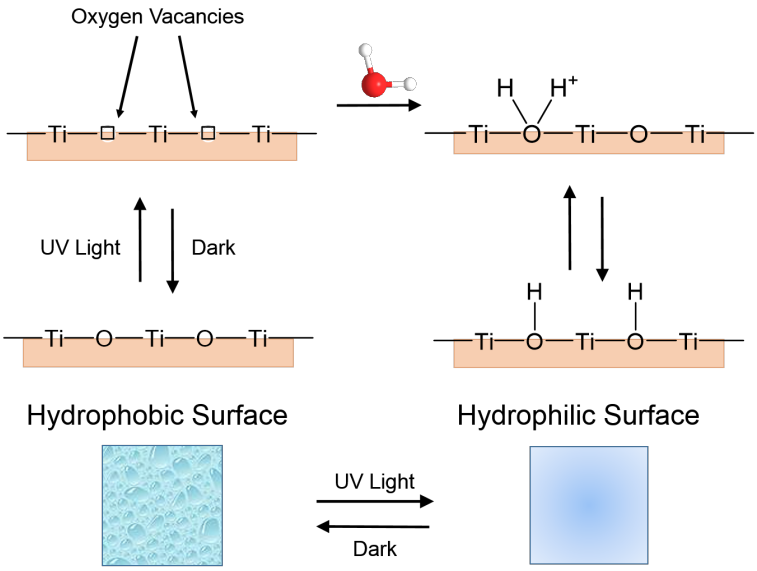

Figure 1.19 Mechanism of the photo-induced superhydrophilicity under UV irradiation. Adapted from Fujishima et al. [93].

towards the surface to reduce the Ti(IV) species to Ti(III) whilst the holes oxidise the O_2^- anions. During this process, oxygen vacancies are created with the elimination of the oxygen atoms. These vacancies can then be occupied by adsorbed species, and if water is present, the adsorbed OH groups make the surface of the material hydrophilic. The presence of these OH groups adsorbed on the bridging oxygen atoms in the lattice structure increases the hydroxylation content of the material, thus enhancing the formation of the $^{\cdot}OH$ radicals.

1.7.7 Formation of the Ligand-to-Metal Charge Transfer (LMCT)

Along with the deposition of metals on the surface of semiconductors, another method of extending the activity of wide band gap semiconductors to the visible range is the sensitization of the material with dyes or via the formation of complexes with the adsorbed molecules and the surface of the semiconductor itself [45, 247, 193, 198]. The adsorbed organic compounds do not necessarily have to absorb light themselves, in fact, in this process, the visible light induced charge transfer occurs from the HOMO of the adsorbate to the conduction band of the TiO_2. Figure 1.20 shows the different cartoons for the dye sensitization (a) and for

the LMCT process (b). The first mechanism is initiated by the HOMO-LUMO electron transfer of the adsorbed dye on the TiO_2 surface. After this initial excitation, the HOMO electrons are then injected in the TiO_2 conduction band, and become available for further reactions. The oxidised dye can be regenerated as soon as suitable electron donors become available in the system. The latter LMCT mechanism is characterized by the excitation of the ground state electrons of the adsorbate which are then injected into the conduction band of the semiconductor without involving any excited state from the adsorbate. The oxidised adsorbate can either undergo further degradation into smaller molecules or it can be regenerated by suitable electron donors in the reaction medium or by the back electron transfer from the recombination of the electron from the conduction band of the semiconductor to the adsorbate itself. Typically, the formation of the LMCT complex can be observed by the appearance

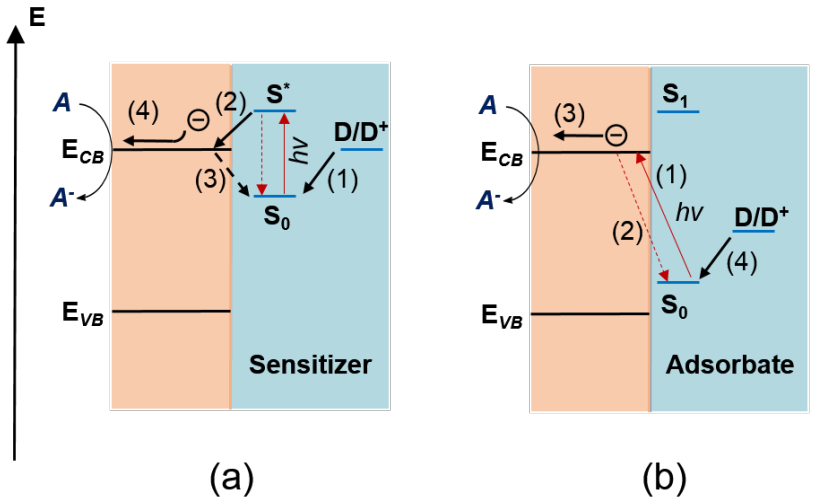

Figure 1.20 Schematic illustration of two similar types of visible light sensitization of TiO_2. **(a)** Dye sensitization: (1) excitation of the dye by visible light absorption, (2) electron transfer from the excited state of the dye to TiO_2 CB, (3) recombination, (4) electron transfer to the acceptor, and (5) regeneration of the sensitizer by an electron donor. **(b)** LMCT sensitization: (1) visible light-induced LMCT transfer, (2) recombination, (3) electron transfer to the acceptor, and (4) regeneration of adsorbates by an electron donor. S, D, and A represent the sensitizer (or adsorbate), electron donor, and electron acceptor, respectively. (S_0 ground state, S^* and S excited state of the sensitizer adsorbate). Adapted from Zhang et al. [253].

of an absorption band in the visible range with a subsequent colouration of the material,

which cannot be seen for the TiO_2 alone. The most important difference between the dye sensitization process and the LMCT is the fact that for the former, the positioning of the HOMO-LUMO gap is the determining factor in the dye visible light absorption properties, whereas for the latter, the adsorbate does not necessarily have to absorb light as the HOMO level is the only parameter to be considered. For this specific reason, LMCT complexes are much more flexible and grant some freedom in the design and application of different substrates specifically for environmental applications in which many organic pollutants can form stable complexes with the surface of metal oxides semiconductors and can be degraded using solar light.

1.8 Aim of the Work

This work will focus on a multidisciplinary approach and will try to answer some of the questions regarding the activity of TiO_2 based materials for the selective oxidation of bio-derived molecules, specifically on glucose and cellobiose. The aim of this PhD is to gather basic information regarding the activity of semiconductor photocatalysis under visible light, enhancing the activity of TiO_2 oxides by creating novel materials through the creation of metallic AuAg nano-alloys in order to extend and enhance the photoactivity under visible light. The project can be divided in the following workpackages:

- Assessment of the activity of TiO_2 under visible and UVA light in the oxidation of glucose. Identification of the optimum reaction conditions.
- Assessment of the activity of several metal supported Ag/TiO_2 materials in the oxidation of glucose. Does the presence of the metal affect the reaction pathway? Which products can be obtained by tailoring the properties of the support?
- Identification of the reaction pathway of the oxidation of glucose under UVA and visible light.

- Is it possible to extend the visible light response of the Ag/TiO_2 materials by coupling a second metal such as Au?
- Can cellobiose, a model compound for cellulose, react in a similar fashion to glucose and produce partial oxidation products under visible and UVA light?

Ultimately, the radical chemistry of the oxidation of glucose and the hydrolytic oxidation of cellobiose will be investigated to obtain fundamental understanding of the key factor governing this specific class of reactions, understanding the effect of several catalytic parameters in order to build a bottom up approach robust enough to efficiently and, most importantly, provide the fundamental analytical and methodological tools for a correct understanding of the valorisation of sugars, with the ultimate intent of using cellulose as a reactant.

Chapter 2

Materials and Methods

DO YOU SEE THE LIGHT?

Rev. C. James

2.1 Chemicals

The following reagents were used:Gold (III) chloride trihydrate (99.9%), Silver nitrate (> 99.0%),Titanium (IV) Oxide Aeroxide P25 (Acros Organics), $NaBH_4$ (Sigma-Aldrich), Titanium (IV) oxide anatase 99.8%, Titanium (IV) oxide rutile 99.99% (Sigma-Aldrich), Acetonitrile (MeCN) HPLC Grade 99.9% (Fisher Chemical), Poly (ethylene glycol)-block-poly (propylene glycol)-block-poly (ethylene glycol) (Pluronic P123, Mn 5800), Polyvinyl alcohol (PVA, average MW 130,000, 99+% hydrolyzed) (Sigma-Aldrich).
HPLC calibration standards:D-(+)-Cellobiose ($\geq$ 99%), D-(+)-Glucose $\geq$ 99.5% (GC), D-Gluconic acid sodium salt > 99%, D-(-)-Arabinose $\geq$ 98%, D-(+)-Glyceraldehyde $\geq$ 98%, D-(-)-Erythrose $\geq$ 75%, Formic acid $\geq$ 95% were all purchased from Sigma-Aldrich and used without further purification. 1,6-Anhydro-β-D-cellobiose $\geq$ 96% was purchased from Carbosynth (Carbosynth Limited , UK)

Other chemicals: H_2SO_4 (> 95%) (Fischer Chemicals), Ultrapure water resistivity > 1MΩx cm at 25°C (Millipore MILLI-DI, UK).

2.2 Wetness Impregnation (WI) synthesis of the Ag/TiO_2 Catalysts

$AgNO_3$ solutions were prepared by solubilizing the appropriate amount of the salt in H_2O. The support TiO_2-P25 was then suspended in 4 ml of H_2O in a vial under magnetic stirring. The appropriate volume of the metal solution was then added and the solution was left to evaporate under constant stirring at 80°C, until it became a paste. The supported catalysts were then dried overnight under vacuum at 110°C. Finally, the dried catalysts were calcined under static air at 400°C for 3 hours at 2°C min^{-1}. The metal loading was calculated a as weight percentage of the support (Eqn. 2.1).

$$\%\ metal\ loading\ =\ \frac{weight_{metal}}{weight_{support} + weight_{metal}} * 100 \tag{2.1}$$

2.3 Colloidal Synthesis of the Au_xAg_{1-x}/TiO_2 Bimetallic Catalysts

P123 as Stabilizing Agent

Aqueous solutions at the desired concentration of the $HAuCl_4 \cdot 3H_2O$ (1.5 mM), $AgNO_3$ (1.5 mM), and $NaBH_4$ (1 g L^{-1}) were prepared following the procedure reported by Huang et al. [109]. An appropriate amount of the precursor metal solution was added to 25ml of a Pluronic P123 triblock copolymer solution and stirred vigorously for 5 minutes until complete dissolution, and the metal/P123 ratio was set at 5 for all the mono and bimetallic colloids. For the bimetallic catalysts soon after the addition of the first metal an appropriate

amount of the gold solution was added. Immediately after the addition of the metals, 15 ml of a freshly prepared $NaBH_4$ solution were added drop-wise into the stirred mixture.

The prepared colloidal solution was then analysed spectrophotometrically to assess the successful formation of the metal nanoparticles. The preformed colloids where then added to a 40 ml TiO_2 aqueous suspension and the volume was then adjusted to 100 ml with distilled water and the solution was stirred at room temperature for 1 hour. After stirring, the slurry solution was then filtered and washed with distilled water until neutral pH.

The solid was dried overnight at room temperature (RT). The powders were then collected from the filter and refluxed with 50 ml of water at 80°C for 2 hours to remove the excess of the templating agent. They were then filtered, washed with water, dried at RT, and finally ground to a fine powder.

The total metal loading on the support was 1 wt% and the molar ratio between Au and Ag was calculated as follows:

$$
\begin{aligned}
[Au]_{stock} &= 0.0015\,M \\
Au\,MW &= 196.96\,g\,mol^{-1} \\
Total\ metal\ loading &= 0.010\,g \\
Volume\ [Au]_{stock}\ required &= \frac{0.0015 * 196.96}{0.01} = 0.338\,L
\end{aligned}
$$

The obtained values for the monometallic colloids where then multiplied by the molar ratio and the results are reported in Table 2.1.

Polyvinyl Alcohol (PVA) as Stabilizing Agent

Following the work published by bin Saiman et al. [30] a gold colloidal solution was prepared. The appropriate quantity of chloroauric acid was dissolved under stirring in a round bottom flask with a small amount of water (10ml). A PVA 1 M water solution was prepared and added

Table 2.1 Synthetic parameters for the Au and Ag loadings for each of the mono and bimetallic catalysts synthesised.

Catalyst	Ag (ml)	Au(ml)	Ag (mol)	Au (mol)	Ag (g)	Au (g)	Metal loading (wt%)[a]
Au 1%	0	33.8	0	5.07E-05	0.00E+00	9.98E-03	1.00
$\mathbf{Au}_{0.95}\mathbf{Ag}_{0.05}$	1.7	32.9	2.55E-06	4.93E-05	2.75E-04	9.71E-03	1.00
$\mathbf{Au}_{0.85}\mathbf{Ag}_{0.15}$	5.4	30.8	8.11E-06	4.62E-05	8.74E-04	9.09E-03	0.99
$\mathbf{Au}_{0.50}\mathbf{Ag}_{0.50}$	21.9	21.9	3.29E-05	3.28E-05	3.55E-03	6.47E-03	1.00
$\mathbf{Au}_{0.15}\mathbf{Ag}_{0.85}$	46.6	8.3	6.97E-05	1.24E-05	7.52E-03	2.45E-03	0.99
$\mathbf{Au}_{0.05}\mathbf{Ag}_{0.95}$	56.2	3	8.4E-05	4.5E-06	9.06E-03	8.86E-04	0.99
Ag 1%	61.8	0	9.28E-05	0	1.00E-02	0.00E+00	1.00

[a] Values referred to a synthesis with 1 gram of TiO_2

to the metal solution to reach PVA/metal 1.2 w/w ratio. A fresh $NaBH_4$ 0.1 M water solution was then prepared and transferred into the flask to achieve a molar ratio of $NaBH_4$/metal of 5. The obtained solution was then magnetically stirred for 30 min. The desired amount of titania was then suspended in 20 ml of water and the suspension was then acidified to pH 1 with H_2SO_4. Subsequently, other 20 ml of water were used to remove the TiO_2 residues and rinse the glassware. After 2 hours of stirring the solution was filtrated and washed with distilled water until a neutral pH value was obtained. The solid was dried overnight at RT. The powders were then collected from the filter and refluxed with 50 ml of water at 80°C for 2 hours to remove the excess of ligand and reducing agent. The obtained solid was filtered, washed with water, dried at RT and ground to a fine powder.

2.4 Synthesis of Cellobionic Acid

Cellobionic acid was synthesised as a standard for proof of its formation during the photocatalytic process. The synthesis of cellobionic acid follows the same procedure described for the production of lactobionic acid from lactose Forsberg et al. [89]. This approach was chosen due to the similar molecular structure and reactivity of the two compounds. Typically, 2.90 g of the disaccharide were solubilized in the minimum amount of water (21 ml) at 40°C in a ultrasonic bath given the poor cellobiose solubility (12 g L^{-1}) at room temperature and then 1.85 g of I_2 (7.3 mmol) was solubilized in 15 ml of CH_3OH and added to the cellobiose

solution under stirring. Subsequently, a 4% w/w KOH solution was prepared solubilizing 1.65 g of the hydroxyde in 50 ml of CH_3OH and added dropwise. Upon the addition of the KOH the pale yellow color of the iodine solution gradually disappeared and to speed up the process, the solution was heated to 40°C until transparent. The reaction mixture was then cooled in a refrigerator at 4°C overnight to precipitate the cellobionic acid crystals. The recover solid was then filtrated from the mother solution and dried in a rotavapor. The dry solid was then weighed yielding 0.34 g of potassium cellobionate crystals. The purity of the solid was then assessed using ^{1}H and ^{13}C NMR along with mass spectrometry analysis (HPLC-QTOF) and ATR-FTIR measurements of the solid. For the characterization results the reader is invited to see Appendix B.1.

2.5 Thermal Pretreatments

The different TiO_2 polymorphs were dried under vacuum at 100°C before the reactions and the TiO_2-P25 was heat treated under static air at 500 and 600°C respectively to change the rutile to anatase ratio. The catalyst after the heat treatment procedure were ground and stored in a desiccator until further use.

2.6 Catalyst Characterization Techniques

2.6.1 UV-Vis Spectroscopy

UV-Vis

UV-VIS absorbance analyses were performed in a 10 mm quartz cuvette in the range 200-820 nm using a Thermo Scientific Evolution 220 spectrophotometer (Thermo Scientific, UK). Instrument settings were: bandwidth 2 nm, integration time 0.01 s, data interval 0.20 nm and scan speed 1200 nm min^{-1}. Baseline was obtained with distilled water.

Solid UV-Vis

The solid UV-Vis analysis of the catalysts was performed using a UV-2550 Shimadzu spectrophotometer equipped with a ISR-2200 integrating sphere (Shimadzu Corp, JP) in the range 200-800 nm with a 1 nm sampling interval and a 5 nm slit with using $BaSO_4$ as reference. The reflectance data were used to calculate the Kubelka-Munk function using the absolute reflectance (R_∞) to evaluate the bandgap of the solid samples (see Appendix C.1).

2.6.2 X-ray Diffraction (XRD)

X-ray diffraction (XRD) patterns were recorded using in transmission mode using a PANalytical X'Pert Pro HTS diffractometer with a slit of 0.04° at a scanning rate of 9° min^{-1} in the range 4-90° using a Cu-Kα radiation (λ=1.54Å).

2.6.3 Attenuated Total Reflectance Infrared Spectroscopy (ATR-FTIR)

The ATR-FTIR spectra were recorded using a HTS-XT Bruker Tensor 27 (Bruker, USA) equipped with a Quest ATR accessory (Specac, USA) with a high throughput diamond crystal in the range 6000-400 cm^{-1} (resolution 4 cm^{-1}) and 32 interferograms were recorded for each sample.

2.6.4 X-ray Photoelectron Spectroscopy (XPS)

Samples were sent for XPS analysis at NEXUS National EPSRC XPS User's Service hosted by nanoLAB at Newcastle University. The XPS analysis was performed with a Thermo K-Alpha (Thermo Scientific, East Grinstead, UK) with a microfocused monochromatic Al Kα source (1486.6 eV, 12 kV, 3 mA, 36 W) with a spot size of 400 by 800 μm. The data aquired was obtained from the analysis of 3 positions per sample with a general 30 scan

survey and a 10 scan survey for the high resolution regions. The raw data was corrected using the C1s binding energy at 284.7 eV. The recorded spectra were fit with the leastsquares to produce Gaussian-Lorentzian functions after the subtraction of background noise.

2.6.5 Scanning Electron Microscopy (SEM)

Scanning electron microscopy analysis were performed on a Hitachi S-4800 Field Emission Microscope Figure 2.1. Some of the instrument specifications are reported in Table 2.2. The utilization of this microscope was limited to the EDS analysis (Section 2.6.7) to evaluate the metal loading content and to examine morphological changes in the support structure, as the resolution of the instrument is not sufficient for the determination and analysis of nanometric metal nanoparticles due to charging effects of the support.

Figure 2.1 Picture of the Hitachi S-4800 microscope used in this study

Table 2.2 Instrument specification for the microscope used in this work.

Resolution (nm)	
15 kV Accelerating Voltage, Working Distance 4 mm	1 nm
1 kV Accelerating Voltage, Working Distance 1.5 mm	2 nm
Magnification	
High	100x to 800.000x
Low	30x to 2.000x
Accelerating Voltage	0.5 to 30 kV (in 100 V steps)

2.6.6 Transmission Electron Microscopy (TEM)

The supported metal catalysts were analysed using two different transmission electron microscopes. The first one is a JEOL JEM-2100 LaB_6 (Jeol Ltd, JPN) equipped with a Oxford Instrument Aztec Energy EDX detector located at the Research Complex at Harwell (Figure 2.2a). The second miscroscope is a aberration corrected JEOL JEM-2100F (Figure 2.2b) located at the Nanoinvestigation Centre at Liverpool (NiCal). This microscope is equipped with a "CESCOR" Probe Corrector (CEOS, GmbH) with a TEAM EDS detector. Both systems are equipped with a high resolution Gatan cameras and are operated at 200 kV. The instruments have similar characteristics as reported in Table 2.3. The main difference

(a) JEM-2100 LaB_6 Microscope **(b)** JEM-2100F Microscope

Figure 2.2 Pictures of the Transmission Electron Microscopes used in this study.

between the JEM-2100F and the JEM-2100 LAB_6 is the presence of the aberration correction module in the 2100F which grants superior resolution and the possibility of achieving clear sub-nanometric resolution, allowing for the measurements of lattice planes and the analysis of the composition of the supported metal nanoparticles. The catalyst powders were suspended

Table 2.3 Instrument specifications of the two microscopes used in the study

	Resolution	Ultrahigh resolution (UHR)	High resolution (HR)
JEM 2100-LaB_6	**Point Image**	0.194 nm	0.23 nm
	Lattice Image	0.14 nm	0.14 nm
	Acceleration Voltage	80,100,120,160,200 kV	
	Min. step	50 V	
	Magnification	×2000 to 1.500.000	
JEM 2100F	**Point Image**	0.19 nm	0.23 nm
	Lattice Image	0.1 nm	0.1 nm
	Acceleration Voltage	80-200 kV	
	Min. Step	50 V	
	Magnification	x2000-1.500.000	x1500-1.200.000

in methanol under sonication and deposited dropwise on copper grids with 300 mesh holey carbon film (Agar Scientific, UK).

2.6.7 Energy-Dispersive X-ray Spectroscopy (EDX)

The SEM used was equipped with a Oxford Instruments Inca Energy EDX Detector. The electron accelerating voltage was 30 kV with a probe current of 20 μA.

2.6.8 Inductively Coupled Plasma Optical Emission Spectrometry Analysis (ICP-OES)

ICP analyses were performed by Mr.George Miller at the Analytical Services in the Chemistry Department with an instrument ICP-OES-SoP, Spectro Ciros CCD. Prior to the analysis, 10 mg of the supported metal catalysts were digested in glass vials using 4 ml of freshly prepared aqua regia. After 60 minutes of digestion, the samples were then diluted with 6 ml of water to neutralize the acid and the samples were then submitted for the analysis.

The required elemental lines were selected for their intensity and lack of interferences before being calibrated with certified standards, matrix matched and within a previously established concentration range via a 3 point calibration curve. Each peak then being

maximised with background compensation applied before final recalculation of the method and with a correlation coefficient R^2>0.9993. Instrument parameters from optimisation were, Plasma power 1400 W with a nebulising flow of 0.82 L min^{-1}, coolant flow of 12.0 L min^{-1} and auxiliary flow of 1.0 L min^{-1} Line selection for each element was, Ag 328.068 and 338.289 nm, Au 242.795 and 267.595 nm respectively. Typical %RSD values were between 1-2% indicating a stable plasma with consistent sample injection and aspiration.

2.7 Products Analysis and Characterization

2.7.1 High Performance Liquid Chromatography (HPLC)

The glucose stock solutions and reaction products were analysed with a 1200 HPLC Agilent (Agilent, USA) system equipped with a photodiode array detector (DAD) and a refractive index detector (RID). The analytical column used was an Aminex HPX-87H (300 mm x 7.8 mm), 9 μm particle size (Bio-Rad CA, USA) kept at 65°C and using a 0.025 M H_2SO_4 as eluent with a flow rate of 0.65 ml min^{-1}. The products concentration and glucose conversion was determined using calibration curves (see Appendix A.1).

2.7.2 HPLC- Quadrupole Time of Flight Mass Spectrometry (HPLC-QTOF)

The accurate mass of the oxidized products obtained from glucose were analysed with an Agilent 6510 Q-TOF LC/MS system and interpreted using Agilent MassHunter Workstation Software (Version B.06.00). The column used for the mass spectrometry analysis was a Varian MetaCarb 67H (300 mm x 6.5 mm) (Agilent, USA) kept at 65°C using a 0.1% w/w formic acid aqueous solution at a flow rate of 0.8 ml min^{-1}. The Q-TOF was operated in positive ESI mode (see Appendix:A.2).

2.7.3 Nuclear Magnetic Resonance (NMR)

NMR analysis was performed on a Bruker Avance III HD NanoBay 400MHz instrument equipped with a BBFO probe. Samples were prepared by solubilisation of known amounts in D_2O and the ^{1}H, ^{13}C spectra were acquired with the following settings:

Table 2.4 Typical NMR settings used for the ^{1}H, ^{13}C spectra aquisition.

Parameters	^{1}H	^{13}C
Time Domain	65536	65536
Sweep Width (ppm)	10000	24038
Acquisition Time (sec)	3.3	1.36
Dwell Time (μsec)	50	20.8
Receiver Gain	64	203
Total Scans	16	256
Frequency (MHz)	400	100

2.8 Description and Setup of the Photoreactors

Several reactor configurations were used in this work to assess the contribution of the light intensity and of different wavelength ranges to the photoactivity of the photoactive materials synthesised. As described in the Chapter 2, 3 different setups were used: a 300 W and 1000 W Xenon lamps and a Luzchem photoreactor. In the following sections, the peculiarity of each system will be discussed individually.

2.8.1 Luzchem Photoreactor

The luzchem photoreactor used in this study (Figure 2.3) offers good versatility as several lamps can be installed on this system allowing different experimental configurations, additionally, the combination of different lamps can be used to stress test some materials under different conditions. Typically, for all our studies, 14 lamps of the same range were installed and used, but the information relative to the emission spectra of the visible and UVA lamps is available only for the 8 overhead lamps configuration.

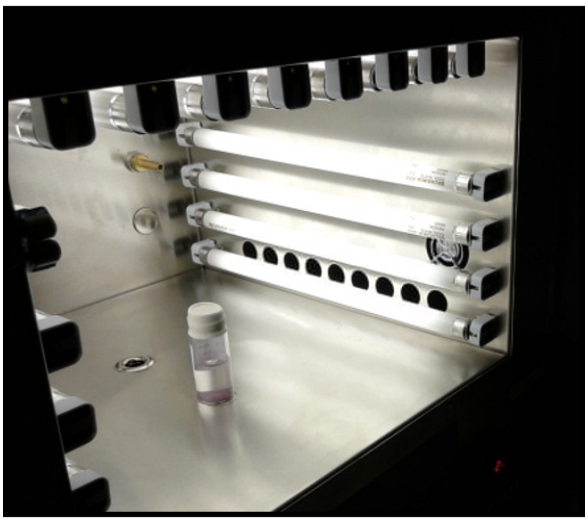

Figure 2.3 Picture of the inside of the Luzchem photoreactor equipped with the visible light lamp. In the middle of the reactor the position of the reaction vial was fixed in all reactions.

We can consider the emission spectra to be representative in terms of the power distribution profile, but the actual power value at different wavelengths could not be monitored, and the value are expected to generally higher in both cases (UVA and visible light).

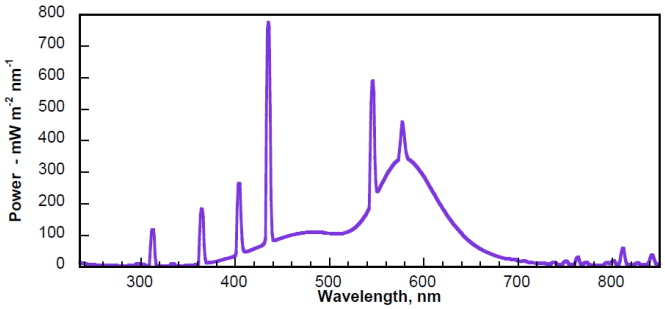

Figure 2.4 Emission spectrum for the 8 overhead visible light lamps configuration in the range 230-850 nm

2.8.2 Xenon Lamps

Incoherent light sources such as Xenon lamps are commonly used for the testing of solar cells, creams, plastics and other photoactive materials as the emission profiles of these light bulbs mimic the natural sunlight allowing controllable indoor testing facilities under laboratory

Table 2.5 Energy distribution on the sample for a reactor configuration with 8 visible light lamps. The values are divided in spectral region and the contribution of each is reported as a % value. The division between UVA and UVB was set at 315 nm

Region	Range (nm)	Power (mW m^{-2})[b]	Energy (%)[a]
UVC	235-280	269	0.51
UVB	281-315	670	1.28
UVA	316-400	1754	3.34
Visible	401-700	47837	91.16
NIR	701-850	1945	3.71

[a] Values relative for a configuration with 8 overhead lamps

[b] Values reported in the Luzchem exposure standard LES-Vis-01 available from www.luzchem.com

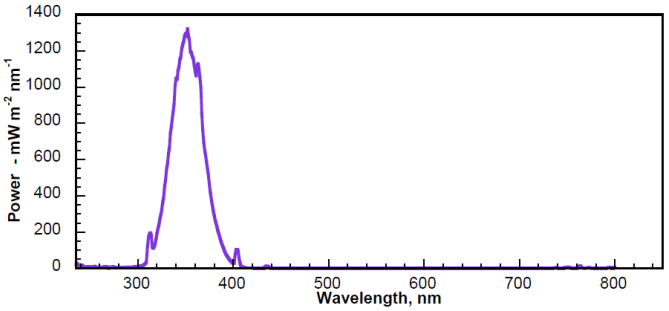

Figure 2.5 Emission spectrum for the 8 overhead UVA light lamps configuration in the range 230-850 nm

Table 2.6 Energy distribution on the sample for a reactor configuration with UVA 8 lamps. The values are divided in spectral region and the contribution of each is reported as a % value. The division between UVA and UVB was set at 315 nm

Region	Range (nm)	Power (mW m^{-2})[b]	Energy (%)[a]
UVC	235-280	367.5	0.67
UVB	281-315	1209	2.19
UVA	316-400	52670	95.51
Visible	401-700	711	1.29
NIR	701-850	187	0.34

[a] Values relative for a configuration with 8 overhead lamps

[b] Values reported in the Luzchem exposure standard LES-UVA-01 available from www.luzchem.com

conditions. These experimental set-ups take into account several factors such as the intensity and uniformity of the light beam and the air mass or AM1.5G (Figure 2.6a) which is the

global average for light travelling through 1.5 Air Mass and take into account the O_2, H_2O and CO_2 absorption peaks at ground level (Figure 2.6b). The systems used in this work do not take into account the air mass parameter as the concept idea behind the use of these illumination sources is to try and mimic the properties of photoactive materials exposed to a wide range of wavelengths as the ultimate aim for the exploitation of these materials is to harvest the highest amount of solar irradiation from the UV to the infra-red part of the spectrum.

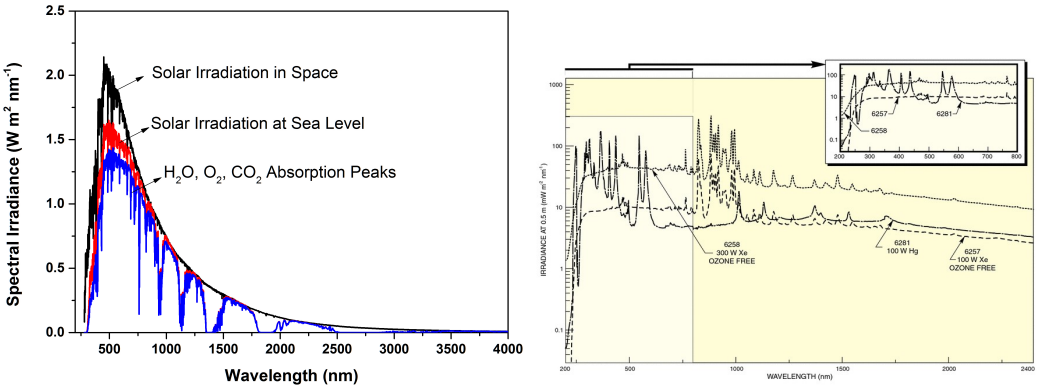

(a) **(b)**

Figure 2.6 ASTM G-173-03 Irradiance spectra (a) and 300 W Xenon lamp irradiance spectrum (b).

The set-up of the 300 and 1000 W system is very similar due to the nature of the light sources. In fact, they both require liquid IR filters to prevent the reaction mixture from overheating and to avoid the undesired effect of the IR irradiation on the catalytic activity of the materials. To avoid the evaporation of the water inside the chamber after prolonged exposure, the liquid IR filter has to be kept at a constant temperature, therefore it was connected to a peristaltic pump in a close circulating water system. These sources emit a wide range of wavelengths, from the UV region to the IR therefore, it is important to select among this continuum of radiation, which is the desired range of operation. Therefore, with the combination of the IR filter (Figure 2.8a) and of the visible light filters (Figure 2.8b)[1], it is possible isolate certain regions of the electromagnetic spectrum and obtain reproducible

[1]Spectral information available at www.newport.com

results. The effect of the liquid filter performances was monitored using a 40 ml vial with 15

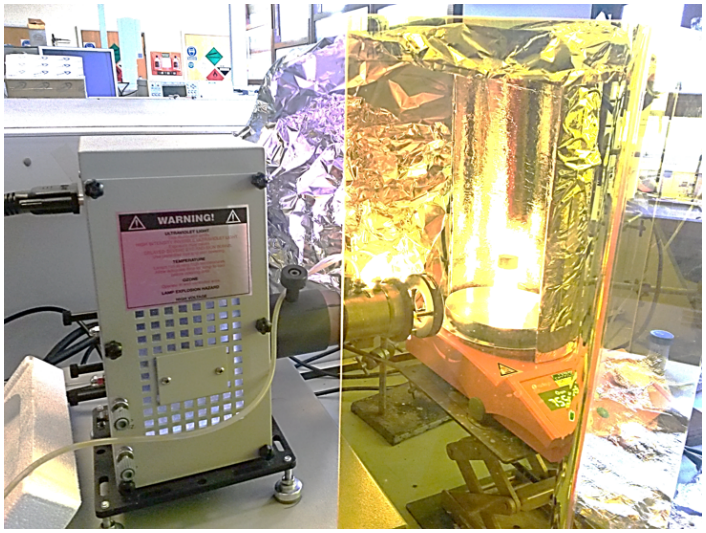

Figure 2.7 Typical configuration for the Xenon lamps.

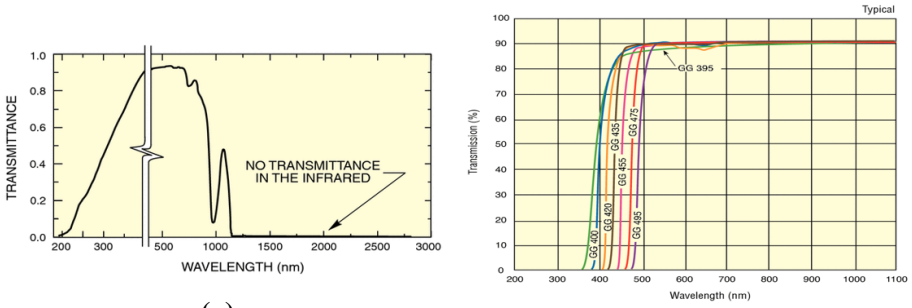

(a) **(b)**

Figure 2.8 Spectrum of action of the IR filter (2.8a) and cut-off values for several filters (2.8b)

ml of water. A thermocouple was inserted in the vial and the top was sealed off with parafilm to prevent water evaporation during the test. The peristaltic pump and the lamp were turned on and the temperature variation was monitored every 15 minutes for the first two hours and then at different time intervals over a 6 hours period and it can be seen in Figure 2.9 how the temperature is kept constant throughout the 6 hours after it reaches equilibrium after 1 hour of irradiation. The temperature variation is <5°C and therefore has negligible effect on the kinetics and of photo-initiated processes as stated in the Section 1.7.3 of the introduction.

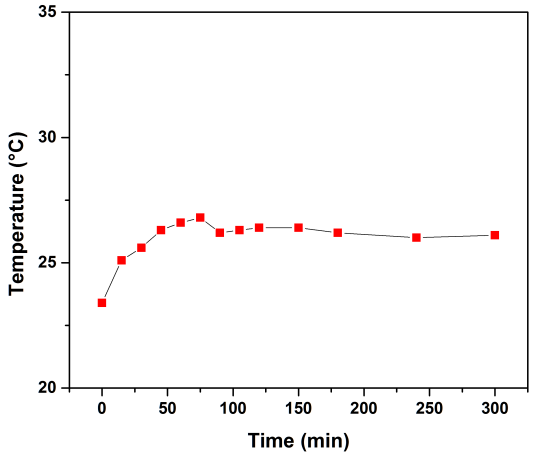

Figure 2.9 Temperature variation over 6 hours of irradiation under visible light for the 300 W Xenon lamp equipped with the IR liquid filter and the visible light filter with λ=420 nm.

2.9 Evaluation of the Catalyst Activity

Typically, the catalyst testing was performed in 16 ml borosilicate glass vials which are transparent to the wavelength range used and do not interfere with the light sources. Glucose solutions at different concentration were prepared solubilising the substrate in a 50/50 v/v MeCN/H_2O solution. Once the solution was transferred, the vial was sealed with a rubber septum to prevent the evaporation of the sample. It has to be noted that for these sets of experiments, no particular procedure was used to purge the reaction mixture of solubilised oxygen. Subsequently an appropriate amount of catalyst (14 mg) was added to the solution. The reactions were performed at different reaction times and samples were taken every 30 minutes in the first 2 hours and at the end of the reaction. The photocatalytic reactions were performed using three different systems: a Luzchem Photoreactor (Mod. LZC-4, Luzchem Research Inc. ON, CAN) equipped with 14x8 W UVA lamps for a total power of 112 W. The temperature was kept constant at 30°C for all the reactions run in the Luzchem Photoreactor. The second system was a 300 W Xenon Oriel Lamp (Mod. 6258, Newport, UK) controlled by a power supply (Mod.69911, Newport, UK). The third lamp used was a 1000 W Xenon Oriel Arc Lamp (Mod.6271, Newport, UK) controlled by digital power supply (Mod.69920,

Newport, UK). Both lamps were equipped with UV filters with a cut-off value of 420 nm (Mod.FSQ-GG420, Newport, UK. Additionally, due to the intense irradiation energy of the lamps, liquid IR filters were installed (Mod.61945 and Mod.6123NS for the 300 W and 1000 W respectively) to prevent the reaction mixture from overheating and the temperature of the reaction mixture was kept at 25±3°C. The vials were kept under magnetic stirring at 1300 rpm and at a constant distance (0.014 m) from the light source for all experiments.

2.9.1 Catalyst Recycling

The recycling of the Ag catalyst under visible and UV radiation was performed following a pyramidal scheme: for the first run 3 reactions were run for two hours under the same experimental conditions. The first three reactions were run using 14 mg of catalyst respectively, the catalyst recovered was then centrifuged and the supernatant was removed. The catalysts were then washed with H_2O and ethanol 3 times to remove any organics adsorbed on the catalyst. The washed powders were then dried overnight at 50°C and then ground. The recovered catalyst was then used in the second run for 2 reactions and, after the reaction, it was treated following the procedure described above. Finally, for the third run, only one reaction was analysed. The values provided for the conversions and the products selectivity for the first and the second run are the average of the results obtained for each of the reactions.

2.9.2 Conversion

Glucose conversion values were calculated as follows:

$$Conversion\ (\%)\ =\ \frac{[A]_{in}-[A]_{out}}{[A]_{in}} \tag{2.2}$$

The cellobiose conversion value was calculated as follows:

$$Conversion\ (\%)\ =\ \frac{[B]_{in}-[C]_{out}}{[B]_{in}} \tag{2.3}$$

In which B is the concentration of the initial cellobiose and C is the concentration of the cellobionic acid being produced during the reaction. As the two molecules coelute as because of the close k factor values due to the close proximity of the retention times of cellobionic acid (t_R=6.89 min) and cellobiose (t_R=7.01 min) (Appendix A.1) the area of the cellobionic acid was determined by analysing the peak obtained on the DAD detector thus calculating the corresponding concentration with the calibration curve available. The corresponding concentration value was then imput in the calibration curve obtained with the RID detector to calculate the equivalent area of the peak and this value was then subtracted to the cellobiose RID peak value to obtain the net cellobiose concentration for each sample.

2.9.3 Product Distribution Values

The product distribution values were calculated as follows and as an example gluconic acid (%) is reported below:

$$Gluconic\ Acid\ \ (\%)\ =\ \frac{[Gluconic\ Acid]_{out}}{[Gluconic\ Acid]_{out}+[A]_{out}+[E+\ G]_{out}+[F]_{out}} \tag{2.4}$$

In which A is arabinose, E+G are erythrose and glyceraldehyde and F is formic acid. It has to be noted that erythrose (t_R=10.87 min) and glyceraldehyde (t_R=10.72 min) coelute

under the analysis conditions used, and by analysing the RID response factor (Appendix A.1) for glyceraldeyde (m = 12320) and erythrose (m =12771) the average of these two values was used to report the overall concentration of these two molecules together. The product distribution values for the cellobiose reactions were calculated using Equation: 2.4. As regards the determination of the $C_{11}H_{20}O_{11}$ product from the oxidation of cellobiose, due to the absence of commercially available standards and the impossibility of isolating and fully characterize the molecular structure, the calibration curve for cellobiose was used to determine the concentration of this molecule.

2.9.4 Catalyst Specific Activity

The catalytic activity was evaluated by dividing the moles of substrate (A) converted over the grams of catalyst used in the reaction multiplied by the reaction time in hours:

$$Specific\,Activity = \frac{A\,converted\,(mmol)}{grams\,catalyst * hour} \tag{2.5}$$

Chapter 3

Optimization of the Reaction Parameters

THE BAND!

J. Blues

3.1 Introduction

Many photocatalytic processes are associated with unselective reactions aimed at the abatement of organic pollutants and other contaminants in the purification of water and gas streams [227, 4, 120]. In these applications, TiO_2-based materials show great potential as they are generally chemically stable, nontoxic and have high reactivity. Nonetheless, the mechanistic aspects behind these photo-initiated reactions are still unclear as the role of the species present on the surface of these materials can dramatically influence their reactivity. The identification of the factors that govern the kinetics and resolving each individual reaction step is a key aspect in the development of highly efficient photocatalytic systems. Typically the reference material used to benchmark the catalytic properties of various systems is the Evonik Degussa P25 which is a mixture of anatase and rutile in a ratio 3:1 often with small traces of brookite. The presence of multiple phases and structural defects in P25 make it difficult to characterize the adsorption-desorption properties of each phase and their role in

the production of radical species during the photo initiated reaction. Of the many possible phases only rutile and anatase proved to be photoactive [67]. The difference between the two crystalline phases is the relative position and coordination of Ti and O in the lattice structure. Both anatase and rutile have a tetragonal structure, but the conduction band values observed for anatase and rutile differ being 3.2 eV 3.0 eV respectively [229, 11]. The bandgap directly affects the ability of semiconductors to convert the incident light in chemical energy, and thus it is important to tailor the catalyst properties according to the application in order to maximise the quantum efficiency of the process. In fact, the radical species produced during a photocatalytic reaction are responsible for the redox process in solution and their mobility and ability to diffuse are key parameters. In a recent paper Kim and co-workers[131] demonstrated via a single molecule detection study that the photogenerated $^{\cdot}OH$ radicals are able to diffuse from the anatase surface into the bulk of the solution whereas when rutile is used, the radicals remain surface bound. The different mobility of the $^{\cdot}OH$ radicals produced when using the two different crystalline phases, might help to explain why P25 is the best material due to its polycrystalline nature, as the reactive species might migrate from the rutile to the anatase and then being subsequently released to the bulk of the solution. As previously mentioned, not only the mobility and the production rate of radical species have to be investigated, but also, and most importantly, the interaction between the substrate with the catalyst surface plays a pivotal role in the kinetics of any chemical reaction. In fact, in a recent paper the formation of a complex between TiO_2-glucose was identified as responsible for the activity under visible light of TiO_2 powders for the reduction of Cr (VI) to Cr (III) in solution. The presence of a ligand to metal charge transfer complex (LMCT) allowed electrons to be injected directly on the conduction band of TiO_2 thus making them available to react (Figure 3.1) [130]. For these reasons we decided to investigate the possible application of TiO_2 in the selective photochemical upgrade of bio-derived molecules to produce high-value chemicals from simple carbohydrates. Glucose was used as a probe

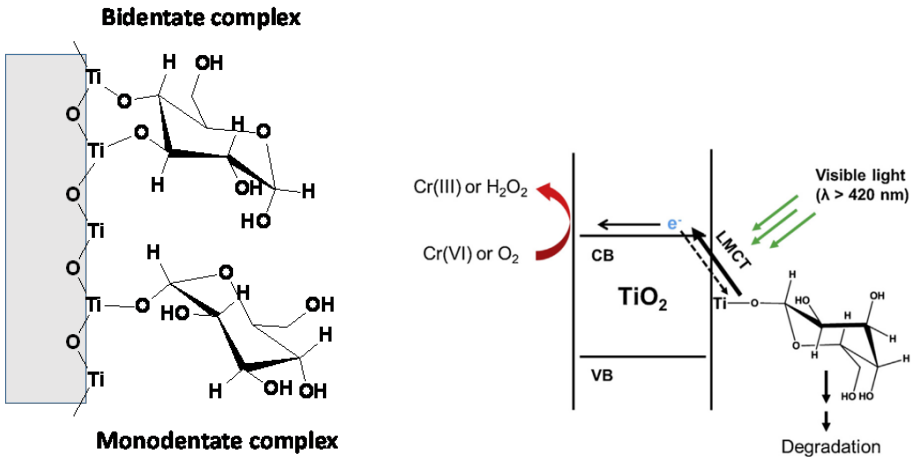

(a) (b)

Figure 3.1 (3.1a) Two possible configuration of the glucose-TiO_2 complex; (3.1b) Ligand to metal charge transfer complex responsible for the TiO_2 photoactivity under visible light.
Taken from Kim et al. [130].

molecule in this study as it is the cheapest and most available carbohydrate from biomass and, being a rather simple substrate to work with, it allows a greater understanding of the reaction mechanism and optimum reaction conditions.

3.2 Results and Discussion

3.2.1 Effect of the Catalyst to Substrate Ratio

In order to make photocatalytic processes feasible, the ultimate aim, as for conventional chemical processes, is to achieve the lowest catalyst to substrate ratio without hindering the catalytic activity of the material and preserving key parameters such as selectivity, product distribution, and turn over frequency. Most importantly, when designing a reaction protocol, it is preferable not to work in mass-transfer-limiting conditions, as the adsorption-desorption mechanism might alter or significantly slow down the reaction rate thus affecting the chemistry of the reaction involved. For these reasons, specifically in photocatalysis, as it is an area in its infancy, it is necessary to study the effect of different substrate concentration

values on the aforementioned parameters. In this first part of the study the TiO_s-P25 catalyst concentration was kept constant (1 g L^{-1}) and the glucose concentration increased from the initial 2.8 to 20 mM , under both visible and UVA light. Figure 3.2 shows the glucose conversion as a function of time under UVA and visible light at varying catalyst to substrate ratios. Under visible light at the lowest glucose concentration of 2.8 mM the conversion reaches 41% after 240 minutes on line. This value is higher than under UVA light where the final conversion is 32%. When the glucose concentration was increased, the samples exposed to UVA light showed higher conversion for the 10 mM solution and at the highest substrate concentration value (20 mM) no differences were observed. This trend can be explained

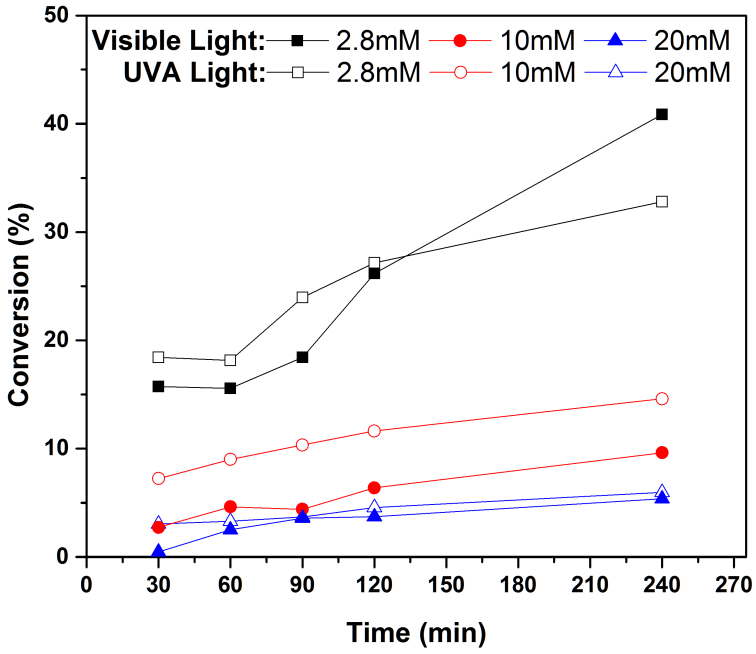

Figure 3.2 Time on line (TOL) glucose conversion under visible and UVA light over 240 minutes for the different catalyst to substrate ratio values.

considering the formation of the TiO_2-glucose complex (Figure 3.1) identified by Kim et al. [130], as it appears that under visible light the interaction of glucose molecules with the TiO_2 surface is favourable and that the reaction rate benefits from the formation of this complex as it increases the catalyst activity. When the concentration of glucose reaches a critical value,

it is safe to assume that the active sites to which glucose can bind to are already occupied and, therefore, there is no significant increase in the reaction rate.

Kisch [132] reported that the evaluation of the quantum yield efficiency of photocatalysts and the comparison of the reaction rates in heterogenous photocatalysis is a complex problem to solve. In fact, the rate of any photoreaction is controlled by the product of the quantum yield and the absorbed light intensity, with the latter, depending on the concentration of the light-absorbing species. It was found that photochemical reactions rates are determined

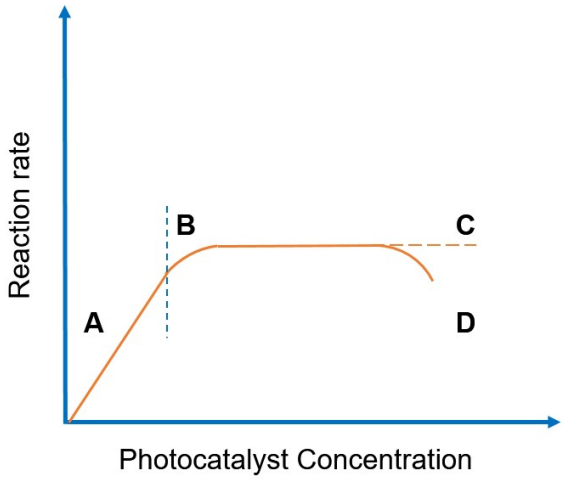

Figure 3.3 Heterogeneous photocatalysis reaction rate dependence on catalyst concentration. Adapted from Kisch [132].

by the catalyst concentration; in fact, initially, the reaction rate increases linearly with the photocatalyst concentration due to increment of the photon absorption (Figure 3.3 A to B) and then it reaches a plateau value corresponding to the saturation of the light absorption and not to diffusion limitations (B to C). Additionally, it was reported that the optimum concentration for TiO_2-catalysed reactions to be in the range of 0.5 to 3.0 g ml^{-1} depending on the configuration of the light sources used.

The catalyst concentration used in this work was optimised at the maximum stirring speed used (1300 rpm). In fact, at this stirring speed, the catalyst could be suspended completely, and it was observed that at values grater than 1 mg ml^{-1} the catalyst could not be entirely

suspended thus not making it available to participate in the reaction. In fact, initial catalytic runs performed with a catalyst concentration of 3 mg ml^{-1} did not show greater substrate conversion values implying that the optimum region of photon absorption shown in Figure 3.3 between the point B and C had been exceeded and that the reduced light penetration due to scattering actually decreased the reaction rate (Figure 3.3 D). Therefore, as reported by Kisch [132], the semi-quantitative comparison between photocatalytic activities should be performed at the plateau region such as in this study. From the specific activity values reported in Table 3.1 it can be seen that despite the increased substrate concentration from 2.8 to 20 mM the activity of the catalyst does not change. In fact, if one was expecting to witness mass transfer limitations, these values would decrease with the increased substrate concentration, but it does not appear to be the case in the concentration range used in this study. The importance, on the other hand, of the catalyst concentration was studied in preliminary tests using 40 mg of catalysts (not reported) showed negligible conversion values due to the scattering of the incident light. Additionally, tests using higher concentration of glucose (50 and 100 mM) were run to assess the effect of mass transfer limitations, but these concentration exceeded the linear response of the HPLC detector and it was found that the dilution of the crude reaction mixture caused sample instability and unreliable results.

It has to be noted that the HPLC determination of the products in the liquid phase showed good relative standard deviation trends, with values generally lower than 1% for the standard compounds considered in this study. The small error associated with each measurement and the good reproducibility of the analysis (Appendix A.1) allow to assume that mass balance values lower than 100% are due to the mineralisation of glucose to CO_2 and H_2 as reported in the literature [123, 61, 92]. The quantitative determination of the gaseous products can be performed with headspace analysis but this technique was not available during this study.

Additionally, the glucose conversion reported below is just an indication of the activity of the system, but does not take into account the selectivity of the process towards the partial

oxidation products or towards the total mineralisation of the substrate to produce H_2 and CO_2 (Table 3.1). Surprisingly, the specific activity values reported in Table 3.1 show that there

Table 3.1 Glucose conversion, gluconic acid selectivity and mass balance values for the reactions performed at increased substrate concentration under visible and UVA light.

Glucose Concentration (mM)	Glucose Conversion (%)	Gluconic Acid (%)	Arabinose (%)	Erythrose + Glyceraldehyde (%)	Formic Acid (%)	Mass Balance (%)	Specific Activity (mmol g^{-1} h^{-1} [c])
2.8 [a]	42.1	7.4	20.0	16.7	56.0	90.4	21.2
10 [a]	9.6	9.8	26.2	20.1	43.9	99.7	17.7
20 [a]	5.4	12.0	30.0	18.5	39.5	100.0	19.4
2.8 [b]	36.6	0.0	44.8	9.2	46.0	80.9	18.5
10 [b]	14.6	6.2	43.2	13.5	36.9	95.6	21.4
20 [b]	6.0	7.3	46.7	12.1	33.9	98.5	21.6

Reaction conditions:
[a] 240 min, 14 mg of catalyst, Visible light;
[b] 240 min, 14 mg of catalyst, UVA light;
[c] Catalytic activity expressed as moles of glucose converted over grams of catalyst per hour

is not much difference in terms of the catalytic activity under UVA and visible light, and the activity of the catalyst appears to be constant with the increased glucose concentration. Under UVA light the excitation of the TiO_2 bandgap does not seem to have an effect as the specific activity values are comparable with the ones obtained under visible light. Therefore, the formation of the glucose-TiO_2 comples shows similar activity than under UVA light where the formation of the LMCT does not occur due to the presence of reactive radical species on the catalyst surface as confirmed by the FT-ATR analysis of the recovered catalyst after the reaction. The increased glucose concentration also affects the mass balance values, as for the lowest glucose concentration, after 240 minutes of reaction values as low as 90.4 and 80.9% were recorded for the samples exposed to visible and UVA light respectively.

Interestingly, even when the incident irradiation is not sufficient to promote electrons in the TiO_2 conduction band, glucose is still mineralized and this pathway happens to have significant impact on the overall reaction mechanism only at the lowest substrate concentration. On the other hand, for the reactions run with a glucose concentration of 10 and 20 mM the mass balance displays +98% values under visible light, and as expected, under UVA light the glucose mineralisation still plays a significant role because in this case

the support is an active part of the catalytic system as under these conditions the photons have enough energy to promote electrons from the valence to the conduction band.

These results show similar chemical reactivity of TiO_2 towards the production of partial oxidation products as recently reported by Colmenares et al. [61] (Scheme 3.1) for TiO_2-based catalysts under UV light and similar catalyst and substrate concentrations. Recently, Chong et al. [53] reported the conversion of aldoses with TiO_2-based materials with the addition of precious metals (Rh, Pt, or Pt) as co-catalysts. In this case, the reaction mechanism reported (Scheme 4.1) does include the presence of oxidised species as for the previous one but the production of formic acid and hydrogen.

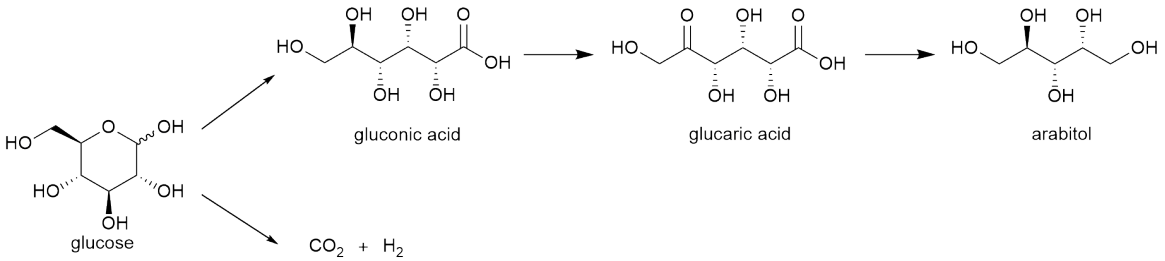

Scheme 3.1 Proposed reaction mechanism showing the formation of oxidation products along with the total mineralisation of the substrate to produce H_2 and CO_2. Adapted from Colmenares et al. [61].

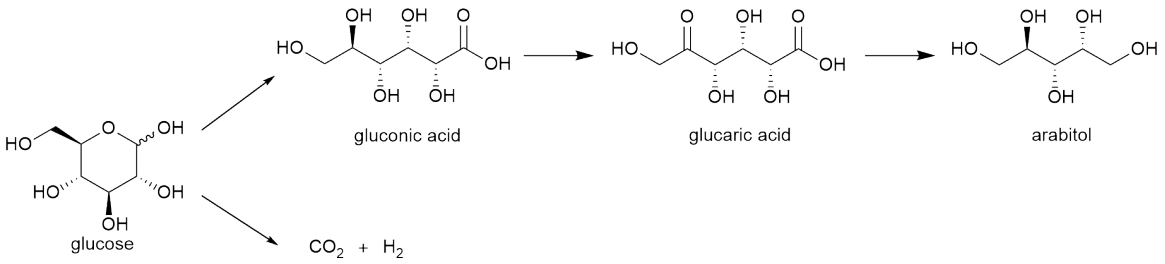

Scheme 3.2 Proposed reaction mechanism showing the glucose α-scission with the elimination of formic acid and H_2.Adapted from Chong et al. [53].

3.2.2 Effect of the TiO_2 Crystalline Structure

All TiO_2 polymorphs can be described as distorted TiO_6 octahedra with an apical distance of the two Ti-O bonds of ca.1.980Å for both anatase and rutile longer than the four equatorial

bonds. Anatase shows higher distortion as the equatorial bonds are ca.1.934 Å (Figure 3.4) instead of the 1.948 Å measured for the rutile phase (Figure 3.5) [51]. These differences in

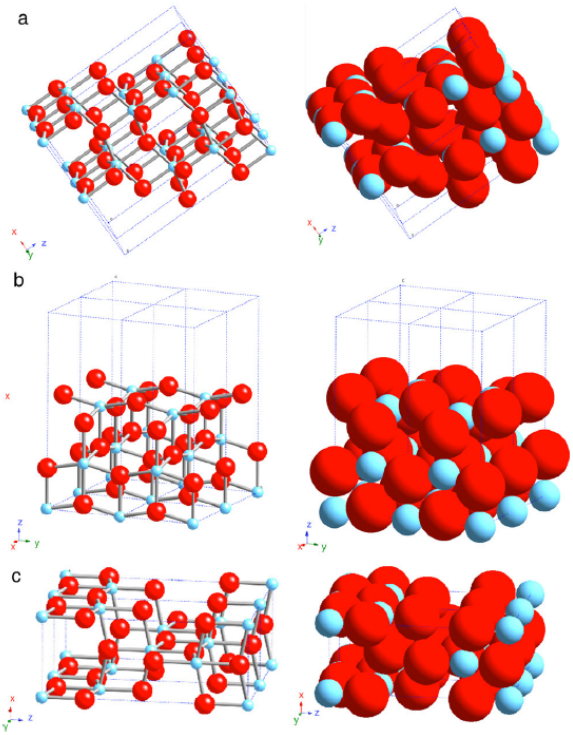

Figure 3.4 Representation of the low-index anatase phases (a) (110); (b)(100); (c) (001)

the bonds length in addition to the different coordination of the octahedrons in the anatase and rutile crystalline phases, explain the different density of the two materials (4.250 cm^3 g^{-1} for rutile and 3.894 cm^3 g^{-1} for anatase) and the positioning of the electronic band structures as confirmed by the solid UV-Vis analysis (Figure 3.6). There are several examples in the literature on the superior activity of TiO_2-P25 due to the synergistic effect of the presence of both rutile and anatase phases in the same solid [189, 24, 113]. In fact, the presence of rutile and anatase along with a minor amorphous content (generally lower than 5%), forms a heterojunction between the two phases, and the difference in the bandgap position and the presence of an interface, can enhance the separation of the electron-hole pair formed during the process and, at the same time, reduce the recombination rate, thus making the reactive species available for longer [188, 28, 95, 208, 252]. In this set of experiments rutile,

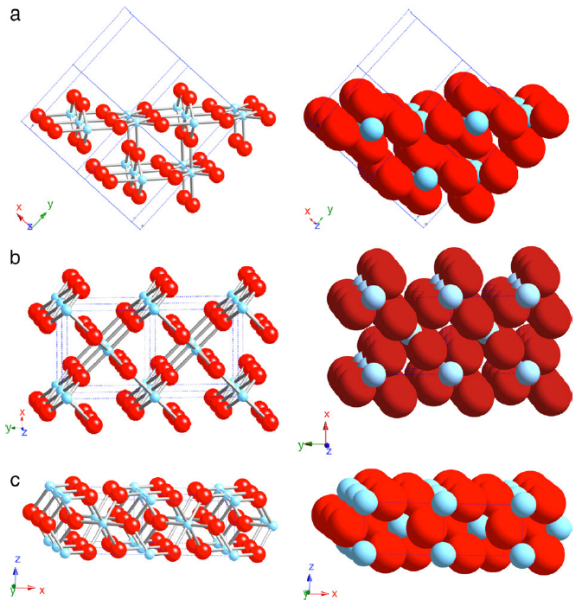

Figure 3.5 Representation of the low-index rutile phases (a) (101); (b)(100); (c) (001)

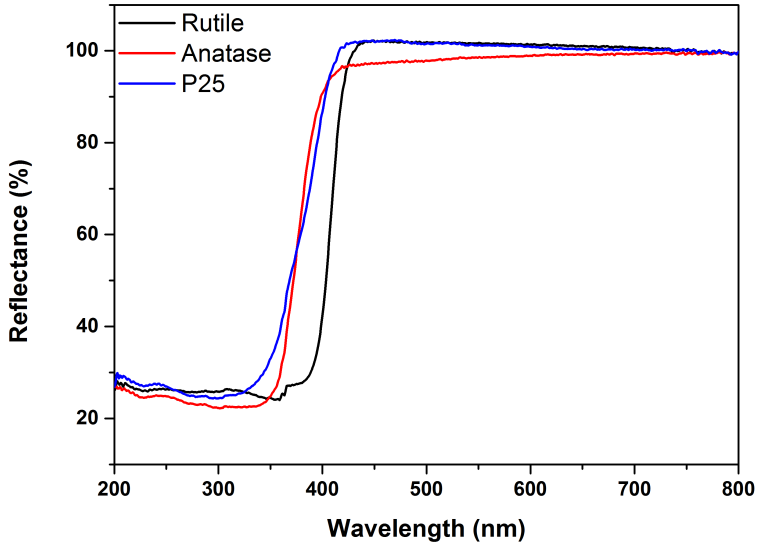

Figure 3.6 Solid UV-Vis spectra of the different TiO_2 polymorphs (rutile and anatase) and Degussa P25.

anatase and TiO_2-P25 were used to assess their respective catalytic activity in the glucose oxidation. As the reaction were previously optimized, all reaction were carried out with a catalyst concentration of 1 g L^{-1} and a 20 mM glucose stock solution. Surprisingly, when testing the different catalyst, rutile proved to have higher photo-activity than anatase, with comparable performances with the P25 displaying a glucose conversion of 4.3% and 4.6%

respectively, whilst anatase displayed only 2% after 120 minutes under UVA irradiation. A similar trend can be seen under visible light as P25 outperforms both rutile and anatase displaying a glucose conversion of 3.7% against 1.7% and 0.1% respectively. Additionally, gluconic acid could not be detected when the pure crystalline phases were used as a catalyst under visible light, with only P25 showing 14.9% selectivity to the acid intermediate. On the other hand, anatase under UVA irradiation gave a much higher gluconic acid selectivity value of 19.9% if compared with P25 (8.9%) and rutile (6.9%) (Table 3.2). Anatase poor

Table 3.2 Effect of the different TiO_2 crystalline structures on the product selectivity, product concentrations and total mass balance for the reactions run under visible light and UVA light.

Catalyst	Glucose Conversion (%)	Gluconic Acid (%)	Arabinose (%)	Erythrose + Glyceraldehyde (%)	Formic Acid (%)	Mass Balance (%)	Specific Activity (mmol g^{-1} h^{-1})[c]
Rutile [a]	1.7	0.0	32.2	33.4	34.5	100.0%	11.9
Anatase [a]	0.1	0.0	49.5	50.5	0.0	100.0%	1.0
P-25 [a]	3.7	14.9	23.4	13.9	47.8	100.2%	26.8
Phys Mix [a]	1.1	16.7	25.3	21.0	37.0	100.8%	8.2
Rutile [b]	4.3	6.9	27.4	25.9	39.8	99.4%	31.2
Anatase [b]	2.0	19.9	29.0	9.8	41.3	100.3%	14.4
P-25 [b]	4.6	8.9	43.4	14.7	33.0	99.3%	33.1
Phys Mix [b]	3.0	10.4	29.3	14.4	45.9	100.5%	21.1

[a] Visible light
[b] UVA light
[c] Reaction conditions: Glucose 20 mM, 14 mg catalyst

specific activity (1.0 mmol g^{-1} h^{-1}) compared with rutile (11.9 mmol g^{-1} h^{-1}) under visible light can be explained in two different ways the first one is due to the bandgap positioning of the two materials. Anatase with a bandgap value of 3.2 eV (387 nm) is located in the low-transmittance region of the visible light filter whilst rutile with a bandgap of 3.0 eV (413 nm) is close to the 50% transmittance value of the filter and therefore, more photons are available to initiate the photocatalytic process (See Figure 3.11 in Section 3.2.4). In the literature, albeit with some discrepancies, anatase is usually found to be the most photoactive TiO_2 phase. Ryu and Choi [204], demonstrated the substrate-specific photocatalytic activity of TiO_2 phases towards specific substrates, demonstrating the superior rutile activity on anatase for the degradation of dye orange 7. Moreover, the performances of rutile, anatase and the combination of the two phases were evaluated in the degradation of different pollutants in

aqueous solutions. We can conclude that, for the oxidation of glucose, the specific interaction substrate-support is favourable for rutile, despite its lower surface area compared with anatase. From these preliminary results, it is clear that the different TiO_2 allotropic structures, not only have an effect on the glucose conversion but, interestingly, also on the product distribution. In order to demonstrate the synergistic effect of the two crystalline phases, rutile and anatase in a proportion 1:3 (to mimic the typical composition of P25) were mixed together and the mixture was tested under the same experimental conditions. Interestingly, the selectivity values for the partial oxidation products observed after 120 minutes of visible light irradiation are similar to the ones observed for the P25 after the same reaction time, but significantly different from the ones obtained when the pure TiO_2 phases were used as no gluconic acid was detected in both cases. What is surprising in all 3 cases, is that the different crystalline phases are active, to some extent, at wavelengths greater than 420 nm, which is surprising as in this range, the incident photons do not have sufficient energy to promote electrons in the TiO_2 conduction band. The formation of a photoactive ligand to metal charge transfer (LMCT) TiO_2-glucose complex has been proven to be effective in the reduction of metal ions in solution as the organometallic complex is able to inject electrons directly in the conduction band of the TiO_2 thus making them available for further reactions [130]. In fact, all the catalysts tested in this section, showed the color transition from white to yellow as reported by Kim et al. [130] in their work, therefore, confirming the formation of the glucose-TiO_2 complex. Direct measurements to confirm of the presence of the LMCT complex were performed on the Ag-decorated TiO_2 catalysts described in the following chapter. In fact, in this case, the presence of such complex is mandatory to extend the TiO_2 activity to the visible part of the spectrum and the results obtained are in good agreement with the previous findings deported by Kim et al. [130].

The possibility of extending the activity of an inorganic material via the formation of a metalorganic complex in which the reactant acts as a co-catalyst demonstrates the pivotal

role of the adsorption mechanisms and the possible interactions between the photoactive material and the substrate, not only in photodegradation processess, but more interestingly, for their application in selective photocatalytic oxidative reactions.

3.2.3 Effect of the Calcination Temperature

Rutile is the thermodynamically stable TiO_2 phase, however, the small differences in the Gibbs free energy between the different phases are small (4-20 kJ mol^{-1}) therefore, the other allotropic structures can be obtained as metastable phases. The transition of the other polymorphs to rutile does not occur at low temperature, but by heat treatment at moderate temperatures from 300-500°C it is possible to increase the rutile content, whilst at higher temperatures (>600°C) it becomes the dominant phase. Specifically, P25 was treated at 500 and 600°C to allow the transition of the other metastable phases to rutile and assess whether the increase rutile content could have an impact on the catalytic performances on the glucose oxidation reaction.

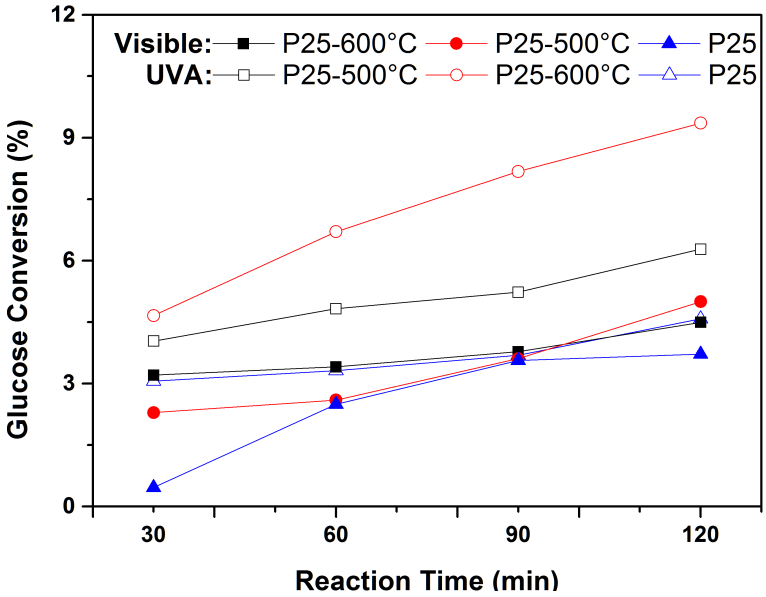

Figure 3.7 TOL glucose conversion of the P25 calcined samples under visible and UVA light

As shown in Figure 3.8, by increasing the temperature during the heat treatment process, the rutile content increases noticeably at 600°C. In fact, if these spectra are compared with the ones shown in Figure 3.6 for the different TiO_2 crystalline phases, it can be seen how the sample treated at 600°C shows a different absorption profile with a similar trend as shown by the pure rutile phase. The simple UV-Vis analysis of such materials, can provide

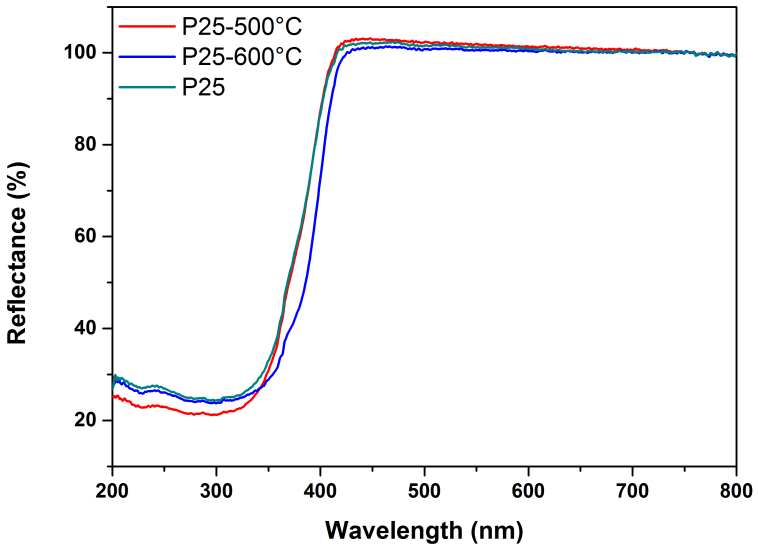

Figure 3.8 Solid UV-Vis spectra of the starting P25 and of the heat treated samples at different temperatures.

qualitative information regarding the alteration of the composition of the material, albeit the precise quantification of the phases present in the solid sample, for which XRD analysis is a necessary tool.

The increase rutile loading on the treated materials was also determined by powder X-ray diffraction (PXRD) of the powders. The rutile content increased from 8.2% in the untreated P25 to 28.2% for the sample treated at 600°C (Figure 3.9). The increase in the rutile content was determined by comparing the intensity of the rutile (110) peak at a 2Theta angle of 27.355 with the anatase (101) at 25.176.The relative ratio of the two phases was calculated without accounting for the amorphous content which has been proven elsewhere to be between 8 and 13 wt% [190, 233]. The treated P25 powders namely, P25-500°C and P25-600°C were tested and, as expected, the materials with higher rutile content displayed higher catalytic activity with a glucose conversion of 9% under UVA light compared with 4.6% of the untreated P25 for the P25-600°C (Table 3.3), whereas under visible light there were no substantial differences in the performances of the two materials. The increased rutile content directly affects the activity of the catalyst incrementing its turnover frequency under UVA light and, interestingly, similar product distribution values were observed compared

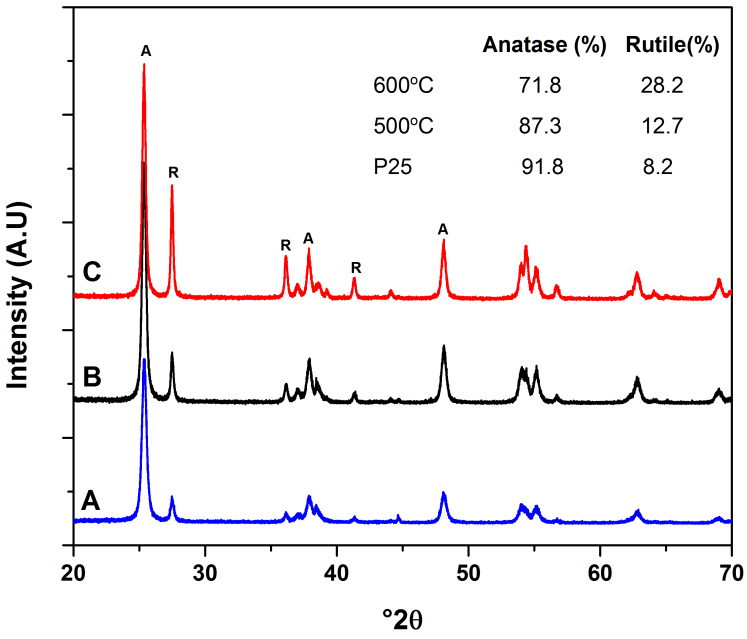

Figure 3.9 PXRD pattern for A) TiO_2 –P25, B) P25-500°C and C) P25-600°C.

with the untreated P25 under both visible and UVA light. The heat treated TiO_2-P25 samples

Table 3.3 Effect of P25 calcination temperature on the product selectivity, product concentration and total mass balance for the reactions run under UVA and visible light

Catalyst	Glucose Conversion (%)	Gluconic Acid (%)	Arabinose (%)	Erythrose + Glyceraldehyde (%)	Formic Acid (%)	Mass Balance (%)	Specific Activity (mmol g^{-1} h^{-1})[c]
P-25 [a]	3.7	14.9	23.4	13.9	47.8	100.2	26.8
P-25-500°C [a]	4.5	12.1	25.8	19.5	42.6	98.4	33.2
P-25-600°C [a]	5.0	12.9	32.8	19.9	34.4	98.0	36.9
P-25 [b]	4.6	8.9	43.4	14.7	33.0	99.3	33.1
P-25-500°C [b]	6.3	6.6	44.4	12.1	37.0	100.1	44.8
P-25-600°C [b]	9.4	7.2	41.4	12.1	39.2	96.2	69.1

[a] Visible light
[b] UVA light
[c] Reaction conditions: Glucose 20 mM, 14 mg catalyst

specific activity reported in Table 3.3 shows a direct correlation between the increased rutile content and the higher activity observed. In fact, an increment from 26.8 (P25) to 36.9 mmol g^{-1} h^{-1}(P25-600°C) was observed under visible light and similarly from 33.1 to 69.1^{-1} h^{-1} under UVA irradiation. The UVA activity observed follows the expected trend, in fact, in these conditions, the incident photons have enough energy to start the photocatalytic process, whilst under visible light conditions, the catalytic activity is only due to the formation of the

LMCT complex, with the TiO_2 not being excited at all due to its bandgap level but acting more as a charge carrier which allows redox processes to happen on the surface.

3.2.4 Effect of the Lamp Power, Filters and Solvent Used

Photocatalytic processes are designed to replace conventional chemical reactions with greener and more sustainable alternatives. To do so, milder conditions are required along with non-toxic solvent to make these processes appealing alternatives. Another important aspect one has to consider is the power of the energy source used to drive these chemical reactions. Conventionally, pressure, temperature and contact time are the parameters engineers have to tune to maximise productivity and reduce running costs, whilst in photocatalysis, the main question is, how much power is required to run a reaction efficiently? In the literature, there are no benchmark parameters regarding the power of the light source, and on the range of wavelengths/conditions (UVA, UVA and visible light, and pure visible irradiation only) to be used when testing new materials [17]. The aim of the part of this work was to test the two Xenon lamps available (300 W and 1000 W) under the same experimental conditions to assess the effect of the light intensity on the glucose conversion . The irradiation power was measured with a PMA 2100 radiometer (Solar Light Company, Inc., USA) equipped with an ISO classiefied Class 1 pyranometer PMA2145 (Solar Light Company, Inc., USA) which measures the power of the incident radiation from 310 to 2800 nm. Due to the nature of the the sensor, it was not possible to measure the light intensity inside the vial, therefore, the values reported in Table 3.4 represent the power of the irradiation on shining on the vial. Initially,

Table 3.4 Irradiance power of the Xenon lamps used measured at 0.014 m from the lamp over a period of 5 minutes.

Lamp	**Lamp hours (h)**	**Power (kW m^{-2})**	
		420 nm	**No Filter**
1000 W	200	27.4	33.1
300 W	600	4.5	5.8

the two systems were tested using P25 as catalyst and a 20 mmol L^{-1} glucose solution in a 50/50 MeCN/H_2O mixture as previously reported by Colmenares et al. [61]. Glucose conversion was found to be 22.8% and 13.7% and with the filters in place, the conversion dropped to 1.7% and 3.7% for the 1000 W and 300 W respectively (Table 3.5). When pure

Table 3.5 Product distribution observed for the TiO_2 samples tested with the Xenon lamps with and without visible light filters.

Lamp Power (W)	Cut off filter	Glucose Conversion (%)	Gluconic Acid (%)	Arabinose (%)	Erythrose + Glyceraldehyde (%)	Formic Acid (%)	Mass Balance (%)	Specific Activity (mmol g^{-1} h^{-1})[c]
1000[a]	yes	1.7	0.0	44.9	55.1	0.0	99.1	12.7
1000[a]	no	22.8	5.6	59.3	15.0	20.1	90.1	164.1
1000[b]	yes	2.1	21.2	23.1	28.8	26.9	99.7	15.0
1000[b]	no	9.5	7.9	62.0	15.9	14.2	96.5	67.3
300[a]	yes	3.7	11.2	31.4	23.8	33.5	101.0	26.8
300[a]	no	13.7	9.2	55.1	16.8	18.9	95.3	97.9
300[b]	yes	2.2	23.9	35.3	40.8	0.0	99.5	15.9
300[b]	no	6.4	10.0	51.4	20.6	18.0	98.1	46.2

[a] MeCN/H_2O
[b] H_2O
[c] Reaction conditions: Glucose 20 mM, 14 mg catalyst

H_2O was used as reaction medium, conversion values dropped to 9.5% (1000 W) and 6.4% (300 W) without filters, and to around 2% with the filters installed (Figure 3.10b, 3.10a, Table 3.5). Clearly, the significant differences in the conversion values can be explained

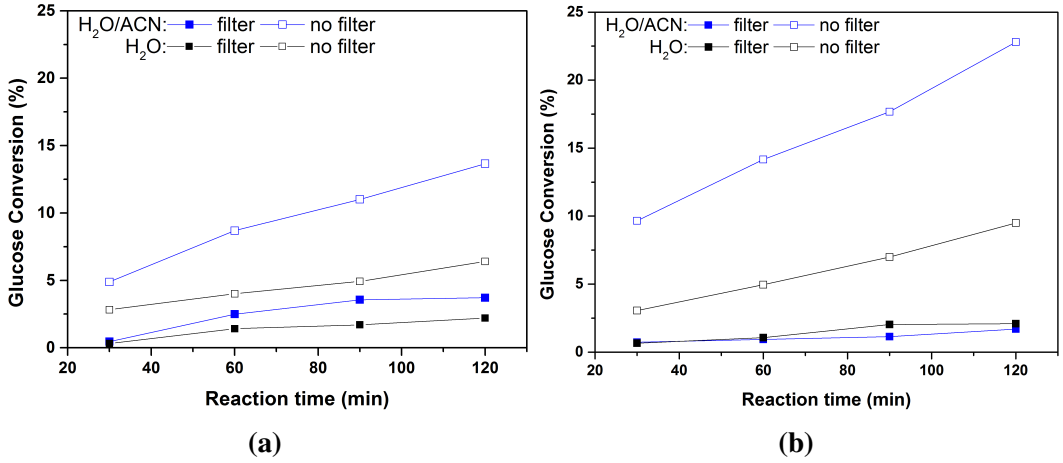

Figure 3.10 Glucose conversion obtained using two different Xenon lamps 300 W (3.10a) and 1000 W (3.10b) with and without the visible light filter using H_2O and the 50/50 v/v H_2O/MeCN mixture.

taking into account the different activity of the support under those conditions. Generally,

UV light filters are defined by their cut-off value which is defined as 50% transmittance of the radiation at the nominal wavelength. This value, clearly implies a certain degree of transmission of the wavelengths in the range ±20 nm of the nominal value. Therefore, even with the filter installed, it is possible to partially excite the TiO_2 bandgap thus explaining the apparent activity under visible light along with the formation of the LMCT complex (Figure 3.11). If we compare the specific activity values reported in Table 3.5 the dramatic

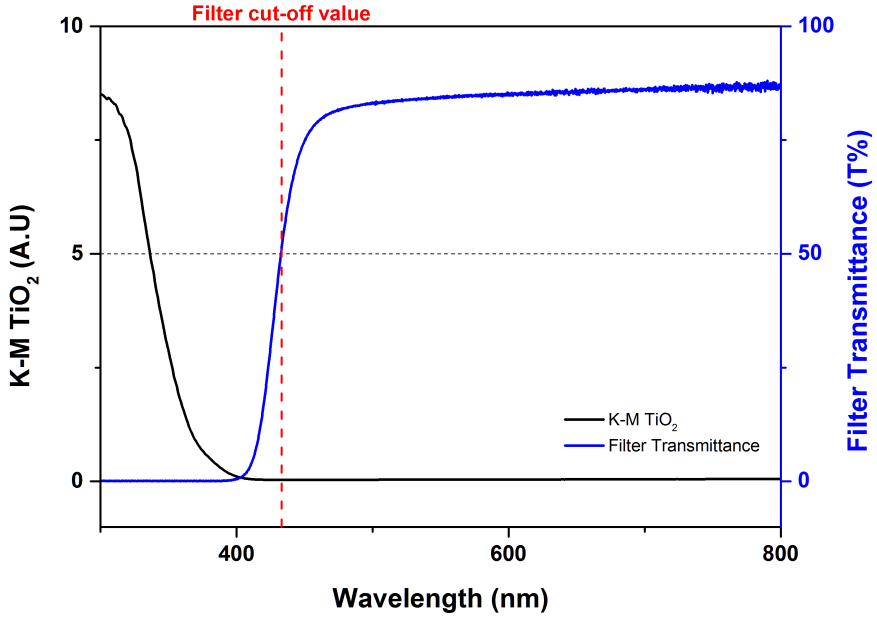

Figure 3.11 Filter Transmittance profile (blue) and the TiO_2 Kubelka-Munk function in the 300-800 nm range. The cut off value defined at the 50% transmittance is partially transparent in 400-420 nm range.

effect that the visible light filter has on the glucose conversion is evident. In fact, for the 300 W lamp, there is a threefold increase in the catalyst activity with the MeCN/H_2O mixture (15.9 to 46.2 mmol g^{-1} h^{-1}) and also when pure H_2O is used. The 1000 W lamp shows even higher differences, in fact for the MeCN/H_2O mixture the catalyst activity observed without filter is 13 times higher (164.1 mmol g^{-1} h^{-1}) than the one observed with the filter installed (12.7 mmol g^{-1} h^{-1}). The ultimate aim of photocatalytic processes is to harvest solar light as efficiently as possible without filtering any wavelength, but on the other hand, to harvest the widest possible region of the electromagnetic spectrum in order to maximise

the overall efficiency of the process. In fact, when the filters are removed, the catalyst is exposed to both the UVA and visible part of the spectrum and under these circumstances photons have enough energy to start the photocatalytic process and the conditions are similar to what would happen if solar light was used. These results clearly show that the power of the light source along with its irradiance flux and area, have to be chosen according to the experimental set-up used. In fact, more irradiance does not necessarily imply better results. Lower power lamps have also benefits as the arc sources are smaller and, in some cases, even brighter than more powerful lamps, thus it is possible to achieve high flux densities on small targets as well as with small lamps. It is also worth considering that smaller lamps are easier to operate, and they do not require additional filters to dissipate the heat produced and avoid thermal variations in the reaction mixture. Therefore, the application of every lamp is really reaction and configuration sensitive and the choice on which configuration to use has to be made carefully. Additionally, when photocatalytic results are reported, information on the lamp hours and on the average lifetime of the irradiating source should also be available, as the performances of the same lamp throughout its life cycle vary dramatically. The solvent choice also has an impact on the substrate conversion in photochemical reactions. The use of acetonitrile in photocatalysis, despite not being an ideal green solvent, is due to the fact that this molecule has no absorption in the ultraviolet nor visible region of the spectrum (Figure 3.12), it is a polar and aprotic solvent, and has very little chemical reactivity.

In the literature there are some examples of H_2O/MeCN mixtures in photochemical applications, but the role of the MeCN is not yet fully understood because of the complexity of the chemistry involve [213, 62, 59]. Redmond and Fitzmaurice [197], proved that the TiO_2 flatband potential is also affected by non-aqueous solvents, and they reported that in the absence of the proton adsorption-desorption mechanism the negative values were observed in MeCN, EtOH and MeOH. When electrolytes and water are added to the systems, significant positive shifts were observed. Therefore, when considering a photocatalytic system it is

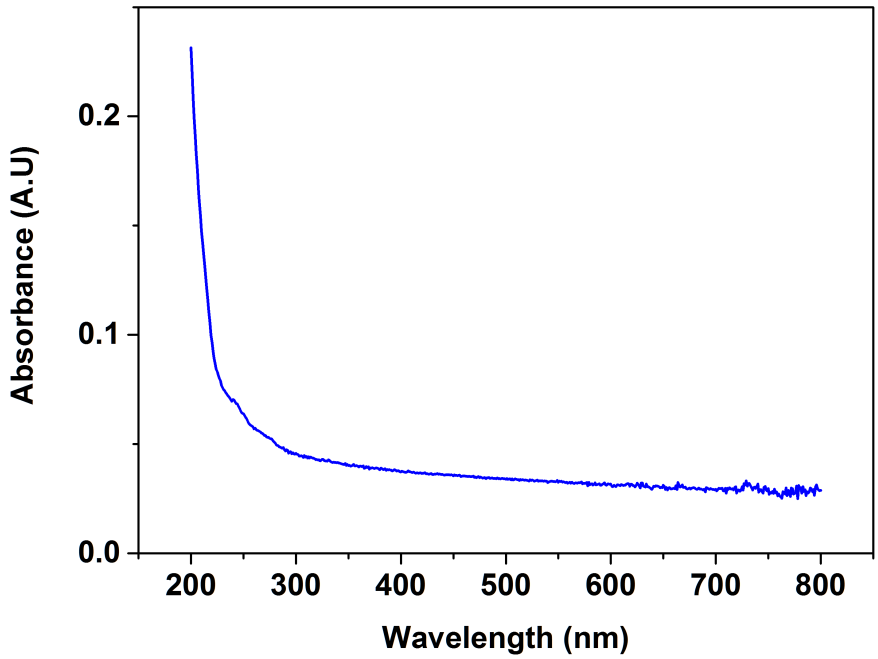

Figure 3.12 UV-Vis MeCN absorption spectrum.

necessary to consider the effect of the solvents on the zero point charge value of the material as the adsorbed species along with the effect of the solvent might affect dramatically the photo activity of the material. Various authors suggested that the lifetime of singlet oxygen ($^1O_2$) species produced during the photochemical process might be increased in when aprotic and polar solvents are present in the solution [110]. Therefore, the longer lifetime of radical species in MeCN compared to pure water would explain the catalyst activity in different reaction media, but the determination and quantification of these reactive radicals, exceeds the purpose of this work.

3.3 Conclusions

The work shown in this chapter introduces the possibility of using TiO_2 as a interesting material to perform selective photocatalytic oxidations. The preliminary results testify the importance of the substrate-semiconductor interactions, and the possibility of running reactions at wavelength values which are outside the optimum theoretical value referred to the

bandgap of the semiconductor. In fact, the formation of LMCT complexes partially extends the activity of semiconductors which are active under UV irradiation to the visible part of the spectrum. This concept cannot be extended *tout court* to all semiconductors due to the influence of several parameters (pH, zero charge point, hydroxylation of the surface *etc*) but this scenario has to be taken into account when approaching new reactions for the first time as the results obtained might be significantly influenced by this phenomenon. The surprising activity of these materials under the experimental conditions considered, introduces the following chapter in which the addition of metal nanoparticles on the semiconductor surface is used to extend the range of activity at even higher wavelengths with significant effect on the mass balance, conversion and the specific activity values.

Chapter 4

Glucose Photo-oxidation

DO YOU SEE THE LIGHT?

Rev. C. James

4.1 Introduction

Glucose is the most common and cheapest carbohydrate available in nature as it is easily extracted from many plants (i.e. cane sugar or beetroot), or easily obtained from corn and other crops. It can be obtained from starch or any waste lignocellulosic biomass via the hydrolysis of its component polysaccharides (cellulose and hemicellulose). Glucose can be valorised into platform chemicals such as glucaric acid, arabitol, levulinic acid and hydroxymethylfurfural by variety of chemical, catalytic and enzymatic pathways [27]. Early reviews surveyed the possible application of glucose oxidation products as chiral intermediates with potential application in the pharmaceutical industry and as precursors for vitamin C and other high value chemicals [202]. Commercially, it is a precursor to gluconic acid which is used in the pharmaceutical, food, health and textiles industry [115]. Glucose transformations are typically carried out by fermentation and enzymatic routes but these often suffer from poor rates, low yields and the cost of the enzyme used [115]. An

alternative, highly selective route using a heterogeneous catalyst offers a potentially more robust alternative route. As early as the 1940's a number of researchers showed the efficiency of Pt and Pd based catalysts for the production of gluconic acid resulting in a number of patents [70]. More recently, Au, Pd and Pt have been shown to be active and selective leading to a resurgence and further effort to make the reaction a more economically viable process [167, 163, 21, 251, 26, 29]. However, the reaction still suffers from generally low conversion values and the presence of the competitive isomerization of glucose to fructose at high pH levels [1]. To date, few groups have attempted the photocatalytic selective oxidation of sugars using both visible and UV light sources. Those that have, have obtained significantly different results due to the complexity of these novel chemical reactions [53, 60, 63]. For the first time in this work we combine previous knowledge with a systematic approach which allowed us to draw a general reaction mechanism considering the most plausible reaction pathways involved in the photo transformation of glucose in solution.

4.2 Catalyst Testing

0.5–1.5 wt% Ag/TiO_2 catalysts were prepared by wet impregnation and tested under both UVA and visible light (Section 2.9). Blank reactions conducted in the dark showed no reaction nor did the exposure of the substrate to light in the absence of the catalyst. Figure 4.3 shows the glucose conversion and product selectivity under UVA and visible light over bare TiO_2 and the Ag/TiO_2 catalyst. The reaction medium was a water/acetonitrile 50/50 v/v mixture. Tests using pure water resulted in no activity and glucose is not soluble in pure acetonitrile (MeCN).

4.3 Results and Discussion

4.3.1 Effect of the Lamp Power, Filters and Solvent Used

In the previous chapter (Section 3.2.4) the effect of several parameters was analysed when pure TiO_2 was used as catalyst. Is it possible to draw the same conclusions also for a metal supported catalyst? To answer this question the 1 wt% Ag/TiO_2 and the untreated P25 were tested and the results compared with each other using the same approach as for the pure TiO_2 (3.2.4). Figure 4.1 shows the conversion values for the TiO_2 and the 1 wt% Ag/TiO_2 for the 300 and 1000 W lamps obtained in the different reaction media used. It can be seen that

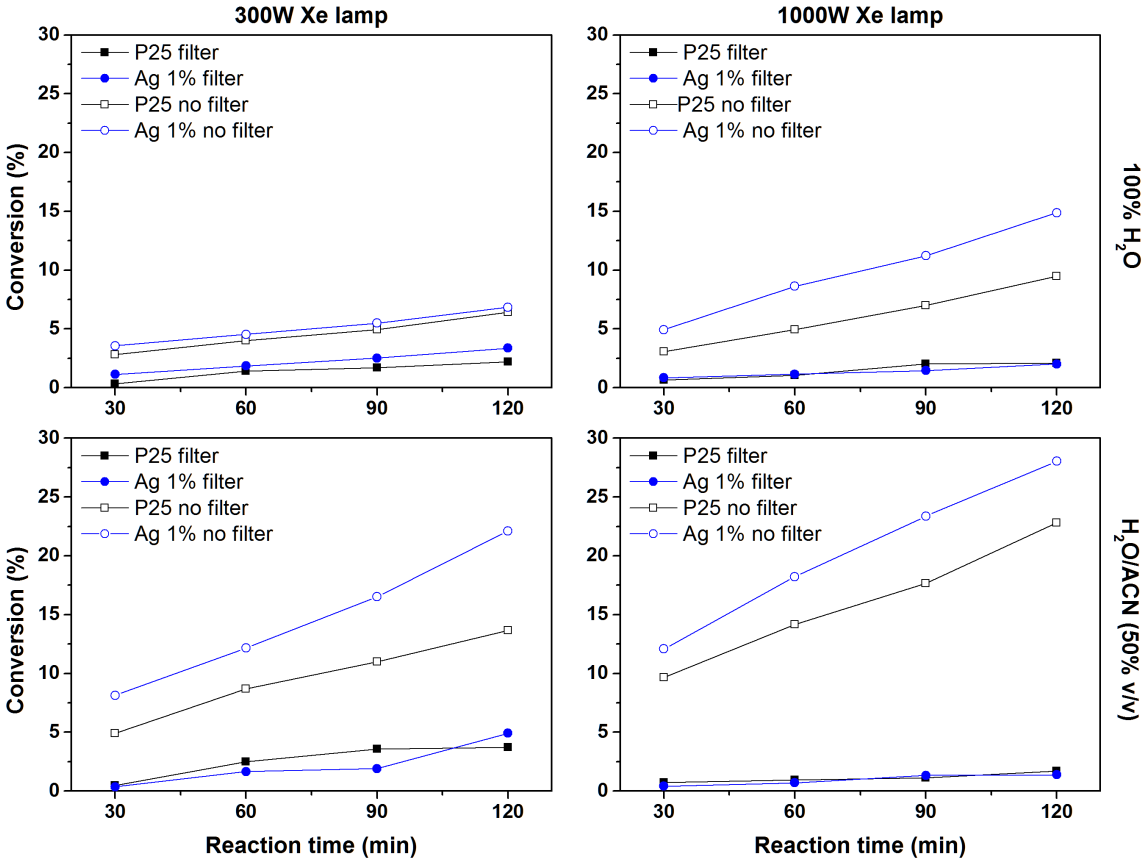

Figure 4.1 Glucose conversion values for the 1 wt% Ag/TiO_2 and for the TiO_2 under the same experimental conditions.

when the 420 nm filter is installed, the conversion is significantly lower in all cases. When

the filter is removed the conversion is generally higher with the 1 wt% Ag/TiO_2 catalyst displaying the highest activity in all cases (Table 4.1) .

Table 4.1 Product distribution observed for the TiO_2-P25 and for the 1 wt% Ag/TiO_2 samples tested with the Xenon lamps with and without visible light filters.

Lamp Power (W)	Catalyst	Cut-off filter (%)	Conversion (%)	Mass Balance (%)	Specific Activity (mmol g^{-1} h^{-1})[c]
1000[a]	TiO_2-P25	yes	1.7	99.1	12.2
1000[a]	TiO_2-P25	no	22.8	90.1	164.1
1000[a]	1%Ag/TiO_2	yes	1.4	100.2	10.0
1000[a]	1%Ag/TiO_2	no	28.0	87.1	199.4
1000[b]	TiO_2-P25	yes	2.1	99.7	15.0
1000[b]	TiO_2-P25	no	9.5	96.5	67.3
1000[b]	1%Ag/TiO_2	yes	2.0	99.6	14.6
1000[b]	1%Ag/TiO_2	no	14.9	93.6	105.5
300[a]	TiO_2-P25	yes	3.7	101.0	26.8
300[a]	TiO_2-P25	no	13.7	95.3	97.9
300[a]	1%Ag/TiO_2	yes	4.9	99.8	35.6
300[a]	1%Ag/TiO_2	no	22.1	90.6	159.0
300[b]	TiO_2-P25	yes	2.2	99.5	15.9
300[b]	TiO_2-P25	no	6.4	98.1	46.2
300 [b]	1%Ag/TiO_2	yes	3.4	99.4	24.0
300[b]	1%Ag/TiO_2	no	6.8	97.4	48.7

[a] $MeCN/H_2O$
[b] H_2O
[c] Reaction conditions: Glucose 20 mM, 14 mg catalyst

The higher activity of the catalyst has to be compared with the mass balance values, as the direct glucose mineralization is undesired as the aim is to produce partial oxidation products and not H_2 and CO_2. In fact, when the filters are removed, the Ag/TiO_2 catalyst displayed mass balance values as low as 86% with the 1000 W lamp (Figure 4.2). These values despite being significantly lower than the 99+% obtained with the filters installed, are a good indication that the combination of UV + visible light has increased the activity of the material as both the support + the metal nanoparticles are excited at the same time as reported in Figure 1.16 in Section 1.6.1, but a compromise has to be made with the amount of gases evolved which can be used as a feed in other processes.

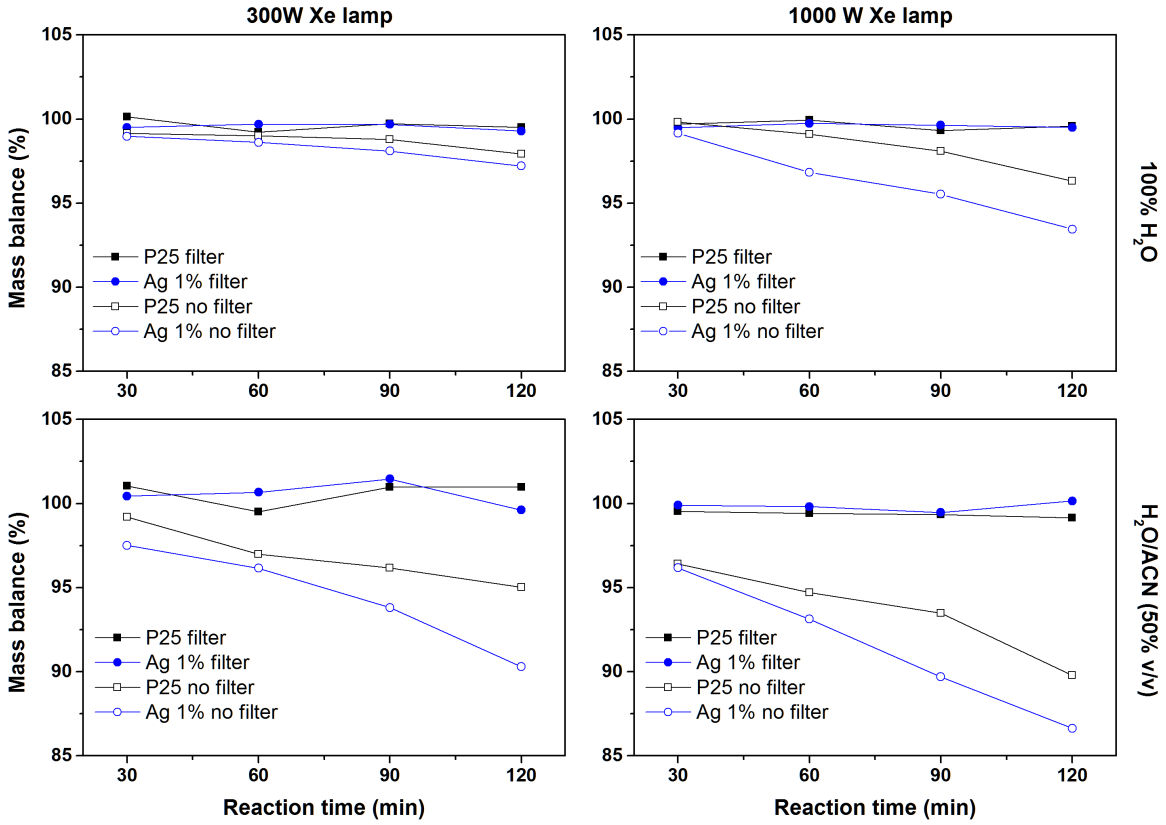

Figure 4.2 Mass balance values for the 1 wt% Ag/TiO_2 and for the TiO_2 under the same experimental conditions.

4.3.2 Effect of the Metal Loading

Glucose conversion under UVA and visible light are displayed in Figure 4.3.The optimum conditions for selective oxidation were obtained using 20 mM of the substrate giving selectivity to organic products of >95% in all cases. Under UVA light the initial rate of glucose production was greater with the 1.5 wt% Ag/TiO_2 and showed a moderate increase from 9 to 11.5 % conversion over the course of the 120 min reaction. If these results are compared with the ones obtained with the naked TiO_2 it can be seen that there is no significant difference between this material and the metal supported catalysts. In fact, despite the similar glucose conversion values, the mass balance observed after 120 min is significantly lower for the TiO_2 catalyst at *ca.* 95%, therefore, we can prove that under UVA light the selectivity to the undesired mineralisation products increased with increasing Ag loading (Figure 4.6). The

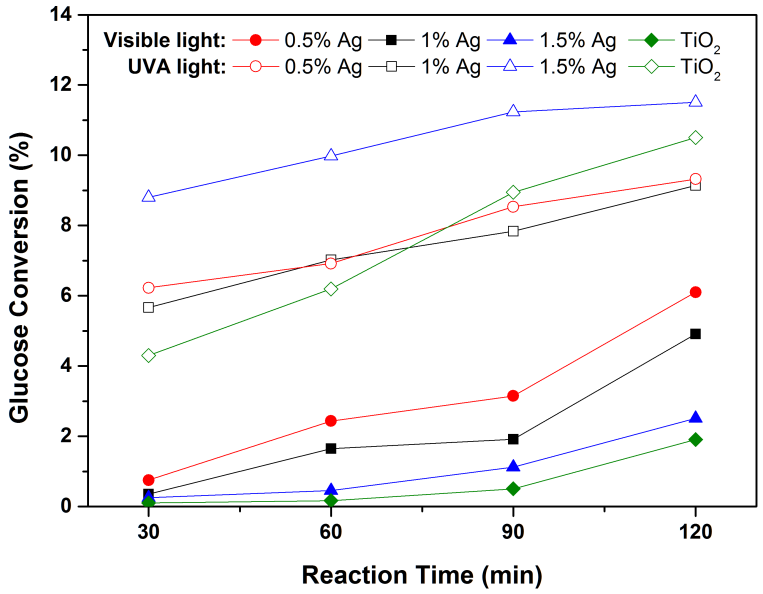

Figure 4.3 Time on line glucose conversion under visible and UVA light over 120 minutes of reaction time for Ag/TiO_2 and the blank TiO_2 catalysts. 50/50 v/v $MeCN/H_2O$, 14 mg catalyst, 20 mM glucose stock solution.

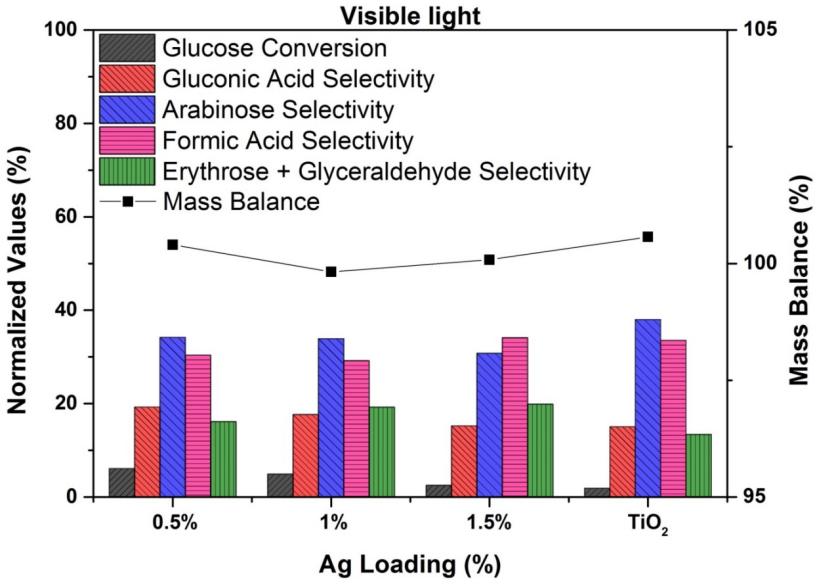

Figure 4.4 Conversion, selectivity and mass balance data after 120 min of reaction time under visible light.

promotional effect of the silver plasmonic nanoparticles was more pronounced under visible light resulting in a 3 fold increase in activity for the 0.5 wt% Ag/TiO_2 catalyst when compare to the bare TiO_2, which displayed a modest conversion of just 2% after 120 min reaction but

this increased to 6% with the addition of 0.5 wt% Ag. The mass balance in all cases was >99% showing that under visible light the formation of H_2 and CO_2 is limited (Figure 4.4). Under visible light the increased Ag loading actually decreased the glucose conversion after 120 min from 6 to 3 % indicating that Ag dispersion or the availability of the TiO_2 surface is critical for this reaction under visible light as seen previously [101]. For this specific reason it appears that for the oxidation of glucose under visible light the best Ag loading is 0.5 wt%. The reasons for the catalytic enhancement when supporting Ag nanoparticles on TiO_2 can be understood analysing the electronic properties of the metal in respect to the electron structure of the support. As introduced in Section 1.5.1, noble metals have workfunctions larger than that of TiO_2 (4.2 eV). Specifically, Ag has a workfunction of 4.26 eV for polycrystalline structures but it can vary if different surfaces are considered; (100) face: 4.64 eV, (110) face: 4.52 eV, (111) face: 4.74 eV [81, 162, 82].The different workfunction of the metal is responsible for the creation of a Schottky barrier at the metal-TiO_2 interface (Figure 1.11) which slows down the h^+/e^- recombination rate thus prolonging their lifetime, and enhancing the activity of the TiO_2 as shown in 1.6.1, this process is measurable and has been proven elsewhere [216, 128, 150]. In a recent study by Fu et al. [92] the effect of Pt loading on TiO_2 was demonstrated in the H_2 production rate from glucose. It was found that the catalyst with the highest activity was also the one with the highest dispersion of the metal nanoparticles on the catalyst surface. In our case, the experimental results seem to follow a similar trend, as the highest activity under visible light was observed with the 0.5 wt% Ag/TiO_2 catalyst. The activity of the catalyst cannot be simply correlated to the particle size distribution values as for the set of materials tested there are no significant differences (Figure 4.5), but rather, the effect of the increased metal loading has to be taken into account. In fact, there must be a correlation between the amount of Schottky barriers formed and the metal loading, and perhaps, below a certain loading value, the correlation between these two parameters is respected, but when the Ag wt% exceeds a certain value (>0.5 wt% in this

case) the surface of the semiconductor is covered by the nanoparticles and cannot effectively contribute to the reaction. Additionally, the recombination mechanisms which are slowed down by the presence of the metal centre can also be promoted if the nanoparticles are in close proximity with each other (Section 1.6). Under UVA light, the highest conversion

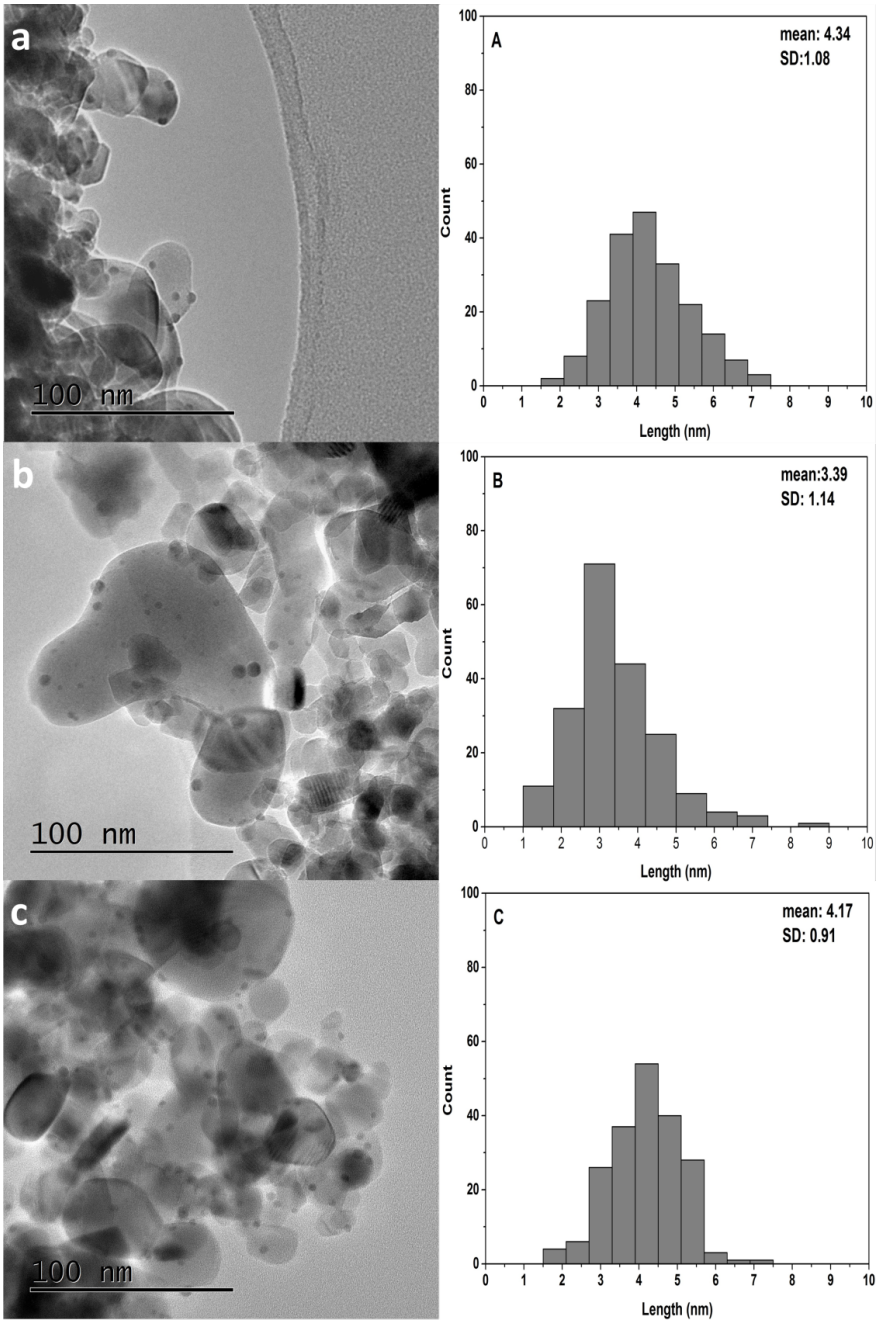

Figure 4.5 Transmission electron microscopy and particles size distributions of a)0.5 wt% Ag/TiO_2, b)1 wt% Ag/TiO_2, c)1.5 wt% Ag/TiO_2

observed was with the 1.5 wt% Ag/TiO_2 catalyst and this results seems to contradict the previous findings under visible light. In the first chapter of this work (Section 1.6.1) the different irradiation states of plasmonic metal on semiconductor surfaces were analysed (Figure 1.16), and under UV light, both the semiconductor and the metal nanoparticle can be excited simultaneously. Under UV irradiation, the dominant reaction mechanism is the charge-separation mechanism in which the photogenerated electrons are transferred from the conduction band of the semiconductor to the metal nanoparticle [258]. Even in this case, the presence of the Schottky barrier at the metal-semiconductor interface, prevents the undesired h^+/e^- recombination and the photocatalytic activity is enhanced in this case as well.

Additionally, another mechanism is based on the intraband transition of the electrons within the metal nanoparticle from fully occupied *d*-bands below the Fermi energy to half-filled *sp* bands. The activity under ultraviolet irradiation is due to the promotion of 4*d* electrons to the 5*sp* band for Ag, but this mechanism is also valid for Au and Pt nanoparticles with transitions from 5*d*-6*sp* orbitals [44, 235, 261, 52, 13]. The holes left in the inner *d* band have greater tendency for capturing electrons from electron donor molecules present in solution than outermost *sp* orbitals [52], and this mechanism shows similar properties to the h^+/e^- couple generated in a semiconductor, in fact in this case the electron vacancy in the *d* orbital acts as a h^+. Under these conditions, the energy of the UV irradiation is much higher than the LSPR and the catalytic enhancement cannot be related to the LSPR of the metal nanoparticles, but to the simultaneous excitation of the semiconductor and the electrons in the metal nanoparticle.

Remarkably, the 0.5 wt% Ag/TiO_2 catalyst showed 6.1% conversion under visible light whilst the the 1 wt% Au/TiO_2 showed only 3.3% conversion under the same experimental conditions. Au-based photocatalytic reactions are well known in the literature and Au/TiO_2 is considered a standard catalyst as it shows good activity under visible light towards the mineralization of dyes and degradation of pollutants. Applications of this material in selective

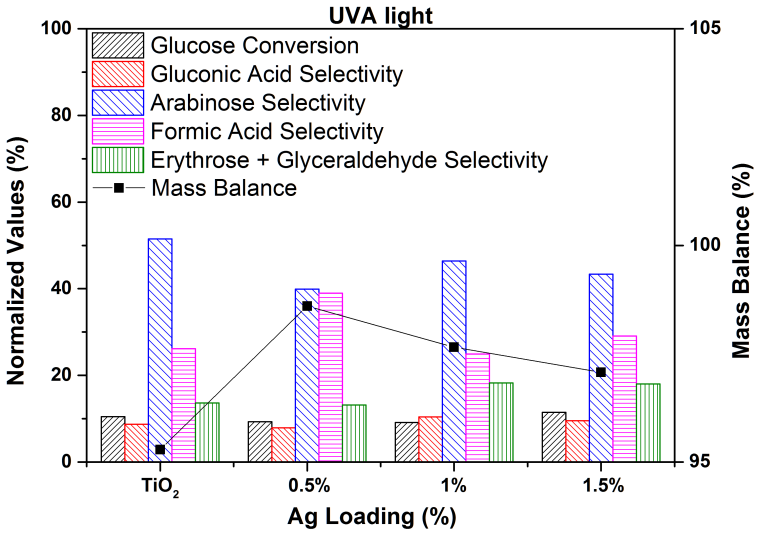

Figure 4.6 Conversion, selectivity and mass balance data after 120 min of reaction time under UVA light.

Table 4.2 Conversion and selectivity data for Ag/TiO_2 and Au/TiO_2 at 2 h and 24 h reaction times obtained under UVA and visible light.

Catalyst	Glucose Conversion (%)	Gluconic Acid Selectivity (%)	Arabinose (%)	Formic Acid (%)	Erythrose + Glyceraldehyde (%)	Mass Balance (%)	Specific Activity (mmol g^{-1} h^{-1})[d]
0.5 wt% Ag/TiO_2[a]	6.1	19.3	34.2	30.4	16.1	100.4	43.7
1 wt% Ag/TiO_2[a]	4.9	17.7	33.9	29.2	19.2	99.8	34.9
1.5 wt%Ag/TiO_2[a]	2.5	15.2	30.8	34.1	19.9	100.1	18.0
TiO_2[a]	1.9	15.1	38	33.5	13.4	100.6	13.8
1 wt% Au/TiO_2 [a]	3.3	20.4	32.3	23.6	23.7	100.6	23.6
TiO_2;[ac]	14.7	8.0	31.0	45.6	15.4	96.5	8.8
1 wt% Au/TiO_2;[ac]	21.1	17.2	27.2	40.0	15.6	99	12.4
1 wt% Ag/TiO_2;[ac]	22.8	15.4	32.8	32.3	19.4	98.1	13.5
0.5 wt% Ag/TiO_2[b]	9.3	7.9	39.9	39	13.2	98.6	65.8
1 wt% Ag/TiO_2[b]	9.1	10.4	46.4	24.9	18.3	97.7	64.9
1.5 wt% Ag/TiO_2[b]	11.5	9.5	43.4	29.1	18.0	97.1	84.4
TiO_2[b]	10.5	8.7	51.5	26.1	13.6	95.3	75.4
1 wt% Au/TiO_2[b]	14	10.3	44.8	17.4	27.5	96.3	101.0
TiO_2;[bc]	15.6	0	48.9	48.7	24.5	91.4	9.2
1 wt% Au/TiO_2;[bc]	32.9	2.7	68.9	17.7	10.7	82.1	19.6
1 wt% Ag/TiO_2;[bc]	19.6	3.7	49.1	33.5	13.7	90.9	11.5

[a] Reactions performed visible light
[b] Reactions performed UVA light
[c] Reactions performed for 24 hours
[d] Specific activity calculated as mmol of glucose over grams of catalyst per hour

photo-oxidation reactions are somewhat limited and, for this reason, a 1 wt% Au/TiO_2 catalyst was used as benchmark. Remarkably, the 0.5 wt% Ag/TiO_2 showed 6.1% glucose conversion after 120 min whilst the 1 wt% Au/TiO_2 displayed only a 3.3% conversion under the same experimental conditions. In order to push the conversion at higher values, the metal supported

1 wt% Ag/TiO_2, the 1 wt% Au/TiO_2 and the naked TiO_2 were tested over 24 hours under visible and UVA light to assess the effect of the different metal on the conversion and product distribution values. Table 4.2 shows that the two metal supported catalysts displayed similar activity under visible light with a glucose conversion of 21.1% and 19.6% for the 1 wt% Au/TiO_2 and the 1 wt% Ag/TiO_2 respectively. Both metal supported catalysts showed higher activity than the naked TiO_2 catalyst which displayed a glucose conversion after 24 hours under visible light of 14.7%. In addition to an increase in the glucose conversion values, the presence of the metal also affects the product distribution values. In fact, after 24 hours the Au and Ag supported catalysts showed lower formic acid selectivity values (40 and 32.3% respectively) if compared with the 45.6% observed with the naked TiO_2. The decrease in the formic acid selectivity provides important information regarding the reaction pathway. In fact, when the metal nanoparticles are present on the semiconductor surface, the gluconic acid selectivity increases from 8.0 obtained with TiO_2 to 17.2% (Au/TiO_2) and 15.4% (Ag/TiO_2), whilst there are no major differences in the other products. Additionally, under UVA irradiation the gluconic acid selectivity drops to 2.7 and 3.7% for the 1 wt% Au/TiO_2 and the 1 wt% Ag/TiO_2 respectively. Even in this case the formic acid selectivity decreases significantly (17.7%, Au/TiO_2; 33.5% Ag/TiO_2) if compared with the 48.7% observed with the naked TiO_2. We can assume than when the production of gluconic acid increases, the formation of formic acid decreases as the Ruff-degradation pathway is preferred over the α-scission described by Chong [53]. Under these conditions, there is a general decrease in the partial oxidation products such as erythrose and glyceraldehyde from 24.5% (TiO_2) to 10.7% (Au/TiO_2) and 13.7% (Ag/TiO_2) which further confirms that under these conditions the higher activity of the support promotes the unselective oxidation of sugars. Additionally, the decoration of the catalyst surface with metal nanoparticles seems to further promote this unselective reaction pathway as confirmed by the low mass balance values observed for Ag/TiO_2 (90.9%) and Au/TiO_2 (82.1%). Under UVA light the Au/TiO_2 catalyst displayed

higher conversion values after 2 hours (14%) and 24 hours (32.9%) whereas 1 wt% Ag/TiO_2 showed 9.1% and 19.6% after 2 and 24 hours respectively. Interestingly, after 24 hours of irradiation, the product distribution values do not show any changes in the relative selectivity values. The importance of the activity under UVA irradiation is second to the visible light activity as the latter accounts for 40% of the solar irradiation at ground level, therefore it is preferable to have a material which is better performing under these conditions, with the activity under any UV irradiation being an important contribution. Additionally, Ag is much cheaper than Au and it might be a promising alternative as a photoactive catalyst for a wide range of applications. FTIR analysis of the used 0.5 wt% Ag/TiO_2 catalysts and its comparison with the pure chemicals (Figure 4.7) shows the presence of the reactant and one of the main reaction products adsorbed on the catalyst surface after recycling and multiple washes with ethanol and water. A detailed analysis of the stretching frequencies is provided in Table 4.4.

Table 4.3 FTIR stretching frequencies of the adsorbed species on the 0.5 wt% Ag/TiO_2 recycled under UVA and visible light

Catalyst	Glucose (blue) (cm^{-1})	Gluconic acid (black) (cm^{-1})
0.5 wt%Ag Xe 1^{st}	915, 995, 1050, 1149, 1340, 1460	1095, 1202, 1401, 1636
0.5 wt%Ag Xe 2^{nd}	915, 995, 1050, 1149, 1340, 1460	1095, 1202, 1401, 1636
0.5 wt%Ag UVA 1^{st}	-	1636
0.5 wt%Ag UVA 2^{nd}	-	-

Table 4.4 Assigned FTIR frequencies to glucose and gluconic acid adsorbed on the catalyst surface

IR (cm^{-1})	Glucose (blue) assignment [116]	IR (cm^{-1})	Gluconic acid (black) assignment [228]
1460	$\delta CH_2 + \delta OCH + \delta CCH$	1636	νCOO^- antisym
1340	$\delta CCH + \delta OCH$	1401	νCOO^- sym
1149	$\nu CO + \nu CC$	1202	$\nu CO + \delta COO$
1050	$\nu CO + \nu CC$	1095	$\nu CO + \delta COO$
995	$\nu CO + \nu CC$		
915	$\nu CO + \nu CCH + \nu_{asym}$ ring of pyranose		

The presence of adsorbed species after use is a clear indication of the stability of the glucose–TiO_2 complex under visible light, whereas under UVA light there are no traces of the adsorbed intermediates. This can be explained with the well-established activity of the support (TiO_2) under UVA light which hinders the formation of the complex due to the increased presence of highly reactive species (*e.g.* $^{\cdot}OH$, h^+) in close proximity or on the catalyst surface. Under visible light, due to the partial TiO_2 excitation, these species are not readily generated therefore their concentration is significantly lower, thus explaining the different reactivity of the same system under UVA and visible light.

4.3.3 Identification of the Reaction Pathway

Two potential reaction pathways have been proposed [61, 53] but because of the different experimental conditions used by the authors these pathways are representative of their respective systems. In the reaction mechanism suggested by Chong et al. [53], the role of the co-catalyst (Rh) on the TiO_2 is not clear and in this reaction scheme the oxidation of glucose appears to produce the smaller monosaccharide along with formic acid and H_2 (Scheme 4.1). This does not fully explain the presence of the gluconic acid in solution. Stapley and BeMiller

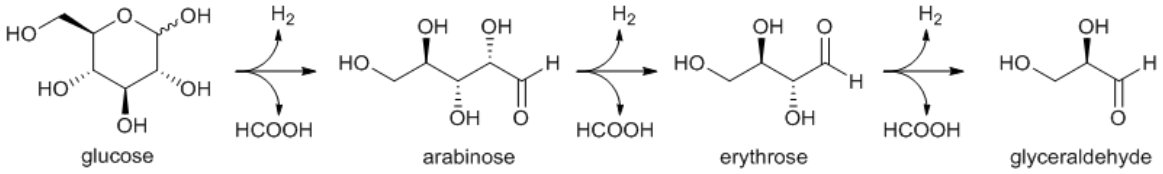

Scheme 4.1 Proposed reaction mechanism showing the α-scission process for the successive formation of shorter chain aldoses via the formation of hydrogen and formic acid [53].

[222] reviewed the decarboxylation of sugar acids according to different mechanisms for the production of smaller carbohydrates (Scheme 4.2). Specifically, the reaction of interest is the so-called Ruff degradation which involves the decarboxylation of aldonic acids by Fe (III) and H_2O_2 in a Fenton-like system to produce aldoses with one less carbon. Moreover, it was shown that Ti (IV) behaves similarly thus explaining the reaction mechanism in the

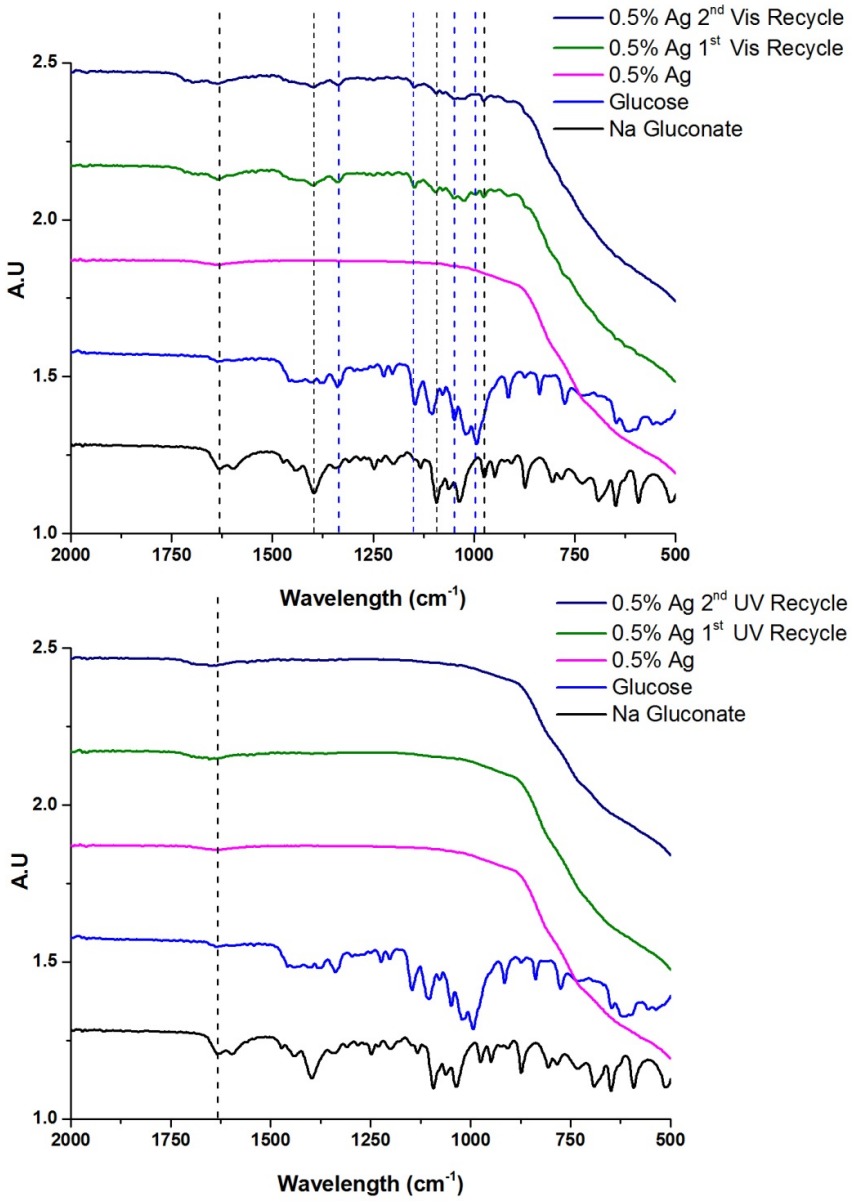

Figure 4.7 FT-IR analysis of the 0.5 wt% Ag/TiO_2 catalyst before and after multiple reaction cycles under visible (top) and UVA light (bottom). Comparison with glucose and gluconate. Catalyst recycled twice, washed with ethanol and water and dried overnight under vacuum.

absence of Fe (III). In this case the product distribution is in agreement with α-scission type mechanism proposed by Chong et al. [53] where the aldose is formed along with formic acid and H_2 but with the addition of the gluconic acid as an intermediate. To explore this further the reaction was carried out with gluconic acid as the reactant with the same catalyst to substrate ratio as for the previous reactions. Figure 4.8 shows the gluconic acid conversion

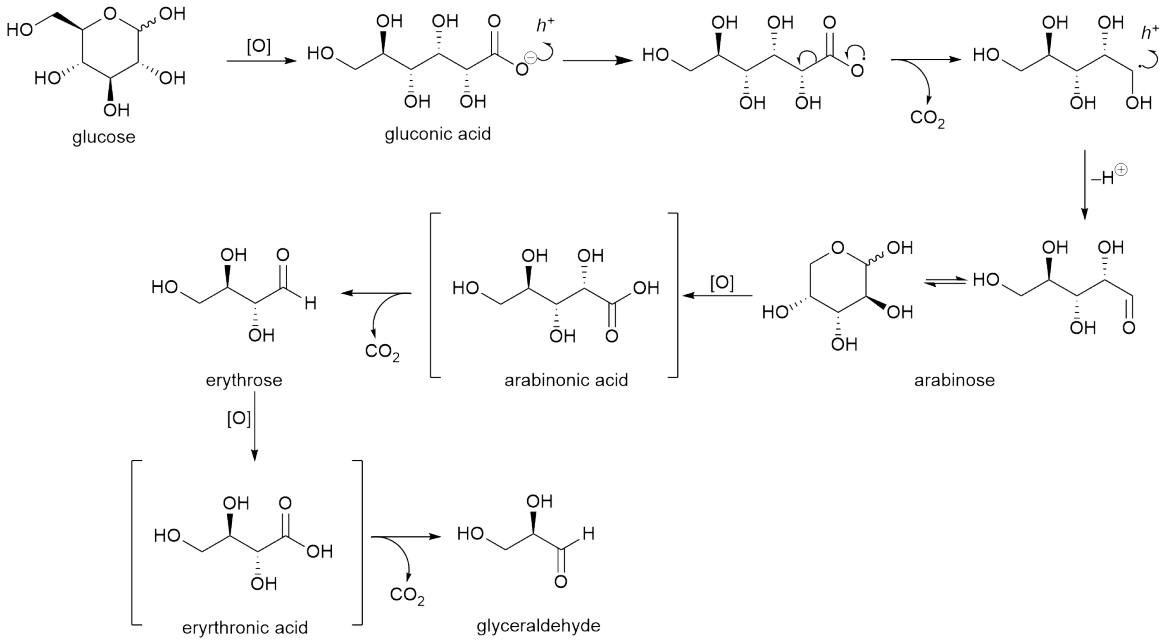

Scheme 4.2 Proposed reaction mechanism showing the Ruff degradation following the photo-Kolbe process for the successive formation of shorter chain aldoses via the photocatalysed sequential oxidation and decarboxylation of monosaccharides into smaller carbohydrates [222].

and product selectivity as a function of time with the 0.5 wt% Ag/TiO_2 catalyst. It is clear that the aldoses are indeed formed from gluconic acid and that the reaction proceeds via the partial oxidation of glucose to gluconic acid. Again, it is worth noting that mass spectroscopy of the products from the gluconic acid experiment revealed no glucaric acid present indicating that under these conditions the sequential oxidation of gluconic acid to glucaric acid does not take place. Furthermore, no arabitol was observed in any of the reactions (Figure 4.9). In a recent work on the photo-oxidation of glucose using TiO_2-based materials, Colmenares et al. [61] reported the presence of arabitol in the reaction mixture as one of the main reaction products formed during the glucose photo-oxidation. As the reaction conditions used in this study were really similar to ours, it was surprising to notice the complete absence of arabitol from the reaction mixture, with these results being confirmed by the HPLC-QTOF analysis performed on commercially available standards and on some of the reaction samples. Scheme 4.3 shows a possible pathway for the production of arabitol from glucose. Even in

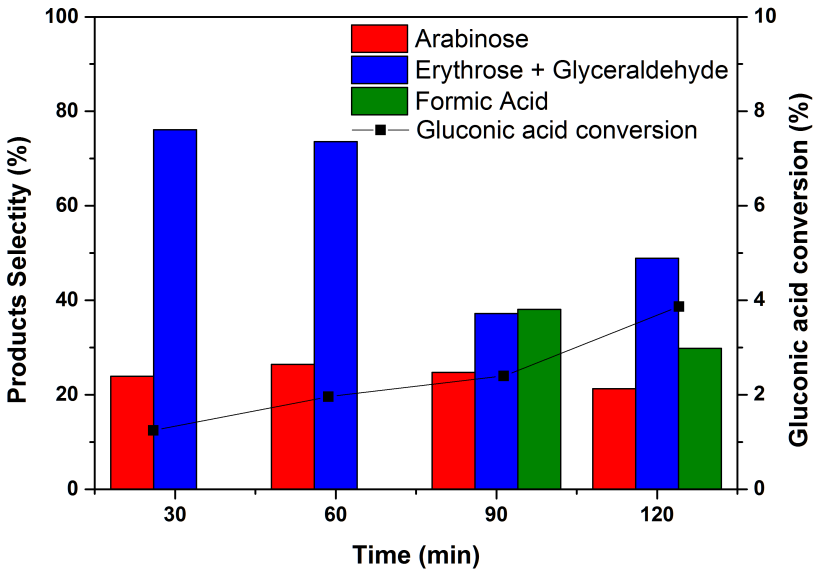

Figure 4.8 Gluconic acid conversion over 0.5 wt% Ag/TiO_2 under visible light irradiation and selectivity to aldose products. 50/50 v/v $MeCN/H_2O$, 14 mg catalyst, 20 mM gluconic acid stock solution

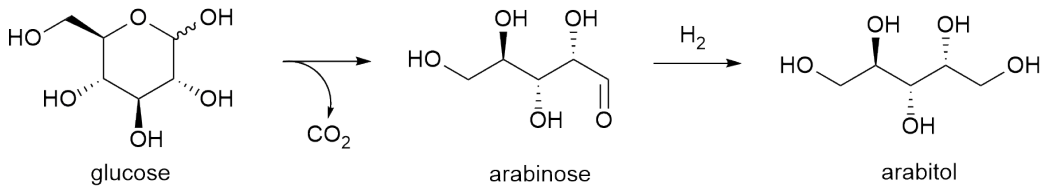

Scheme 4.3 Suggested reaction scheme for the formation of arabitol from glucose based on Colmenares et al. [61] results.

this case, there is a decarboxylation reaction either via α-scission mechanism or via the Ruff degradation with a subsequent hydrogenation of the aldehyde to the corresponding alcohol. If one assumes that the α-scission is the dominant reaction pathway, H_2 is formed in a 1:1 molar ratio for each glucose molecule converted, but nonetheless, it seems quite unlikely that the hydrogen formed, at atmospheric pressure, can be activated via some spill-over mechanism to hydrogenate arabinose to arabitol. If this was actually the case, than we would have observed other hydrogenation products coming from glucose in the first place, and then from the other partial-oxidation products. It seems quite likely than the identification of arabitol was a simple mistake in the chromatographic determination, as the experimental

conditions used in this study do not seem to support the hypothesis of a one-pot oxidation-reduction mechanism. From these data it is apparent that the glucose is first oxidised to the

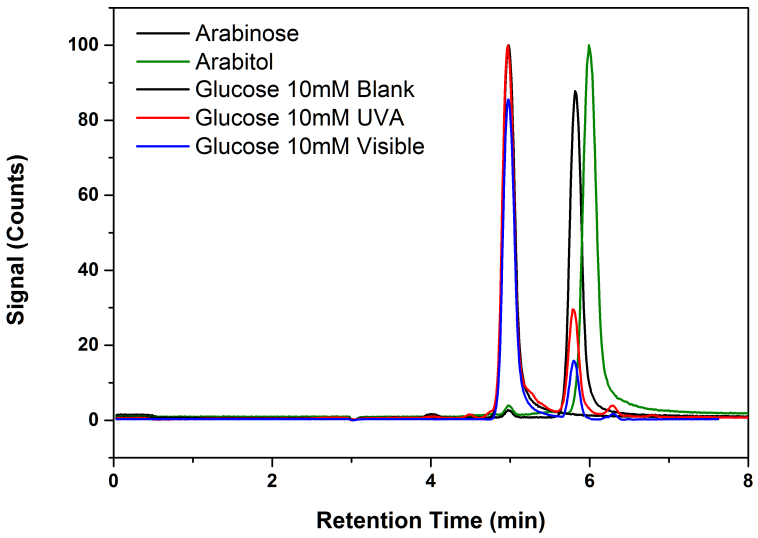

Figure 4.9 Mass spectra analysis of arabinose and arabitol as standards. Additionally, the chromatograms were superimposed over two test reaction samples after irradiation under UVA and visible light. It can be seen that no arabitol is detected.

gluconic acid before undergoing an α-scission of the $C_1 - C_2$ bond allowing the formation of arabinose and formic acid. The arabinose then undergoes subsequent repeat carbon-carbon cleavages to form the erythrose and glyceraldehyde. Furthermore, the presence of CO_2 as a product cannot solely be attributed to the mineralisation of formic acid as previously reported.[53] The reaction mechanism is still debated, and multiple reaction pathways are suggested by different research groups but most of them, according to the reviewer, seem to be ill-conceived or contradictory.[222, 221] Nonetheless, they report the experimental evidence that transition metal ions can catalyse the decarboxylation of organic acids and specifically TiO_2 under UVA light. In fact, the holes h^+ generated during the photo-catalytic process act as anodes oxidising the organic molecules absorbed on the surface. Because of the high oxidizing potential, the molecules adsorbed on the surface after the decarboxylation can be further oxidised to CO_2 (Scheme 4.2).

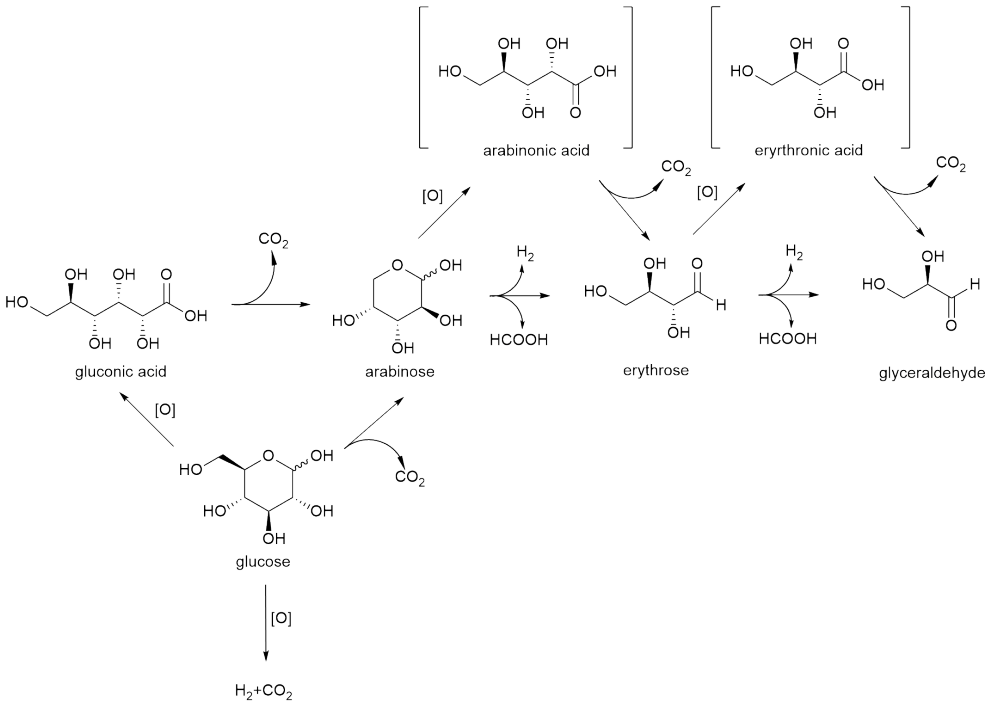

Scheme 4.4 Proposed global reaction mechanism for the photo-conversion of glucose to valuable chemicals.

Scheme 4.4 shows for the first time the combination of the α-scission for the production of lower chain carbohydrates with the loss of H_2 and HCOOH along with the photo-Kolbe mechanism for the production of the corresponding sugar acid and its subsequent decarboxylation to produce a lower chain carbohydrate. These two mechanism have to be combined with the direct mineralization process which produces H_2 and CO_2. These three reaction pathways contribute to the conversion of glucose, and at the current status of this research it is safe to say that the direct mineralization pathway is minimized as shown by the good mass balance values, but, on the other hand, it is not yet possible to determine which of the two remaining reaction pathways is the dominant one.

4.3.4 Catalyst Characterisation and Recycling Studies

Figure 4.5 shows the TEM micrographs and particle size distribution determined for 300 particles. As can be seen all catalysts have particles in the size range of 1-8 nm with a

mean particle size of approximately 4 nm. Although the 1wt% Ag/TiO_2 had a mean average of 3.39 nm, recycling experiments indicate that the particle size has a minimal effect on the activity of the catalyst. It has been shown previously that plasmonic effects become negligible in nano particles smaller than 2 nm and size differences between particle of < 5 nm have negligible effect on absorbance wavelength [76, 257, 5]. The elemental analysis (Table 4.5) showed the actual loading to be lower than the theoretical one in all cases but tolerable.

The chemical environment and valence state was determined by XPS analysis. Figure 4.10 shows the peaks for Ag of $3d_{3/2}$ and $3d_{5/2}$. The binding energy for Ag, Ag_2O and AgO are very close within the range 367.3-368.4 eV but there is a clear shift in binding energy from 368.1-367.7 eV with increased Ag loading indicative of the formation of Ag^{+1} species [141, 259, 260, 241].

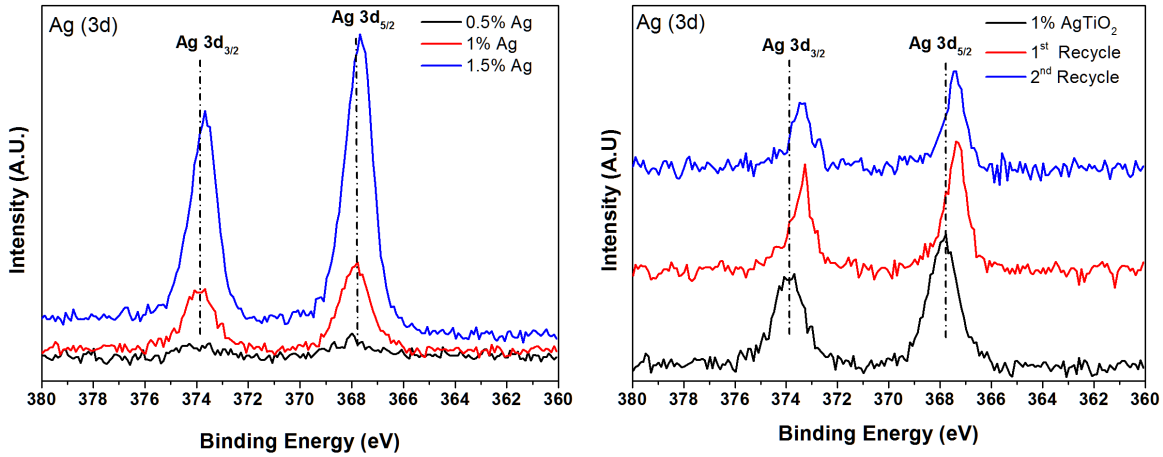

Figure 4.10 XPS analysis of the fresh Ag/TiO_2 catalysts (left) and of the 1 wt% Ag/TiO_2 after multiple recycling (right).

The ease of oxidation Ag nanoparticles under air is not without precedent.[127, 153] However the presence of both metallic silver and the oxides in all the catalysts cannot be discounted as Ag^0 was evident form the TEM analysis of 0.5 wt% Ag/TiO_2 where the interplanar distance of 0.24 nm for the particles can be attributed to the preferential exposure of the 111 plane (ICDD 01-071-3672). Representative UV-Vis spectra of the 1 wt% Ag/TiO_2

are shown in Figure 4.11. In this figure, the blueshift of the plasmon resonance is noticeable

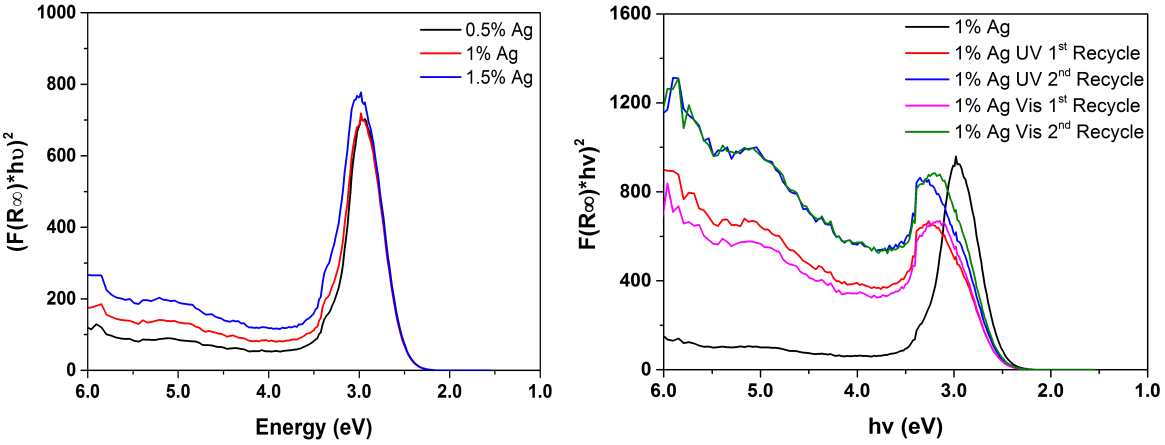

Figure 4.11 Solid UV-Vis analysis of the fresh Ag/TiO_2 catalysts (left), and of the 1 wt% Ag/TiO_2 after multiple recycling under UVA and visible light (right).

in all recycled catalysts. Additionally, there is a decrease in the peak intensity after the first run but this trend is inverted after the second recycling after which the plasmon intensity value is similar to the one observed for the fresh catalyst. This shift in the absorption band can be explained with the different oxides phases present on the catalyst and with the change in the morphology of the metal nanoparticles over multiple reuses.

Table 4.5 Elemental analysis and XPS data for the Ag/TiO_2 catalysts and for the recycled 1 wt% Ag/TiO_2.

Catalyst	Ag content (wt%) [a]	Ag content (At%) [a]	Ag $3d_{5/2}$ Binding Energy (eV)	Surface Concentration (At%) [b]	Chemical State
0.5 wt% Ag/TiO_2	0.30 (±0.11)	0.06	368.1	0.01	Ag/Ag_2O
1 wt% Ag/TiO_2	0.78(±0.15)	0.18	368.0	0.08	Ag/Ag_2O
1.5 wt% Ag/TiO_2	1.34(±0.15)	0.3	367.7	0.89	Ag/Ag_2O
Recycle 1[c]			367.4	0.05	AgO
Recycle 2 Xe	0.67(±0.15)	0.15	367.3	0.03	AgO
Recycle 2 UVA	0.75(±0.16)	0.15			

[a] Determined by EDX analysis over 3 areas.
[b] Determined by XPS.
[c] 1 wt% Ag/TiO_2 after 3 recycles; 2h under visible light

To test the stability and re-usability the 1 wt% Ag/TiO_2 catalyst was recycled twice. The glucose conversion under both UVA and visible light remains at *ca.* 10 and 4% respectively retaining the same mass balance and product selectivity over the course of a 120 min test.

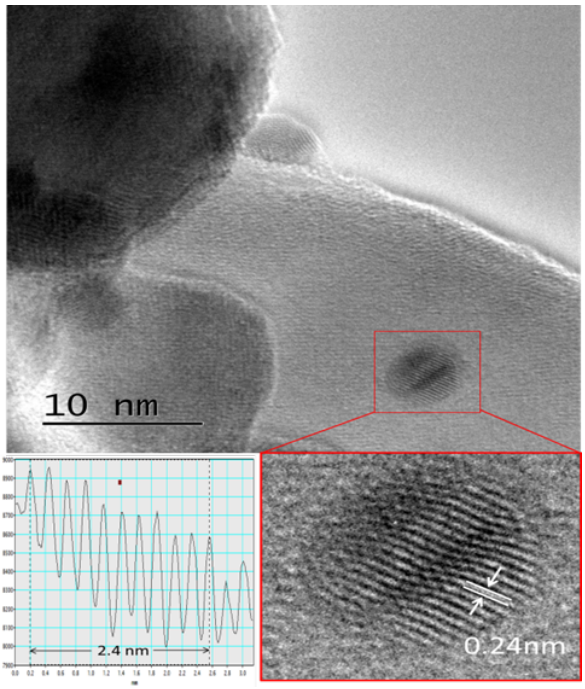

Figure 4.12 HRTEM analysis of 0.5 wt% Ag/TiO_2 showing Ag particles of *ca.* 4.5 nm. Bottom right: expanded image of Ag nanoparticle showing interplanar distances of 0.24 nm, Bottom left: Profile fit for 10 lattice planes

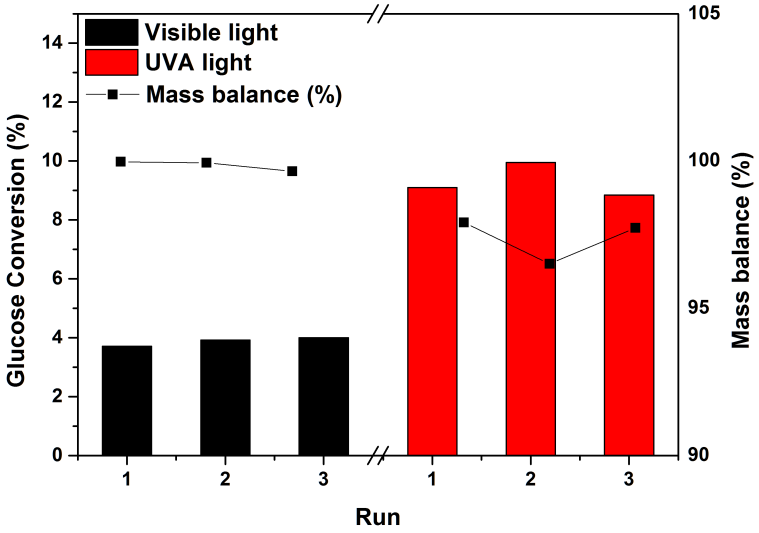

Figure 4.13 Catalyst recycle runs for the 1 wt% Ag/TiO_2 under visible (black) and UVA light (red). The conversion and the mass balance values reported are taken from the samples after 120 min of reaction.

Analysis of the catalyst after reuse shows that it does undergo change. In fact, the XPS analysis (Table 4.5, Figure 4.10) shows that the binding energy shifts to 367.3 eV indicative

of Ag^{+2} and therefore, the presence of AgO species [141, 259, 260, 241]. The attenuation of the signal corresponds to an apparent decrease in the surface concentration from 0.08 to 0.03 At%. However, the elemental analysis by EDX shows that the bulk concentration remains near constant at *ca.* 0.1 At% (a value in good agreement with the 0.08At% obtained with the XPS analysis) proving that there is no leaching and the lower surface concentration is due to particle sintering.[183] Further investigation by EDX mapping showed that the lower surface concentration as determined by XPS is a result of light induced particle agglomeration as large particles >200 nm can be seen throughout the titania matrix (Figure 4.14c). Interestingly, the same effect is not seen for the catalysts recycled under UVA light (Figure 4.14b).

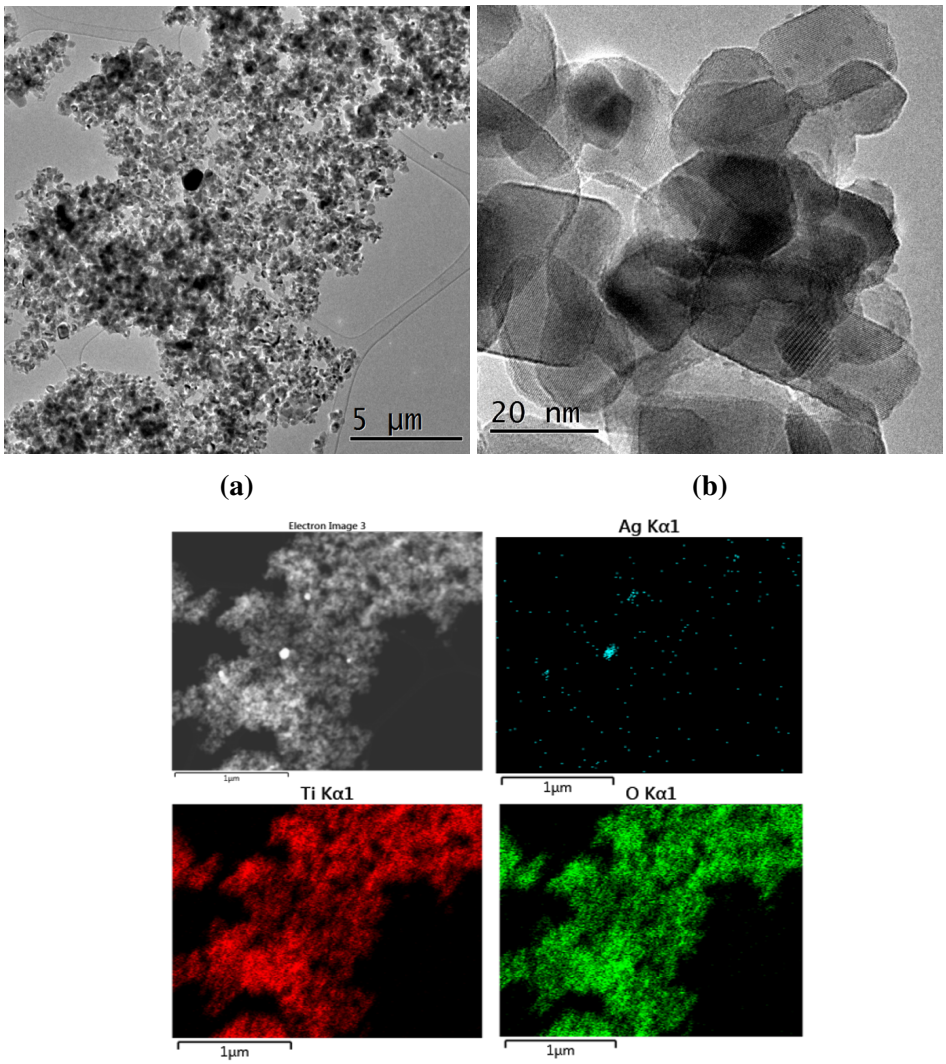

.

Figure 4.14 TEM micrograph of the recycled catalyst 0.5 wt% Ag/TiO_2 used under visible light (4.14a) and under UVA light (4.14b); (4.14c) EDX analysis of recycled 0.5 wt% Ag/TiO_2 used under visible light

4.4 Photo-dispersion of Supported Metal Nanoparticles

Silver nanoparticles are known to show photochromic behaviour when exposed to differnt light sources. Even in our case, after the exposure to different light sources, the grey powders turned to a brownish-gray color as reported by Naoi et al. [181]. The color changes are due to the changes in the morphology and size of the nanoparticles and to changes in the

refractive index of the material. In fact, it is known that the surface plasmon resonance depends on the refractive index of the surrounding material and red-shifts are possible as the refractive index increases. The absorption of glucose as reported by Kim et al. [131] alters the refractive index of TiO_2 and the local composition of the matrix could also be the origin of the diversity in the absorption profile of the Ag nanoparticles after multiple reuses in addition to what has been stated before (Figure 4.11). Figure 4.15 reports the first example of photochromism for TiO_2-supported Ag nanoparticles and how this material tends to mimic the incident wavelength by changing its original greyish color to blue, green, red or white according to the width of the bandpass filter used. Several theoretical explanations have been

Figure 4.15 Multicoloured Ag/TiO_2 film. Each spot (6 mm diameter) was irradiated successively with a blue, green, red, or white light. A xenon lamp and an UV-cut filter (blocking light below 400 nm) were used with an appropriate band-pass filter (blue, 460 nm, 10 mW cm^{-2}, 1 h; green, 520 nm, 11 mW cm^{-2}, 30 min; red, 630 nm, 10 mW cm^{-2}, 30 min) or without any band-pass filter (white, 480 mW cm^{-2}, 10 min). Taken from Naoi et al. [181].

provided [122, 181, 187] but this model accounts for color changes at the solid-gas interface and does not take into account, or only partially, the effect of solvents in the photochromic mechanism. The photochromic transition starts with the photoreduction of the Ag^+ species under UV light with the formation of Ag nanoparticles which show the characteristic plasmon resonance band thus imparting the typical brownish-gray color (Figure 4.16(a)→(b)). If the film is then irradiated with a monochromatic light, the particles are then oxidised to the colorless Ag^+ ions (this mechanism happens only when oxygen is present as e^- acceptor) and due to the oxidation, only the light at that excitation wavelength is reflected by the

film, while the other particles absorb the other wavelengths thus showing only the excitation wavelength color (Figure 4.16(c)). This mechanism can be reversed by shining UV light over the film again. All the literature found on the topic is mainly focused on the properties

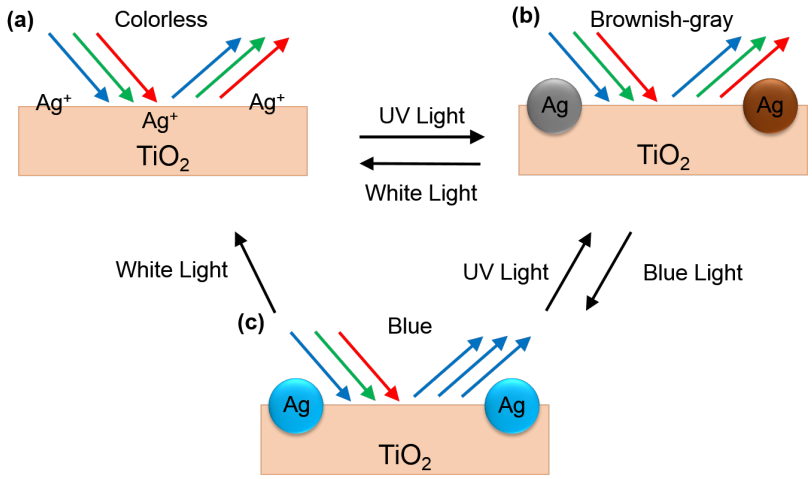

Figure 4.16 Adapted from Kawahara et al. [122].

of these materials rather than on the analysis of the surface-bound mechanisms and on the possible effects on the morphology of the Ag nanoparticles. In order to assess and try to correlate the photochromism of this material with possible morphological changes of the metal nanoparticles on the catalyst surface, the 1.5% Ag/TiO_2 catalyst was exposed for 4 hours to visible and UVA light respectively in the different reaction media used in this study and the recovered catalyst was characterized by TEM, SEM and EDX analysis. It was found during the TEM analysis that the fresh Ag/TiO_2 catalyst had a narrow particle size distribution value of 4.10 ± 0.83 nm, but upon exposure to any light source this value becomes significantly smaller in the four cases reported in Figure 4.17, with a general decrease in the particle size distribution to *ca.* 1 ± 0.3 nm. The redeposition of Ag nanoparticles and the creation of smaller satellites metallic structures is not without precedent as reported by Kazuma et al. [124] under visible light and IR irradiation as part of the photochromic nature of the material. What has not been reported in the literature is the simultaneous conglomeration of the well dispersed Ag nanoparticles into big conglomerates under both

UVA and visible light. In fact, Figure 4.19 shows the effect of the incident irradiation on the redistribution and conglomeration of the supported nanoparticles in different reaction media. It can be seen how under UVA light the conglomeration produces particles up to 60 nm in size, whilst under visible light particles up to 500 nm were observed with a much larger particle size distribution value (Appendix E.1). This "photo-sintering" mechanism can be explained considering the different excitation mechanisms happening under UVA and visible light. It is known that upon visible light irradiation, the LSPR frequency also produces localised hotspots which are used to provide heat in microreactors for ethanol steam reforming. The heat produced during the excitation of Au nanoparticles with a low power laser is sufficient to vaporize the fluid without excessive heating of the immediate surroundings or the need to preheat the reactants feed [3]. Huang et al. [108] recently showed that Ag nanoparticles behave similarly and can be superheated upon irradiation with laser pulses, and in this case, Ag nanoparticles were supported on a Si wafer and irradiated with femtolaser pulses and it was found that the particles rearranged in bigger structures after 10000 pulses (10 s). The LSPR was sufficient to overheat the Ag particles above their melting point and due to the strong electric fields present during the excitation process [185] particles in close proximity could conglomerate in bigger structures [154, 151, 22]. The 1.5 wt% Ag/TiO_2 catalyst used in this study Figure 4.5(c) showed really good particle size distribution and dispersion values before exposure to any light source, therefore the two mechanisms described above are likely to happen simultaneously upon visible light irradiation and cause this redistribution-conglomeration dualism. Under UVA light the presence of the intraband transitions do not cause overheating of the metal nanoparticles, but the presence of electric field at the Schottky metal-support interface might cause the conglomeration of the particles but at a lesser extent as seen in Figure 4.19.

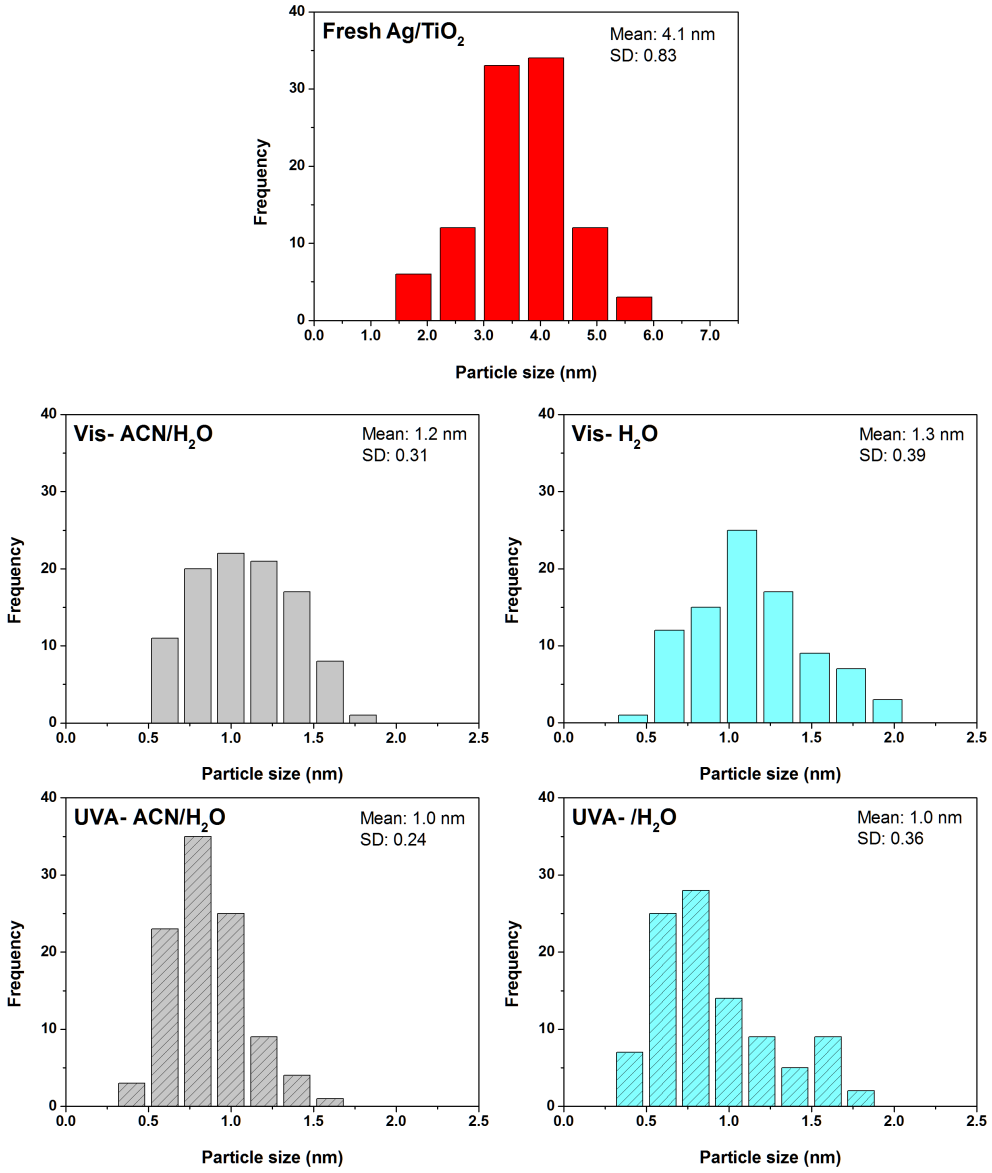

Figure 4.17 Particle size distribution values for the 1.5 wt% Ag/TiO_2 after 4 hours of exposure to visible and UVA light. The effect of the reaction medium was also evaluated by suspending the catalyst in pure H_2O and in the $MeCN/H_2O$ 50/50 v/v mixture.

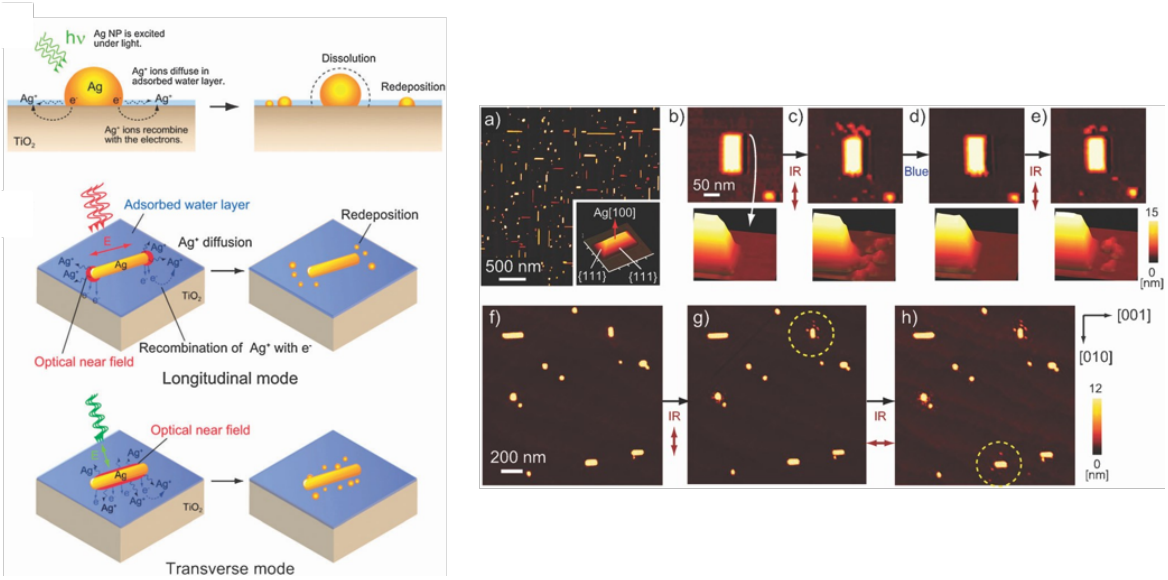

Figure 4.18 Schematic representation of the oxidation of Ag nanoparticles via the LSPR and the subsequent redeposition of smaller satellite Ag nanoparticles (top-left) and for a nanorod under polarized light along box axes (bottom-left). On the right are reported some AFM images before and after irradiation of some Ag nanorods with the formation of satellite Ag nanoparticles on TiO_2. Taken from Kazuma et al. [124], Kazuma and Tatsuma [125]

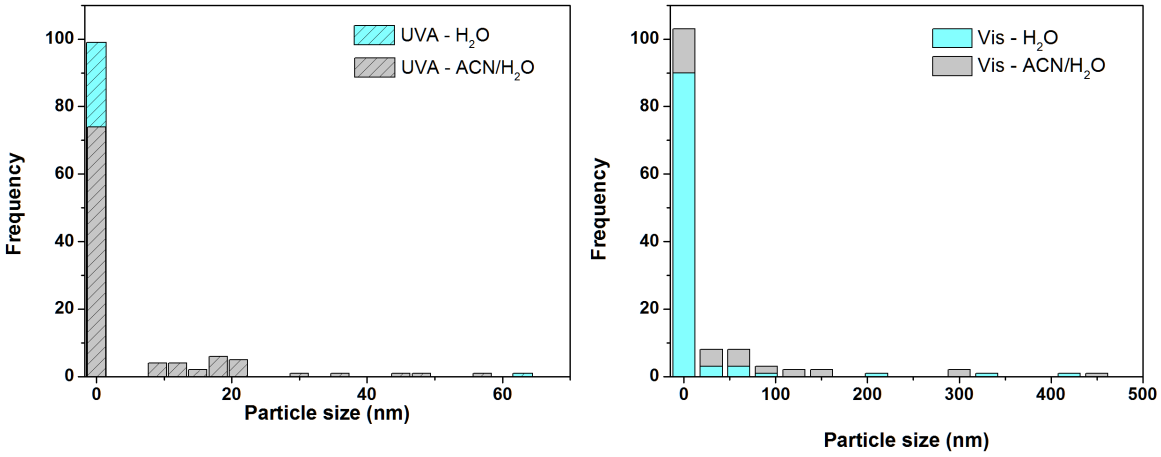

Figure 4.19 Particle size distribution values for the 1.5 wt% Ag/TiO_2 after 4 hours of exposure to visible and UVA light. The effect of the reaction medium was also evaluated by suspending the catalyst in pure H_2O and in the $MeCN/H_2O$ 50/50 v/v mixture.

4.5 Activity of Unsupported Metal Nanoparticles

In 2004 Comotti et al. [64] reported for the first time the activity of unsupported Au nanoparticles in the glucose oxidation reaction. In their study, the Au sols were formed from the usual metal precursor ($HAuCl_4$) with $NaBH_4$ used as reducing agent in a ratio 5:1 with the metal content in solution. Interestingly, glucose was used both as the stabilizing agent for the colloidal solution and as a reactant in large excess (0.35 M). They also reported that the average particle size distribution for the glucose-stabilised sol was around 3.6 nm and that the colloid thus prepared was stable for several hours if not exposed to air. Au proved to be the best performing metal with a reported glucose conversion of *ca.* 30% after 17 minutes under controlled pH (9.5). Along with Au several other metals were tested (Pd, Au, Pt, Ag, Cu) but none of them displayed the same activity (Figure 4.20). In this work the selectivity towards

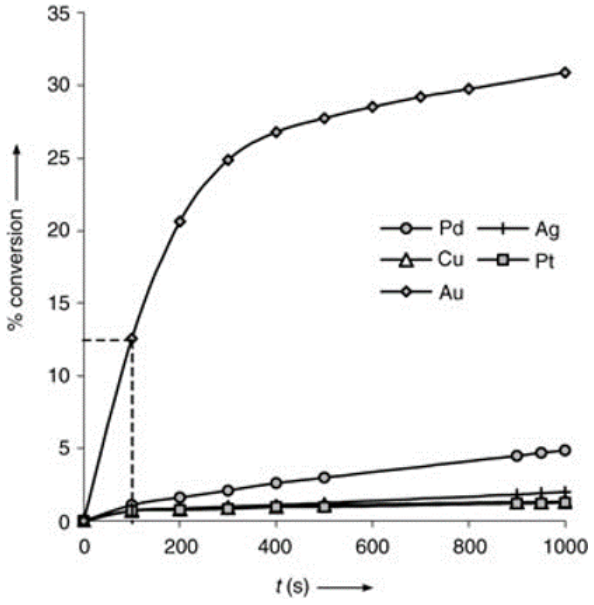

Figure 4.20 Glucose conversion for several unsupported metal colloidal solutions. Typical reaction parameters: Metal: 10^{-4} M; Glucose: 0.35 M; T: 30°C. Taken from Comotti et al. [64].

gluconic acid was not reported, as it was associated with the amount of NaOH added to maintain the pH at a constant level and calculated using the 1:1 stoichiometry of the reaction for the neutralization of gluconic acid to sodium gluconate. As no other reaction products

were reported, it was decided to test the unsupported Au nanoparticles to assess whether or not the reaction would follow the same reaction pathway as with the supported metal nanoparticles.

In order to do this, the same experimental configuration as in Comotti et al. [64] work was used in addition to a test in the absence of light under controlled pH and temperature. Figure 4.21 shows the pH variations during the reaction. After a period of equilibration of

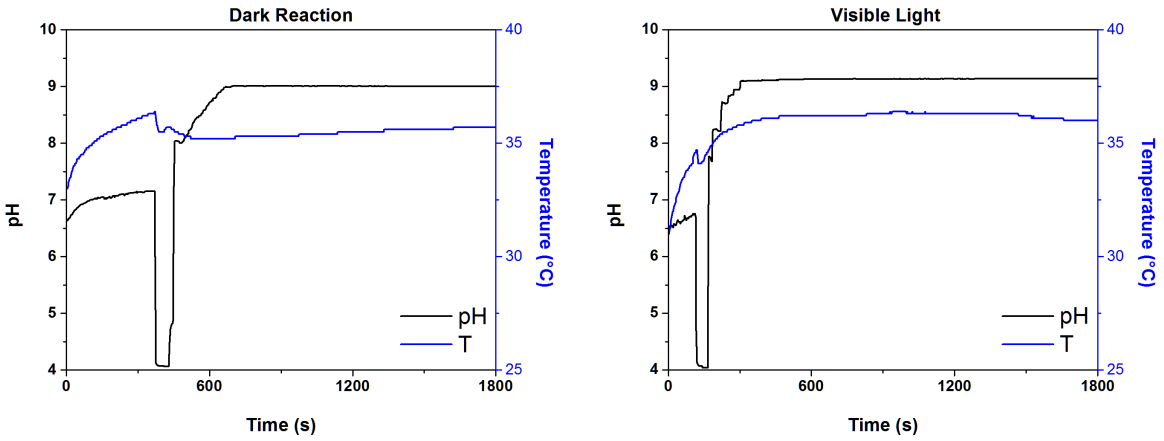

Figure 4.21 Glucose conversion for several unsupported metal colloidal solutions. Typical reaction parameters: Metal: 10^{-4} M; Glucose: 0.35 M

around 330 seconds the pH decreases from 7 to 4 in both cases before the addition of NaOH for reasons not yet fully understood. Samples were taken every 5 minutes and analysed with HPLC as reported in Appendix A.1 and none of the products identified previously was detected in solution. There is then a discrepancy between the addition of NaOH to maintain the pH at a constant level and the concentration of sodium gluconate formed from the neutralization of the gluconic acid. Figure 4.22 clearly shows the absence of gluconic acid from the reaction mixture after 1800 seconds of irradiation time. Even in our case the solution color changed from the typical purple to a colorless solution, but we could not associate the color transition with the production of gluconic acid nor to the NaOH consumption as the HPLC analysis showed no traces of the reaction products even at reaction times much longer

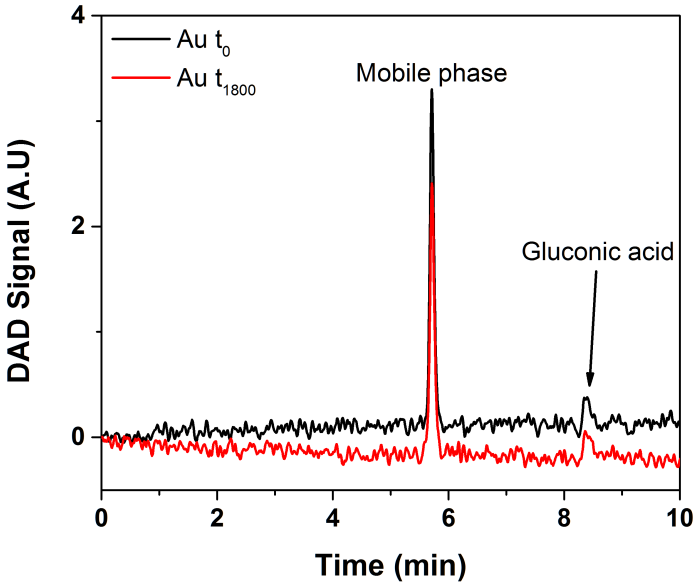

Figure 4.22 Representative chromatograms acquired at 210 nm at the beginning of the reaction and after 1800 seconds.

than those reported by Comotti et al. [64]. From these results the activity of Au sols appears to be controversial and will have to be investigated further in the future.

4.6 Conclusions

After the optimization of the operational parameters described in the previous chapter, the aim of this part of the work was to focus on ameliorating the activity of the catalyst by supporting metal nanoparticles on the surface of the semiconductor. With the addition of Ag nanoparticles the catalyst activity improved substantially under UVA and visible light showing better performances than the 1wt% Au/TiO_2 catalyst used as a comparison. On the other hand, the negligible activity of Au unsupported nanoparticles testifies the importance of the metal-semiconductor-substrate interactions. In fact, with the FTIR analysis, which confirmed the presence on the catalyst surface of multiple adsorbed species, it was possible to draw a global reaction mechanism (Scheme 4.4) to account for the presence of all the reaction products formed during the photocatalytic process. By recycling the catalyst it was possible to analyse the morphological changes of the metal nanoparticles and correlate these variations with the catalytic activity of the different materials. Ag/TiO_2 proved to be a really good catalyst for this reaction, but unfortunately its excitation wavelength in the range 390-410 nm limits its application as it excludes most of the visible part of the spectrum. Therefore, a different approach is needed to try and harvest visible light at different wavelengths simultaneously in order to maximise the efficiency of the process. The analysis of the reactivity on a simple carbohydrate such as glucose with the monometallic Ag/TiO_2 catalyst will prove to be fundamental in the understanding of the results obtained with cellobiose in the next chapter.

Chapter 5

Cellobiose Photo-oxidation

What light?

E. Blues

5.1 Introduction

The thorough investigation of the reaction conditions in Chapter 3 on the oxidation of glucose to a gluconic acid intermediate led us to investigate the effect of the presence of metal nanoparticles on the TiO_2 surface and their effect on the product distribution (Chapter 4). The consistent results obtained coupled with a robust analytical system, allowed us to use cellobiose, a more complex substrate, in order to understand the chemical reactivity of this disaccharide and assess the different reactivity if compared with a simple glucose molecule. This bottom up approach is useful to gradually impart more complexity to the system without neglecting any of the important factors which influence photochemical reactions. Gold, silver, copper and other noble metals on a nanometric scale, exhibit the extraordinary property of responding upon light excitation with a charge transfer mechanism which activates molecules that are adsorbed on the surface or that are in close proximity to the metal nanoparticles itself. This mechanism is well known in the literature and it

is currently used to degrade organic pollutants at room temperature and at atmospheric pressure. Specifically, gold nanoparticles are being studied for the oxidation of different substrates, such as alcohols, aldehydes and various hydrocarbons with promising results. On the other hand, photocatalysis by nanoparticles and semi-conductor oxides continues to receive attention due to its efficiency at converting solar energy to useful chemical energy resulting in mild reaction conditions, and a high intrinsic activity for the conversion of different substrates. A review by Colmenares and Luque [58] highlights the advances in photocatalytic processes as a result of the continual requirement for environmentally friendly methods for pollution abatement, hydrogen generation and the transformation of renewable feedstock to higher value intermediates. In fact, heterogeneous photocatalysts have been used in water splitting processes, water-air purification, artificial photosynthesis and many more. Herein, we report the first example of the photo-catalysed selective oxidation and hydrolysis of the model compound cellobiose along with evidence for the radical cleavage of β-1,4 glycosidic bond. Cellobiose can be cleaved via photocatalytic reaction under visible light to yield glucose and other smaller chain monosaccherides. Crucially, the mineralisation pathway that leads to formation of CO_2 and H_2 is suppressed resulting in the formation of valuable organic products.

5.2 Results and Discussion

5.2.1 Catalytic Testing

The catalyst were tested as described in Section 2.9, with the Luzchem Photoreactor equipped with UVA lamps and with the 300 W Xenon lamp equipped with visible light filters (Appendix 2.8). The different reactors configurations allowed us to apply the same rationale in the reaction design used in the previous chapters when glucose activity was investigated (Chapters 3 and 4).

5.2.2 Identification of the Reaction Pathway Using HPLC-QTOF

The identification of the main reactions involved in the photo-oxidation of glucose described in Section 4.3.3, proved to be extremely useful in the identification of the cellobiose photo-oxidation reaction pathway. It is known that disaccharides have different hole-scavenging properties than simple sugars and therefore, some differences in their reactivity are to be expected.

The main difficulty in determining the reaction pathway was the identification of the intermediates and reactions products as for some of them, there are no commercially available standards or reference materials. For this reason cellobionic acid had to be synthesised and purified following the procedure reported in Appendix B.1.

The identification of the key intermediates and reaction products was performed using HPLC-QTOF (Section 2.7.2) and the method developed in Appendix A.2. With the application of mass spectrometry techniques it was possible to identify, deconvolute, and isolate from the chromatographic peaks the main species and reconstruct the reaction mechanism from the TOL data. Initially, pure cellobiose and cellobiosan at known concentration were solubilized in water and the total ion chromatograms (TIC) were recorded for each of the standards considered. Figure 5.1 shows the TIC chromatograms for the three standards considered and shows the level of chromatographic separation obtained. Because every molecule fragments differently during the QTOF analysis, it was possible to gather data on the fingerprint of each of the species produced by analysing their fragmentation patterns and take these into account to avoid possible misinterpretation of the mass spectra. Table 5.1 shows the main fragments originated during the analysis along with the relative abundances and the difference between the theoretical mass and the measured one for each specific ion. The difference in ppm expresses the accuracy of the instrument in measuring the mass against the theoretical value. By combining the data from the mass spectrometry it was possible to identify 4 possible reaction pathway for the oxidation of cellobiose and the formation of lower carbon chain

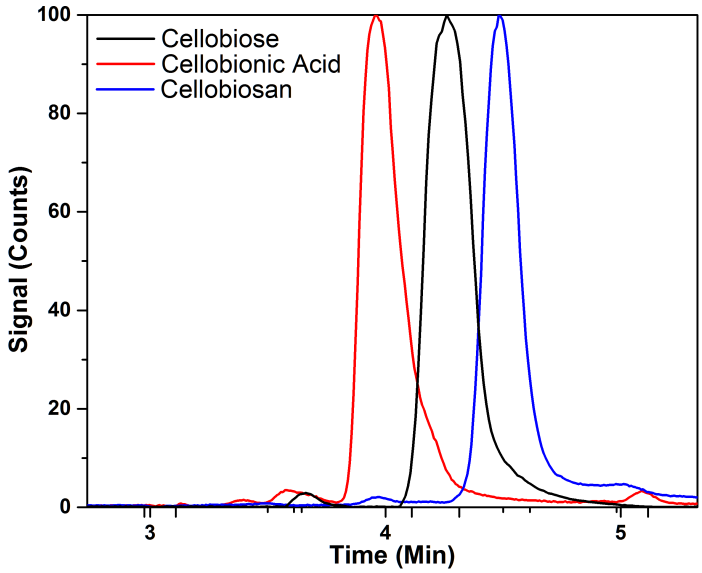

Figure 5.1 Equimolar (2.8 mM) TIC chromatograms for the 3 standard compounds available: cellobiose (black) cellobionic acid (red) and cellobiosan (blue).

Table 5.1 Main fragments originated during the QTOF analysis of the standard compounds.

Standard	Compound Label	Retention Time (min)	Mass	Abundance	Target Mass	Difference (ppm)
Cellobiose	$C_{12}H_{20}O_{11}$	3.82	340.1010	2759	340.1006	1.33
	$C_{12}H_{22}O_{12}$	3.895	358.1097	4659	358.1111	-3.93
	$C_{12}H_{22}O_{11}$	3.961	342.1171	1211803	342.1162	2.44
	$C_{11}H_{20}O_{10}$	4.127	312.1057	9979	312.1057	0.08
Cellobiosan	$C_{12}H_{18}O_{11}$	3.768	338.0858	969	338.0849	2.24
	$C_{12}H_{22}O_{12}$	3.859	358.1123	2044	358.1111	0.37
	$C_{12}H_{22}O_{11}$	3.975	342.1173	51594	342.1162	0.29
	$C_{12}H_{20}O_{11}$	4.199	340.1008	3244	340.1006	1.73
	$C_{12}H_{20}O_{10}$	4.478	324.1058	1391251	324.1056	0.46
Cellobionic Acid	$C_{12}H_{20}O_{12}$	3.487	356.0955	3644	356.0955	0.05
	$C_{12}H_{20}O_{11}$	3.770	340.1022	198472	340.1006	4.89
	$C_{12}H_{20}O_{12}$	3.840	358.1116	1254716	358.1111	1.3
	$C_{12}H_{22}O_{11}$	3.969	342.1168	674295	342.1162	1.72
	$C_{11}H_{20}O_{11}$	4.002	328.1007	3595	328.1006	0.55
	$C_{11}H_{18}O_{10}$	4.027	310.0901	1252	310.0900	0.32
	$C_{11}H_{20}O_{10}$	4.218	312.1053	887	312.1057	-1.15

disaccharides. The first reaction scheme (Scheme 5.1) shows the oxidation of cellobiose by a $^{\cdot}OH$ radical with a loss of a H_2 molecule to produce the corresponding lactone, which is rapidly hydrolysed to the corresponding cellobionic acid. The second reaction (Scheme 5.2) is the oxidation of the lactone to a six-member ring diketone and its subsequent hydrolysis to

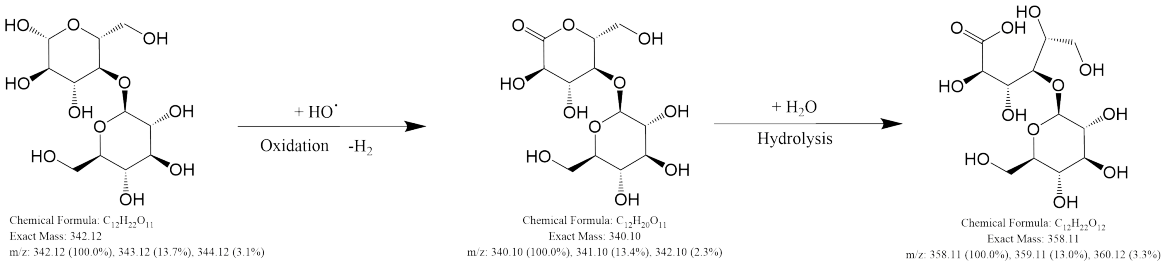

Scheme 5.1 Reaction 1 (R1)

produce another acid $C_{12}H_{20}O_{12}$[1] The third reaction mechanism (Scheme 5.3) involves the

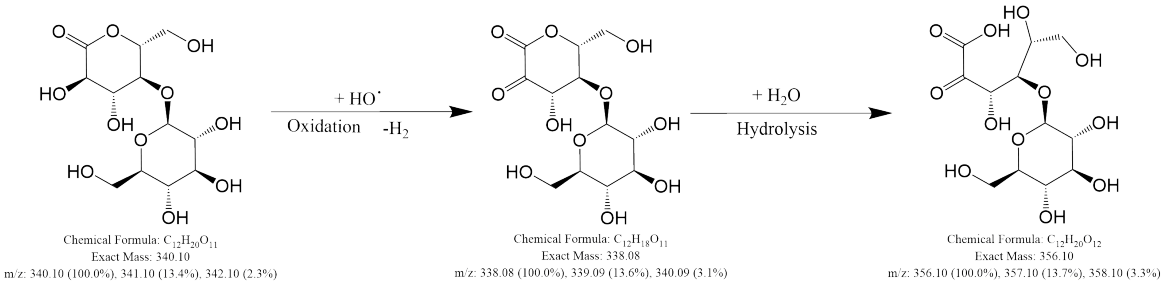

Scheme 5.2 Reaction 2 (R2)

loss of a HCOH group after the ·OH radical oxidation on the starting cellobiose. The loss of

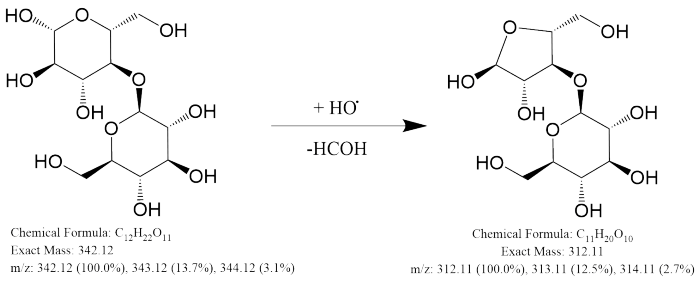

Scheme 5.3 Reaction 3 (R3)

the HCOH functional group leaves behind a stable five-member ring pentose attached to the glycosidic moiety ($C_{11}H_{20}O_{10}$) and this can further react with a similar reaction pathway as the one hypothesized for cellobiose. As shown in the last reaction scheme (Scheme 5.4), the

[1]This acid could not be isolated and characterized any further due to the complexity of the reaction mixture and the impossibility of isolating the compounds for further NMR analysis.

five-member ring can undergo the radical oxidation with the loss of a H_2 molecule followed by the hydrolysis of the formed lactone to the corresponding acid.

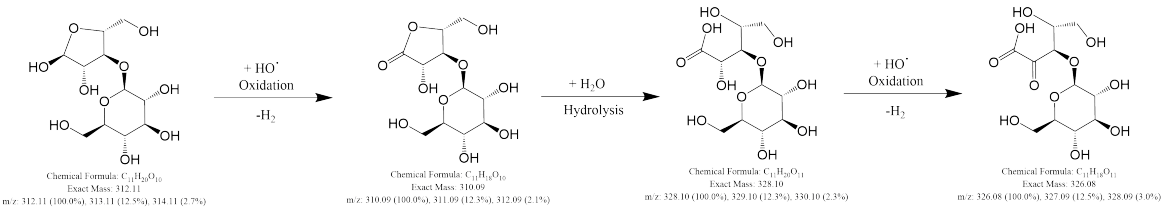

Scheme 5.4 Reaction 4 (R4)

A complete overview of the reaction schemes combined can be seen in Scheme 5.5. All these reaction schemes hypothesize that the oxidation reactions occur because of the OH· attack but, on the other hand, it is not possible at this stage to rule out the presence of other reactive radical species which could contribute to this process. These mechanisms were first identified analysing the chromatograms obtained using TiO_2, and two metal supported catalysts (1%wt Au/TiO_2, 1%wt Ag/TiO_2) synthesised with the P123 colloidal method described in Section 2.3. In order to distinguish between the molecular ions produced during the analysis and the species actually present in the reaction mixture, the samples were run for 24 hours under visible light using the 300 W Xenon lamp. In Table 5.2 are reported

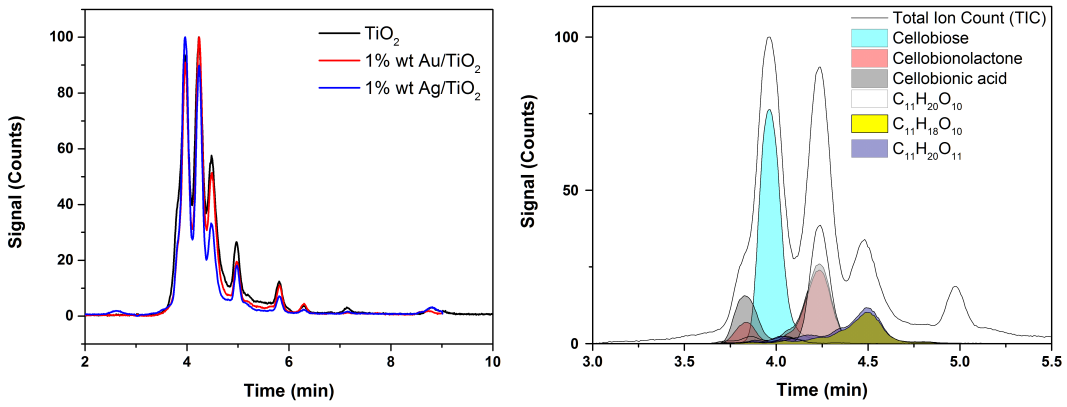

(a) **(b)**

Figure 5.2 5.2a TIC chromatograms for the 24 hours reaction under visible light with TiO_2 (black) 1%wt Au/TiO_2 (red) and 1wt% Ag/TiO_2 (blue) and the deconvoluted peaks for the reaction products identified during the QTOF analysis (5.2b).

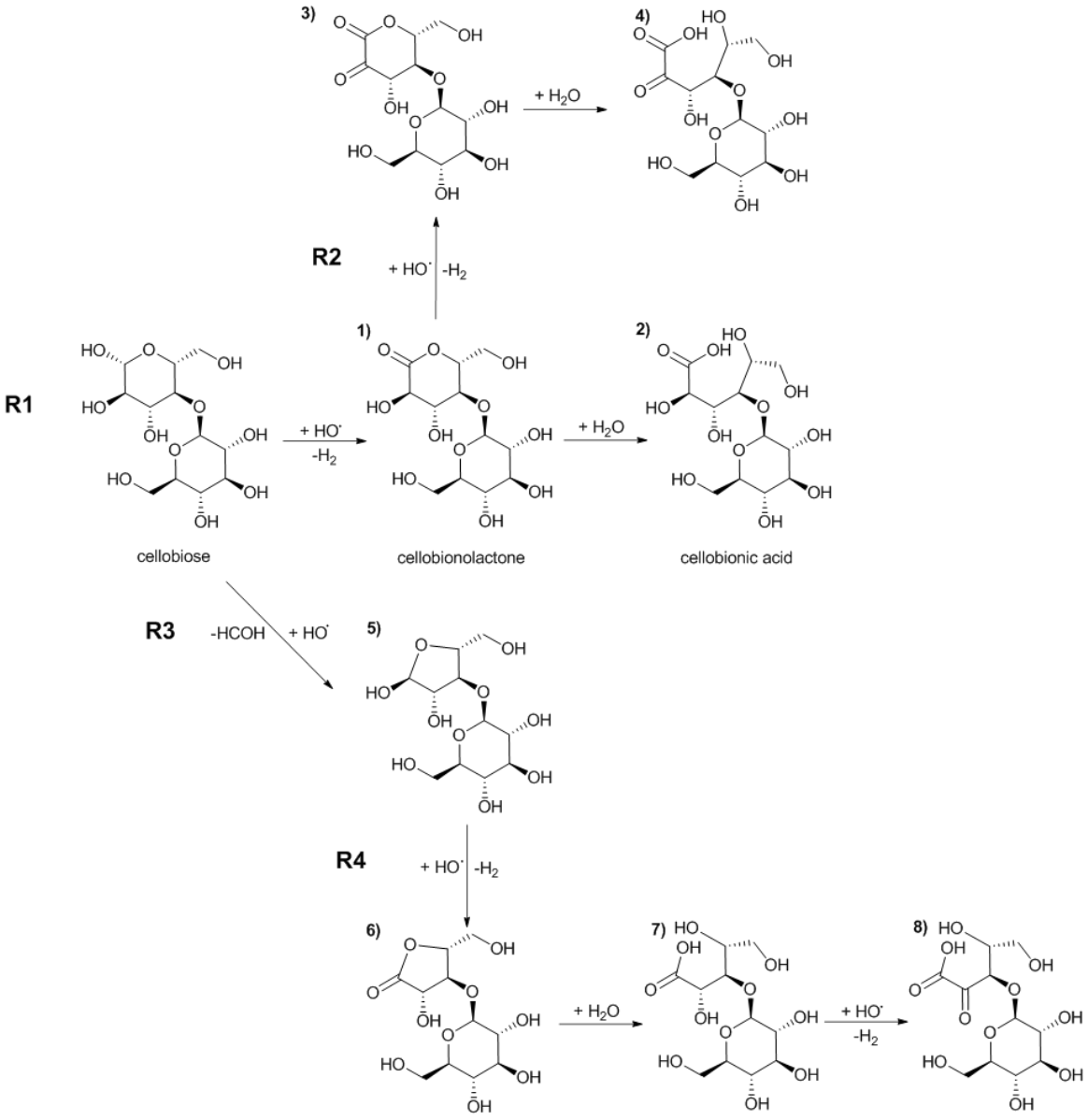

Scheme 5.5 Plausible global reaction pathway identified from the QTOF analysis

the selectivity values for the main reaction products for the three catalysts considered and the selectivity towards each of the reaction schemes. The second part of the table provides useful information as it is possible, through the initial QTOF analysis to evaluate, for such a complex system, the activity of each catalyst for a specific reaction. Interestingly, the 1%wt Au/TiO_2 proved to be, under these conditions, the worst performing catalyst in the R1 as the selectivity is only 34.1% compared with the 41.8% and 40.9% recorded for the TiO_2 and

1wt% Ag/TiO_2 respectively. As regards R2 all three catalysts showed similar performances with overall selectivity values towards this pathway lower than 9%. The addition of the metal on the TiO_2 surface incremented the activity of the material for R5 which involves the reactivity of the $C_{11}H_{20}O_{10}$ in the set of reactions similar to the cellobiose one. These results

Table 5.2 Main target ions for the product identified with the QTOF analysis. In this table the formula of the identified compound and its dominant ion are reported along with the ion counts for each of the catalyst considered after 24 hours of reaction time.

			Products Selectivity (%)			**Reaction Selectivity (%)**		
	Compound	**Target Ion**	**TiO_2**	**Ag/TiO_2**	**Au/TiO_2**	**TiO_2**	**Ag/TiO_2**	**Au/TiO_2**
R1	**1**	$[C_{12}H_{20}O_{11}\text{-Na}]^+$	12	10.2	9.4	41.8	40.9	34.1
	2	$[C_{12}H_{22}O_{12}\text{-Na}]^+$	29.8	30.7	24.7			
R2	**3**	$[C_{12}H_{18}O_{11}\text{-Na}]^+$	2.6	4.6	3.3	5.4	8.8	6.8
	4	$[C_{12}H_{20}O_{12}\text{-Na}]^+$	2.8	4.2	3.5			
R3+R4	**5**	$[C_{11}H_{20}O_{10}\text{-Na}]^+$	30.9	18.5	28.3	30.9	18.5	28.3
R5	**6**	$[C_{11}H_{18}O_{10}\text{-Na}]^+$	14.7	22.4	20	21.9	31.9	30.7
	7	$[C_{11}H_{20}O_{11}\text{-Na}]^+$	5.8	6.9	8.2			
	8	$[C_{11}H_{18}O_{11}\text{-Na}]^+$	1.4	2.6	2.5			

did not take into account the cellobiose conversion as they were intended to investigate the reaction mechanism with three different catalyst in order to obtain further information on the chemistry involved and try to delineate a plausible reaction mechanism and qualitatively assess the effect of the metal on the product distribution. Therefore, the quantification of the products was not possible at this stage as this information was used to synthesise the cellobionic acid (B.1 and to purchase cellobiitol and the other partial oxidation products. A detailed account of the effect of the metal loading and of the alloying of Au and Ag will be covered in 5.3.1.

5.2.3 Experimental Reaction Pathway

The HPLC-QTOF analysis was a necessary first step to obtain some crucial information about the nature of the products being formed during the photocatalytic process. This technique, due to the high sensitivity, generates large amounts of data, and their interpretation sometimes

leads to misleading results, due to the formation of additional species present in low quantities during the analysis that are actually absent in the reaction sample. The understanding of the reaction mechanism involving the reactivity of glucose during a photo-oxidation process, can be translated to cellobiose, and again, 3 main reaction pathways can be detected which take into account the most plausible reaction products.

The first reaction is the oxidation of cellobiose to the corresponding acid via a lactone intermediate which subsequently decarboxylates following the photo-Kolbe mechanism (Scheme 5.6); the second is the α-scission with the loss of formic acid to produce the $C_{11}H_{20}O_{11}$ disaccharide described previously following the same mechanism proposed by Chong et al. [53], and the last one is the direct cellobiose photo-reforming to produce CO_2 and H_2 (Scheme 5.8). Interestingly, in addition to the the three different reaction mechanism

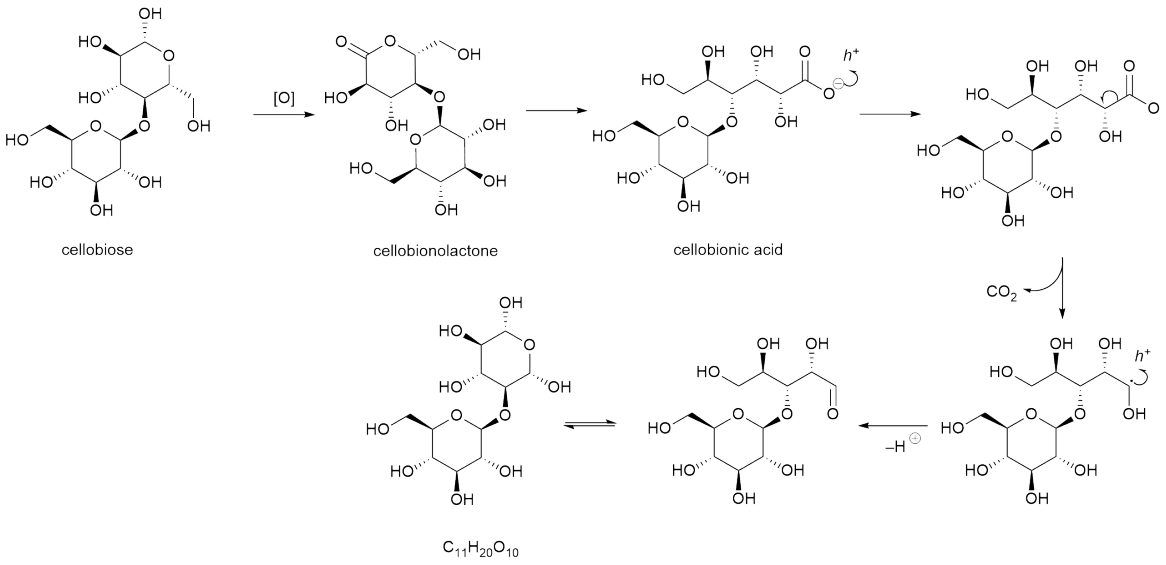

Scheme 5.6 Photo-Kolbe decarboxylation of cellobiose via the cellobionic acid intermediate to produce the $C_{11}H_{20}O_{10}$ disaccharide.

illustrated above, it was found that cellobiose can be photocatalytically hydrolysed to glucose, and that once glucose is formed, it reacts following the same reaction pathway illustrated in Chapter 4, Section 4.3.3. The combination of the oxidation pathway and the hydrolytic cleavage of the β-1,4 glycosidic bond is shown in Scheme 5.9. Additionally, this reaction

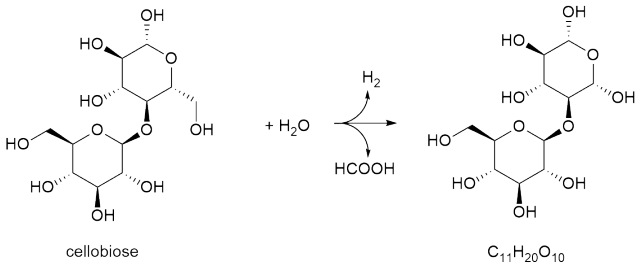

Scheme 5.7 α-scission with the loss of formic acid and hydrogen to produce a pentose moiety on the $C_{11}H_{20}O_{10}$ disaccharide.

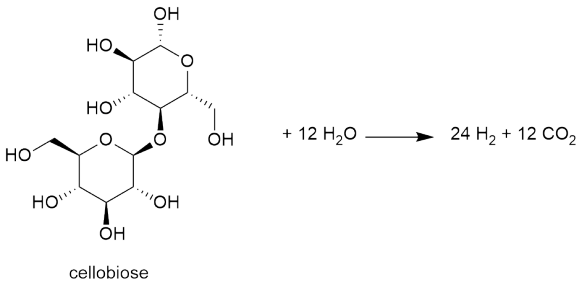

Scheme 5.8 Suggested reaction pathway for the photo-reforming of cellobiose to produce H_2 and CO_2.

scheme combines the photo-Kolbe reaction mechanism with the α-scission one as the two mechanism can occur simultaneously the latter without the presence of the acid intermediate. The 98+% mass balance values obtained demonstrate how the direct mineralization pathway to form H_2 and CO_2 is suppressed, and the loss of carbon is due to the formation of CO_2 during the photo-Kolbe mechanism.

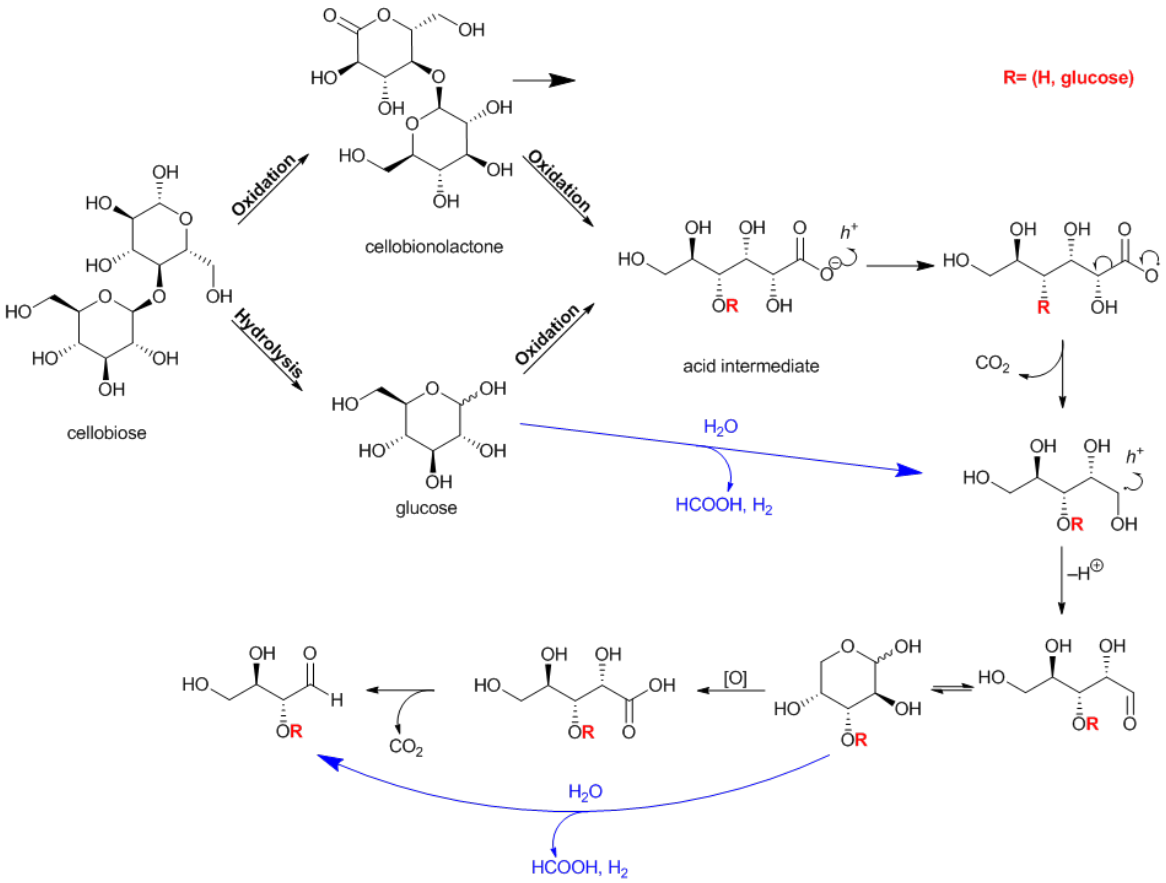

Scheme 5.9 Combined reaction mechanism for the cellobiose photo-oxidation and the photo-initiated hydrolysis of the β-1,4 glycosidic bond.

5.3 Catalytic Data

5.3.1 Effect of the Substrate Concentration and Reaction Medium

The experimental method applied to assess and evaluate the effect of the substrate concentration and reaction medium is the same as the one applied for glucose in Section 4.3.1. allow As for glucose, the effect of the substrate concentration was assessed by increasing the cellobiose concentration from a 2.8 mM to 10 mM whilst keeping constant the quantity of the suspended catalysts (14 mg). Additionally, the reaction medium composition was changed from pure H_2O to the 50/50 v/v H_2O/MeCN mixture. Under these conditions the mono and bimetallic supported colloidal catalysts were tested under visible and UVA light. Figure 5.3

reports the product distribution values obtained for the 2.8 mM cellobiose solution. It is clear from the four bar charts how the reaction medium affects the product distribution values. In fact, cellobionic acid is the primary reaction product when H_2O is used with selectivity generally being between 45 and 65% for both visible and UVA light.

Interestingly, with just water as a solvent, gluconic acid is produced under both UV and visible light but is absent when the H_2O/MeCN mixture is used. In this case, due to the higher photoactivity of the material and the effect of the acetonitrile in solution, gluconic acid is not only a product of the hydrolytic cleavage of the β-1,4 glycosidic bond but it is also a reagent in the photo-Kolbe reaction pathway and it quickly reacts under these conditions to form arabinose, erythrose, glyceraldehyde and formic acid as previously reported (Chapter 4). The hydrolytic step does not seem to occur under visible light irradiation as only the cellobiose oxidation products are detected with overall selectivity values between 70 and 75% with formic acid being the third major product after the $C_{11}H_{20}O_{10}$ disaccharide. This indicates that for the 2.8 mM cellobiose solution, the preferred reaction pathway under visible light in the H_2O/MeCN mixture is the α-scission of cellobiose with the production of formic acid and a lower carbon chain disaccharide (Scheme 5.7), whilst under the more aggressive UVA irradiation, the reactions are driven further with the formation of gluconic acid as a short lived intermediate which rapidly reacts to produce shorter carbon chain carbohydrates. When the substrate concentration is increased to 10 mM the (Figure 5.4) cellobionic acid selectivity increases for both the H_2O and the H_2O/MeCN mixture between 40-55% and 55-50% respectively. In this case, unlike for the 2.8 mM solution, gluconic acid can be found in both systems, but the photoactivity of the material is not sufficient to start the photo-Kolbe mechanism under visible light. In fact none of the products originated from this reaction is observed under these conditions. Under UVA light the differences between the different catalysts considered are not so evident as, generally, cellobionic acid is the primary oxidation product along with the $C_{11}H_{20}O_{10}$ which together make up for

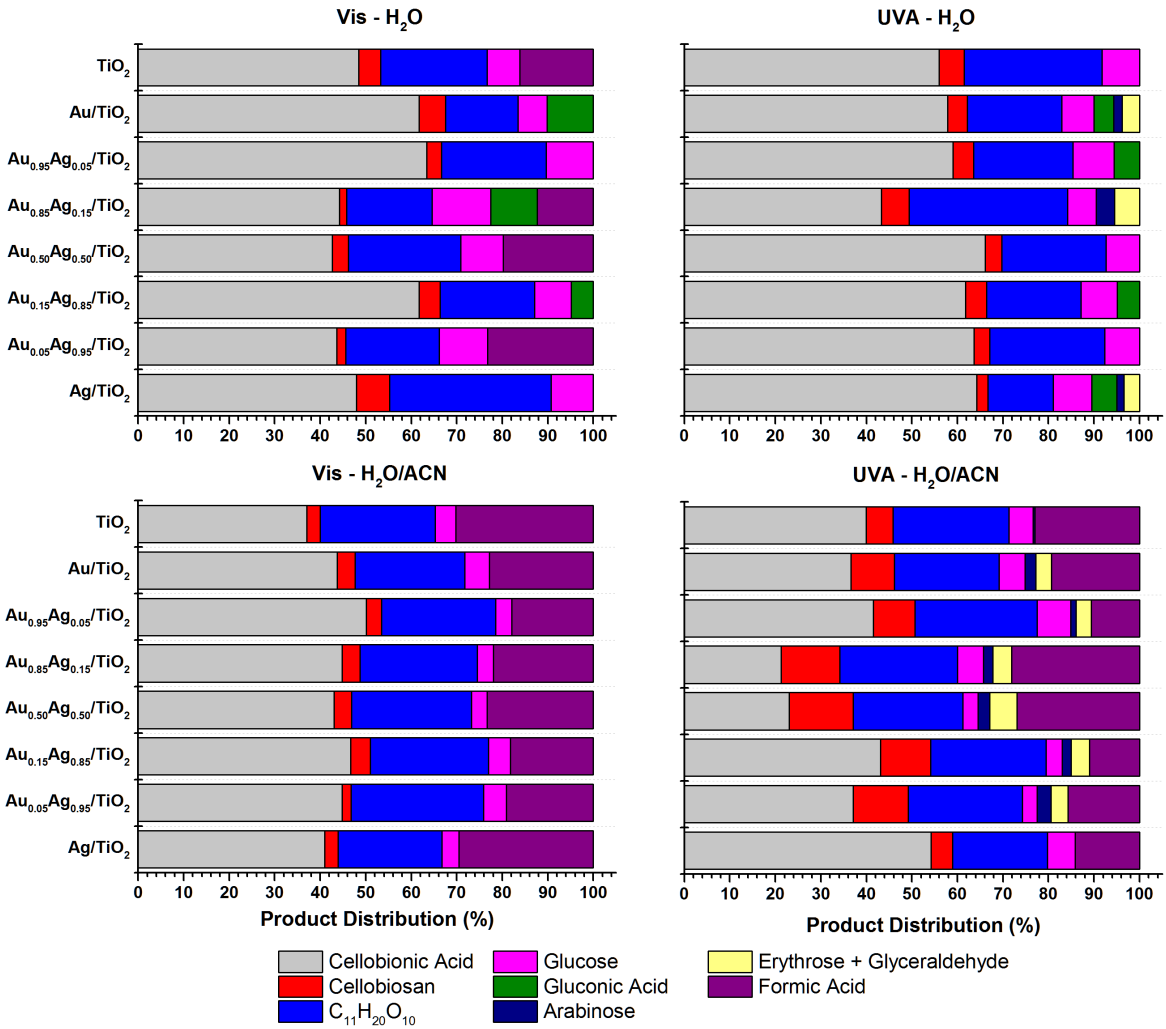

Figure 5.3 Product distribution values for the $Au_{0.85}Ag_{0.15}/TiO_2$ obtained varying the reaction medium and the light source for the 2.8 mM cellobiose solution.

almost 80% of the total product distribution. [2] Due to the increased surface coverage, the adsorption-desorption mechanism of the reactant and the reaction product might happen at different rates thus causing mass-transfer limitations caused by the presence of a cellobiose-TiO_2 complex. Lee et al. [143] reported a computational study of the possible interaction of glucose and cellobiose on kaolinite ($Si_2Al_2O_5(OH)_4$) an aluminosilicate material used industrially for several applications. Figure 5.5 shows the cellobiose molecular structure with attention to the geometry of the β-1,4 glycosydic bond. Lee et al. [143] showed that

[2] A chemical name for this compound could not be assigned as the techniques used allowed only the determination of its brute formula and did not provide any information on its structure.

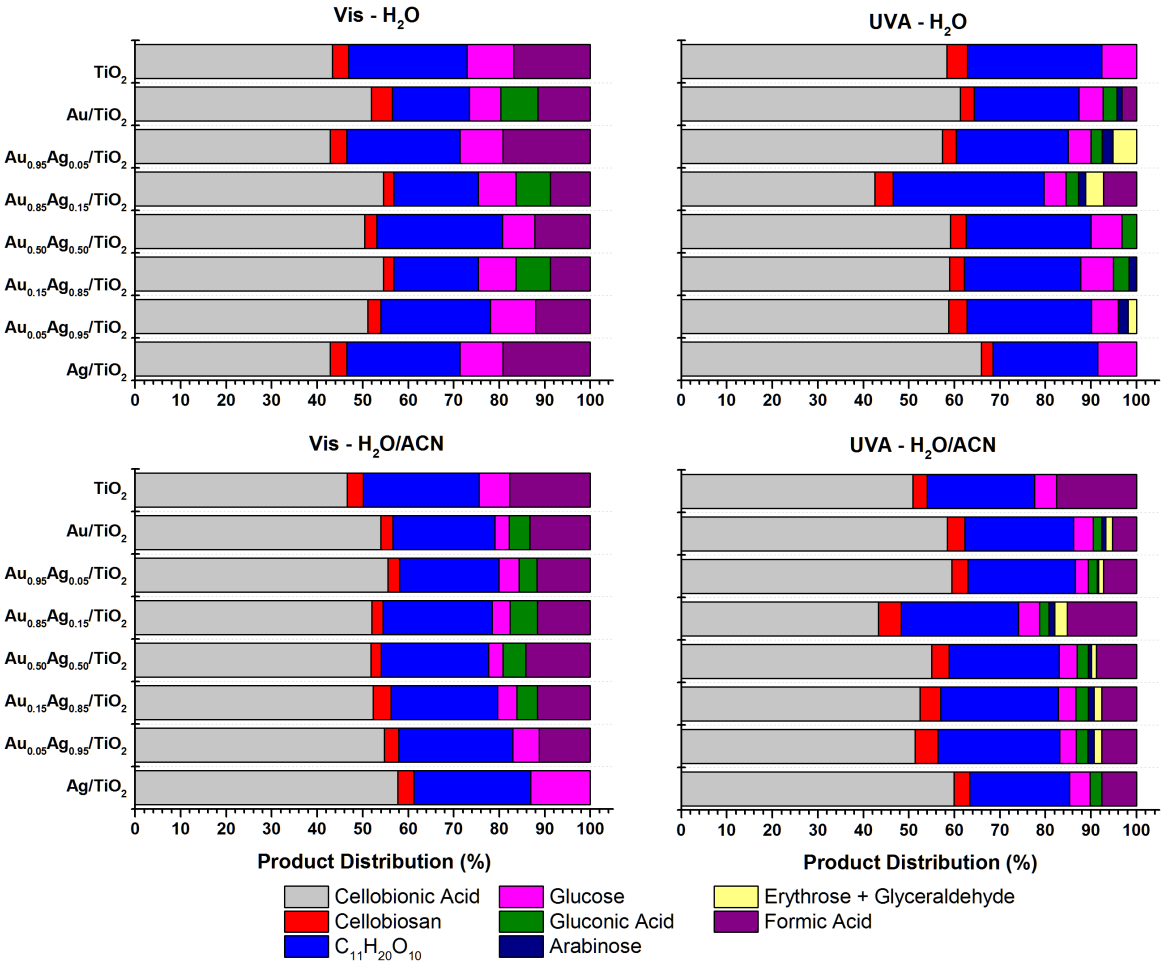

Figure 5.4 Product distribution values for the $Au_{0.85}Ag_{0.15}/TiO_2$ obtained varying the reaction medium and the light source for the 10 mM cellobiose solution.

according to the "up" or "down" position of the molecule on the kaolinite surface, different interaction via hydrogen bonds are formed with the latter maximising the interactions with the surface as shown in Figure 5.6. A similar scenario can be possible on the

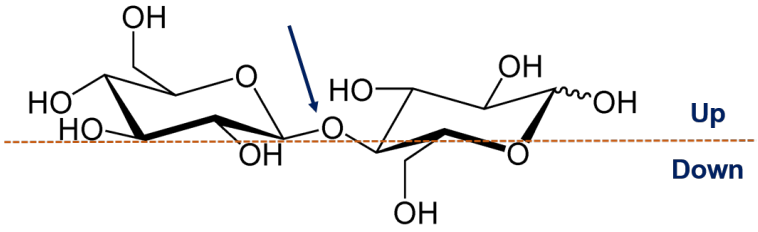

Figure 5.5 Cellobiose molecular structure with the highlighted β-1,4 glycosydic bond.

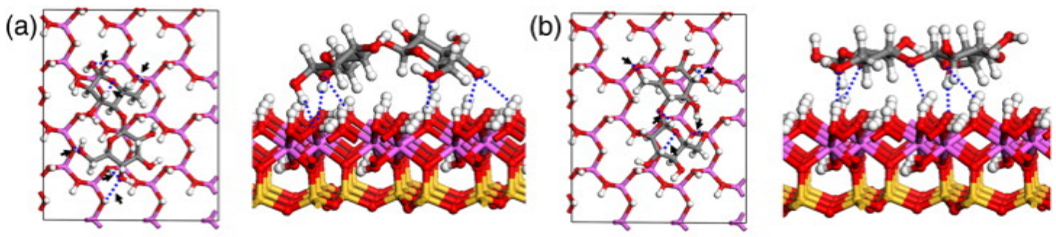

Figure 5.6 Optimized structure of the adsorbed cellobiose on kaolinite surfaces with the hydrogen bonds configuration (blue dot line and arrow) on a fully hydroxylated surface for the : (a) "up" side of the cellobiose; (b) "down" side of the cellobiose. The White, red, pink, yellow color denote hydrogen, oxygen, aluminum, and silicon atoms respectively. Taken from Lee et al. [143].

fully TiO_2 hydroxylated surface specifically upon UV irradiation with the photo-induced superhydrophilicity (Section 1.7.5). Unlike for glucose, the FT-IR analysis of the used catalysts did not provide enough information to confirm the formation of a TiO_2-cellobiose complex, albeit the presence of some common stretching frequencies around 1600 cm^{-1} in the carboxylic group functionality range. When the substrate concentration is increased,

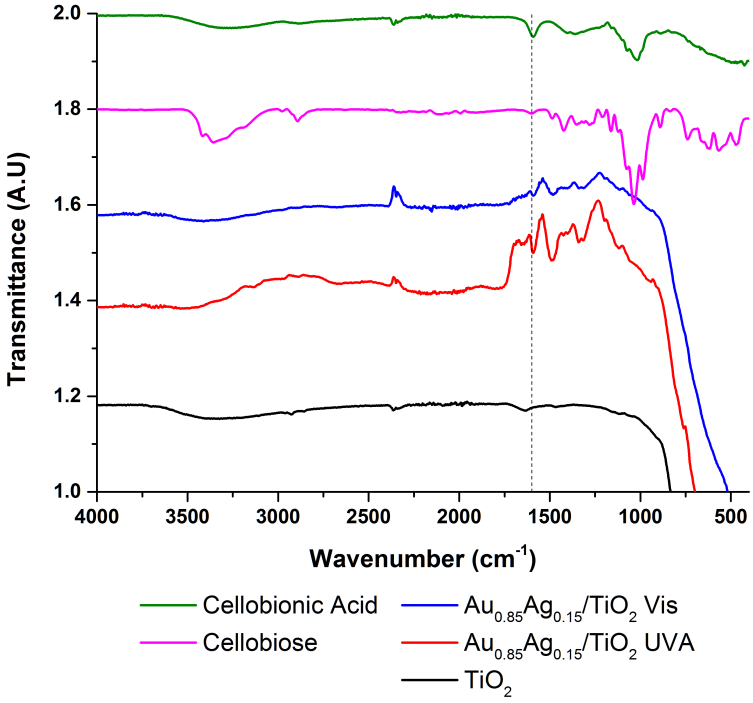

Figure 5.7 FT-IR analysis of cellobiose and cellobionic acid as standards and of the $Au_{0.85}Ag_{0.15}/TiO_2$ catalyst after visible and UVA irradiation.

we can assume a diminished availability of the active sites on the surface with a subsequent

reactivity decrease. In this case, the identification of gluconic acid was possible in both reaction media and under both light sources. This trend is similar to the initial studies performed on the naked TiO_2 P25 in which the selectivity to the system was imparted by increasing the catalyst to substrate ratio (Chapter 3, Section 3.2.1). The variation of the substrate concentration does not only have an effect on the product distribution but most importantly, on the cellobiose conversion as shown in Figure 5.8. In fact, when the 2.8 mM cellobiose solution was used, 100% conversion was reported for all the bimetallic catalysts after only 90 minutes of reaction in the H_2O/MeCN mixture and the conversion value dropped significantly when pure water was used under the same UVA illumination conditions. The same drop in conversion could be observed under visible light with the H_2O/MeCN mixture showing superior conversion values than when pure water was used. The increased activity and the high conversion values observed for the 2.8 mM cellobiose solution also corresponded with lower mass balance values. As shown in Table 5.3 for the $Au_{0.85}Ag_{0.15}/TiO_2$ when UVA light is use in combination with the water/organic mixture the mass balance value drops down to 78.4% whilst when water is used this value is 93.4%. For the 10 mM cellobiose solution, the +99% mass balance values prove that the direct mineralization to CO_2 and H_2 does not occur at high substrate loading. Nonetheless, H_2 and CO_2 can be produced during the photo-Kolbe mechanism and the α-scission. Therefore, mass balance values lower than 100% are to be expected. The small experimental error associated to the chromatographic determination of the large number of species in the liquid phase causes an overestimation of the total amount of the oxidation products thus making necessary the set-up of an experimental configuration for the head-space analysis to monitor and quantify the evolution of gaseous products during the reaction and relate the quantity of these products to the ones present in solution.

Previous results shown in Chapter 3 and Chapter 4 the presence of the MeCN in the reaction mixtures clearly affects the catalyst reactivity as described in 3.2.4 and even in

for this specific substrate, the MeCN presence directly affects the flatband position, the surface charges on the support and the lifetime of the radical species in solution as it has been demonstrated that MeCN increases the lifetime of singlet oxygen (^{1})O_2 in solution [35, 197].

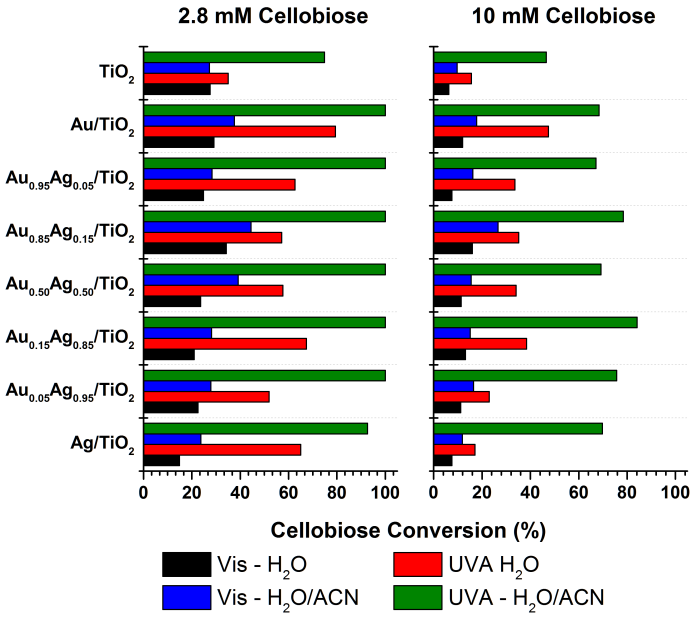

Figure 5.8 Cellobiose conversion for the 2.8 (left) and 10 mM (right) solutions with the different reaction media considered under visible and UVA light.

Table 5.3 Catalytic performance of the $Au_{0.85}Ag_{0.15}/TiO_2$ material under visible and UVA light and in the different reaction media considered.

Cellobiose Stock Solution (mM)	Reaction Medium	Light Source	Cellobiose Conversion (%)	Mass Balance (%)
2.8	H_2O/MeCN	Visible	44.5	102.5
2.8	H_2O	Visible	34.2	103.4
2.8	H_2O/MeCN	UVA	100.0	78.4
2.8	H_2O	UVA	57.2	93.4
10	H_2O/MeCN	Visible	26.7	104.7
10	H_2O	Visible	13.2	103.0
10	H_2O/MeCN	UVA	78.4	101.0
10	H_2O	UVA	35.2	99.9

Photo-oxidations, unlike conventional catalytic processes, due to the high reactivity of the radical species involved and the complex chemistry, are unlikely to produce only one product. In fact, these reaction are generally exploited for inherently unselective processes

such as pollutant degradations or organic abatement. In this case, the selectivity towards partially oxidised products and specifically cellobionic acid, is for all the catalysts used between 40 and 70%. If we also consider the presence of gluconic acid in solution these values are significantly higher and clearly show the possibility of obtaining useful chemicals with a relatively inexpensive reactor configuration using solar light. Cellobionic acid can be converted to isobutanol with *E. Coli* [75], gluconic acid, arabinose are used in the production of metal chelating agents, as precursors for pharmaceutical compounds, and as reactants in the bio-ethanol production plants. Recently, erythrose has shown promising results as an anti cancer agent as it can effectively kill tumoral cells in vitro [155], and last but not least, the annual production of formic acid in 2009 was around 720 kton year$_{-1}$ and has a wide range of applications [31]. This study clearly does not focus on the production of a single specific compounds, it rather showcases the possibility of obtaining useful chemicals from biomass by using visible light, using incredibly mild conditions, and obtaining better selectivity and conversion results than the ones recently obtained using a Au/TiO_2 by Amaniampong et al. [7]. It is also clear that in order to have commercially feasible reactions, the downstream purification process has a pivotal in the commercialization of a new process has it can have a significant impact on the running costs of the plant and might hinder the cost/benefit of having a clean solar-powered plant if this produces a complex crude mixture to be purified. It is now known at the moment the level of purification required by the industry on some of these feedstocks as they are relatively new resources and many processes and purification steps are being designed at the moment and, according the author's best knowledge, there are no minimum requirements or guidelines available on the topic.

5.4 Colloidal Synthesis and Stability

5.4.1 P123 as Stabilizing Agent

The mono and bimetallic colloidal solutions were prepared following the synthetic protocols illustrated in Section 2.3 and 2.3. The first analysis to be performed on the fresh solutions, was the UV-Vis measurement to assess the presence of the reduced metal nanoparticles in solution, in fact the presence of the plasmon band around 560 nm for Au and 389 nm for Ag is an indication of the successful reduction step and the formation of zero-state metal nanoparticles. More interestingly, with the addition of a second metal (Ag) and the formation of nanoalloys, it is possible to shift the maximum of absorption to lower wavelength values and therefore, tune the visible light absorption properties of the material as it can clearly be seen in Figure 5.9.

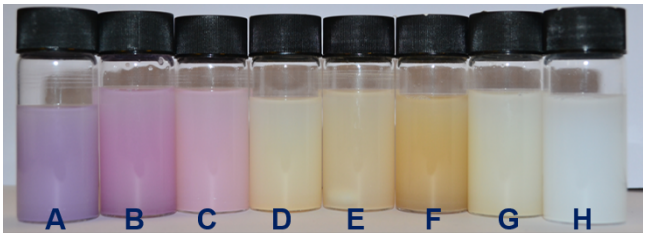

Figure 5.9 Supported 1% w/w AuAg metal nanoparticles. From left to right: Au/TiO_2 (A), $Au_{0.95}Ag_{0.05}/TiO_2$ (B), $Au_{0.85}Ag_{0.15}/TiO_2$ (C), $Au_{0.50}Ag_{0.50}/TiO_2$ (D), $Au_{0.15}Ag_{0.85}/TiO_2$, $Au_{0.05}Ag_{0.95}/TiO_2$ (E), $AuAg/TiO_2$ (F), Ag/TiO_2 (G), TiO_2 (H). On the left the 1%w/w Au/TiO_2 (A) shows the classic purple color and with the addition of Ag as a second metal we obtain the grayish color of the 1% w/w Ag/TiO_2 catalyst (G). On the far right the naked TiO_2 (H) is shown as a comparison.

Additionally, if the molar ratio of the second metal added, in this case silver, is plotted against the maximum absorption of the LSPR, a linear relationship between the two parameters can be extrapolated (5.10b). Core-shell bimetallic nanoparticles are characterized by the presence of two SPR bands, corresponding to the absorbance of the separated metal clusters as core or shell. In our case the presence of only one SPR peak, confirms the presence of nanoparticles with random Ag distribution rather than with defined Au(Ag) or Ag(Au)

core-shell structures, or worse, a distribution of pure Au and Ag monometallic nanoparticles [109, 236, 153, 152, 179]. The freshly prepared colloidal solutions were then supported on

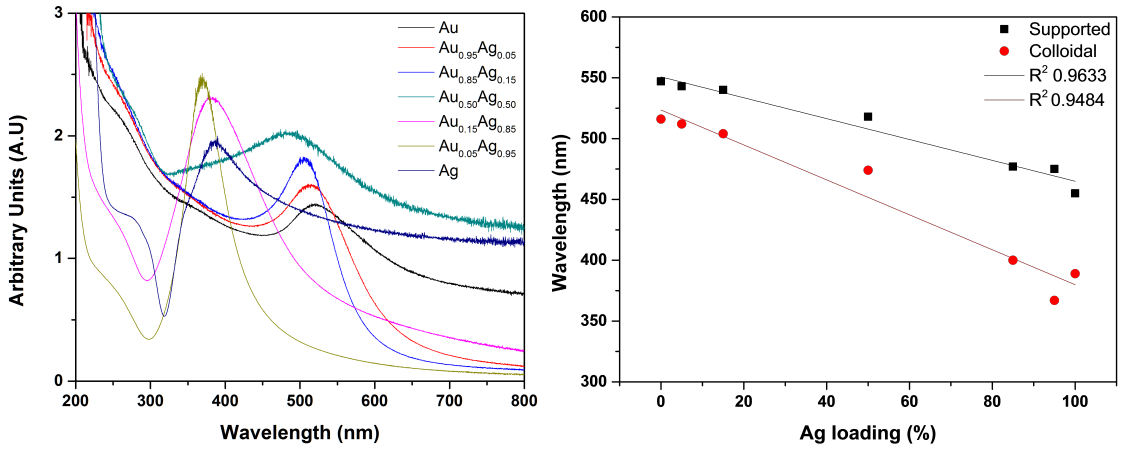

Figure 5.10 5.10a UV-Vis spectra of the unsupported mono and bimetallic colloidal solutions; 5.10b Maximum of absorption (nm) for the unsupported colloidal (■) and supported (●) bimetallic nanoparticles as a function of the Ag molar loading in the nanoalloy.

TiO_2 and solid UV-Vis analysis was performed on the dried materials ground to a fine powder to assess the successful deposition of the metallic nanoparticles on the semiconductor surface and evaluate possible shifts of the SPR band. Figure 5.11 shows the absorption profiles in the 200-800 nm range of the mono and bimetallic catalyst. The absorptions in the 300-600 nm range are due to the SPR resonance, and the increased absorbance at wavelength values lower than 300 nm is due to the absorption of the incident irradiation by the TiO_2 band gap. The metal supported catalysts were then digested using a freshly prepared aqua regia solution (Section 2.6.8) to evaluate the actual metal loading of the material using ICP. These results are reported in Table 5.4 and show good agreement between the theoretical value and the calculated one.

Additionally, the stability of the colloidal solution was measured to assess their lifetime and storage properties. Gold and silver solutions were stored in the dark at room temperature for a week and were analysed by UV-Vis over this time frame. The stability of the colloids varies significantly with time; in fact, Ag colloids showed a significant decrease in absorption

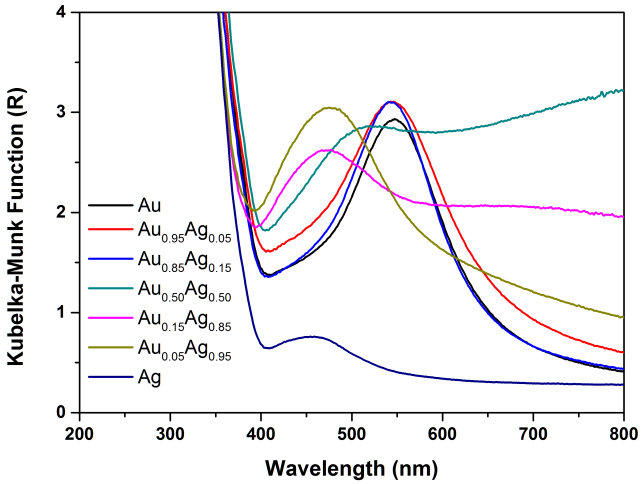

Figure 5.11 Solid UV-Vis spectra of the supported AuAg metal nanoparticles.

Table 5.4 Elemental analysis of the AuAg/TiO_2 catalyst and molar ratio of the two metals obtained by ICP.

Catalyst	**Au (ppm)**	**Ag (ppm)**	**Metal Loading** [a] **(ppm)**	**Metal loading (ppm)**	**Molar ratio** [b]	**Molar ratio**[c]
Au	9.65(±0.01)	-	10.4	9.65	-	-
$Au_{0.95}Ag_{0.05}$	9.20(±0.10)	0.40(±0.02)	9.8	9.60	19	12.6
$Au_{0.85}Ag_{0.15}$	8.68(±0.08)	1.22(±0.02)	10.0	9.9	5.7	3.9
$Au_{0.50}Ag_{0.50}$	6.07(±0.03)	2.54(±0.03)	10.1	8.6	1.0	1.3
$Au_{0.15}Ag_{0.85}$	2.18(±0.01)	5.89(±0.05)	9.7	8.1	0.2	0.2
$Au_{0.05}Ag_{0.95}$	0.64 (±0.005)	4.48(±0.04)	9.9	5.1	0.05	0.1
Ag	-	5.42(±0.05)	9.6	5.42	-	-

[a] nominal metal loading
[b] nominal Au/Ag molar ratio
[c] calculated Au/Ag molar ratio

after 1 day with this negative trend continuing throughout the week (Figure 5.12a). On the other hand, Au colloids showed good stability as shown in Figure 5.12b the absorption profile does not vary significantly. Along with the absorption measurements to obtain qualitative information on the stability of the sol prepared, the variation of the SPR wavelength was plotted as a function of time to gather information on the shifts of the plasmon band. Figure 5.13 shows how for the Au sol, the profile remains constant for over 40 days, with a slight increase in the absorbance values due to the formation of bigger nanoparticles as it is well documented in the literature [48, 170, 200]. For the Ag sols, two different P123 ratios were considered in order to increment the lifetime of the metal nanoparticles in solution and

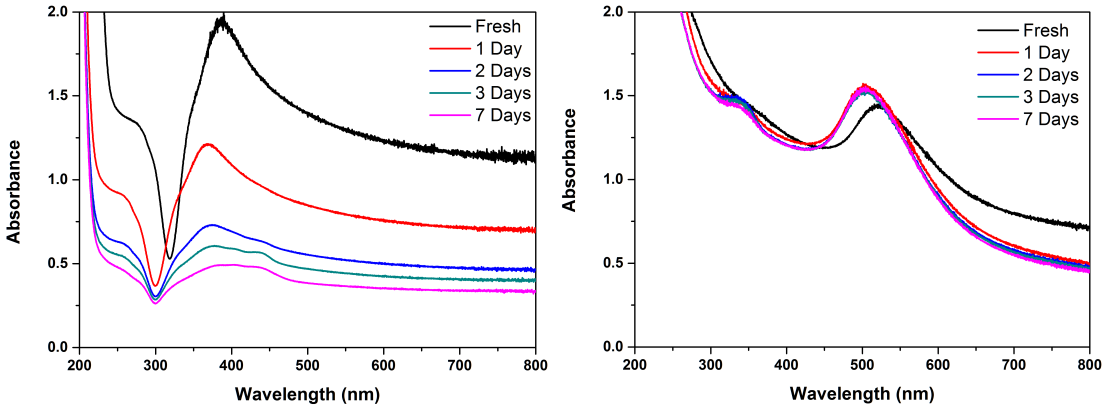

Figure 5.12 UV-Vis spectra for the Ag (5.12a) and Au sols (5.12b) over 7 days.

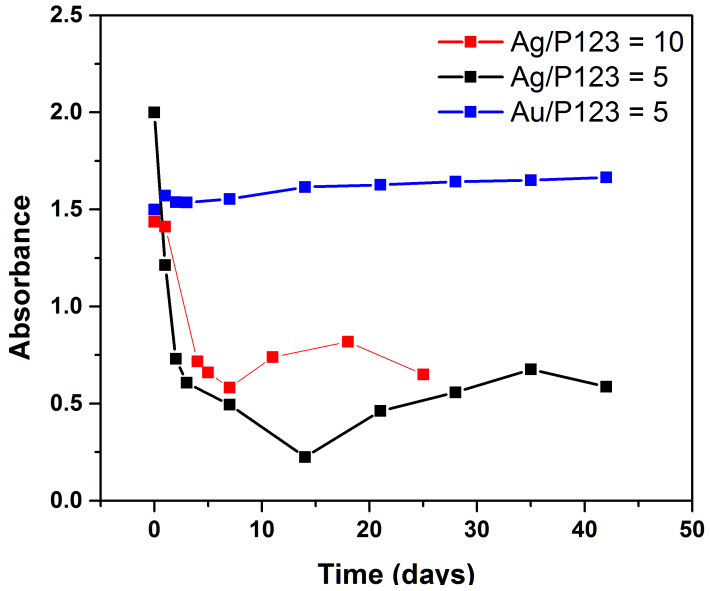

Figure 5.13 Stability of the monometallic colloidal solutions and variations of the SPR absorbance as a function of time.

avoid agglomeration and precipitation phenomena. Despite the increase from a metal/P123 ratio from 5 to 10, the trend observed in both systems shows similar features with a significant drop in the absorbance just after 1 day and with fluctuating values due to the formation large suspended particles and some precipitates which affected the measurements. It is clear then, how when Ag sols are considered, the short lifetime of this precursor, imparts fast synthesis protocols and short storage times, whilst, when Au sols are used, these are stable

for longer time, but variations may occur over long period of times as the colloids tend to thermodynamically conglomerate.

5.4.2 PVA as Stabilizing Agent

The application of PVA as stabilizing agent in the synthesis of Au colloids is well known in the literature [129, 157] and this method was compared against the P123 method. Figure 5.14 shows how with P123 the SPR band is more intense than when PVA is used. For this it has to be considered that the metal/ligand ratio is significantly different (1:5 for P123 and 1:1.2 for PVA) but it is the first indication of how different stabilizing agents impart different absorption properties (547 nm for PVA and 538 nm for P123) due to the different size of the colloidal nanoparticles. The solid UV-Vis analysis is not sufficient to discriminate between

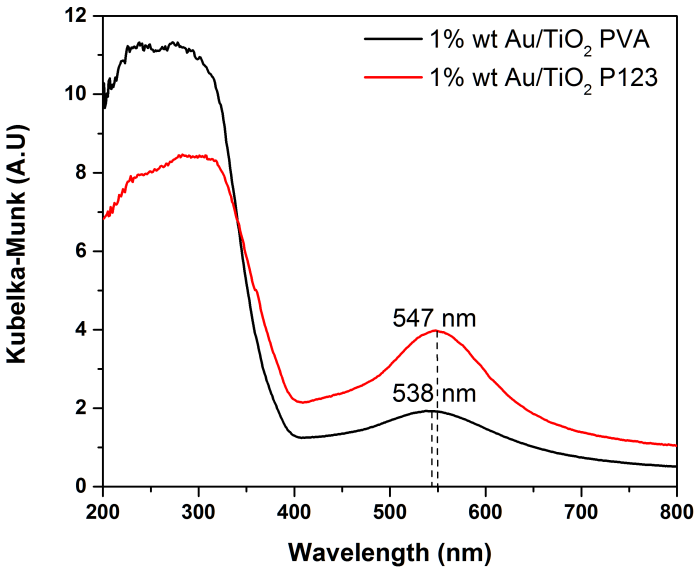

Figure 5.14 Solid UV-Vis spectra of the supported 1%wt Au/TiO_2 catalysts synthesised using PVA (black) and P123 (red) stabilizing agents.

the differences in the particle size distribution values for the metallic nanoparticles and, for this reason, TEM microscopy was used to calculate the PSD for the two catalysts. The shift observed in the solid UV-Vis spectra of the supported catalysts, can be explained by the PSD values as with PVA the average is 4.10 nm whilst with P123 is 6.83 nm (Figure 5.15).

The different molecular weight and chain length of the two stabilizing agents used produces particles with different sizes during the enucleation process. In fact, it is well known that by using different ligands it is possible to tune the shape and size of metal nanoparticles for different applications [168, 119].

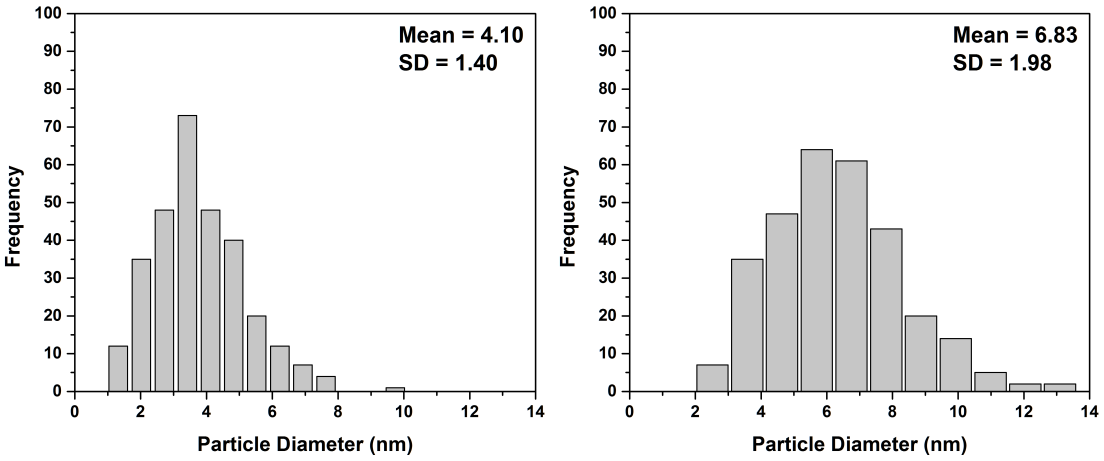

(a) **(b)**

Figure 5.15 PSD values for the Au catalyst synthesised with PVA (5.15a) and P123 (5.15b) obtained for a total particle count of 300.

The considerations on the colloidal stability and on the different synthetic protocols were part of the initial training on the synthesis of different catalysts during my PhD. The possibility of tuning the plasmon resonance band by using P123 as stabilizing agent and the higher catalytic activity of the catalysts synthesised following the paper by Huang et al. [109] made us discard the catalyst prepared with PVA, and that is the main reason why all the catalytic and characterization data shown in this chapter will mention exclusively the P123 bimetallic catalysts.

5.5 Catalyst Characterization and Recycling Studies

5.5.1 TEM Characterization

The determination of the particle size distribution and the analysis of the metallic nanoparticles was possible with the application of high resolution electron transmission microscopy (HRTEM) which allowed for some selected catalysts the determination of the interplanar lattice distance and the identification of the AuAg nanoalloy for the bimetallic nanoparticles with the EDS analysis on some of the samples. In the F.1 Figure F.1 are reported the micrographs for the mono and bimetallic supported nanoparticles whose samples provided at least 300 nanoparticles to obtain a particle size distribution profile (Figure F.2).

The PSD average value is centred around 7 $\pm$ 2 nm for the pure Au catalyst and then the average values varies according to the Ag loading but without following a specific trend. What can be noticed instead from Figure F.2, is that with the increasing Ag content in the bimetallic catalysts the standard deviation becomes broader from 1.55 nm for the equimolar $Au_{0.50}Ag_{0.50}/TiO_2$ to 2.58 nm for the $Au_{0.15}Ag_{0.85}/TiO_2$ along with a decreasing PSD value to smaller nanoparticles, the decrease in the particle size seems to be a feature of the Ag-rich catalysts, as specifically for the $Au_{0.05}Ag_{0.95}/TiO_2$ and the Ag/TiO_2 the PSD curves could not be obtained as the dimensions of the nanoparticles did not offer enough contrast and their measurement was not possible. Figure 5.16 shows a close-up of some AuAg nanoparticles present on the $Au_{0.05}Ag_{0.95}/TiO_2$ catalyst and it can be seen how their sub-nanometric size makes their measurement difficult. The Ag/TiO_2 the STEM analysis reported in Figure 5.17 reveals the presence of large metallic conglomerations in some areas of the fresh catalyst surface. The presence of these large conglomerates did not impair the catalyst activity during the first run, but it is a clear sign that the colloidal synthesis of Ag nanoparticles offers more challenges than the Au-sols as highlighted in the previous section (Section 5.4.1) produces wider particle size distribution values with various morphological features if compared with

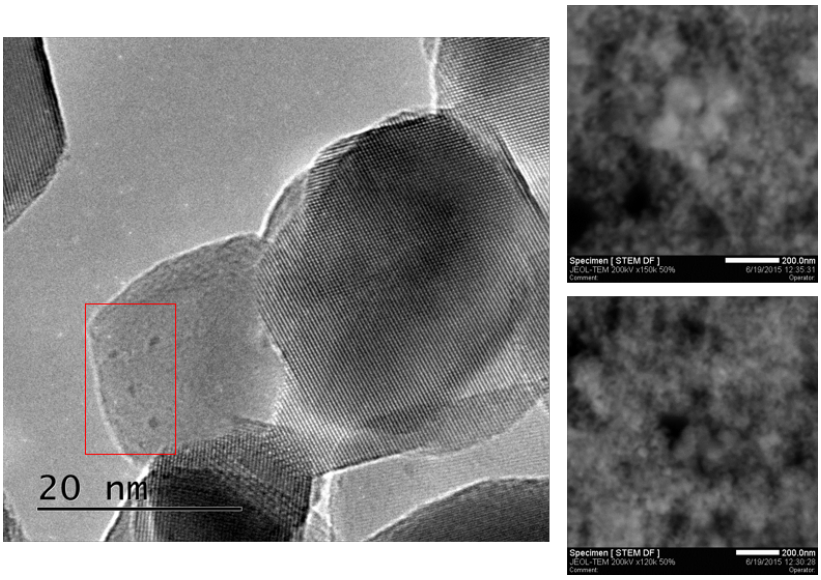

Figure 5.16 Micrograph of the $Au_{0.05}Ag_{0.95}/TiO_2$ bimetallic catalyst and STEM images acquired for the same material.

the Wetness Impregnation approach (Section 2.2) used to synthesise the Ag-based catalysts in Chapter 4. The ICP results assessed the correct metal loading on the catalysts (Table 5.4)

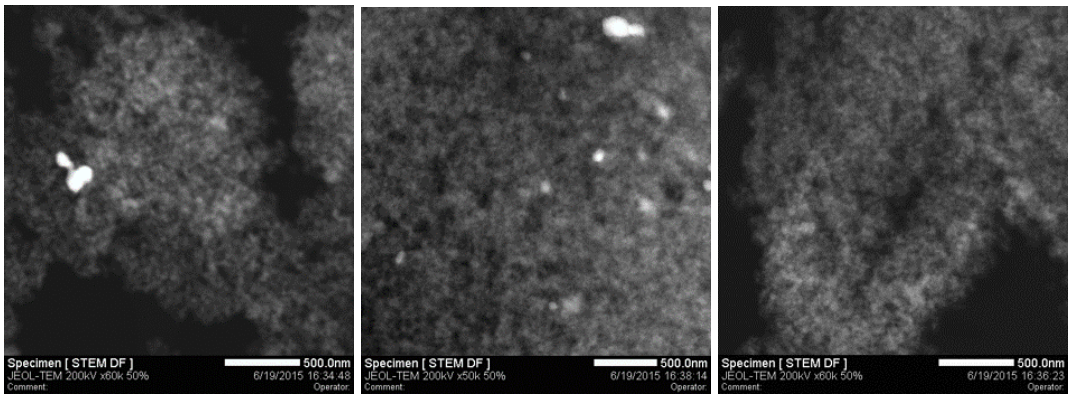

(a) **(b)** **(c)**

Figure 5.17 STEM images of the Ag/TiO_2 catalyst. The bright spots are due to the metallic Ag conglomerates.

STEM images were recorded to rule out the presence of metallic conglomerates on the catalyst surface but these measurements provided negative results to further confirm the small size and high dispersion of the metal on the catalyst surface.

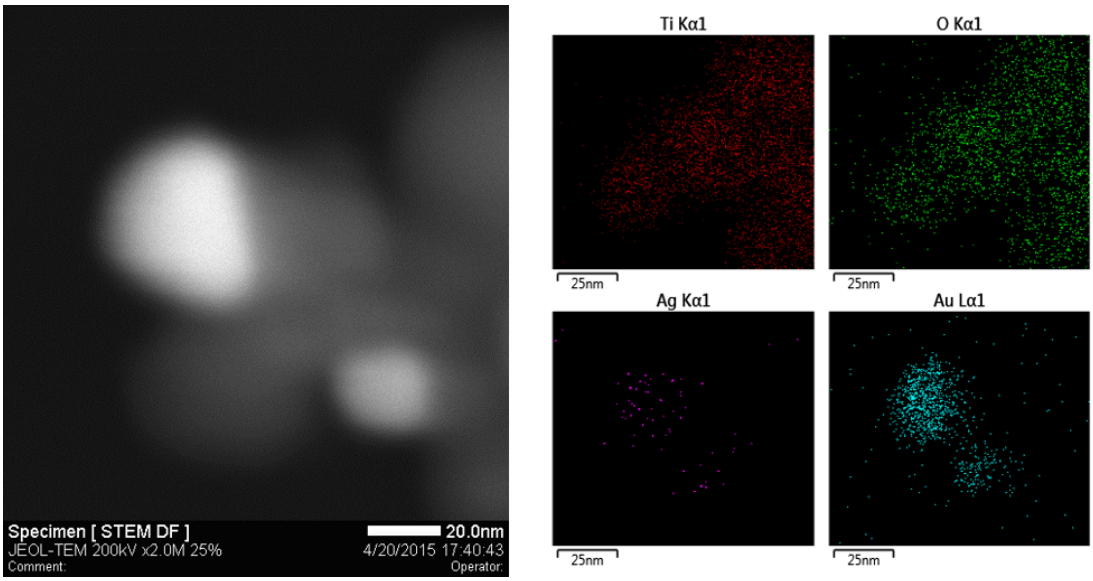

Figure 5.18 STEM analysis of the fresh $Au_{0.85}Ag_{0.15}/TiO_2$ catalyst under visible light. On the right it is possible to see the EDS elemental mapping images for the Au and Ag.

The EDS elemental mapping of the nanoparticle showed in Figure 5.18 shows the coexistence of Au and Ag atoms within the same nanoparticle, and to further confirm the presence of the alloy, 3 different particles were mapped and the by using the EDS elemental weight percentage, it was possible to calculate the molar ratio values as reported in Table 5.5. The theoretical Au/Ag molar ratio for the 1%wt $Au_{0.85}Ag_{0.15}/TiO_2$ should be 5.66 and it can

Table 5.5 Au/Ag molar ratio values calculated from the EDS elemental mapping on three different nanoparticles.

Sample	Metal	Weight (%)	Au/Ag Molar Ratio
1	Au	89.94 (± 3.36)	4.8
	Ag	10.16 (±3.36)	
2	Au	88.05 (±1.52)	4.0
	Ag	11.95(± 1.64)	
3	Au	91.18 (±0.34)	5.6
	Ag	8.82 (± 0.65)	

be seen that the values reported for the nanoparticles analysed are in good agreement with the expected result. Figure 5.18 shows A STEM image with the relavtive EDS elemental mapping of the fresh catalyst $Au_{0.85}Ag_{0.15}/TiO_2$. The presence of the two metals within

the same metal nanoparticle is a good indication of the possible presence of a AuAg alloy but further high-angle annular dark-field imaging (HAADF-STEM) along with diffraction patterns are required to further analyse the crystalline structure of the metal nano-composite.

5.5.2 XPS Characterization

The XPS spectra recorded for the Au-rich and the Ag-rich catalysts are reported in 5.19b and 5.19a respectively. It can be noted that for the Ag/TiO_2 the Ag(3d) peak at 367.7 eV has a much lower intensity than the ones recorded for the bimetallic AuAg catalysts. The apparent lower Ag concentration on the material can be explained with the XPS analysis protocol. In

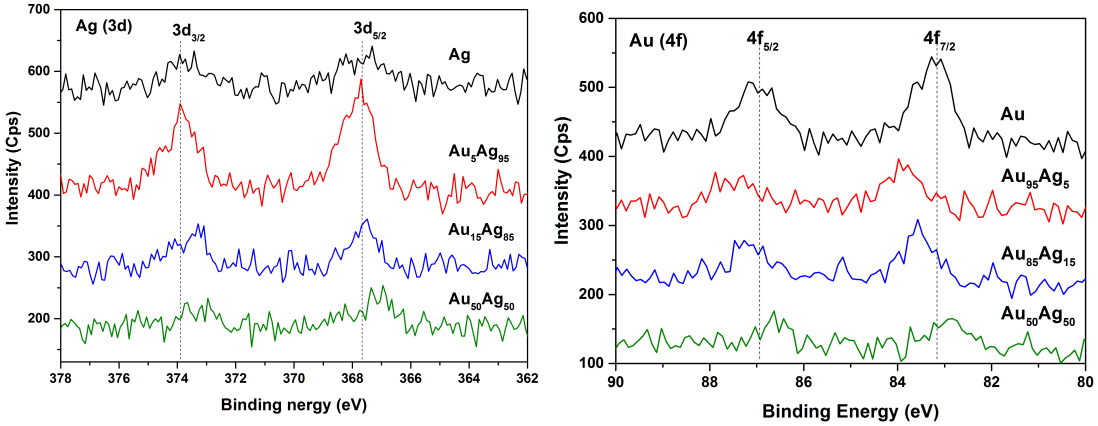

(a) **(b)**

Figure 5.19 XPS detailed regions for the Ag 3d (5.19a) and Au 4f (5.19b) peaks for mono and bimetallic Au_1Ag_{1-x}/TiO_2 catalysts.

fact, this is a surface sensitive technique and it is sensitive to the surface concentration of the desired species. From the STEM images in Figure 5.17, it is clear that the distribution of the Ag nanoparticles on the catalyst surface is far from homogeneous. The three images show areas of the catalyst surface with big metal conglomerates and other areas in which the small size of the metal nanoparticles makes them undetectable.

Due to the be poor distribution on the surface, the signal recorded will be very much area dependent thus making it it impossible to get a representative statistical sample. In

fact, despite the good correlation observed from the ICP values with the theoretical loading, the XPS signal for the pure Ag sample does not seem to match the actual concentration of the metal, as the $Au_{0.05}Ag_{0.95}$ catalyst shows a higher Ag $3d_{5/2}$ signal. Nonetheless, it can be seen how for the relative Au/Ag peak intensity follows the predicted trend expected by varying the metal content and the corresponding molar ratio values. The values reported for the binding energy of the monometallic Au/TiO_2, Ag/TiO_2 and the Au_1Ag_{1-x}/TiO_2 bimetallic catalysts provide information on the oxidation state of each metal and the presence of electron-transfer processes in the bimetallic catalysts. The presence of the metallic Au $4f_{7/2}$ peak around 82.4-83.7 eV, whilst for Ag, the presence of the peak around 367.7 eV confirms the presence of Ag^{+1} is in good agreement with previously reported results. As previously reported for the Ag/TiO_2 catalysts synthesised with the WI method, Ag is easily oxidised upon exposure to air to form Ag_2O, thus explaining the presence of the Ag ionic species on the dried catalyst. Since Ag^+ ions do not present a plasmon band (Figure 5.10a) and would have been washed off during the reflux step to remove the stabilising ligand, their formation has to happen after the synthesis and supporting of the colloids during the storage of the catalyst.

What is interesting to notice is the shift of the Au binding energy with the increased Ag molar ratio as reported by Kennedy et al. [127], in which they attribute the blue-shift of the Au $4f_{7/2}$ to charge transfer from Ag to Au atoms for the AuAg/TiO_2 core-shell bimetallic nanoparticles. Similarly, the Ag $3d_{5/2}$ peak shows a red-shift with the increased Au concentration to further corroborate the hypothesis of a charge transfer mechanism between the two metals even if in this case, the nanoparticles do not present a core-shell structure. If the cellobiose conversion values reported in Figure 5.8 are related to the metal composition of the nanoparticles, the positive effect of this charge-transfer mechanism between the Au and Ag atoms can be appreciated as all the bimetallic catalysts show enhanced catalytic values if compared with the corresponding monometallic ones. As reported by Kennedy et al. [127]

Table 5.6 XPS analysis of the binding energy values for Ag and Au in the mono and bimetallic catalysts

Catalyst	Binding Energy (eV)			
	Au $4f_{7/2}$	**Au $4f_{5/2}$**	**Ag $3d_{5/2}$**	**Ag $3d_{3/2}$**
Au	83.3	87	-	-
$Au_{0.95}Ag_{0.05}$	83.9	87.3	-	-
$Au_{0.85}Ag_{0.15}$	83.5	87.1	-	-
$Au_{0.50}Ag_{0.50}$	82.9	86.6	367.2	373.2
$Au_{0.15}Ag_{0.85}$	-	-	367.6	373.6
$Au_{0.05}Ag_{0.95}$	-	-	367.8	373.9
Ag	-	-	367.7	373.8

this effect might be due to the creation of electron reservoirs in which photo-excited electrons are captured thus increasing their lifetime and enhancing the overall photoactivity of the material. In Figure 5.20 are reported the conversion values for the different light sources and reaction media used in this study. It is clear that under UVA light the presence of the two metals, independently of the molar ratio has a beneficial effect on the cellobiose conversion when the 10 mM stock solution was used. For the 2.8 mM gold showed higher activity than the bimetallic catalysts but the performances of these catalysts were superior to ones of the Ag/TiO_2 under UVA and visible light.

5.5.3 Catalyst Recycling

The recycling studies were performed on the $Au_{0.85}Ag_{0.15}/TiO_2$ catalyst under UVA and visible light using a 10 mM cellobiose solution following the recycling procedure highlighted in Section 2.9.1. The catalyst was reused three times under visible and UVA light respectively and the catalytic results are reported in Figure 5.21. Under both illumination systems, the overall cellobiose conversion decreased with time whilst the mass balance values remain unaltered. For the UVA and visible light runs showed similar trends; additionally, despite the lower cellobiose conversion, the product distribution did not seem to change as, once again, cellobionic acid was the primary reaction product along with the $C_{11}H_{20}O_{11}$ disaccharide. Unlike the previous results obtained in Chapter 4 with the Ag/TiO_2 for the glucose photo-

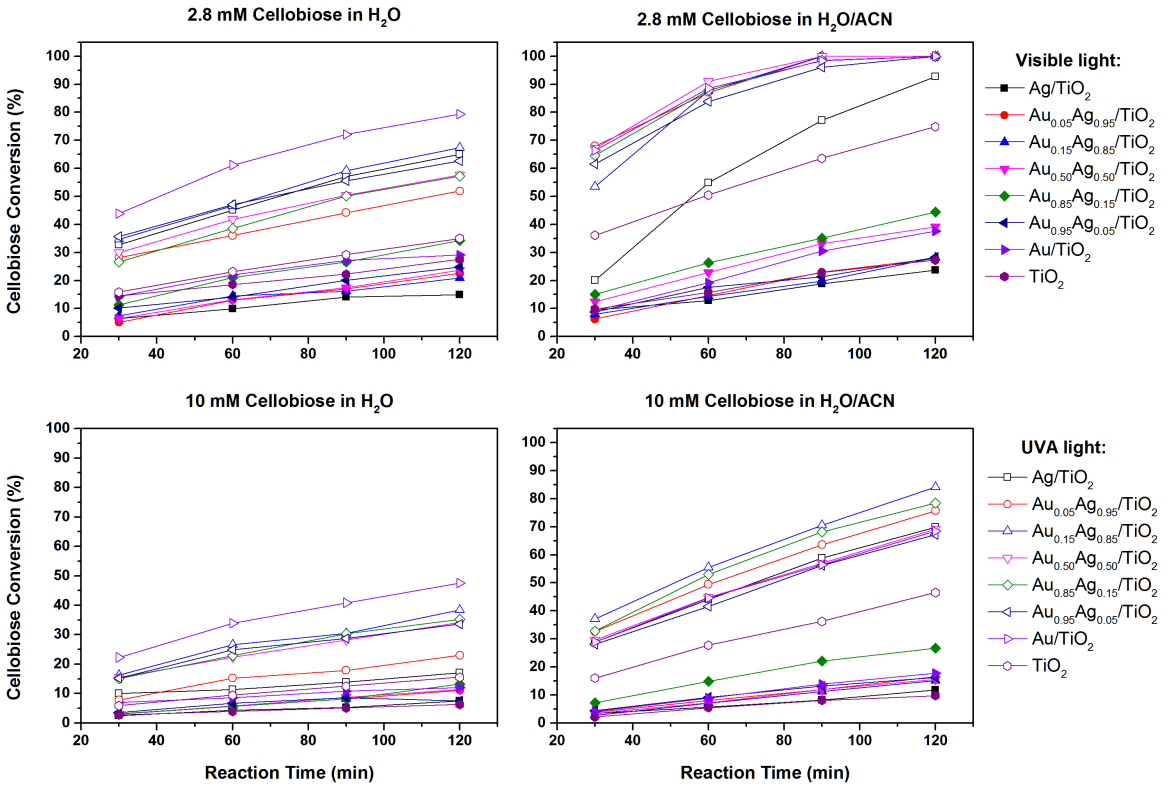

Figure 5.20 Cellobiose conversion for the catalysts considered in this study as a function of the substrate concentration and the reaction medium under UVA irradiation (*e.g.*□) and under visible light (*e.g.*■) as shown by the left hand side legend.

oxidation reaction in which the catalysts showed outstanding stability over three runs with no loss of catalytic activity, in this case the performances of the $Au_{0.85}Ag_{0.15}/TiO_2$ are somewhat disappointing and required further characterization of the recycled material to glean information on the possible causes of the catalyst deactivation. The solid UV-Vis was the first characterization technique used to determine possible shifts or changes of the LSPR resonance. Figure 5.22 shows the spectra for the recycled $Au_{0.85}Ag_{0.15}/TiO_2$ under UVA and visible light. If compared with the fresh absorption profile, the reused catalyst generally displays a decrease in the intensity of the LSPR band with this trend being more pronounced for the visible-light-reused catalysts. For the UVA, after the initial decrease in the first run, the intensity of the band is constant and does not shift any further. This might imply that during the first reaction the nanoparticles on the surface undergo some physical transformation (*eg.*

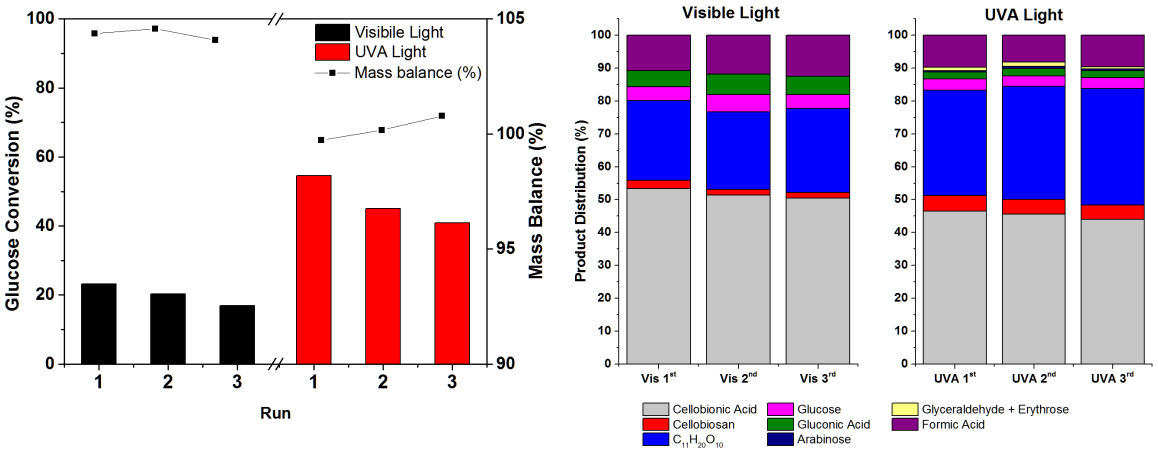

Figure 5.21 Recycling experiments on $Au_{0.85}Ag_{0.15}/TiO_2$: cellobiose conversion and mass balance (left) and Product distribution values for the $Au_{0.85}Ag_{0.15}/TiO_2$ after multiple reuses under visible (left) and UVA light (right).

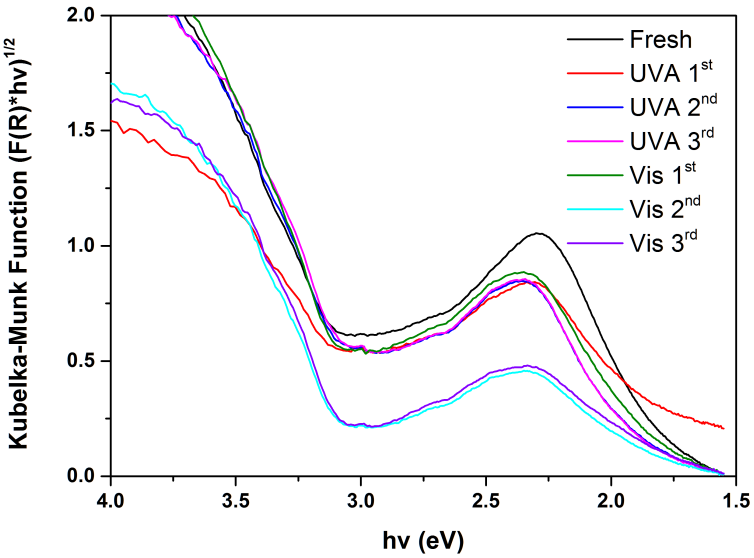

Figure 5.22 UV-Vis spectra of the recycled $Au_{0.85}Ag_{0.15}/TiO_2$ catalyst after multiple reuses under visible and UVA light.

change in oxidation state or morphological changes) and this configuration is preserved in the next cycles, whilst under visible light these morphological changes continue throughout the recycling studies. These morphological changes might follow a similar process to the one observed for the pure Ag/TiO_2 in which, due to the photochromic effect, and the localised super-heating due to the LSPR, the particles are mobile non the surface of the catalyst and

undergo a redistribution-conglomeration process (Section 4.4). In order to fully understand the general trend for these alloyed catalysts, further analysis on the recycled materials are necessary to asses the mobility of the nanoparticles with different Au/Ag ratios. HRTEM was used to obtain information on the morphological changes on the some metal nanoparticle. In Figure 5.23 are reported two high resolution micrographs of a bimetallic nanoparticle for the $Au_{0.85}Ag_{0.15}/TiO_2$ catalyst before and after multiple reuses under UVA light.

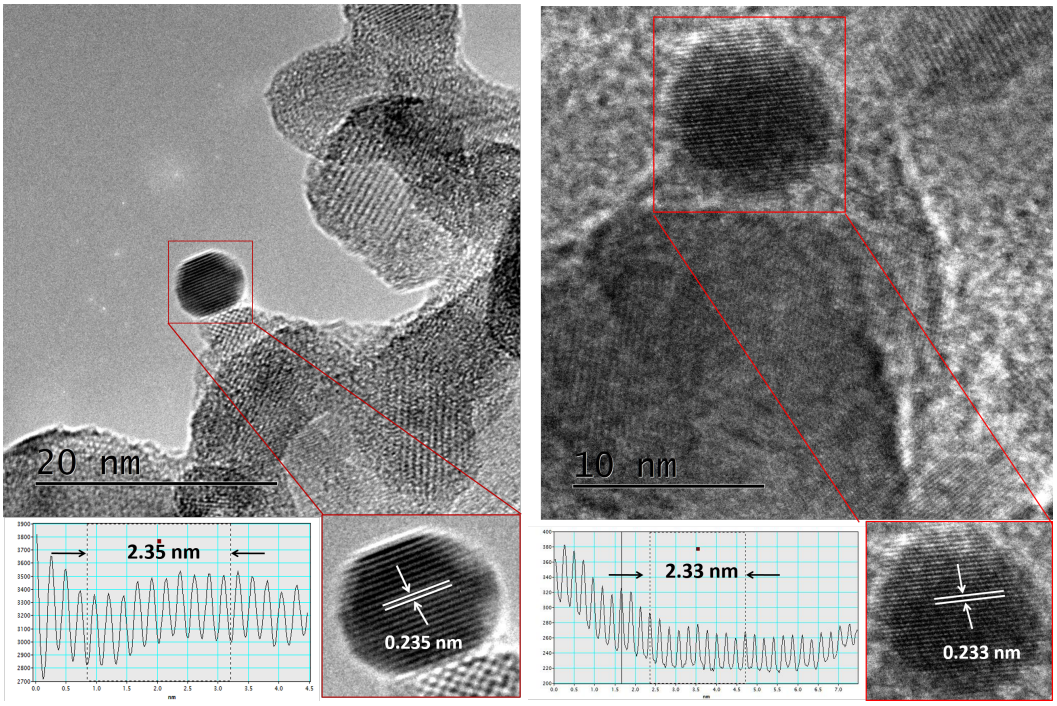

Figure 5.23 HRTEM images of the $Au_{0.85}Ag_{0.15}/TiO_2$ fresh catalyst (5.23a) and after 2 reuses under UVA light (5.23b).

In our case for the $Au_{0.85}Ag_{0.15}$ the 0.235 nm interplanar distance fits well with the Au (111) preferentially exposed plane and Ag (111) planes which measure 0.2355 and 0.2359 nm respectively. After multiple reuses the interplanar distance decreases down to 0.233 nm and this might imply a rearrangement of the two metals in the metal nanoparticles, but will have to be confirmed by further high-resolution EDS analysis and HAADF-STEM characterization.

5.6 Conclusions

In this chapter the effect of the preparation of Au/TiO_2 catalysts was correlated with their catalytic performances with the P123 method showing the highest catalytic activity, and this stabilising ligand was chosen for the preparation of the AuAg colloidal solutions. With the addition of a second metal, it was possible to shift the LSPR frequency of the material to a wide range of wavelength values in order to maximise the response of these materials to visible light irradiation. By alloying the Au and Ag a general increase on the catalytic performances of the bimetallic catalysts was observed under UVA and visible light if compared with the pure monometallic Au and Ag/TiO_2. Additionally, it was found that cellobiose showed similar chemical reactivity to glucose, undergoing the same oxidative pathways (photo-Kolbe, α-scission) mechanisms with the addition of the unprecedented photo-initiated hydrolytic step. For the first time the one-pot oxidative hydrolysis of cellobiose was reported with the identification of a global reaction mechanism using 1 wt% $Au_1Ag_{(1-x)}/TiO_2$ catalysts. The good catalytic activity and recyclability of these materials make them appealing materials for the various photocatalytic applications.

Chapter 6

Conclusions

HAVE YOU SEEN THE LIGHT?

Rev. C. James

YES! YES! JESUS H. TAP-DANCING CHRIST... I HAVE SEEN THE LIGHT!

J. Blues

The final aim of this work was to shed some light on the possibility of using the power of the sun as a viable driving force for green and sustainable chemical reactions and to provide the fundamental experimental tools for the understanding and analysis of the photo-reactivity of simple carbohydrates in order to provide the basis for the research on cellulosic materials. The use of photocatalysis in the literature has been associated with non selective reactions for the degradation of pollutants in water streams, the production of H_2 from various organics or from water-splitting reactions. Only recently, has photocatalysis started to be exploited to run selective oxidation reactions with promising results. Due to the necessity of exploiting biomass as a raw material and the need to find greener processes, in recent years a few studies have been published on the application of light-driven reactions to convert cellulose and other simple carbohydrates to produce H_2. The presence of partial oxidation products in the liquid

phase has always been neglected as most of the research was focused on the production of hydrogen as the next green fuel.

There was then a need to try and bridge the production of these gaseous products with other useful bio-derived molecules given the amount of chemical functionalities present on these feedstocks. The approach used in this study involved some detailed studies on the photo-chemical properties of TiO_2, a well known photoactive material. With the systematic analysis of several key parameters such as the catalyst to substrate ratio and irradiation source it was possible to discover that H_2 and CO_2 only accounted for a fraction of the reaction products. Clearly, the total mineralization pathway had to be suppressed somehow in favour of other reaction products given the high glucose conversion values registered. The catalyst/substrate ratio played a fundamental role in driving the reaction down different reaction pathways. In fact, unlike previous results, in this study the substrate concentration was several orders of magnitude greater than the values present in the literature, which as a consequence, resulted in the complete suppression of the mineralization pathway as the main reaction scheme. Another striking result observed was the activity of TiO_2 under visible light conditions. In fact, at 420 nm the incident photons do not have enough energy to promote electrons from the valence band to the TiO_2 conduction band, and the results published by Kim et al. [130] proved the existence of a ligand to metal charge transfer complex between glucose and the surface of the semiconductor. This type of complex was investigated for the first time, as before the interaction between substrate-semiconductor was investigated only for the application of dyes as sensitisers to extend the TiO_2 activity under visible light. The substantial difference between the dye-sensitisation approach and the LMCT is that dyes usually possess chromophore groups due to the presence of substituted aromatics rings and the π electrons on these rings are responsible for the charge transfer mechanism.

The possibility of having charge transfer complexes with molecules that do not absorb visible light irradiation and do not have unsaturated bonds, testifies the importance of the

adsorption-desorption properties and the specific interactions between hydroxylated surfaces and the substrate and opens up the possibility of dual-exploitation of specific substrates both as enhancers of the catalytic activity of the semiconductor and as reactants. The glucose double role during its photocatalytic oxidation made it difficult to understand the kinetics of the reaction and understand the global reaction pathway. In fact, only a few works are available on the upgrading of glucose to valuable chemicals using a photocatalytic approach and some the results reported in the literature are sometimes difficult to interpret due to the different reaction set-ups and analytical methods used.

For this reason the identification of the reaction schemes involved in the glucose reactivity has been the most important part of this work. The puzzle could be solved combining different reaction mechanisms reported in the literature for Fenton systems by Stapley and BeMiller [222]. Their work focused on the description of the oxidative decarboxylation of sugars with the use of Fe(III) and H_2O_2 for the production of aldoses. This reaction mechasim was then translated to a photo-Fenton system using the Ti(IV) metallic centre on the semiconductor surface as part of the redox process. The application of this approach allowed for the identification and quantification of all the reaction products in this work and to rule out the presence of arabitol as reported by Colmenares et al. [61] with the application of the powerful HPLC-QTOF mass spectrometry technique. Nonetheless, the photo-Kolbe mechanism alone could not explain the presence of formic acid in solution and it was evident that the photocatalytic oxidation of glucose could follow an additional reaction pathway. Thanks to the recent results published by Chong et al. [53],α-scission reaction mechanism with the formation of formic acid and H_2 from glucose along with other partial oxidation products was identified and allowed for the complete identification of the reaction species if combined with the photo-Kolbe mechanism.

From this it is clear from the literature that the amount of information available on the specific reactivity of bio-derived molecules is limited and fragmented, and the general

understanding of these mechanisms is sometimes misled by the specific experimental set-ups adopted by each research group and the complex reactivity of these systems. For these reasons, this PhD work focused on the utilization of a well known catalyst such as TiO_2 and on how to extend and improve its catalytic activity. The use of Au and Ag nanoparticles to extend the activity of semiconductor to the visible light part of the solar spectrum has been widely reported in water splitting reactions and pollutant degradations. The use of Pd, Pt, and Rh was reported by Chong et al. [53] along with Cr, Cu, and Ni by Colmenares et al. [61] but the effect of the plasmon resonance was never investigated as these metals were added as co-catalysts.

The addition of different Ag wt% metal loadings proved to be an effective way of improving the catalytic performances of the support, and the addition of 0.5 wt% Ag showed better conversion values than a 1 wt% Au/TiO_2 used as a comparison. Initially, it was decided to use Ag as its cost is much cheaper than for the Au precursor thus making it more interesting for a possible commercial application. The high activity and no leaching of the metal over multiple runs with no significant loss of activity was an exciting result, despite the morphological changes of the metal nanoparticles on the catalyst surface with the formation of large metal conglomerates. As the main aim of photocatalytic reactions is to exploit the widest range of visible light wavelength values, the use of only one metal with a very narrow plasmon band resonance in the region of 380-410 nm is not ideal as it cannot be excited by photons at energy levels that do not match this interval. Therefore, the coupling of Au and Ag with the formation of nanoalloys was decided could be a promising technology as it could allow to tailor the response of this material from 380-560 nm which are the LSPR frequency values of Ag and Au respectively, thus covering a large part of the visible light spectrum.

Unlike for the Ag/TiO_2 catalysts synthesised with the WI method, the delicate tailoring of the visible light properties requires a more controlled synthetic approach and the colloidal preparation of nanoalloys has been reported for various metals with reproducible protocols

and consistent results. The protocol used allowed a strict and precise control over the composition of the catalysts as confirmed by the ICP and EDS analysis. Most importantly, during the synthesis of the sols, the phase separation of pure Ag and Au nanoparticles was ruled out with the UV-Vis analysis as only one sharp peak was noticeable as a clear indication of the formation of the nanoalloy. Additionally, by plotting the maximum of absorption as a function of the Ag molar ratio in the alloy a good linear correlation between the two parameters could be found. This could allow a further engineering of the colloidal preparation which, with the addition of a third metal, could extend the properties of these nanoalloys even further.

The control over the synthetic protocol was a promising start, but it was not certain if the alloys would have a positive effect due to the synergy of the two metals on the conversion of a bigger and more complex substrate such as cellobiose. Indeed, when the catalysts were tested under UVA and visible light, in both conditions the synergy of the presence of Au and Ag metal had a positive effect on the catalytic activity with the supported alloyed nanoparticles being more active than the corresponding monometallic Au/TiO_2 and Ag/TiO_2. $Au_{0.85}Ag_{0.15}/TiO_2$ proved to be the best performing alloyed catalyst and displayed good activity with only 5% conversion decrease over three runs. The product distribution values remained within experimental error with no substantial differences between each test. In addition to the unprecedented effect of the Au/Ag alloying in selective photo-oxidation reactions, cellobiose displayed similar reactivity to glucose. Cellobiose hydrolysis has been investigated with mineral acids (H_2SO_4, HCl, H_3PO_4) but the use of concentrated acid solutions poses problems for practical applications due to the corrosion of the equipment and reactors. Therefore, research moved on to try and functionalise materials with acid groups, and it was found that by using mesoporous silica materials (SBA-15) with the addition of acid groups good glucose yields could be obtained but careful tuning of the reaction conditions was necessary to avoid the formation of humins, char, and other dehydration products. At the

beginning of my PhD I investigated the possibility of embedding different acid functionalities to mesoporous materials, but the reaction conditions required high temperature (T>150°C) and most of the time the hydrothermal conditions required produced chars and humins as reported in Table 6.1 with the commercial Amberlyst catalysts. The testing of the catalyst

Table 6.1 Activity of some selected materials for the hydrolysis of cellobiose under hydrothermal conditions with a 1:1 catalyst to substrate ratio.

Catalyst	Temperature (°C)	Cellobiose Conversion (%)	HMF Yield (%)	Glucose Yield (%)
BLANK		33.4	0.3	0.0
AMB15 DRY		36.9	0.2	3.4
AMB15 WET		34.2	0.2	1.7
AMB A21	150	36.4	0.2	0.7
Al-MCM41		32.9	0.3	1.3
BLANK		55.9	1.72	16.42
AMB15 DRY		94.2	1.1	54.1
AMB15 WET		90.77	1.3	49.4
AMB A21	190	51.2	1.76	6.7
Al-MCM41		60.2	2.1	21.6

Reaction conditions: 300 mg of cellobiose, 300 mg of catalyst, 2 hours.

performances under hydrothermal conditions showed that under autogenous pressure and at slightly higher temperatures (150 and 190°C) the catalytic activity increases significantly. For the interpretation of these results it is important to keep in mind that the acidity of water increases with temperature and in the range from 150°C to 350°C under autogenous pressure, has a K_w =11.2 instead of the K_w=14 at 25°C, and for this reason, water turns out to be a powerful reaction partner that can act as a base or acid catalyst. The changing in the behaviour of water as a solvent, explains why the cellobiose without catalyst in MilliQ water for 2 hours at 150°C shows a conversion of 33.4% with a production of HMF of 0.3%, and these values increase at 190°C for which a cellobiose conversion of 55.9% with an HMF yield of 1.7% was obtained. The latter result shows the dramatic increment of the water acidity at 190°C which causes a six-fold HMF yield increase. The results obtained at 150°C

show that among the catalyst tested Amberlyst 15 DRY shows a cellobiose conversion value of 94.2% and the highest yield of glucose (54.1%) with a selectivity towards the production of HMF of 2.4%; similar values are obtained with the Amberlyst 15 WET with a conversion of cellobiose of 90.7%, a yield of glucose of almost 50%, and with the HMF selectivity value of 2.7%. Unlike the results obtained under the reflux conditions, the stability and the reactivity of the Amberlyst 15 DRY and WET is similar, but if the water is taken into account, these values decrease sensibly, and the net conversion of cellobiose due to the presence of the solid acid catalyst is around 35%. It is then clear how the Al-MCM41 is not active towards the hydrolysis of cellobiose nor towards the dehydration of glucose into HMF, because the product distribution is similar to the one obtained with the blank reaction under the same experimental conditions. The results obtained at a higher temperature (190°C) do not show a differentiation in the product distribution or in the catalytic activities of the materials considered. It can be seen how the conversion values are higher than the ones obtained at 150°C, but this increment is mainly due to the increased activity of water rather than in an increased activity of the catalysts, which is present but at a lower extent. Even the reaction in which the Amberlyst A21 and the Amberlyst 15 DRY were combined in equal quantities did not show any synergistic effect of the two catalysts in the production of HMF. Theoretically, the Amberlyst 15 DRY would break down the glycosidic bond and produce glucose, which should have been isomerised into fructose by the Amberlyst A21. This reaction had selectivity towards the production of HMF of 5.2% with a glucose yield of 18.8% on a conversion of cellobiose of 61.5%. These results show how glucose in the experimental condition used behaves as an intermediate, and that water itself works as an efficient catalyst for the hydrolysis of cellobiose.

A different approach was used to try and improve the hydrolytic rate by using $ZnCl_2$ concentrated solutions, as it is known that molten salts solutions are capable of penetrating cellulosic fibres and loosing the H-bond network as shown in Figure 6.1 [9]. Several attempts

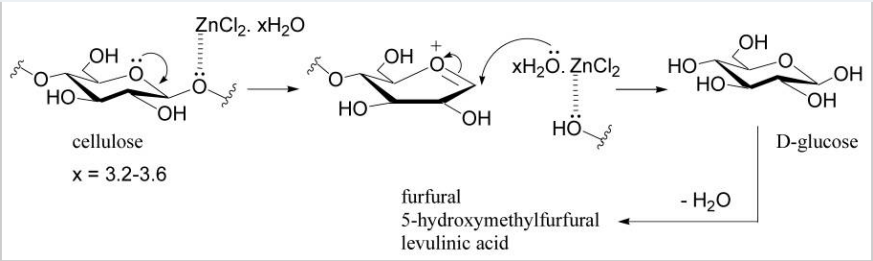

Figure 6.1 Formation of Zn-Cellulose complex in molten salts hydrates. Taken from Amarasekara and Ebede [9].

were made with $ZnCl_2$ concentrated solutions up to 66 wt% but the results were really disappointing as the presence of the metal ions with the subsequent formation of HCl under hydrothermal conditions increased the humins formation rate as it can be seen in Figure 6.2. Additionally, the high concentration of Cl^- ions caused corrosion problems on the high pressure equipment and the use of these molten salts was not pursued any further as the presence of Zn^{2+} causes problems during the HPLC analysis as these ions strongly bind to the stationary phase causing irreversible changes to the polymer particles in the chromatographic column. From these preliminary studies the hydrolysis of a simple disaccharide appears to

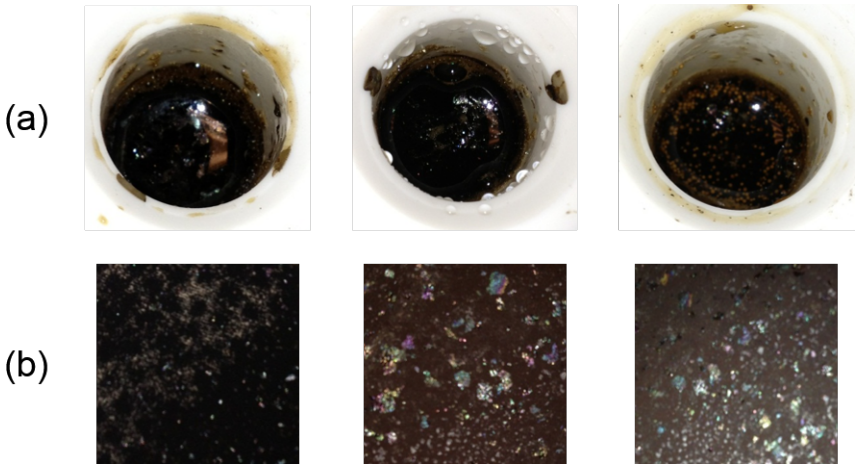

Figure 6.2 (a) Filtrated samples obtained from the hydrolysis of cellobiose using $ZnCl_2$ under hydrothermal conditions. (b) Aspect of the reaction mixtures after 2 hours under hydrothermal conditions with $ZnCl_2$ 66% w/w.

be challenging as it requires harsh reaction conditions and the presence of mineral acids or high concentration of metal salts which are not green reactants for sustainable chemistry.

The photocatalytic approach used in this study required very mild reaction conditions (room temperature, atmospheric pressure), if compared with the "conventional" chemical approach. Recently, Amaniampong et al. [7] showed for the first time the one pot hydrolysis of cellobiose with TiO_2-supported metal nanoparticles (Au, Ag, Pd) and this work offers the perfect benchmark to assess if photocatalysis can be exploited as a possible alternative to substitute conventional processes with much energy-demanding ones. If one takes a look at the global reaction mechanism (Scheme 6.1) the chemistry of this photo-initiated reaction might look non-selective and rather complex. If compared with the reaction mechanism

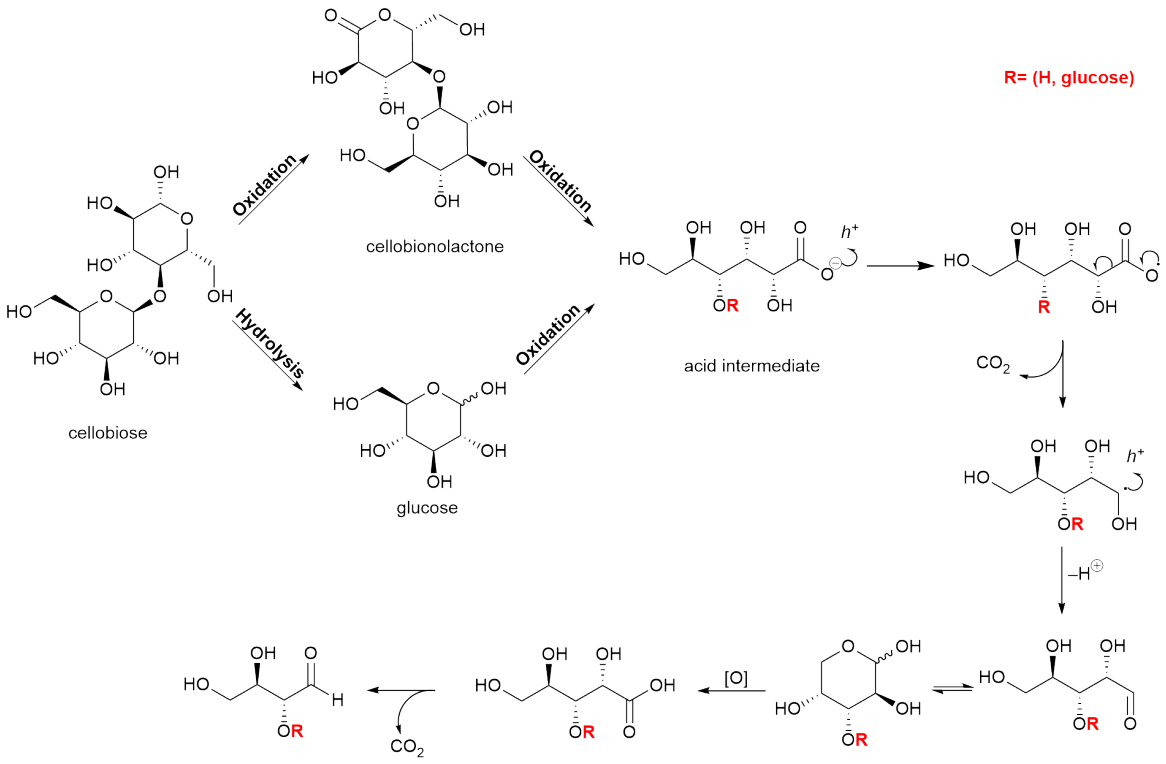

Scheme 6.1 Combined reaction mechanism for the cellobiose photo-oxidation and the photo-initiated hydrolysis of the β-1,4 glycosidic bond.

described by Amaniampong et al. [7] and reported in Scheme 6.2, it is obvious that the chemistry involved in the second case is even more complicated that the one observed in this work. In fact, the global reaction scheme identified for the cellobiose photocatalytic oxidation is made of a series of subsequent reactions which following the α-scission (I) or

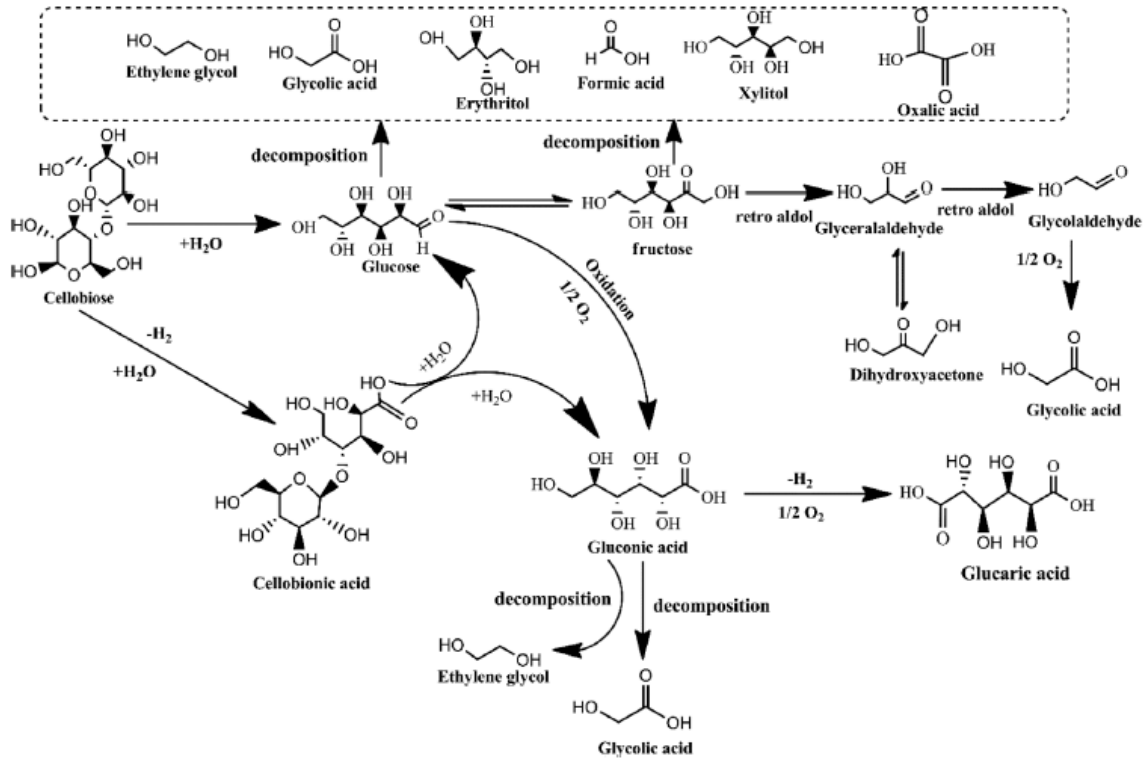

Scheme 6.2 Suggested reaction pathway of the cellobiose conversion to gluconic acid and other derivatives. Taken from Amaniampong et al. [7].

the photo-Kolbe (II) mechanism can either eliminate HCOOH and H_2 (I) or CO_2 and H_2 (II) but with the formation of the same reaction products. The fundamental difference between the two reaction mechanism is that the photo-Kolbe pathway requires the formation of the carboxylic acid intermediate whilst the α-scission directly eliminates the products without the acid intermediate.

On the other hand, the reaction pathway illustrated in Scheme 6.2 shows several different reactions with the result of having a complex reaction mixture with several molecules formed from the non selective glucose decomposition rather than from a systematic reactivity as registered for the photocatalytic approach. Additionally, the 100% cellobiose conversion was achieved using a 3 mM cellobiose solution and 100 mg of catalyst in 12 hours, whilst in this work, the cellobiose concentration was 10 mM and only 14 mg of catalyst and only 2 hours of reaction time.

If the catalytic results obtained with the 2.8 mM cellobiose stock solution, it is evident that photocatalysis is a much more efficient way of converting the same substrate in a sixth of the time at room temperature and atmospheric conditions instead of heating the reaction mixture up to 145°C and adding 10 bar of O_2 pressure. This work is meant to be a first

Table 6.2 Cellobiose conversion catalytic data obtained with our photochemical approach compared with [7] obtained with different bimetallic catalysts.

	Reaction Time (h)	Cellobiose Conversion (%)	Xylitol (%)	Glucose (%)	Gluconic Acid (%)	Ethylene Glycol (%)	Glycolic Acid (%)	Glyceraldehyde (%)	Formic acid Acid (%)	Sorbitol (%)	Fructose (%)	Cellobionic Acid (%)
$Au_{0.85}Ag_{0.15}$ [a]	2	100	0	5.7	0	0	0	4.1	28.1	0	0	21.3
Pd-Au [b]	11	97	2.3	-	5.1	21.3	34.3	2.5	11.7	9.9	0	0
Co-Au [b]	12	97.2	-	-	24.4	7.6	28.6	26	-	-	6.5	0

[a] Reaction conditions: cellobiose 10 mmol, catalyst 14 mg, H_2)/MeCN 14 ml, pressure: ambient, temperature: 25°C, stirring speed 1300 rpm.
[b] Reaction conditions: cellobiose: 0.6 mmol, catalyst 100mg, H_2O: 20 mL, pressure (O_2): 1 MPa, temperature: 145°C, stirring speed: 1200 rpm.

step towards the demonstration that by tuning the reaction conditions it is indeed possible to obtain light-driven processes that are even more efficient than the conventional ones, and the data reported in the previous chapters and highlighted in Table 6.2 clearly show that this is a concrete possibility for future developments.

6.1 Future Work

6.1.1 High Throughput Testing

The main drawback of using Xenon lamps to test the activity of different materials is that due to the nature of the set-up, only one sample can be exposed to the light. This is an evident bottle neck which limits the testing capability. One attempt made during this PhD to speed up the testing step, was to create a carousel set-up which would allow for the simultaneous testing of up to 6 different catalysts (Figure 6.3). The rotation speed of the carousel was controlled by a overhead stirrer motor being careful not to impart too much centrifugal force which would deposit the catalyst on the bottom of the vial. Inside every reaction vessel small magnet bars allowed the stirring of the reaction mixture and counteract the centrifugal force imparted by the rotation of the carousel. With the revolution of disc, the illumination of

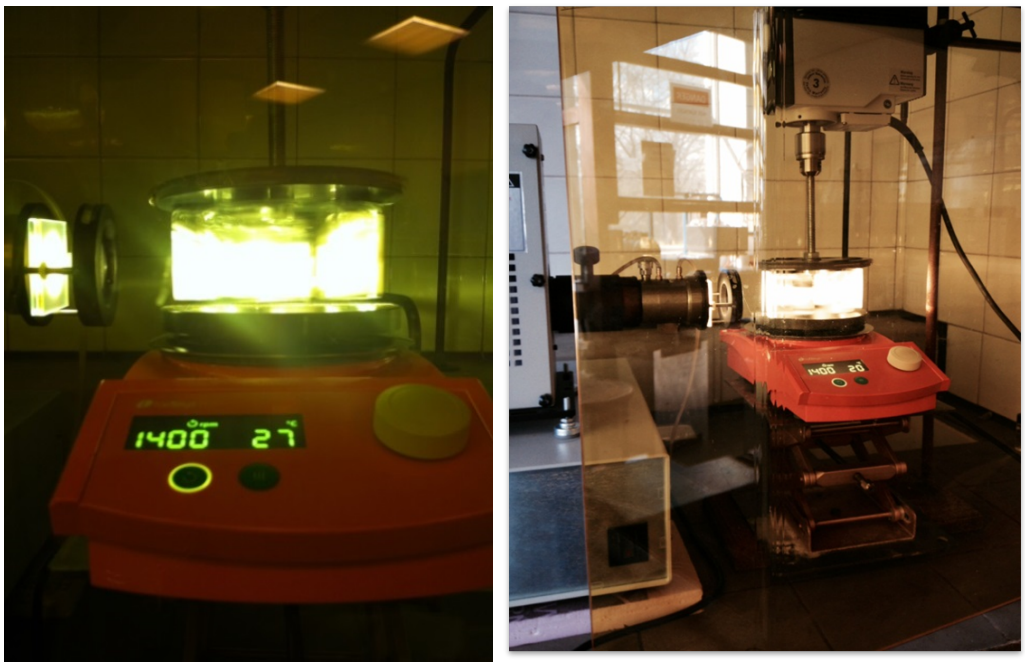

(a) **(b)**

Figure 6.3 High throughput system created to test up to 6 catalysts at once.

each vial is not constant and therefore, the total illumination time has to be increased to compensate the "on-off" nature of the set-up. This system was advantageous from the high throughput perspective as 6 samples could be pre-screened but 24 hours of illumination time were required to obtain comparable results with a single 2 hours run. A different illumination set up is then required to analyse multiple samples at once, maybe with the illumination source on the top of the photoreactor to grant an even illumination area over multiple stirred samples.

6.1.2 Use of Alternative Metals

CuAg Catalysts

Gold and silver are the two precious metals with the most intense LSPR band, but Al and Cu also present much much weaker visible light excitation, but they might be used in visible light photocatalysis as co-catalysts. Figure 6.5a clearly shows the lower LSPR intensity for

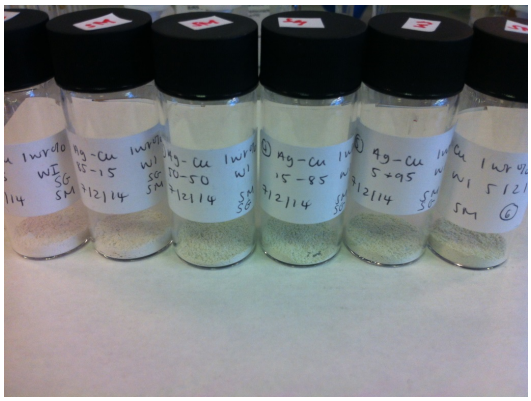

Figure 6.4 WI Synthesised catalysts -1 wt% $Cu_1Ag_{(1-x)}/TiO_2$ (High Ag loading (left) to high Cu loading (right))

the 1 wt% $Cu_1Ag_{(1-x)}/TiO_2$ catalysts synthesised with a WI protocol, and Figure 6.5b clearly shows that the level of control over the tuning of the LSPR band as a function of the second metal added is not as accurate as for the colloidal preparation. Preliminary results obtained

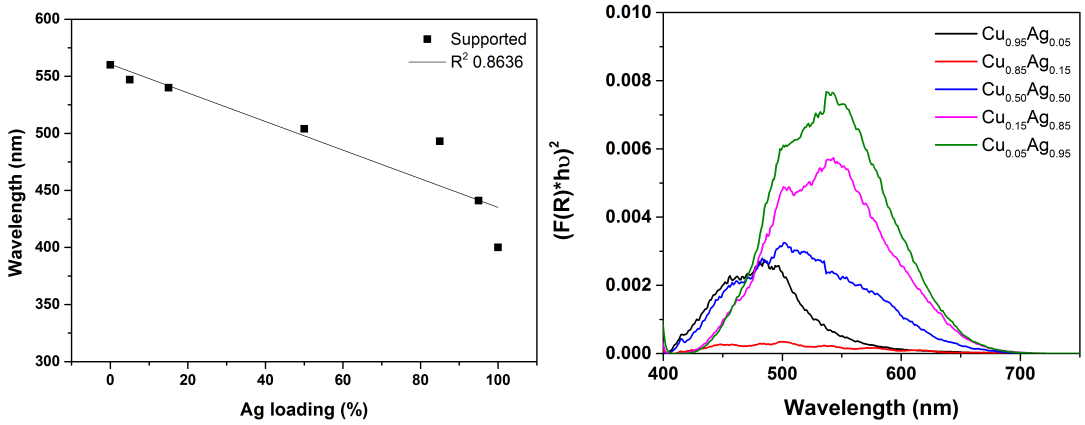

Figure 6.5 6.5a solid UV-Vis spectra of the supported bimetallic $CuAg/TiO_2$ catalysts;
6.5b Maximum of absorption (nm) for the unsupported colloidal (■) as a function of the Ag molar loading in the nanoalloy.

by testing these materials on the carousel set-up showed that the Ag-rich catalysts are the ones with the highest catalytic activity, thus confirming the importance of the intensity of the LSPR in harvesting visible light and initiating the photocatalytic process.

CuAu Catalysts

Alloys such as Au-Cu and Au-Ag have attracted attention because they exploit a metal which is cheaper than Au. Sugano et al. [224] suggested that when Au NPs are co-immobilized onto the surface of TiO_2 with a metal co-catalyst (*e.g.* Cu), gold acts as an electron donor for the second metal through the TiO_2 electron states, ensuring the other metal is not in an oxidised state. Figure 6.7 shows that the two Cu-rich sets of catalysts did not perform well

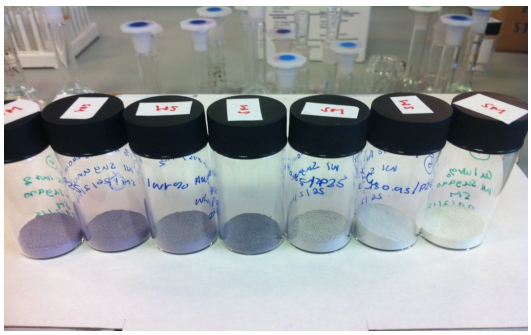

Figure 6.6 1 wt% $Cu_1Au_{(1-x)}/TiO_2$ (High Au loading (left) to high Cu loading (right))

under the same experimental conditions. In fact, the addition of Cu seems to worsen the catalytic performances of the material due to the weak LSPR band of this transition metal. With these preliminary results, the presence of AuAg nanoalloys seems to be necessary for efficient photocatalytic processes. Clearly, much work will have to be done to further extend the activity of these materials at even higher wavelength values and this will be possible by altering the shape and the nanostructures of these materials. In Figure 6.8 are reported a few examples of AuAg nanocubes and nanocages with the corresponding UV-Vis spectra. These structures cover almost entirely the visible range, but their supporting on semiconductor surfaces and their testing in photochemical application has not been exploited yet.

6.1.3 Cellulose

Glucose and cellobiose were used as probe molecules to assess their chemical activity and obtain fundamental understanding on the reaction mechanisms and the product distribution.

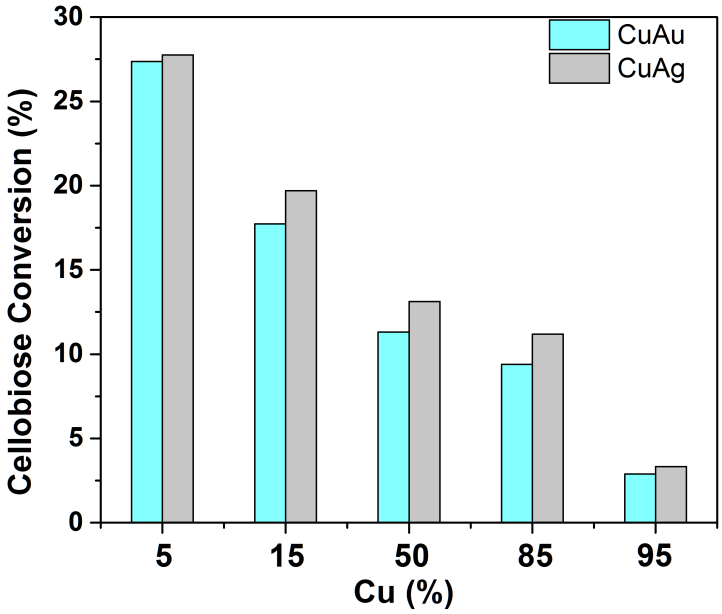

Figure 6.7 Cellobiose conversion values reported with the carousel set-up for the CuAg and CuAu set of catalysts.

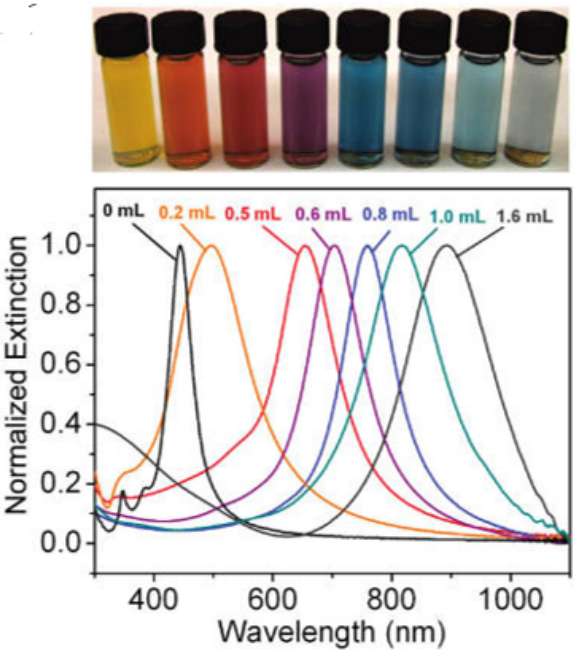

Figure 6.8 Au nanoboxes and nanocages prepared by reacting Ag nanocubes with different volumes of a $HAuCl_4$ solution and corresponding UV-Vis spectra. Taken from Skrabalak et al. [218].

As stated in the introduction the ultimate aim is to use cellulose as starting material and try to obtain similar product distributions. The main challenge in using cellulose as a feedstock is the complex molecular structure: the extensive H-bond network between the different glucose chains make this material almost insoluble and difficult to react [88, 9, 96, 32, 133, 262]. Only one attempt by Fan et al. [86] has been made to try and convert cellulose under UV light using a 66 wt% $ZnCl_2$ solution and selectivity towards HMF were reported following the reaction scheme (Figure 1.7). In this work an attempt was made by using similar reaction parameters than the ones used for the glucose and cellobiose testing but using α-cellulose as substrate.

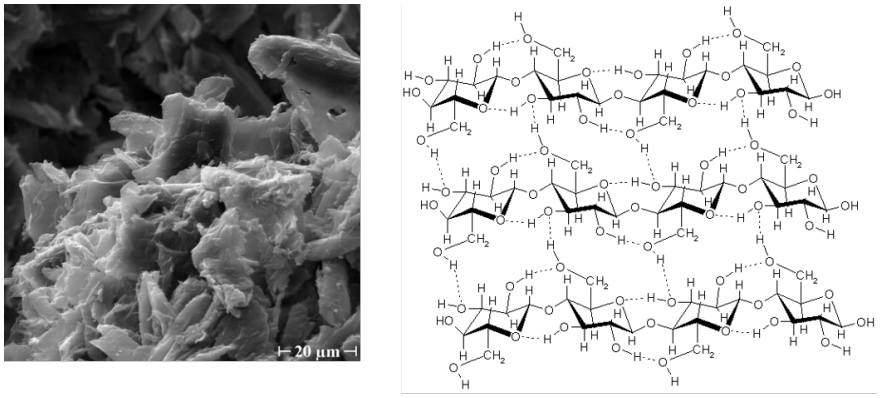

Figure 6.9 SEM picture of the α-cellulose used in this study (a) and its molecular structure with the H-bond network in evidence (b)

Unfortunately, even after 24 hours of reaction time the reaction mixture did not show any traces of the products previously identified. This recalcitrance towards any chemical reactivity was to be expected and moving from cellobiose directly to cellulose was probably too optimistic. The importance of the interactions between the substrate and the reaction medium, the accessibility of the β-1,4 glycosidic bond to the reactive species in solution are key parameters to take into account when dealing with these macromolecules. In future studies, glucose oligomers might be used at increasing level of complexity in order to

assess until which point photocatalytic reactions can successfully convert these substrate into commodity chemicals.

The aim is to integrate photocatalytic reactions with the regular processing of pulp or biomass and to provide an alternative route for the valorisation of this feedstock. If pretreatments are necessary and cannot be substitute with alternative ways, it is important to try and optimise the downstream processes, and if these can provide well characterized reaction mixtures, the similarity with the oil fractioning and distillation workflows are evident, as in this case research will be focused on the separation of the different organic fractions obtained via conventional methods, and photochemical ones.

Moreover, this study focused on the feasibility of using a photocatalytic approach to convert bio-derived molecules without focusing on the specific production of a target molecule. For this reason, more work will have to be done in order to tune the selectivity towards molecules of interest (cellobionic acid, gluconic acid) which already have applications in the chemical industry. This will be possible by changing the catalyst composition, or coupling the photocatalytic oxidation with other reactions and use the reaction mixture as a pretreated feedstock for further chemical transformation (etherification, esterifications).

References

[1] Abbadi, A. and van Bekkum, H. (1995). Effect of pH in the Pt-catalyzed oxidation of d-glucose to d-gluconic acid. *Journal of Molecular Catalysis A: Chemical*, 97(2):111 – 118.

[2] Acton, Q. (2012). *Carboxylic Acids Advances in Research and Application: 2012 Edition*. ScholarlyEditions.

[3] Adleman, J. R., Boyd, D. A., Goodwin, D. G., and Psaltis, D. (2009). Heterogenous catalysis mediated by plasmon heating. *Nano Letters*, 9(12):4417–4423.

[4] Ahmed, S., Rasul, M., Martens, W., Brown, R., and Hashib, M. (2011). Advances in heterogeneous photocatalytic degradation of phenols and dyes in wastewater: A review. *Water, Air, & Soil Pollution*, 215(1-4):3–29.

[5] Aikens, C. M., Li, S., and Schatz, G. C. (2008). From discrete electronic states to plasmons: TDDFT optical absorption properties of Ag n (n = 10, 20, 35, 56, 84, 120) tetrahedral clusters. *The Journal of Physical Chemistry C*, 112(30):11272–11279.

[6] Akpan, U. and Hameed, B. (2009). Parameters affecting the photocatalytic degradation of dyes using TiO_2-based photocatalysts: A review. *Journal of Hazardous Materials*, 170(2–3):520 – 529.

[7] Amaniampong, P. N., Jia, X., Wang, B., Mushrif, S. H., Borgna, A., and Yang, Y. (2015). Catalytic oxidation of cellobiose over TiO_2 supported gold-based bimetallic nanoparticles. *Catal. Sci. Technol.*, 5:2393–2405.

[8] Amaniampong, P. N., Li, K., Jia, X., Wang, B., Borgna, A., and Yang, Y. (2014). Titania-supported gold nanoparticles as efficient catalysts for the oxidation of cellobiose to organic acids in aqueous medium. *ChemCatChem*, 6(7):2105–2114.

[9] Amarasekara, A. S. and Ebede, C. C. (2009). Zinc chloride mediated degradation of cellulose at 200°C and identification of the products. *Bioresource Technology*, 100(21):5301 – 5304.

[10] Amarasekara, A. S., Owereh, O. S., and Ezeh, B. (2011). Interactions of d-cellobiose with p-toluenesulfonic acid in aqueous solution: a ^{13}C NMR study. *Carbohydrate Research*, 346(17):2820 – 2822.

[11] Amtout, A. and Leonelli, R. (1995). Optical properties of rutile near its fundamental band gap. *Phys. Rev. B*, 51:6842–6851.

[12] Anastas, P. T. and Kirchhoff, M. M. (2002). Origins, current status, and future challenges of green chemistry. *Accounts of Chemical Research*, 35(9):686–694.

[13] Arce, M., Quaino, P., and Santos, E. (2013). Electronic changes at the Pt(111) interface induced by the adsorption of OH species. *Catalysis Today*, 202:120–127.

[14] Asam, M. R. and Glish, G. L. (1997). Tandem mass spectrometry of alkali cationized polysaccharides in a quadrupole ion trap. *Journal of the American Society for Mass Spectrometry*, 8(9):987 – 995.

[15] Asencios, Y. J., Bellido, J. D., and Assaf, E. M. (2011). Synthesis of NiO–MgO–ZrO_2 catalysts and their performance in reforming of model biogas. *Applied Catalysis A: General*, 397(1–2):138 – 144.

[16] Augugliaro, V., Kisch, H., Loddo, V., López-Muñoz, M. J., Márquez-Álvarez, C., Palmisano, G., Palmisano, L., Parrino, F., and Yurdakal, S. (2008). Photocatalytic oxidation of aromatic alcohols to aldehydes in aqueous suspension of home-prepared titanium dioxide: 1. selectivity enhancement by aliphatic alcohols. *Applied Catalysis A: General*, 349(1–2):182 – 188.

[17] Augugliaro, V., Loddo, V., Pagliaro, M., Palmisano, G., and Palmisano, L. (2010). *Clean by Light Irradiation*. The Royal Society of Chemistry.

[18] Augugliaro, V., Loddo, V., Palmisano, L., and Schiavello, M. (1995a). Heterogeneous photocatalytic systems: Influence of some operational variables on actual photons absorbed by aqueous dispersions of TiO_2. *Solar Energy Materials and Solar Cells*, 38(1–4):411 – 419.

[19] Augugliaro, V., Loddo, V., Palmisano, L., and Schiavello, M. (1995b). Performance of heterogeneous photocatalytic systems: Influence of operational variables on photoactivity of aqueous suspension of TiO_2. *Journal of Catalysis*, 153(1):32 – 40.

[20] Awazu, K., Fujimaki, M., Rockstuhl, C., Tominaga, J., Murakami, H., Ohki, Y., Yoshida, N., and Watanabe, T. (2008). A plasmonic photocatalyst consisting of silver nanoparticles embedded in titanium dioxide. *Journal of the American Chemical Society*, 130(5):1676–1680.

[21] Baatz, C., Thielecke, N., and Prüße, U. (2007). Influence of the preparation conditions on the properties of gold catalysts for the oxidation of glucose. *Applied Catalysis B: Environmental*, 70(1–4):653 – 660.

[22] Baffou, G., Quidant, R., and Girard, C. (2009). Heat generation in plasmonic nanostructures: Influence of morphology. *Applied Physics Letters*, 94(15):–.

[23] Bahnemann, W., Muneer, M., and Haque, M. (2007). Titanium dioxide-mediated photocatalysed degradation of few selected organic pollutants in aqueous suspensions. *Catalysis Today*, 124(3–4):133 – 148.

[24] Bakardjieva, S., Šubrt, J., Štengl, V., Dianez, M. J., and Sayagues, M. J. (2005). Photoactivity of anatase–rutile TiO_2 nanocrystalline mixtures obtained by heat treatment of homogeneously precipitated anatase. *Applied Catalysis B: Environmental*, 58(3–4):193 – 202.

[25] Bard, A. J. (1980). Photoelectrochemistry. *Science*, 207(4427):139–144.

[26] Besson, M., Fleche, G., Fuertes, P., Gallezot, P., and Lahmer, F. (1996). Oxidation of glucose and gluconate on Pt, PtBi, and PtAu catalysts. *Recueil des travaux chimiques des Pays-Bas-Journal of the Royal Netherlands Chemical Society*, 115(4):217–&.

[27] Besson, M., Gallezot, P., and Pinel, C. (2014). Conversion of biomass into chemicals over metal catalysts. *Chemical Reviews*, 114(3):1827–1870.

[28] Bickley, R. I., Gonzalez-Carreno, T., Lees, J. S., Palmisano, L., and Tilley, R. J. (1991). A structural investigation of titanium dioxide photocatalysts. *Journal of Solid State Chemistry*, 92(1):178 – 190.

[29] Biella, S., Prati, L., and Rossi, M. (2002). Selective oxidation of d-glucose on gold catalyst. *Journal Of Catalysis*, 206(2):242–247.

[30] bin Saiman, M. I., Brett, G. L., Tiruvalam, R., Forde, M. M., Sharples, K., Thetford, A., Jenkins, R. L., Dimitratos, N., Lopez-Sanchez, J. A., Murphy, D. M., Bethell, D., Willock, D. J., Taylor, S. H., Knight, D. W., Kiely, C. J., and Hutchings, G. J. (2012). Involvement of surface-bound radicals in the oxidation of toluene using supported Au-Pd nanoparticles. *Angewandte Chemie International Edition*, 51(24):5981–5985.

[31] Bizzari, S. N. and Blagoev, M. (2011). *"CEH Marketing Research Report: FORMIC ACID"*.

[32] Bobleter, O. (1994). Hydrothermal degradation of polymers derived from plants. *Progress in Polymer Science*, 19(5):797 – 841.

[33] Boehm, H. P. (1971). Acidic and basic properties of hydroxylated metal oxide surfaces. *Discuss. Faraday Soc.*, 52:264–275.

[34] Boonstra, A. H. and Mutsaers, C. A. H. A. (1975). Relation between the photoadsorption of oxygen and the number of hydroxyl groups on a titanium dioxide surface. *The Journal of Physical Chemistry*, 79(16):1694–1698.

[35] Boschloo, G. and Fitzmaurice, D. (1999a). Electron accumulation in nanostructured TiO_2 (anatase) electrodes. *The Journal of Physical Chemistry B*, 103(37):7860–7868.

[36] Boschloo, G. and Fitzmaurice, D. (1999b). Spectroelectrochemical investigation of surface states in nanostructured TiO_2 electrodes. *The Journal of Physical Chemistry B*, 103(12):2228–2231.

[37] Bowker, M. (2012). Photocatalytic hydrogen production and oxygenate photoreforming. *Catalysis Letters*, 142(8):923–929.

[38] Bowker, M., Morton, C., Kennedy, J., Bahruji, H., Greves, J., Jones, W., Davies, P., Brookes, C., Wells, P., and Dimitratos, N. (2014). Hydrogen production by photoreforming of biofuels using Au, Pd and Au–Pd/TiO_2 photocatalysts. *Journal of Catalysis*, 310:10 – 15.

[39] Bozell, J. J. and Petersen, G. R. (2010). Technology development for the production of biobased products from biorefinery carbohydrates-the US department of energy's "top 10" revisited. *Green Chem.*, 12:539–554.

[40] Bragd, P., van Bekkum, H., and Besemer, A. (2004). TEMPO-mediated oxidation of polysaccharides: Survey of methods and applications. *Topics in Catalysis*, 27(1-4):49–66.

[41] Bragd, P. L., Besemer, A. C., and van Bekkum, H. (2002). Selective oxidation of carbohydrates by 4-AcNH-TEMPO/peracid systems. *Carbohydrate Polymers*, 49(4):397 – 406.

[42] Branson, J. (2004). System and method for extracting energy from agricultural waste.

[43] Brochette-Lemoine, S., Joannard, D., Descotes, G., Bouchu, A., and Queneau, Y. (1999). Sonocatalysis of the TEMPO-mediated oxidation of glucosides. *Journal of Molecular Catalysis A: Chemical*, 150(1-2):31 – 36.

[44] Bumajdad, A. and Madkour, M. (2014). Understanding the superior photocatalytic activity of noble metals modified titania under UV and visible light irradiation. *Phys. Chem. Chem. Phys.*, 16:7146–7158.

[45] Campbell, W. M., Burrell, A. K., Officer, D. L., and Jolley, K. W. (2004). Porphyrins as light harvesters in the dye-sensitised TiO_2 solar cell. *Coordination Chemistry Reviews*, 248(13-14):1363 – 1379.

[46] Carneiro, J., Yang, C.-C., Moma, J., Moulijn, J., and Mul, G. (2009). How gold deposition affects anatase performance in the photo-catalytic oxidation of cyclohexane. *Catalysis Letters*, 129(1-2):12–19.

[47] Carp, O., Huisman, C., and Reller, A. (2004). Photoinduced reactivity of titanium dioxide. *Progress in Solid State Chemistry*, 32(1-2):33 – 177.

[48] Cepak, V. M. and Martin, C. R. (1998). Preparation and stability of template-synthesized metal nanorod sols in organic solvents. *The Journal of Physical Chemistry B*, 102(49):9985–9990.

[49] Chatterjee, C., Pong, F., and Sen, A. (2015). Chemical conversion pathways for carbohydrates. *Green Chem.*, 17:40–71.

[50] Chen, G., Andries, J., and Spliethoff, H. (2003). Catalytic pyrolysis of biomass for hydrogen rich fuel gas production. *Energy Conversion and Management*, 44(14):2289 – 2296.

[51] Chen, X. and Mao, S. S. (2007). Titanium dioxide nanomaterials: Synthesis, properties, modifications, and applications. *Chemical Reviews*, 107(7):2891–2959.

[52] Chen, X., Zheng, Z., Ke, X., Jaatinen, E., Xie, T., Wang, D., Guo, C., Zhao, J., and Zhu, H. (2010). Supported silver nanoparticles as photocatalysts under ultraviolet and visible light irradiation. *Green Chem.*, 12:414–419.

[53] Chong, R., Li, J., Ma, Y., Zhang, B., Han, H., and Li, C. (2014). Selective conversion of aueous glucose to value-added sugar aldose on TiO_2-based photocatalysts. *Journal of Catalysis*, 314:101 – 108.

[54] Christopher, P., Xin, H., and Linic, S. (2011). Visible-light-enhanced catalytic oxidation reactions on plasmonic silver nanostructures. *Nature Publishing Group*, 3(6).

[55] Clark, J. and Deswarte, F. (2014). *Introduction to Chemicals from Biomass*. Wiley Series in Renewable Resource. Wiley.

[56] Climent, M. J., Corma, A., and Iborra, S. (2011). Converting carbohydrates to bulk chemicals and fine chemicals over heterogeneous catalysts. *Green Chem.*, 13:520–540.

[57] Collinson, S. and Thielemans, W. (2010). The catalytic oxidation of biomass to new materials focusing on starch, cellulose and lignin. *Coordination Chemistry Reviews*, 254(15–16):1854 – 1870.

[58] Colmenares, J. C. and Luque, R. (2014). Heterogeneous photocatalytic nanomaterials: Prospects and challenges in selective transformations of biomass-derived compounds. *Chem. Soc. Rev.*, 43:765–778.

[59] Colmenares, J. C. and Magdziarz, A. (2013). Room temperature versatile conversion of biomass-derived compounds by means of supported TiO_2 photocatalysts. *Journal of Molecular Catalysis A: Chemical*, 366(0):156 – 162.

[60] Colmenares, J. C., Magdziarz, A., Aramendia, M. A., Marinas, A., Marinas, J. M., Urbano, F. J., and Navio, J. A. (2011a). Influence of the strong metal support interaction effect (SMSI) of Pt/TiO_2 and Pd/TiO_2 systems in the photocatalytic biohydrogen production from glucose solution. *Catalysis Communications*, 16(1):1 – 6.

[61] Colmenares, J. C., Magdziarz, A., and Bielejewska, A. (2011b). High-value chemicals obtained from selective photo-oxidation of glucose in the presence of nanostructured titanium photocatalysts. *Bioresource Technology*, 102(24):11254 – 11257.

[62] Colmenares, J. C., Magdziarz, A., Chernyayeva, O., Lisovytskiy, D., Kurzydłowski, K., and Grzonka, J. (2013a). Sonication-assisted low-temperature routes for the synthesis of supported Fe–TiO_2 econanomaterials: Partial photooxidation of glucose and phenol aqueous degradation. *ChemCatChem*, 5(8):2270–2277.

[63] Colmenares, J. C., Magdziarz, A., Kurzydlowski, K., Grzonka, J., Chernyayeva, O., and Lisovytskiy, D. (2013b). Low-temperature ultrasound-promoted synthesis of Cr–TiO_2-supported photocatalysts for valorization of glucose and phenol degradation from liquid phase. *Applied Catalysis B: Environmental*, 134–135:136 – 144.

[64] Comotti, M., Della Pina, C., Matarrese, R., and Rossi, M. (2004). The catalytic activity of "naked" gold particles. *Angewandte Chemie International Edition*, 43(43):5812–5815.

[65] Corma, A., Iborra, S., and Velty, A. (2007). Chemical routes for the transformation of biomass into chemicals. *Chemical Reviews*, 107(6):2411–2502.

[66] Cortright, R. D., Davda, R. R., and Dumesic, J. A. (2002). Hydrogen from catalytic reforming of biomass–derived hydrocarbons in liquid water. *Nature*, 418:964–967.

[67] Dambournet, D., Belharouak, I., and Amine, K. (2010). Tailored preparation methods of TiO_2 anatase, rutile, brookite: Mechanism of formation and electrochemical properties. *Chemistry of Materials*, 22(3):1173–1179.

[68] Das, D. and Veziroglu, T. (2001). Hydrogen production by biological processes: A survey of literature. *International Journal of Hydrogen Energy*, 26(1):13 – 28.

[69] de Nooy, A. E., Besemer, A. C., and van Bekkum, H. (1995). Highly selective nitroxyl radical-mediated oxidation of primary alcohol groups in water-soluble glucans. *Carbohydrate Research*, 269(1):89 – 98.

[70] de Wilt, H. G. J. (1972). Part I. oxidation of glucose to gluconic acid. survey of techniques. *Product R&D*, 11(4):370–373.

[71] Delidovich, I., Taran, O., Matvienko, L., Simonov, A., Simakova, I., Bobrovskaya, A., and Parmon, V. (2010). Selective oxidation of glucose over carbon-supported Pd and Pt catalysts. *Catalysis Letters*, 140(1-2):14–21.

[72] Demirbas, A. (2002). Hydrogen production from biomass by the gasification process. *Energy Sources*, 24(1):59–68.

[73] Deng, W., Liu, M., Tan, X., Zhang, Q., and Wang, Y. (2010). Conversion of cellobiose into sorbitol in neutral water medium over carbon nanotube-supported ruthenium catalysts. *Journal of Catalysis*, 271(1):22 – 32.

[74] Desai, R. L. and Shields, J. A. (1969). Photochemical degradation of cellulosea material. *Die Makromolekulare Chemie*, 122(1):134–144.

[75] Desai, S. H., Rabinovitch-Deere, C. A., Fan, Z., and Atsumi, S. (2015). Isobutanol production from cellobionic acid in escherichia coli. *Microbial Cell Factories*, 14(1):1–10.

[76] Diez, I. and Ras, R. H. A. (2011). Fluorescent silver nanoclusters. *Nanoscale*, 3:1963–1970.

[77] Domon, B. and Costello, C. (1988). A systematic nomenclature for carbohydrate fragmentations in FAB-MS/MS spectra of glycoconjugates. *Glycoconjugate Journal*, 5(4):397–409.

[78] Du, M.-H., Feng, J., and Zhang, S. B. (2007). Photo-oxidation of polyhydroxyl molecules on TiO_2 surfaces: From hole scavenging to light-induced self-assembly of TiO_2-cyclodextrin wires. *Phys. Rev. Lett.*, 98:066102.

[79] Du, P., Moulijn, J. A., and Mul, G. (2006). Selective photo(catalytic)-oxidation of cyclohexane: Effect of wavelength and TiO_2 structure on product yields. *Journal of Catalysis*, 238(2):342 – 352.

[80] Du, Y. and Rabani, J. (2003). The measure of TiO_2 photocatalytic efficiency and the comparison of different photocatalytic titania. *The Journal of Physical Chemistry B*, 107(43):11970–11978.

[81] Dweydari, A. W. and Mee, C. H. B. (1975). Work function measurements on (100) and (110) surfaces of silver. *physica status solidi (a)*, 27(1):223–230.

[82] Eastman, D. E. (1970). Photoelectric work functions of transition, rare-earth, and noble metals. *Phys. Rev. B*, 2:1–2.

[83] Ebringerová, A., Hromádková, Z., and Heinze, T. (2005). Hemicellulose. In Heinze, T., editor, *Polysaccharides I*, volume 186 of *Advances in Polymer Science*, pages 1–67. Springer Berlin Heidelberg.

[84] Egerton, T. and King, C. (1979). The influence of light intensity on photoactivity in TiO_2 pigmented systems. *Journal of the Oil and Colour Chemists Association*, 62(10):386–391.

[85] Enright, B., Redmond, G., and Fitzmaurice, D. (1994). Spectroscopic determination of flatband potentials for polycrystalline TiO_2 electrodes in mixed solvent systems. *The Journal of Physical Chemistry*, 98(24):6195–6200.

[86] Fan, H., Li, G., Yang, F., Yang, L., and Zhang, S. (2011). Photodegradation of cellulose under UV light catalysed by TiO_2. *Journal of Chemical Technology & Biotechnology*, 86(8):1107–1112.

[87] Farrell, A. E., Plevin, R. J., Turner, B. T., Jones, A. D., O'Hare, M., and Kammen, D. M. (2006). Ethanol can contribute to energy and environmental goals. *Science*, 311(5760):506–508.

[88] Fischer, S., Leipner, H., Thümmler, K., Brendler, E., and Peters, J. (2003). Inorganic molten salts as solvents for cellulose. *Cellulose*, 10(3):227–236.

[89] Forsberg, Z., Vaaje-Kolstad, G., Westereng, B., Bunaes, A. C., Stenstrom, Y., MacKenzie, A., Sorlie, M., Horn, S. J., and Eijsink, V. G. (2011). Cleavage of cellulose by a CBM33 protein. *Protein Science*, 20(9):1479–1483.

[90] Fraser, I. M. and MacCallum, J. R. (1986). Photocatalytic dehydrogenation of liquid propan-2-ol by TiO_2. part 1.- kinetics. *J. Chem. Soc., Faraday Trans. 1*, 82:607–615.

[91] Fu, Q. and Sun, W. (2001). Mie theory for light scattering by a spherical particle in an absorbing medium. *Appl. Opt.*, 40(9):1354–1361.

[92] Fu, X., Long, J., Wang, X., Leung, D. Y., Ding, Z., Wu, L., Zhang, Z., Li, Z., and Fu, X. (2008). Photocatalytic reforming of biomass: A systematic study of hydrogen evolution from glucose solution. *International Journal of Hydrogen Energy*, 33(22):6484 – 6491.

[93] Fujishima, A., Hashimoto, K., and Watanabe, T. (1999). *TiO_2 Photocatalysis: Fundamentals and Applications*. BKC.

[94] Fujishima, A., Rao, T. N., and Tryk, D. A. (2000). Titanium dioxide photocatalysis. *Journal of Photochemistry and Photobiology C: Photochemistry Reviews*, 1(1):1 – 21.

[95] Fujishima, A., Zhang, X., and Tryk, D. A. (2008). TiO_2 photocatalysis and related surface phenomena. *Surface Science Reports*, 63(12):515 – 582.

[96] Fukuoka, A. and Dhepe, P. L. (2006). Catalytic conversion of cellulose into sugar alcohols. *Angewandte Chemie International Edition*, 45(31):5161–5163.

[97] Garcia, L., French, R., Czernik, S., and Chornet, E. (2000). Catalytic steam reforming of bio-oils for the production of hydrogen: effects of catalyst composition. *Applied Catalysis A: General*, 201(2):225 – 239.

[98] Geboers, J., Van de Vyver, S., Carpentier, K., de Blochouse, K., Jacobs, P., and Sels, B. (2010). Efficient catalytic conversion of concentrated cellulose feeds to hexitols with heteropoly acids and Ru on carbon. *Chem. Commun.*, 46:3577–3579.

[99] Giannotti, C., Greneur, S. L., and Watts, O. (1983). Photo-oxidation of alkanes by metal oxide semiconductors. *Tetrahedron Letters*, 24(46):5071 – 5072.

[100] Gomez, L., Sebastian, V., Arruebo, M., Santamaria, J., and Cronin, S. B. (2014). Plasmon-enhanced photocatalytic water purification. *Phys. Chem. Chem. Phys.*, 16:15111–15116.

[101] Grabowska, E., Zaleska, A., Sorgues, S., Kunst, M., Etcheberry, A., Colbeau-Justin, C., and Remita, H. (2013). Modification of titanium(IV) dioxide with small silver nanoparticles: Application in photocatalysis. *The Journal of Physical Chemistry C*, 117(4):1955–1962.

[102] Gratzel, M. (2001). Photoelectrochemical cells. *Nature*, 414(6861):338–344.

[103] Greenbaum, E., Tevault, C. V., and Ma, C. Y. (1995). New photosynthesis: Direct photoconversion of biomass to molecular oxygen and volatile hydrocarbons. *Energy & Fuels*, 9(1):163–167.

[104] Gutierrez, L.-F., Hamoudi, S., and Belkacemi, K. (2011). Selective production of lactobionic acid by aerobic oxidation of lactose over gold crystallites supported on mesoporous silica. *Applied Catalysis A: General*, 402(1–2):94 – 103.

[105] Hallenbeck, P. C. and Benemann, J. R. (2002). Biological hydrogen production; fundamentals and limiting processes. *International Journal of Hydrogen Energy*, 27(11–12):1185 – 1193.

[106] Harvey, P. R., Rudham, R., and Ward, S. (1983). Photocatalytic oxidation of liquid alcohols and binary alcohol mixtures by rutile. *J. Chem. Soc., Faraday Trans. 1*, 79:2975–2981.

[107] Hendriks, A. and Zeeman, G. (2009). Pretreatments to enhance the digestibility of lignocellulosic biomass. *Bioresource Technology*, 100(1):10 – 18.

[108] Huang, H., Sivayoganathan, M., Duley, W., and Zhou, Y. (2015). Efficient localized heating of silver nanoparticles by low-fluence femtosecond laser pulses. *Applied Surface Science*, 331:392 – 398.

[109] Huang, X., Wang, X., Wang, X., Wang, X., Tan, M., Ding, W., and Lu, X. (2013). P123-stabilized Au-Ag alloy nanoparticles for kinetics of aerobic oxidation of benzyl alcohol in aqueous solution. *Journal of Catalysis*, 301(0):217 – 226.

[110] Huang, Y.-F., Zhang, M., Zhao, L.-B., Feng, J.-M., Wu, D.-Y., Ren, B., and Tian, Z.-Q. (2014). Activation of oxygen on gold and silver nanoparticles assisted by surface plasmon resonances. *Angewandte Chemie International Edition*, 53(9):2353–2357.

[111] Huber, G. W., Iborra, S., and Corma, A. (2006). Synthesis of transportation fuels from biomass: Chemistry, catalysts, and engineering. *Chemical Reviews*, 106(9):4044–4098.

[112] Hudlicky, M. (1990). *Oxidations in Organic Chemistry*. ACS monograph: American Chemical Society. Wiley.

[113] Hurum, D. C., Agrios, A. G., Gray, K. A., Rajh, T., and Thurnauer, M. C. (2003). Explaining the enhanced photocatalytic activity of Degussa P25 mixed-phase TiO_2 using EPR. *The Journal of Physical Chemistry B*, 107(19):4545–4549.

[114] Hussein, F. H., Pattenden, G., Rudham, R., and Russell, J. J. (1984). Photo-oxidation of alcohols catalysed by platinised titanium dioxide. *Tetrahedron Letters*, 25(31):3363 – 3364.

[115] Hustede, H., Haberstroh, H.-J., and Schinzig, E. (2000). *Gluconic Acid*. Wiley-VCH Verlag GmbH & Co. KGaA.

[116] Ibrahim, M., Alaam, M., El-Haes, H., Jalbout, A. F., and Leon, A. d. (2006). Analysis of the structure and vibrational spectra of glucose and fructose. *Ecletica Quimica*, 31:15 – 21.

[117] Indrakanti, V. P., Kubicki, J. D., and Schobert, H. H. (2009). Photoinduced activation of CO_2 on ti-based heterogeneous catalysts: Current state, chemical physics-based insights and outlook. *Energy Environ. Sci.*, 2:745–758.

[118] Jacoby, W., Blake, D., Noble, R., and Koval, C. (1995). Kinetics of the oxidation of trichloroethylene in air via heterogeneous photocatalysis. *Journal of Catalysis*, 157(1):87 – 96.

[119] Jain, P. K., Lee, K. S., El-Sayed, I. H., , and El-Sayed, M. A. (2006). Calculated absorption and scattering properties of gold nanoparticles of different size, shape, and composition: Applications in biological imaging and biomedicine. *The Journal of Physical Chemistry B*, 110(14):7238–7248.

[120] Janus, M. and Morawski, A. (2007). New method of improving photocatalytic activity of commercial Degussa P25 for azo dyes decomposition. *Applied Catalysis B: Environmental*, 75(1–2):118 – 123.

[121] Kapdan, I. K. and Kargi, F. (2006). Bio-hydrogen production from waste materials. *Enzyme and Microbial Technology*, 38(5):569 – 582.

[122] Kawahara, K., Suzuki, K., Ohko, Y., and Tatsuma, T. (2005). Electron transport in silver-semiconductor nanocomposite films exhibiting multicolor photochromism. *Phys. Chem. Chem. Phys.*, 7:3851–3855.

[123] Kawai, T. and Sakata, T. (1980). Conversion of carbohydrate into hydrogen fuel by a photocatalytic process. *Nature*, 286(5772):474–476.

[124] Kazuma, E., Sakai, N., and Tatsuma, T. (2011). Nanoimaging of localized plasmon-induced charge separation. *Chem. Commun.*, 47:5777–5779.

[125] Kazuma, E. and Tatsuma, T. (2012). Photoinduced reversible changes in morphology of plasmonic Ag nanorods on TiO_2 and application to versatile photochromism. *Chem. Commun.*, 48:1733–1735.

[126] Kelly, K. L., Coronado, E., Zhao, L. L., and Schatz, G. C. (2003). The optical properties of metal nanoparticles: The influence of size, shape, and dielectric environment. *The Journal of Physical Chemistry B*, 107(3):668–677.

[127] Kennedy, J., Jones, W., J.Morgan, D., Bowker, M., Lu, L., J.Kiely, C., P.Wells, P., and Dimitratos, N. (2015). Photocatalytic hydrogen production by reforming of methanol using Au/TiO_2, Ag/TiO_2 and Au-Ag/TiO_2 catalysts. *Catalysis, Structure & Reactivity*, 1(1):35–43.

[128] Khan, M. R., Chuan, T. W., Yousuf, A., Chowdhury, M. N. K., and Cheng, C. K. (2015). Schottky barrier and surface plasmonic resonance phenomena towards the photocatalytic reaction: study of their mechanisms to enhance photocatalytic activity. *Catal. Sci. Technol.*, 5:2522–2531.

[129] Khanna, P., Gokhale, R., Subbarao, V., Vishwanath, A. K., Das, B., and Satyanarayana, C. (2005). PVA stabilized gold nanoparticles by use of unexplored albeit conventional reducing agent. *Materials Chemistry and Physics*, 92(1):229 – 233.

[130] Kim, G., Lee, S.-H., and Choi, W. (2015). Glucose–TiO_2 charge transfer complex-mediated photocatalysis under visible light. *Applied Catalysis B: Environmental*, 162(0):463 – 469.

[131] Kim, W., Tachikawa, T., Moon, G.-h., Majima, T., and Choi, W. (2014). Molecular-level understanding of the photocatalytic activity difference between anatase and rutile nanoparticles. *Angewandte Chemie International Edition*, 53(51):14036–14041.

[132] Kisch, H. (2010). On the problem of comparing rates or apparent quantum yields in heterogeneous photocatalysis. *Angewandte Chemie International Edition*, 49(50):9588–9589.

[133] Klemm, D., Philipp, B., Heinze, T., Heinze, U., and Wagenknecht, W. (2004). *General Considerations on Structure and Reactivity of Cellulose: Section 2.1–2.1.4*, pages 9–29. Wiley-VCH Verlag GmbH & Co. KGaA.

[134] Kolbitsch, P., Pfeifer, C., and Hofbauer, H. (2008). Catalytic steam reforming of model biogas. *Fuel*, 87(6):701 – 706.

[135] Kondarides, D., Daskalaki, V., Patsoura, A., and Verykios, X. (2008). Hydrogen production by photo-induced reforming of biomass components and derivatives at ambient conditions. *Catalysis Letters*, 122(1-2):26–32.

[136] Kortum, G., Braun, W., and Herzog, G. (1963). Principles and techniques of diffuse-reflectance spectroscopy. *Angewandte Chemie International Edition in English*, 2(7):333–341.

[137] Kubacka, A., Fernández-García, M., and Colón, G. (2012). Advanced nanoarchitectures for solar photocatalytic applications. *Chemical Reviews*, 112(3):1555–1614.

[138] Kubelka, P. and Munk, F. (1931). An article on optics of paint layers. *Z. Tech. Phys*, 12(593-601).

[139] Kumar, P., Badrinarayanan, S., and Sastry, M. (2000). Nanocrystalline TiO_2 studied by optical, FTIR and X-ray photoelectron spectroscopy: correlation to presence of surface states. *Thin Solid Films*, 358(1–2):122 – 130.

[140] Kusema, B. T. and Murzin, D. Y. (2013). Catalytic oxidation of rare sugars over gold catalysts. *Catal. Sci. Technol.*, 3:297–307.

[141] Lalitha, K., Reddy, J. K., Sharma, M. V. P., Kumari, V. D., and Subrahmanyam, M. (2010). Continuous hydrogen production activity over finely dispersed Ag_2O/TiO_2 catalysts from methanol:water mixtures under solar irradiation: A structure–activity correlation. *International Journal of Hydrogen Energy*, 35(9):3991 – 4001.

[142] Lang, X., Ma, W., Chen, C., Ji, H., and Zhao, J. (2014). Selective aerobic oxidation mediated by TiO_2 photocatalysis. *Accounts of Chemical Research*, 47(2):355–363.

[143] Lee, S. G., Choi, J. I., Koh, W., and Jang, S. S. (2013). Adsorption of β-d-glucose and cellobiose on kaolinite surfaces: Density functional theory (DFT) approach. *Applied Clay Science*, 71:73 – 81.

[144] Leitner, W. (1995). Carbon dioxide as a raw material: The synthesis of formic acid and its derivatives from CO_2. *Angewandte Chemie International Edition in English*, 34(20):2207–2221.

[145] Levin, D. B., Pitt, L., and Love, M. (2004). Biohydrogen production: prospects and limitations to practical application. *International Journal of Hydrogen Energy*, 29(2):173 – 185.

[146] Li, W., Du, D., Yan, T., Kong, D., You, J., and Li, D. (2015). Relationship between surface hydroxyl groups and liquid-phase photocatalytic activity of titanium dioxide. *Journal of colloid and interface science*, 444:42—48.

[147] Li, Y., Sasaki, T., Shimizu, Y., and Koshizaki, N. (2008). Hexagonal-close-packed, hierarchical amorphous TiO_2 nanocolumn arrays: Transferability, enhanced photocatalytic activity, and superamphiphilicity without UV irradiation. *Journal of the American Chemical Society*, 130(44):14755–14762.

[148] Liang, G., Wu, C., He, L., Ming, J., Cheng, H., Zhuo, L., and Zhao, F. (2011). Selective conversion of concentrated microcrystalline cellulose to isosorbide over Ru/C catalyst. *Green Chem.*, 13:839–842.

[149] Liang, X., Liu, C.-j., and Kuai, P. (2008). Selective oxidation of glucose to gluconic acid over argon plasma reduced Pd/Al_2O_3. *Green Chem.*, 10:1318–1322.

[150] Linic, S., Aslam, U., Boerigter, C., and Morabito, M. (2015). Photochemical transformations on plasmonic metal nanoparticles. *Nature Materials*, 14(6):567–576.

[151] Liu, L., Peng, P., Hu, A., Zou, G., Duley, W. W., and Zhou, Y. N. (2013). Highly localized heat generation by femtosecond laser induced plasmon excitation in Ag nanowires. *Applied Physics Letters*, 102(7):–.

[152] Liu, S., Chen, G., Prasad, P. N., and Swihart, M. T. (2011a). Synthesis of monodisperse Au, Ag, and Au–Ag alloy nanoparticles with tunable size and surface plasmon resonance frequency. *Chemistry of Materials*, 23(18):4098–4101.

[153] Liu, X., Wang, A., Yang, X., Zhang, T., Mou, C.-Y., Su, D.-S., and Li, J. (2009). Synthesis of thermally stable and highly active bimetallic Au–Ag nanoparticles on inert supports. *Chemistry of Materials*, 21(2):410–418.

[154] Liu, Z., Hou, W., Pavaskar, P., Aykol, M., and Cronin, S. B. (2011b). Plasmon resonant enhancement of photocatalytic water splitting under visible illumination. *Nano Letters*, 11(3):1111–1116.

[155] Liu L-L, Yi T, Z. X. (2015). Antitumor effect of d-erythrose in an abdominal metastatic model of colon carcinoma. *Oncology Letters.*, 9(2):769–773.

[156] Lopez, R. and Gomez, R. (2012). Band-gap energy estimation from diffuse reflectance measurements on sol-gel and commercial TiO_2: a comparative study. *Journal of Sol-Gel Science and Technology*, 61(1):1 – 7.

[157] Lopez-Sanchez, J. A., Dimitratos, N., Hammond, C., Brett, G. L., Kesavan, L., White, S., Miedziak, P., Tiruvalam, R., Jenkins, R. L., Carley, A. F., Knight, D., Kiely, C. J., and Hutchings, G. J. (2011). Facile removal of stabilizer-ligands from supported gold nanoparticles. *Nature Chemistry*, 3(7).

[158] López-Tenllado, F., Marinas, A., Urbano, F., Colmenares, J., Hidalgo, M., Marinas, J., and Moreno, J. (2012). Selective photooxidation of alcohols as test reaction for photocatalytic activity. *Applied Catalysis B: Environmental*, 128:150 – 158.

[159] Luken, A., Muhler, M., and Strunk, J. (2015). On the role of gold nanoparticles in the selective photooxidation of 2-propanol over Au/TiO_2. *Phys. Chem. Chem. Phys.*, 17:10391–10397.

[160] Maki-Arvela, P., Tokarev, A. V., Murzina, E. V., Campo, B., Heikkila, T., Brozinski, J.-M., Wolf, D., and Murzin, D. Y. (2011). Kinetics of lactose and rhamnose oxidation over supported metal catalysts. *Phys. Chem. Chem. Phys.*, 13:9268–9280.

[161] Mendez-Ramos, J., Acosta-Mora, P., Ruiz-Morales, J. C., Hernandez, T., Borges, M. E., and Esparza, P. (2013). Turning into the blue: materials for enhancing TiO_2 photocatalysis by up-conversion photonics. *RSC Adv.*, 3:23028–23034.

[162] Michaelson, H. B. (1977). The work function of the elements and its periodicity. *Journal of Applied Physics*, 48(11):4729–4733.

[163] Miedziak, P. J., Alshammari, H., Kondrat, S. A., Clarke, T. J., Davies, T. E., Morad, M., Morgan, D. J., Willock, D. J., Knight, D. W., Taylor, S. H., and Hutchings, G. J. (2014). Base-free glucose oxidation using air with supported gold catalysts. *Green Chem.*, 16:3132–3141.

[164] Mills, A., Davies, R. H., and Worsley, D. (1993). Water purification by semiconductor photocatalysis. *Chem. Soc. Rev.*, 22:417–425.

[165] Mills, A. and Hunte, S. L. (1997). An overview of semiconductor photocatalysis. *Journal of Photochemistry and Photobiology A: Chemistry*, 108(1):1 – 35.

[166] Minero, C., Catozzo, F., and Pelizzetti, E. (1992). Role of adsorption in photocatalyzed reactions of organic molecules in aqueous titania suspensions. *Langmuir*, 8(2):481–486.

[167] Mirescu, A. and Prüße, U. (2007). A new environmental friendly method for the preparation of sugar acids via catalytic oxidation on gold catalysts. *Applied Catalysis B: Environmental*, 70(1–4):644 – 652.

[168] Mock, J. J., Barbic, M., Smith, D. R., Schultz, D. A., and Schultz, S. (2002). Shape effects in plasmon resonance of individual colloidal silver nanoparticles. *The Journal of Chemical Physics*, 116(15):6755–6759.

[169] Moe, S., Holen, A., and Schult, T. (2002). 4-O-beta-d-glucopyranosyl-d-gluconic acid (cellobionic acid) produced by ozonation of cellobiose: isolation by HPLC and assignment of NMR chemical shifts. *Journal of carbohydrate chemistry*, 21(6):513 – 520.

[170] Mogensen, K. B. and Kneipp, K. (2014). Size-dependent shifts of plasmon resonance in silver nanoparticle films using controlled dissolution: Monitoring the onset of surface screening effects. *The Journal of Physical Chemistry C*, 118(48):28075–28083.

[171] Mohamed, O. S., Ahmed, S. A., Mostafa, M. F., and Abdel-Wahab, A.-M. A. (2008). Nanoparticles TiO_2-photocatalyzed oxidation of selected cyclohexyl alcohols. *Journal of Photochemistry and Photobiology A: Chemistry*, 200(2–3):209 – 215.

[172] Mohamed, O. S., Gaber, A. E.-A. M., and Abdel-Wahab, A. (2002). Photocatalytic oxidation of selected aryl alcohols in acetonitrile. *Journal of Photochemistry and Photobiology A: Chemistry*, 148(1–3):205 – 210.

[173] Mohanty, P., Pant, K. K., and Mittal, R. (2015). Hydrogen generation from biomass materials: challenges and opportunities. *Wiley Interdisciplinary Reviews: Energy and Environment*, 4(2):139–155.

[174] Montoya, J., Velásquez, J., and Salvador, P. (2009). The direct–indirect kinetic model in photocatalysis: A reanalysis of phenol and formic acid degradation rate dependence on photon flow and concentration in TiO_2 aqueous dispersions. *Applied Catalysis B: Environmental*, 88(1–2):50 – 58.

[175] Montoya, J. F., Bahnemann, D. W., Peral, J., and Salvador, P. (2014). Catalytic role of TiO_2 terminal oxygen atoms in liquid-phase photocatalytic reactions: Oxidation of aromatic compounds in anhydrous acetonitrile. *ChemPhysChem*, 15(11):2311–2320.

[176] Morris, A. J., Meyer, G. J., and Fujita, E. (2009). Molecular approaches to the photocatalytic reduction of carbon dioxide for solar fuels. *Accounts of Chemical Research*, 42(12):1983–1994.

[177] Mosier, N., Wyman, C., Dale, B., Elander, R., Lee, Y., Holtzapple, M., and Ladisch, M. (2005). Features of promising technologies for pretreatment of lignocellulosic biomass. *Bioresource Technology*, 96(6):673 – 686.

[178] Murphy, V., Shoemaker, J., Zhu, G., Archer, R., Salem, G., and Dias, E. (2011). Oxidation catalysts.

[179] Murugadoss, A., Kai, N., and Sakurai, H. (2012). Synthesis of bimetallic gold-silver alloy nanoclusters by simple mortar grinding. *Nanoscale*, 4:1280–1282.

[180] Murzina, E. V., Tokarev, A. V., Kordás, K., Karhu, H., Mikkola, J.-P., and Murzin, D. Y. (2008). d-Lactose oxidation over gold catalysts. *Catalysis Today*, 131(1–4):385 – 392. Recent advances in catalysis - selected papers from {APCAT} 4 (Singapore, 6-8 December 2006).

[181] Naoi, K., Ohko, Y., , and Tatsuma, T. (2004). TiO_2 films loaded with silver nanoparticles: Control of multicolor photochromic behavior. *Journal of the American Chemical Society*, 126(11):3664–3668.

[182] Ni, M., Leung, D. Y., Leung, M. K., and Sumathy, K. (2006). An overview of hydrogen production from biomass. *Fuel Processing Technology*, 87(5):461 – 472.

[183] Niemantsverdriet, J. W. (2007). *Photoemission and Auger Spectroscopy*, pages 39–83. Wiley-VCH Verlag GmbH & Co. KGaA.

[184] Nishijima, Y., Ueno, K., Yokota, Y., Murakoshi, K., and Misawa, H. (2010). Plasmon-assisted photocurrent generation from visible to near-infrared wavelength using a Au-nanorods/TiO_2 electrode. *The Journal of Physical Chemistry Letters*, 1(13):2031–2036.

[185] Noguez, C. (2007). Surface plasmons on metal nanoparticles: The influence of shape and physical environment. *The Journal of Physical Chemistry C*, 111(10):3806–3819.

[186] Ochiai, T. and Fujishima, A. (2012). Photoelectrochemical properties of TiO_2 photocatalyst and its applications for environmental purification. *Journal of Photochemistry and Photobiology C: Photochemistry Reviews*, 13(4):247 – 262.

[187] Ohko, Y., Tatsuma, T., Fujii, T., Naoi, K., Niwa, C., Kubota, Y., and Fujishima, A. (2003). Multicolour photochromism of TiO_2 films loaded with silver nanoparticles. *Nature Materials*, 2(1):29–31.

[188] Ohno, T., Sarukawa, K., Tokieda, K., and Matsumura, M. (2001). Morphology of a TiO_2 photocatalyst (Degussa, P-25) consisting of anatase and rutile crystalline phases. *Journal of Catalysis*, 203(1):82 – 86.

[189] Ohno, T., Tokieda, K., Higashida, S., and Matsumura, M. (2003). Synergism between rutile and anatase TiO_2 particles in photocatalytic oxidation of naphthalene. *Applied Catalysis A: General*, 244(2):383 – 391.

[190] Ohtani, B., Prieto-Mahaney, O., Li, D., and Abe, R. (2010). What is Degussa (Evonik) P25? crystalline composition analysis, reconstruction from isolated pure particles and photocatalytic activity test. *Journal of Photochemistry and Photobiology A: Chemistry*, 216(2–3):179 – 182.

[191] Ollis, D. F., Pelizzetti, E., and Serpone, N. (1991). Photocatalyzed destruction of water contaminants. *Environmental Science & Technology*, 25(9):1522–1529.

[192] Parra, S., Olivero, J., Pacheco, L., and Pulgarin, C. (2003). Structural properties and photoreactivity relationships of substituted phenols in TiO_2 suspensions. *Applied Catalysis B: Environmental*, 43(3):293 – 301.

[193] Pelaez, M., Nolan, N. T., Pillai, S. C., Seery, M. K., Falaras, P., Kontos, A. G., Dunlop, P. S., Hamilton, J. W., Byrne, J., O'Shea, K., Entezari, M. H., and Dionysiou, D. D. (2012). A review on the visible light active titanium dioxide photocatalysts for environmental applications. *Applied Catalysis B: Environmental*, 125:331 – 349.

[194] Pichat, P. (1994). Partial or complete heterogeneous photocatalytic oxidation of organic compounds in liquid organic or aqueous phases. *Catalysis Today*, 19(2):313 – 333.

[195] Prüße, U., Herrmann, M., Baatz, C., and Decker, N. (2011). Gold-catalyzed selective glucose oxidation at high glucose concentrations and oxygen partial pressures. *Applied Catalysis A: General*, 406(1–2):89 – 93.

[196] Reddy, K. M., Reddy, C. G., and Manorama, S. (2001). Preparation, characterization, and spectral studies on nanocrystalline anatase TiO_2. *Journal of Solid State Chemistry*, 158(2):180 – 186.

[197] Redmond, G. and Fitzmaurice, D. (1993). Spectroscopic determination of flatband potentials for polycrystalline titania electrodes in nonaqueous solvents. *The Journal of Physical Chemistry*, 97(7):1426–1430.

[198] Rehman, S., Ullah, R., Butt, A., and Gohar, N. (2009). Strategies of making TiO_2 and ZnO visible light active. *Journal of Hazardous Materials*, 170(2–3):560 – 569.

[199] Rinaldi, R., Meine, N., vom Stein, J., Palkovits, R., and Schüth, F. (2010). Which controls the depolymerization of cellulose in ionic liquids: The solid acid catalyst or cellulose? *ChemSusChem*, 3(2):266–276.

[200] Rongchao, J., Charles Cao, Y., Encai, H., Métraux, G. S., Schatz, G. C., and Chad, A. M. (2003). Controlling anisotropic nanoparticle growth through plasmon excitation. *Nature*, 425:487–490.

[201] Rose, M., Hausoul, P. J. C., and Palkovits, R. (2013). Nanostructured solid catalysts in the conversion of cellulose and cellulose-derived platform chemicals. chapter 8, pages 182–218. CRC Press.

[202] Röper, H. (1990). Selective oxidation of d-glucose: Chiral intermediates for industrial utilization. *Starch - Stärke*, 42(9):342–349.

[203] Russell, B. K., Mantovani, J. G., Anderson, V. E., Warmack, R. J., and Ferrell, T. L. (1987). Experimental test of the Mie theory for microlithographically produced silver spheres. *Phys. Rev. B*, 35:2151–2154.

[204] Ryu, J. and Choi, W. (2008). Substrate-specific photocatalytic activities of TiO_2 and multiactivity test for water treatment application. *Environmental Science & Technology*, 42(1):294–300.

[205] Sakthivel, S., Neppolian, B., Shankar, M., Arabindoo, B., Palanichamy, M., and Murugesan, V. (2003). Solar photocatalytic degradation of azo dye: comparison of photocatalytic efficiency of ZnO and TiO_2. *Solar Energy Materials and Solar Cells*, 77(1):65 – 82.

[206] Sarina, S., Waclawik, E. R., and Zhu, H. (2013). Photocatalysis on supported gold and silver nanoparticles under ultraviolet and visible light irradiation. *Green Chem.*, 15:1814–1833.

[207] Sauer, T., Neto, G. C., José, H., and Moreira, R. (2002). Kinetics of photocatalytic degradation of reactive dyes in a TiO_2 slurry reactor. *Journal of Photochemistry and Photobiology A: Chemistry*, 149(1–3):147 – 154.

[208] Schneider, J., Matsuoka, M., Takeuchi, M., Zhang, J., Horiuchi, Y., Anpo, M., and Bahnemann, D. W. (2014). Understanding TiO_2 photocatalysis: Mechanisms and materials. *Chemical Reviews*, 114(19):9919–9986.

[209] Serpone, N. (1997). Relative photonic efficiencies and quantum yields in heterogeneous photocatalysis. *Journal of Photochemistry and Photobiology A: Chemistry*, 104(1–3):1 – 12.

[210] Serrano, B. and de Lasa, H. (1997). Photocatalytic degradation of water organic pollutants. kinetic modeling and energy efficiency. *Industrial & Engineering Chemistry Research*, 36(11):4705–4711.

[211] Serrano, B. and de Lasa, H. (1999). Photocatalytic degradation of water organic pollutants: pollutant reactivity and kinetic modeling. *Chemical Engineering Science*, 54(15–16):3063 – 3069.

[212] Shin, H., Byun, T.-H., Lee, S., Bae, S.-T., and Jung, H. S. (2013). Surface hydroxylation of TiO_2 yields notable visible-light photocatalytic activity to decompose rhodamine B in aqueous solution. *Journal of Physics and Chemistry of Solids*, 74(8):1136 – 1142.

[213] Shiraishi, Y. and Hirai, T. (2008). Selective organic transformations on titanium oxide-based photocatalysts. *Journal of Photochemistry and Photobiology C: Photochemistry Reviews*, 9(4):157 – 170.

[214] Shiraishi, Y., Morishita, M., and Hirai, T. (2005). Acetonitrile-assisted highly selective photocatalytic epoxidation of olefins on Ti-containing silica with molecular oxygen. *Chem. Commun.*, pages 5977–5979.

[215] Shkrob, I. A., Marin, T. W., Chemerisov, S. D., and Sevilla, M. D. (2011). Mechanistic aspects of photooxidation of polyhydroxylated molecules on metal oxides. *The Journal of Physical Chemistry C*, 115(11):4642–4648.

[216] Shkrob, I. A. and Sauer, M. C. (2004). Hole scavenging and photo-stimulated recombination of electron-hole pairs in aqueous TiO_2 nanoparticles. *The Journal of Physical Chemistry B*, 108(33):12497–12511.

[217] Shkrob, I. A., Sauer, M. C., and Gosztola, D. (2004). Efficient, rapid photooxidation of chemisorbed polyhydroxyl alcohols and carbohydrates by TiO_2 nanoparticles in an aqueous solution. *The Journal of Physical Chemistry B*, 108(33):12512–12517.

[218] Skrabalak, S. E., Au, L., Li, X., and Xia, Y. (2007). Facile synthesis of Ag nanocubes and Au nanocages. *Nature Protocols*, 2:2182–2190.

[219] Somasundaran, P. (2006). *Encyclopedia of Surface and Colloid Science*. Number v. 1 in Encyclopedia of Surface and Colloid Science. Taylor & Francis.

[220] Spasiano, D., Marotta, R., Malato, S., Fernandez-Ibañez, P., and Somma, I. D. (2015). Solar photocatalysis: Materials, reactors, some commercial, and pre-industrialized applications. a comprehensive approach. *Applied Catalysis B: Environmental*, 170–171:90 – 123.

[221] Stapley, J. A. and BeMiller, J. N. (2007a). The Hofer–Moest decarboxylation of d-glucuronic acid and d-glucuronosides. *Carbohydrate Research*, 342(3–4):610 – 613.

[222] Stapley, J. A. and BeMiller, J. N. (2007b). The Ruff degradation: a review of previously proposed mechanisms with evidence that the reaction proceeds by a Hofer–Moest-type reaction. *Carbohydrate Research*, 342(3–4):407 – 418.

[223] Stillings, R. A. and Nostrand, R. J. V. (1944). The action of ultraviolet light upon cellulose. I. irradiation effects. II. post-irradiation effects 1. *Journal of the American Chemical Society*, 66(5):753–760.

[224] Sugano, Y., Shiraishi, Y., Tsukamoto, D., Ichikawa, S., Tanaka, S., and Hirai, T. (2013). Supported Au–Cu bimetallic alloy nanoparticles: An aerobic oxidation catalyst with regenerable activity by visible-light irradiation. *Angewandte Chemie International Edition*, 52(20):5295–5299.

[225] Suljo, L., Phillip, C., and David, B. I. (2011). Plasmonic-metal nanostructures for efficient conversion of solar to chemical energy. *Nature M*, 10(12):911–921.

[226] Sutton, D., Kelleher, B., and Ross, J. R. (2002). Catalytic conditioning of organic volatile products produced by peat pyrolysis. *Biomass and Bioenergy*, 23(3):209 – 216.

[227] Tacchini, I., Terrado, E., Anson, A., and Martinez, M. (2011). Preparation of a TiO_2-MoS_2 nanoparticle-based composite by solvothermal method with enhanced photoactivity for the degradation of organic molecules in water under uv light. *Micro Nano Letters, IET*, 6(11):932–936.

[228] Tajmir-Riahi, H.-A. and Agbebavi, J. T. (1993). Carbohydrate interaction with monovalent ions. the effects of Li^+, Na^+, K^+, NH_4^+, Rb^+, and Cs^+ on the solid state and solution structures of d-glucono-1,5-lactone and d-gluconic acid. *Carbohydrate Research*, 241:25 – 35.

[229] Tang, H., Lévy, F., Berger, H., and Schmid, P. E. (1995). Urbach tail of anatase TiO_2. *Phys. Rev. B*, 52:7771–7774.

[230] Tarasevich, M., Sadkowski, A., and Yeager, E. (1983). Oxygen electrochemistry. In Conway, B., Bockris, J., Yeager, E., Khan, S., and White, R., editors, *Comprehensive Treatise of Electrochemistry*, pages 301–398. Springer US.

[231] Tauc, J. (1968). Optical properties and electronic structure of amorphous Ge and Si. *Materials Research Bulletin*, 3(1):37 – 46.

[232] Theurich, J., Lindner, M., and Bahnemann, D. W. (1996). Photocatalytic degradation of 4-chlorophenol in aerated aqueous titanium dioxide suspensions: A kinetic and mechanistic study. *Langmuir*, 12(26):6368–6376.

[233] Tobaldi, D., Pullar, R., Seabra, M., and Labrincha, J. (2014). Fully quantitative X-ray characterisation of Evonik Aeroxide TiO_2 P25. *Materials Letters*, 122:345 – 347.

[234] Tseng, I.-H., Chang, W.-C., and Wu, J. C. (2002). Photoreduction of CO_2 using sol–gel derived titania and titania-supported copper catalysts. *Applied Catalysis B: Environmental*, 37(1):37 – 48.

[235] Voisin, C., Fatti, N. D., Christofilos, D., and Vallée, F. (2001). Ultrafast electron dynamics and optical nonlinearities in metal nanoparticles. *The Journal of Physical Chemistry B*, 105(12):2264–2280.

[236] Wang, C., Yin, H., Chan, R., Peng, S., Dai, S., and Sun, S. (2009). One-pot synthesis of oleylamine coated AuAg alloy NPs and their catalysis for CO oxidation. *Chemistry of Materials*, 21(3):433–435.

[237] Wang, K.-H., Tsai, H.-H., and Hsieh, Y.-H. (1998a). The kinetics of photocatalytic degradation of trichloroethylene in gas phase over TiO_2 supported on glass bead. *Applied Catalysis B: Environmental*, 17(4):313 – 320.

[238] Wang, R., Hashimoto, K., Fujishima, A., Chikuni, M., Kojima, E., Kitamura, A., Shimohigoshi, M., and Watanabe, T. (1998b). Photogeneration of highly amphiphilic TiO_2 surfaces. *Advanced Materials*, 10(2):135–138.

[239] Wang, W., Chiang, L.-W., and Ku, Y. (2003). Decomposition of benzene in air streams by UV/TiO_2 process. *Journal of Hazardous Materials*, 101(2):133 – 146.

[240] Webster, D., PAVLACKY, E., and KOVASH, C. (2014). Blocked bio-based carboxylic acids and their use in thermosetting materials.

[241] Wei, W., Mao, X., Ortiz, L. A., and Sadoway, D. R. (2011). Oriented silver oxide nanostructures synthesized through a template-free electrochemical route. *J. Mater. Chem.*, 21:432–438.

[242] Wen, B., Ma, J., Chen, C., Ma, W., Zhu, H., and Zhao, J. (2011). Supported noble metal nanoparticles as photo/sono-catalysts for synthesis of chemicals and degradation of pollutants. *Science China Chemistry*, 54(6):887–897.

[243] Werpy, T. and Petersen, G. (2004). Top value added chemicals from biomass: Volume I – results of screening for potential candidates from sugars and synthesis gas. Technical report, U.S. Department of Energy, Energy Efficiency and Renewable Energy.

[244] Williamson, L. N. and Bartlett, M. G. (2007). Quantitative liquid chromatography/time-of-flight mass spectrometry. *Biomedical Chromatography*, 21(6):567–576.

[245] Xu, Z., Quintanilla, M., Vetrone, F., Govorov, A. O., Chaker, M., and Ma, D. (2015). Harvesting lost photons: Plasmon and upconversion enhanced broadband photocatalytic activity in core@shell microspheres based on lanthanide-doped $NaYF_4$, TiO_2, and Au. *Advanced Functional Materials*, 25(20):2950–2960.

[246] Yu, D., Aihara, M., and Antal, M. J. (1993). Hydrogen production by steam reforming glucose in supercritical water. *Energy & Fuels*, 7(5):574–577.

[247] Yum, J.-H., Walter, P., Huber, S., Rentsch, D., Geiger, T., Nüesch, F., De Angelis, F., Grätzel, M., and Nazeeruddin, M. K. (2007). Efficient far red sensitization of nanocrystalline TiO_2 films by an unsymmetrical squaraine dye. *Journal of the American Chemical Society*, 129(34):10320–10321.

[248] Zaia, J. (2004). Mass spectrometry of oligosaccharides. *Mass Spectrometry Reviews*, 23(3):161–227.

[249] Zhang, D., Yang, M., and Dong, S. (2015). Hydroxylation of the rutile TiO_2(110) surface enhancing its reducing power for photocatalysis. *The Journal of Physical Chemistry C*, 119(3):1451–1456.

[250] Zhang, F., Zhao, J., Shen, T., Hidaka, H., Pelizzetti, E., and Serpone, N. (1998). TiO_2-assisted photodegradation of dye pollutants II. adsorption and degradation kinetics of eosin in TiO_2 dispersions under visible light irradiation. *Applied Catalysis B: Environmental*, 15(1–2):147 – 156.

[251] Zhang, H., Okuni, J., and Toshima, N. (2011). One-pot synthesis of Ag–Au bimetallic nanoparticles with Au shell and their high catalytic activity for aerobic glucose oxidation. *Journal of Colloid and Interface Science*, 354(1):131 – 138.

[252] Zhang, J., Xu, Q., Feng, Z., Li, M., and Li, C. (2008). Importance of the relationship between surface phases and photocatalytic activity of TiO_2. *Angewandte Chemie*, 120(9):1790–1793.

[253] Zhang, X., Chen, Y. L., Liu, R.-S., and Tsai, D. P. (2013). Plasmonic photocatalysis. *Reports on Progress in Physics*, 76(4):046401.

[254] Zhang, X., Ke, X., and Zhu, H. (2012). Zeolite-supported gold nanoparticles for selective photooxidation of aromatic alcohols under visible-light irradiation. *Chemistry – A European Journal*, 18(26):8048–8056.

[255] Zhao, J., Zheng, Z., Bottle, S., Chou, A., Sarina, S., and Zhu, H. (2013). Highly efficient and selective photocatalytic hydroamination of alkynes by supported gold nanoparticles using visible light at ambient temperature. *Chem. Commun.*, 49:2676–2678.

[256] Zhao, X., Zhang, L., and Liu, D. (2012). Biomass recalcitrance. part I: the chemical compositions and physical structures affecting the enzymatic hydrolysis of lignocellulose. *Biofuels, Bioproducts and Biorefining*, 6(4):465–482.

[257] Zheng, J., Nicovich, P. R., and Dickson, R. M. (2007). Highly fluorescent noble-metal quantum dots. *Annual Review of Physical Chemistry*, 58(1):409–431.

[258] Zhou, W. and Fu, H. (2013). Mesoporous TiO_2: Preparation, doping, and as a composite for photocatalysis. *ChemCatChem*, 5(4):885–894.

[259] Zhou, W., Liu, H., Wang, J., Liu, D., Du, G., and Cui, J. (2010). Ag_2O/TiO_2 nanobelts heterostructure with enhanced ultraviolet and visible photocatalytic activity. *ACS Applied Materials & Interfaces*, 2(8):2385–2392. PMID: 20735112.

[260] Zhou, X., Liu, G., Yu, J., and Fan, W. (2012). Surface plasmon resonance-mediated photocatalysis by noble metal-based composites under visible light. *J. Mater. Chem.*, 22:21337–21354.

[261] Zhu, H., Chen, X., Zheng, Z., Ke, X., Jaatinen, E., Zhao, J., Guo, C., Xie, T., and Wang, D. (2009). Mechanism of supported gold nanoparticles as photocatalysts under ultraviolet and visible light irradiation. *Chem. Commun.*, pages 7524–7526.

[262] Zugenmaier, P. (2001). Conformation and packing of various crystalline cellulose fibers. *Progress in Polymer Science*, 26(9):1341 – 1417.

Appendix A

A.1 HPLC Determination of Bioderived Molecules

Sugars are highly polar molecules and for this reason, the common C_{18} reverse-phase columns are not suitable for this analysis, because the molecules would just coelute and thus no separation would occur. To achieve a good level of separation it is necessary to have a polar environment made by the stationary phase, able to interact with the sugars and by the polar eluent phase tuned to maximize the interactions occurring between the analytes and the stationary phase. There are several options available on the market for the sugar analysis and the vast majority of them are based on two different columns:

- DIOL column, in which the silica particles are coated with aliphatic chains with terminal –OH groups
- AMINO column: in which the silica particles are coated with aliphatic chains with terminal $–NH_2$ groups

Both these columns have in common the presence of highly polar terminal groups that are able to interact in several ways with the analytes. In the literature these two types of column are widely applied in the separation of sugars, and sugar alcohols. After having performed a literature background, several methods have been found in the separation of the degradation products of cellulose. Unfortunately, it is not possible to compare the performances of each

method because the chromatograms are often not present in the supporting information of the articles (Table A.1).

Table A.1 Some of the most used analytical method present in the literature for the determination of the degradation products from biomass

Method	Column	Eluent Phase	Detector	Flow rate (ml min^{-1})	Temperature (°C)	Ref.
1	Aminex HPX-87H (9 μm, 300 x7.8 mm)	0.05 mM H_2SO_4	RID	0.7	50	[148]
2	Transgenomic CARBONSep CHO-620 (10μm, 6.5 x 300 mm)	H_2O	RID	0.5	65	[73]
3	Nucleogel OA HY (10 μm, 300 × 7.8 mm)	0.05 mM H_2SO_4	RID + UV-Vis (254 nm)	0.5	80	[199]
4	Varian Metacarb 67C column (8 μm, 300 × 7.8 mm)	H_2O	RID			[98]
5	C_{18} (4.6 x 250 mm)	CH_3OH/H_2O (77/23 v/v)	UV-Vis (284 nm)	0.8		[86]

The determination and quantification of sugars and of the dehydration-hydrogenation products is really challenging. For these reason a lot of effort was put in the development of a robust and reliable analytical method for the quantification of these chemicals. Several columns and experimental conditions had been tested to tune and obtain the best performing analysis set-up. The method that has been applied is the one with the refractive index detection (RID) and the UV-Vis with a diod array detector (DAD), and the column chosen is the Aminex HPX-87H, because the diol columns proved to be unsatisfactory in the separation of the sugars standards due to a poor baseline resolution and the scarce separation between the sugars and the dehydration products. The injection of each standard solution was repeated 3 times and the values for the retention times (t_R) are obtained by averaging the 15 retention times collected for each sample. As it can be seen in, the instrument has a linear response in the concentration range considered, and the linearity between the concentration and the signal is confirmed by the linear regression coefficient R^2 which is greater than 0.995 for each of the molecules considered. In addition, another useful parameter is the capacity factor (k) defined as follows:

$$k = \frac{t_R - t_m}{t_m} \tag{A.1}$$

In which t_R is the retention time for the analyte, t_m is the retention time of the mobile phase. This parameter basically defines the quality of the separation at given conditions for the analytes considered. Usually, to achieve a decent chromatographic separation values of k between 1 and 5 are required. In our case it can be noted how the values of k are generally lower than 1. These are the typical values reported in the literature for the separation of sugars and sugar alcohols achieved with the Aminex column (Table A.2).

Table A.2 Retention time and calibration curve obtained for the standard compounds used in this study

Standard	Retention Time t_R (min)	Range (mM)	Detection	Equation	R^2	k
Glucose	8.66	1-50	RID	y = 25537x - 59	0.9999	0.45
Gluconic Acid	8.50	1-50	RID	y = 24846x - 428	1	0.42
Glucaric Acid	7.56	1-50	RID	y = 25552x - 3824	0.9998	0.27
Glucose	8.41	2-50	DAD 202 nm	y = 1.34x + 1.75	0.999	0.41
Gluconic Acid	8.30	1-50	DAD 202 nm	y = 143.4x - 3.1	1	0.39
Glucaric Acid	7.30	1-50	DAD 202 nm	y = 176.95x - 50.69	0.9999	0.22
Gluconic Acid	8.29	1-50	DAD 210 nm	y = 87.74x - 5.36	1	0.39
Glucaric Acid	7.29	1-50	DAD 210 nm	y = 145.27x - 38.45	0.9998	0.22
Arabinose	10.02	0.05-5	RID	y = 21878x + 232	0.9996	0.68
Arabitol	10.38	0.05-5	RID	y = 20344x + 183	0.9998	0.74
Gluconic Acid	8.50	0.05-5	RID	y = 25124x + 239	0.9996	0.42
Gluconic Acid	8.23	0.05-5	DAD 202 nm	y = 154.76x - 9.23	0.999	0.38
Gluconic Acid	8.23	0.05-5	DAD 210 nm	y = 85.31x - 2.89	0.9908	0.38
Glyceraldehyde	10.72	0.1-2	RID	y = 12320x + 698	0.9977	0.80
Glyceraldehyde	10.46	0.1-2	DAD 202 nm	y = 51.75x + 2.00	0.9991	0.75
Glyceraldehyde	10.45	0.2-2	DAD 210 nm	y = 27.071x + 0.200	0.9997	0.75
Erythrose	10.87	0.1-2	RID	y = 12771x - 73.12	0.9999	0.82
Formic Acid	12.94	0.25-2	DAD 202 nm	y = 36.16-0.32	0.9988	1.17
Cellobiose	7.01	0.2-50	RID	y=49367-1775	0.9999	0.17
Cellobiosan	7.78	0.15-5	RID	y=42379x+24	0.9998	0.30
Cellobionic Acid	6.89	0.125-4	DAD 210 nm	y=63.11x-0.40	0.9999	0.15
$C_{11}H_{20}O_{10}$	7.41	-	RID	y=49367-537	0.9999	0.24
Cellobionic Acid	6.95	0.125-4	RID	y=36710x+24	0.9999	0.16

Despite the generally low capacity factor, the relative standard deviation (%RSD) is generally less than 3% over 3 replicate injections based on the peak area, thus indicating a high reproducibility level of the measurements in the range considered. The analysis of the standard samples confirmed that two independent detectors are required to analyse the samples coming from the degradation of biomass and sugars in general. In fact, the RID is a universal detection system based on the different refractive index between the mobile phase and the analyte, and for this reason it is extremely versatile and it is characterized by high sensitivity. On the other hand, this means that it is really sensitive to multiple parameters,

such as temperature, and eluent phase composition to name but a few. It is clear how there is a price to pay for such high sensitivity and flexibility of this detection system, and it is also clear how it is necessary to couple the RID with another detector to be able to analyse different samples by exploiting different properties. That is the main reason why the application of just one detection system is not sufficient due to the possible presence of matrix effects in real samples. The application of a series of two independent detection systems allowed us to analyse with the DAD detector the oxidation products such as gluconic acid, cellobionic acid, formic acid, and other compounds which absorb in the visible spectrum, whilst the sugars and sugar alcohols were analysed with the RID. In Table A.2 are reported several wavelength values for the some of the standard used. This is because at 202 nm, glucose, and other sugars, present small absorption values, and therefore, it is necessary to exclude the absorbance of these compounds to prevent the underestimation of the concentration of the other coeluting species. Specifically, in the case of glucose, gluconic and glucaric acid, it is fundamental to isolate each of the compounds due to the close retention time and the similar k values (Figure A.1a).

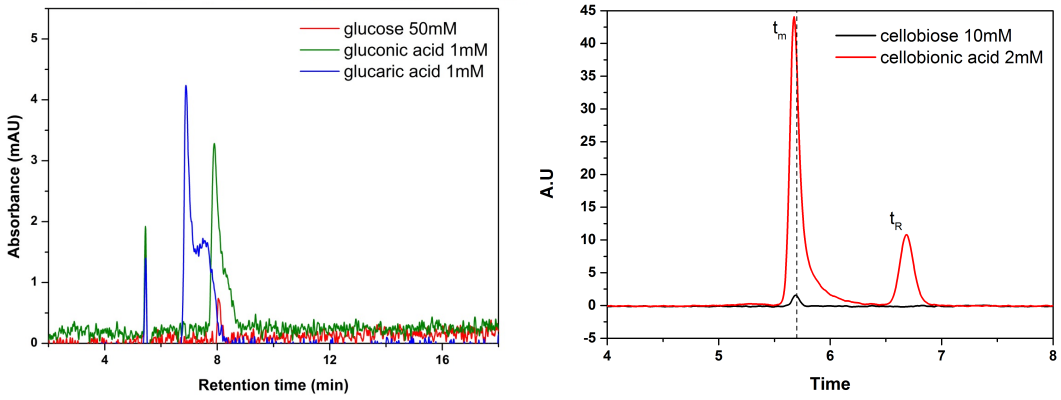

Figure A.1 A.1a DAD signals recorded at 210 nm. It can be seen how the glucose absorption profile (red) is 0 at 8.6 minutes and only gluconic acid can be quantified; A.1b DAD signals recorded at 210 nm. It can be seen how the cellobiose absorption profile (red) is 0 at 7 minutes and only cellobionic acid can be quantified

The same approach was used when the couple cellobiose/cellobionic acid had to be identified. Also in this case, the retention time of both species is very close, thus requiring a decoupling of the peaks (Figure A.1b). In order to determine the concentration of the cellobionic acid produced during the oxidation product, and estimate the conversion of the starting cellobiose, the following approach was used: the cellobionic acid was determined using the calibration curve recorded at RID, the area of the acid was subtracted from the peak relative to the mixture cellobiose plus cellobionic acid to obtain the net contribution of the starting reactant.

A.2 HPLC-QTOF Determination of Bioderived Molecules

The method development discussed in the previous section, gave us fundamental understanding of how to optimize the analysis parameters to achieve baseline separation for each of the standards considered in this work, but unfortunately, reaction mixtures are not always simple to analyse due to the presence of unknown products.

Time-of-flight mass spectrometry (TOF) has seen huge improvements in the past 20 years, and unlike with common quadrupole instruments, it is possible to record and collect spectra over a short period of time, and instead of scanning only one specific mass to charge ratio (m/z) value, it is possible to gather data coming from all the components of the sample as all the ions are pulsed down the flight tube. In fact, the main advantage of this technique relies on the fact that packages of ions are sent down the flight tube, but because of the different molecular weight, smaller ions will reach the detector faster than the heavier ions. Additionally, as the velocity of the impact of the ion on the detector is proportional to its mass, it is possible to calculate the m/z ratio just by knowing how much time it took to reach the detector, thus giving the instrument a theoretical limitless mass range.

There is an obvious limitation to this, and it is due to the amount of ions reaching the detector as this can cause saturation problems, causing shifts in the m/z values and impacting

on the sensitivity of the instrument. The shift in the m/z values can become a serious issue when determining the molecular ions of unknown species for the exact mass identification analysis.

To overcome this difficulty, the ions are decelerated before reaching the detector, increasing the linear range of response to several order of magnitude. TOF instruments are currently used in the pharmaceutical and food industry, but one of the main fields of applications is in proteomics as this technique is particularly useful in determine the molecular structure and fragmentation of proteins, enzyme and metabolites.

The main advantage of using this technique over the standard quadrupole instruments, is the possibility of removing background noise and to decouple the presence of contaminants in the sample. The improved sensitivity allows the identification of compounds with the same unit mass and this makes QTOF an excellent tool for screening multiple compounds of interest at once.[244] Zaia [248] reviewed the application of mass spectrometry techniques

Figure A.2 Picture of the Agilent 6530 QTOF instrument used in this work.

in the analysis of oligosaccharides as they their fragmentation properties are similar to the ones observed from proteins. Based on the nomenclature introduce by Domon and Costello [77] on the fragmentation of oligosaccharides, it is possible to predict, and identify the major species produced during the fragmentation process (Figure A.3). Fragment ions that contain

non-reducing ends are labelled with upper case letters from the beginning of the alphabet (A,B,C) whilst those containing the reducing end are labelled with letters at the end of the alphabet (X,Y,Z). In both nomenclature systems, the subscripts identify the cleaved ions. The A and X ions are formed from the cleavage across the glycosidic bond.

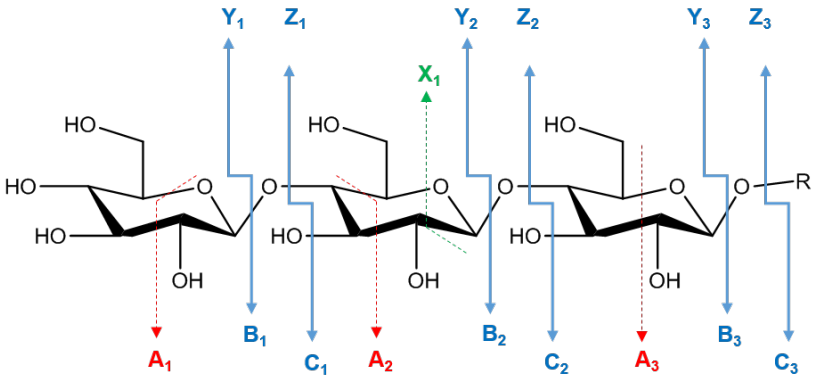

Figure A.3 Nomenclature for the fragmentation pattern of polysaccharides adapted from Domon and Costello [77]

Typically, the species identified with this technique are the protonated molecular ions $[M+nH]^+$, the deprotonated ones $[M-nH]^-$, and the sodiated ions $[M+Na]^+$ for several disaccharides the main fragments are reported in Table A.3.

Table A.3 Lithium product ion abundances during MS/MS analysis.Data adapted from Asam and Glish [14].

		Product ions					
Disaccharide	**Linkage**	**-H_2O[a]** (m/z = 331)	**-$C_2H_4O_2$** (m/z =289)	**-$C_3H_6O_3$** (m/z = 259	**-$C_4H_8O_4$** (m/z =229)	Y_1 (m/z = 187)	B_1 (m/z = 169)
Isomaltose	α-1,6	9.4	100	44.2	14.2	82.3	12.6
Maltose	α-1,4	100	78.4		2.6	67.6	49.2
Cellobiose	β-1,4	100	48.1		7	22.9	55.8
Lactose[b]	β-1,4	100	42.8			80.4	82

[a] Intensity relative to base peak
[b] Galactosyl (1→4) glucose

A.2.1 Instrument Overview

Electrospray Ionisation (ESI)

The sample ionisation step is one of the most important aspects of the QTOF analysis as its duty is to remove the solvent and inject as much analyte as possible in the capillary. In Figure A.4, the schematic layout of the ESI source is shown for the Agilent 6530 used in this work.[1] The HPLC is connetted to the inlet of the nebuliser where the eluent phase and

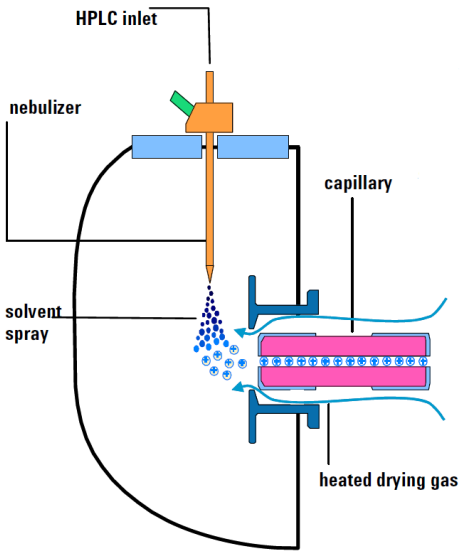

Figure A.4 Electrospray ionisation source installed on the Agilent 6530

the analyte are sprayed in the chamber. Located at an angle (not shown here) is the standard solution nebulising nozzle which is designed to provide a constant flow of a reference mixture which is then sprayed along with the analyte in the capillary. The presence of an internal reference at all times, provides better results and enhanced sensitivity. Located opposite to both nebulisers, there is the drying gas supply, which is a heated N_2 flow (up to 350°C) designed to remove the solvent and allow only the analyte and the standard references to enter the quadrupole chambers. This allows for the complete suppression of solvent effects, chemical equilibria, and the presence of contaminants. Additional to the solvent removal,

[1] Information available on the Agilent 6530 instrument can be found on the manual at www.agilent.com

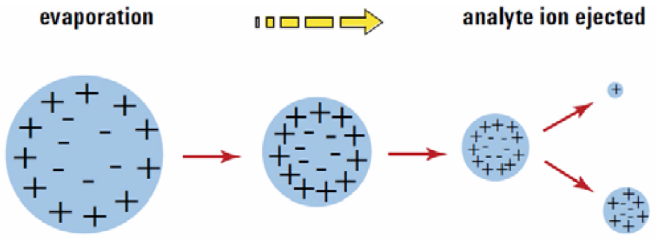

Figure A.5 Coulombian effect and charging mechanisms of the eluent droplets with the formation of a bare ion

the presence of the drying gas charges the solvent droplets due to Coulombian repulsions mechanisms, and the charge on these molecules is high enough (10^8 V cm^{-3}) the ions produced are attracted by the electrical field of the capillary and propelled in the ion optics and to the mass analyser (Figure A.5). For these purposes, the importance of the buffers, and the ionization properties of the solvents use in the chromatographic separation have dramatic impacts on the quality of the mass spectrometry analysis result. Heat capacity, dielectric constant, and surface tension are key variables for a successful and efficient ionization process. Ideally these considerations should be made:

- Use solvents with low heat capacity and surface tension to enhance ion desorption
- Use solvents which do not interfere with the ions in the gas-phase reactions (e.g. proton transfer, ion pair reactions)
- Adjust solvent pH to the polarity of the ions to be analysed
- Reduce, if not avoid totally, the presence of inorganic buffers to avoid salts build-up in the ion source.

QTOF schematics

After being vaporized and accelerate through the capillary, the ions are accelerated in the quadrupole tubes where the ions to be fragmented in the collision cell, and there are subsequently collimated in the skimmer to improve resolution. After being filtered, the ions

arrive on the ion pulser which has an oscillating electric potential, and acts as a trampoline for the incoming ions which are pushed up the flight tube. At the top of the flight tube there is an ion mirror to improve resolution, which deflects the ions down to the detector (Figure A.6).

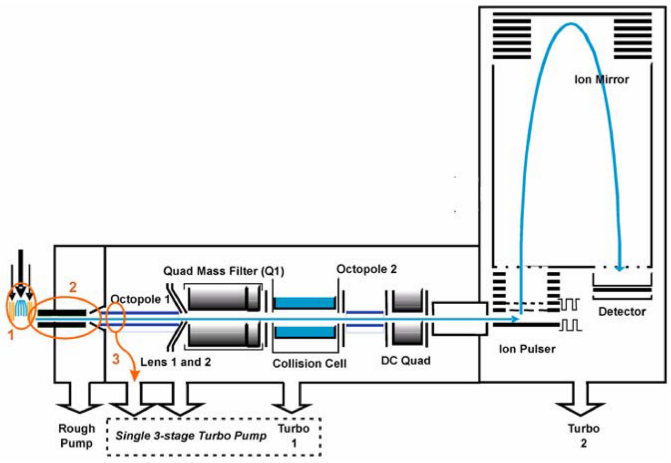

Figure A.6 Schematic representation of a QTOF system. The nebuliser, the capillary and the entrance to the ion optics are circled in orange.

Appendix B

B.1 Synthesis and Characterization of Cellobionic Acid

Because of the lack of standardize protocols for the oxidation of cellobiose to the corresponding cellobionic acid, and adapted protocol for the oxidation of lactose to lactobionic acid was used instead, and further characterization of the reaction products was necessary to confirm the purity of the solid obtained.

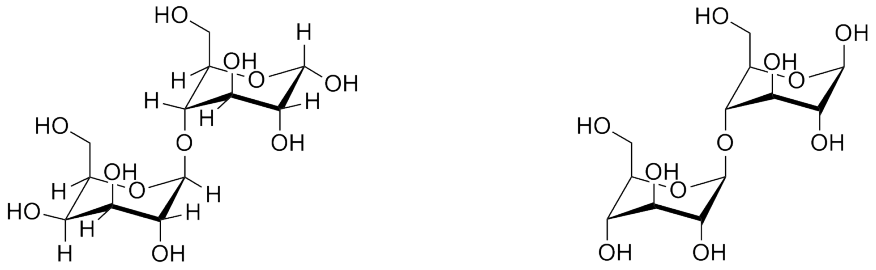

Figure B.1 Molecular structures of lactose (left) and cellobiose (right)

The first characterization technique used was NMR through the acquisition of the ^{1}H and ^{13}C spectra (400 MHz, D_2O. In Figure B.7 the ^{13}C cellobiose spectrum is reported and it is possible to count 18 carbon signals due to the presence of the anomeric carbon (Figure B.2b). As a consequence of the different conformation, there are two possible spacial configuration of the glycosidic unis which produce the α-D-cellobiose and the β-D-cellobiose as shown in Figure B.2a. When cellobiose is oxidised to the corresponding acid, only 12 carbon atoms

are observed due to the loss of the anomeric feature. Additionally, the signal at 178 ppm is a clear indication of the presence of the carboxylic functionality. In the literature previous attemps to determine the structure of cellobionic acid with NMR analysis has been performed after the ozonation of cellobiose by Moe et al. [169] and the ^{13}C spectrum obtained from the cellobionic acid is reported in Figure Figure B.3. Unfortunately, the signal of the carboxylic carbon at 180 cannot be observed, unlike in our case. Further analysis on the ^{1}H spectra of the starting cellobiose and the cellobionic acid (Figure B.4) reveals with how the dashed lines are in correspondence of the duplets at 4.5, 4.7 and 5.2 ppm respectively. Specifically, the duplet at 4.7 ppm was assigned by Moe et al. [169] to the H1 of the glycosidic unit as it is the only signal in the anomeric region. This signal is not detectable in the cellobionic acid spectrum, to further confirm the successful oxidation to the corresponding acid. Additionally to the NMR analysis, HPLC-QTOF of the cellobionic acid was performed. Figures B.8b and B.8a show the m/z values for the fragment of cellobiose and cellobionic acid respectively. It is clear, by looking at the scale on each of the graphs, how the concentration of the starting material defined by the molecular ion ($[C_{12}H_{22}O_{11}]$+Na)$^{+}$= 365.10703 and ($[C_{12}H_{22}O_{12}]$+Na)$^{+}$= 381.10078 for cellobiose and cellobionic acid respectively, is significantly lower (one order of magnitude) for cellobiose, which is present in traces compared with the corresponding acid. In Table B.1 are displayed the main fragments detected, and it has to be noted, that during the analysis the loss of water from disaccharides is a common feature.

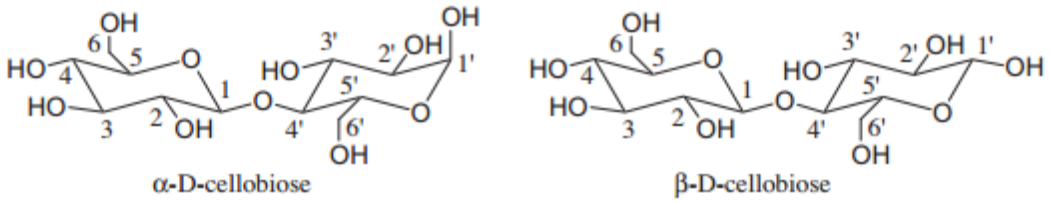

(a) Molecular structures of the α-D-cellobiose and the β-D-cellobiose.

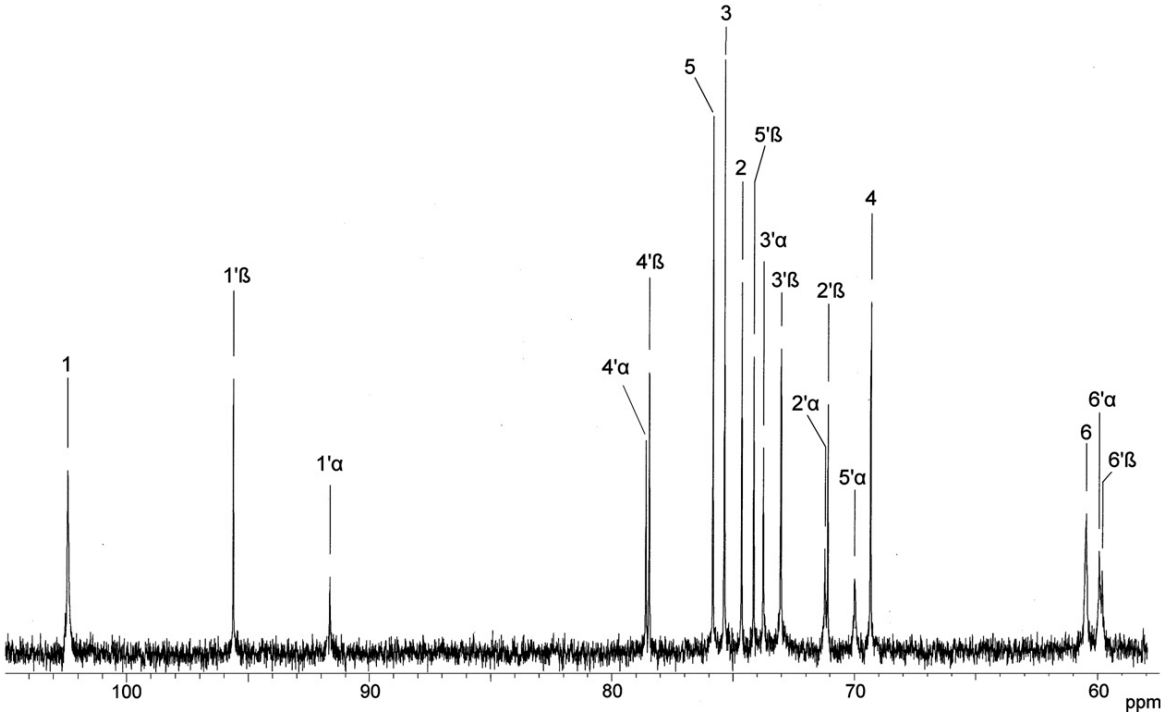

(b) Cellobiose ^{13}C NMR (D_2O, 95ml ml^{-1}) at 23°C

Figure B.2 Molecular structures of the α-D-cellobiose and the β-D-cellobiose (B.2a) and Cellobiose ^{13}C NMR spectra (B.2b). Taken from Amarasekara et al. [10]

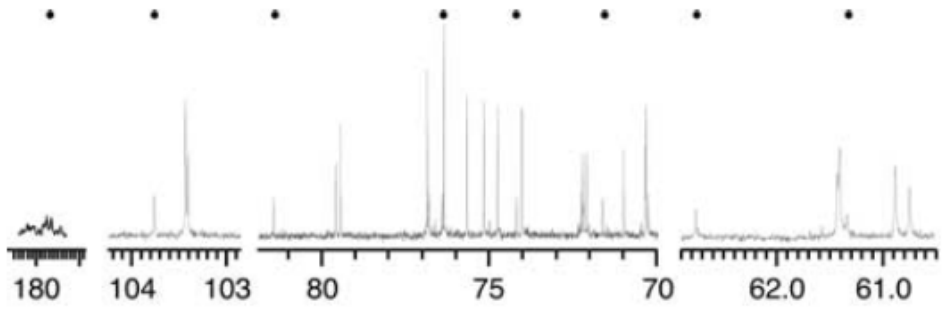

Figure B.3 ^{13}C NMR, the dotted signals are absent in the starting cellobiose. Acquisition parameters: 100 MHz, D_2O, with a pulse angle of 30°, acquisition time of 30 seconds, sweep width of 25125.6 Hz, and a relaxation delay of 1.8 seconds. Taken from Moe et al. [169]

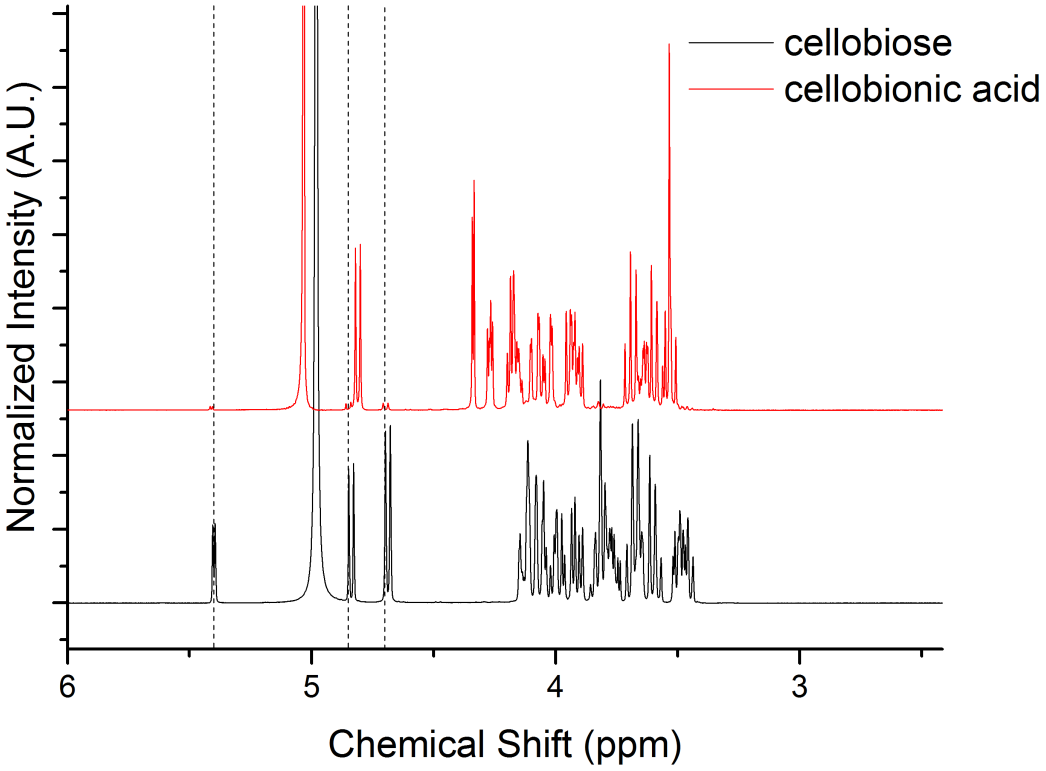

Figure B.4 ^{1}H NMR comparison between cellobiose (black) and cellobionic acid (red).

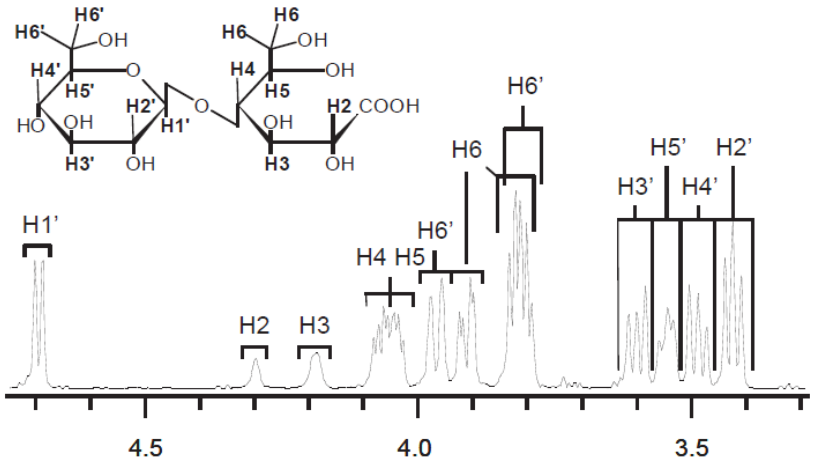

Figure B.5 ^{1}H NMR from Moe et al. [169] for the cellobionic acid extracted from the COSY 2D experiment.

Table B.1 m/z species identified for cellobiose and cellobionic acid for the 2.8 mM standard prepared from the crystallised acid recovered after the synthesis

m/z	Species	Formula & Ion Species
368.11478	$(M+Na)^+$	$([C_{12}H_{22}O_{11}]+Na)^+$
367.11185	$(M+Na)^+$	$([C_{12}H_{22}O_{11}]+Na)^+$
366.11034	$(M+Na)^+$	$([C_{12}H_{22}O_{11}]+Na)^+$
365.10703	$(M+Na)^+$	$([C_{12}H_{22}O_{11}]+Na)^+$
348.09986	$(M+Na)^+[-H_2O]$	$([C_{12}H_{22}O_{11}]+Na)^+[-H_2O]$
347.0957	$(M+Na)^+[-H_2O]$	$([C_{12}H_{22}O_{11}]+Na)^+[-H_2O]$
326.12170	$(M+H)^+[-H_2O]$	$([C_{12}H_{22}O_{11}]+H)^+[-H_2O]$
325.11375	$(M+H)^+[-H_2O]$	$([C_{12}H_{22}O_{11}]+H)^+[-H_2O]$
384.10865	$(M+Na)^+$	$([C_{12}H_{22}O_{12}]+Na)^+$
383.10561	$(M+Na)^+$	$([C_{12}H_{22}O_{12}]+Na)^+$
382.10427	$(M+Na)^+$	$([C_{12}H_{22}O_{12}]+Na)^+$
381.10078	$(M+Na)^+$	$([C_{12}H_{22}O_{12}]+Na)^+$
364.09358	$(M+Na)^+[-H_2O]$	$([C_{12}H_{22}O_{12}]+Na)^+[-H_2O]$
363.09030	$(M+Na)^+[-H_2O]$	$([C_{12}H_{22}O_{12}]+Na)^+[-H_2O]$
341.10806	$(M+H)^+[-H_2O]$	$([C_{12}H_{22}O_{12}]+H)^+[-H_2O]$

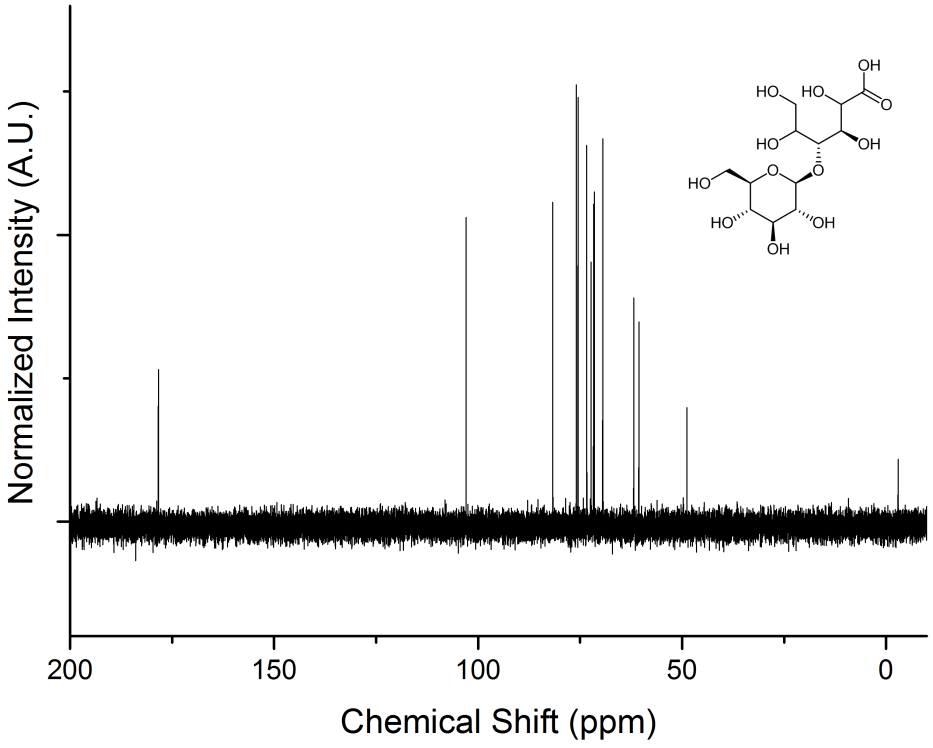

Figure B.6 ^{13}C spectra (400 MHz, D_2O) of the crystallised cellobionic acid

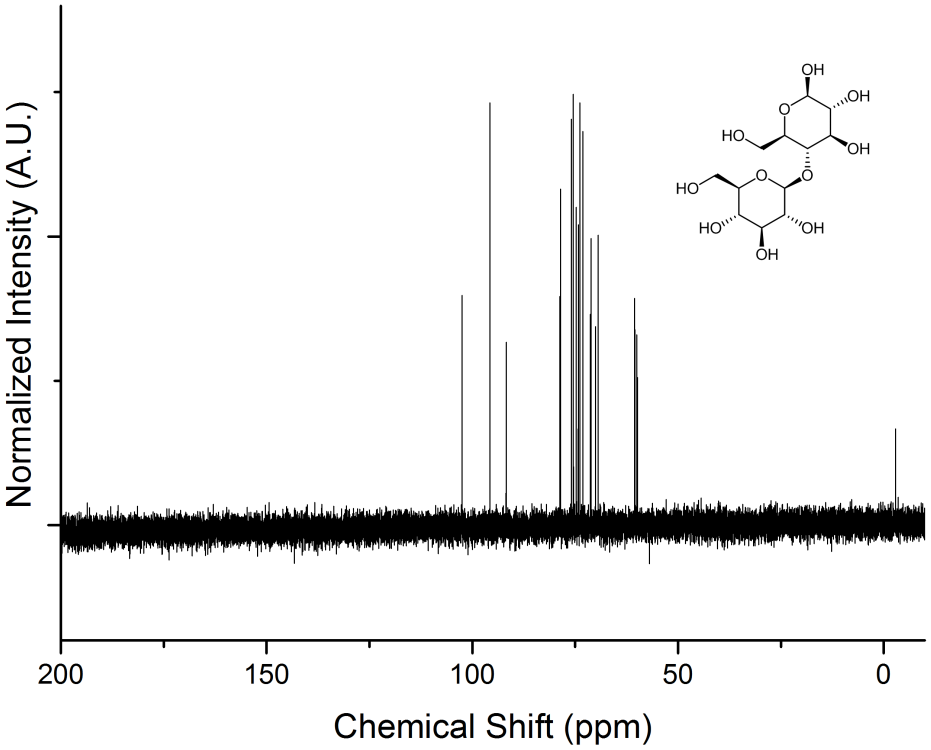

Figure B.7 ^{13}C spectra (400 MHz, D_2O) of the starting cellobiose

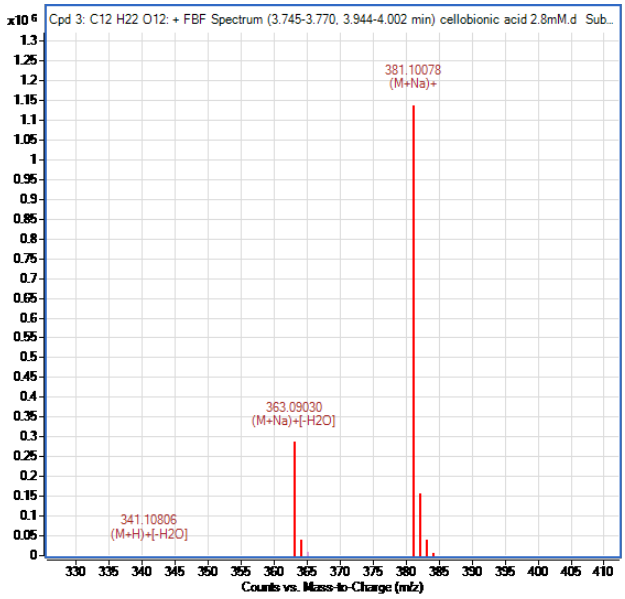

(a) $C_{12}H_{22}O_{12}$

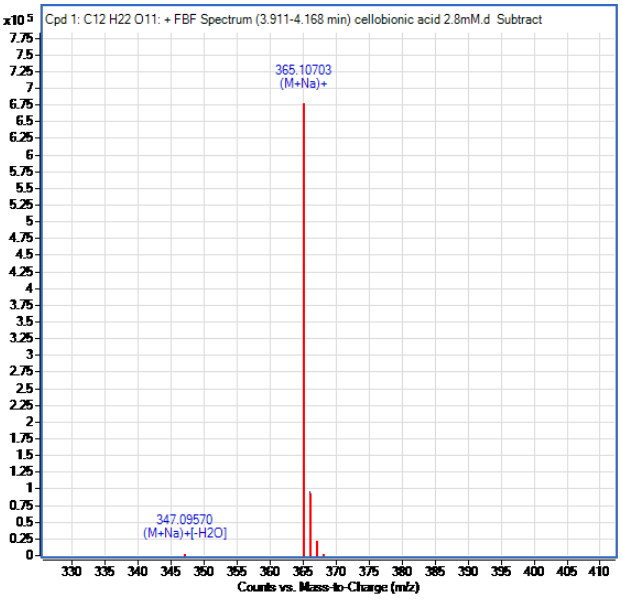

(b) $C_{12}H_{22}O_{11}$

Figure B.8 Cellobionic acid and cellobiose molecular ions and ion species detected

Appendix C

C.1 Solid UV-Vis Measurements

Solid UV-Vis spectroscopy is a powerful and really useful technique as a first screening of powder materials. It is cheap, fast, reliable and it provides important information regarding the structure of the material and its properties. Many research authors use this technique to evaluate the bandgap of semiconductors, and assess the presence of plasmonic metal, or doping ions in the material just by monitoring the powder adsorption in the UV and visible range of the spectrum. Unlike liquid UV-Vis spectroscopy, governed by the Lamber-Beer law in which the absorbance (A_λ) is directly proportional to the concentration of the analyte (c), the length path (l), and the extinction coefficient (ε) (Eqn.C.1), solid UV-Vis uses the reflectance (R) as a variable to describe the properties of the system (Eqn.C.2).

$$A_\lambda = log_{10}(l/T_\lambda) = log_{10}(I_{o\lambda}/I_\lambda) = \varepsilon cl \tag{C.1}$$

In solid samples, when particles are small compared with the beam cross section, but larger than the incident light wavelength, diffraction phenomena occur because of the interaction between light and particles. In random size samples, the incident light is scattered in all directions, and 3 different phenomena are possible: reflection, refraction and diffraction (Figure C.1). All these phenomena are influenced by the size and the packing of the particles,

as when the dimensions are similar to the wavelength value, these three components are impossible to separate and it is generally identified as scattering. The Kubelka-Munk (K-M)

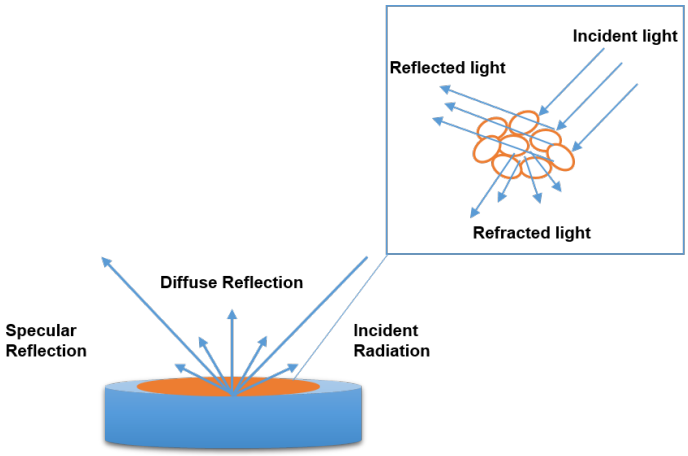

Figure C.1 Diffraction, reflection and refraction phenomena occurring upon light irradiation on solid samples

function is defined by two parameters, the adsorption (K) and the scattering coefficient (S)(Eqn.C.2). These two parameters are function of the particle size of the sample and the thickness of the layer to be analysed, and was originally applied for the analysis of paints on surfaces.[138] This model assumes that the sample layer can be divided in a large number of elementary layers which have boundaries parallel to the ones of the complete layer and have identical optical properties.[138]

$$F(R_\infty) = \frac{(1-R_\infty)^2}{2R_\infty} = \frac{K}{S} \tag{C.2}$$

Due to the difficulty in measuring R_∞, defined as the reflectance of an infinite thick layer, another variable is needed, r_∞ defined as follows:

$$r_\infty = \frac{r_\infty(sample)}{r_\infty(standard\ material)} \tag{C.3}$$

By applying equation C.3 to C.2, we obtain the following expression:

$$F(r_\infty) = \frac{(1-r_\infty)^2}{2r_\infty} = \frac{K}{S} \tag{C.4}$$

Typically, $BaSO_4$ is used as a standard material as it has almost ideal reflecting properties across a wide wavelength range.[136] In fact, several manufacturers, apply a coating of this material inside the integrating sphere to insure a high signal to noise ratio to the detector to obtain higher sensitivity. The typical configuration for a solid UV-Vis spectrophotometer is reported in Figure C.2.[1] Typically, the reflectance profile obtained for TiO_2 materials, is

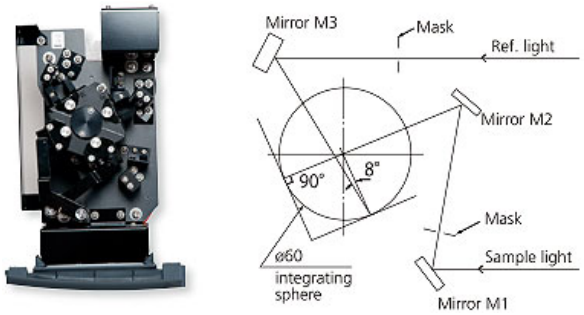

Figure C.2 Typical instrumental configuration for a spectrophotometer equipped with a integrating sphere.

reported in Figure C.3. The typical sigmoid shape of the reflectance is due to the absorption of the material at wavelengths around 400 nm, which causes the reflectance (R) to drop and have a constant value at wavelengths lower than 380 nm. In this work, we used $BaSO_4$ as a reference material to record the absorption profiles of several materials. But in some cases, when the TiO_2 was treated and it was necessary to distinguish between the modification of the support in addition to the presence of metal nanoparticles on the surface, different relationship were used to obtain information on the bandgap positioning and to evaluate the LSPR band position, therefore, sometimes the blank or untreated TiO_2 reflectance spectra was used as reference instead of the $BaSO_4$ blank. It is possible to determine the bandgap of solids using several arrays of equations, based on different assumptions. A good recent

[1] Picture available from the Shimadzu website (www.shimadzu.com)

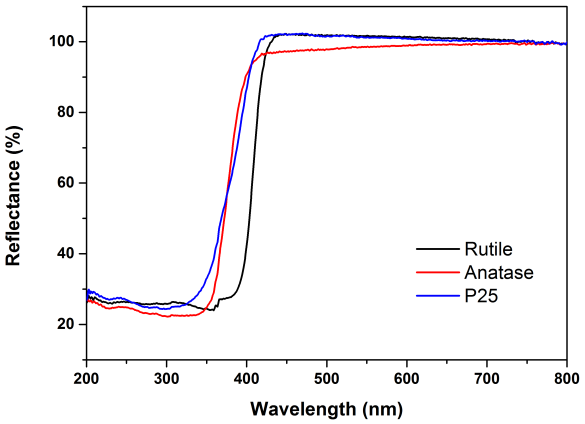

Figure C.3 Typical reflectance profiles obtained from the different TiO_2 polymorphs using $BaSO_4$ as reference

review on the application of different equations was published by Lopez and Gomez [156]. In this study, the Kubelka-Munk function (C.2) was modified multiplying the $F(R_\infty)$ by $h\nu$ to obtain the energy of the bandgap in eV and by using a coefficient (n) associated with the specific transition considered. Therefore, the equation C.2 can be rewritten as follows identifying α as the extinction coefficient:

$$\alpha(h\nu) = (F(r_\infty) \cdot h\nu)^n \tag{C.5}$$

The coefficient is reported to be n=1/2 for direct allowed transition (Figure C.4a), and n=2 for indirect allowed transition (Figure C.4c). The so called Tauc plot is the result of the relationship between C.5 and $h\nu$. [231]

From Figure C.5 it is clear how the amount of information obtainable from the simple UV-Vis spectrum is not sufficient to assess the presence of metal nanoparticles on the surface of the TiO_2 especially if their absorption happens to be in the region where the semiconductor absorbs light. It is necessary to de-convolute the spectra and the Tauc plot obtained using n=2 is displayed in Figure C.5b. The presence of the metal on the surface of the semiconductor is now clear, and additionally, it is possible to examine the nature of the nanoparticles (mono, bimetallic, core-shell) according to the peak shape and positioning.

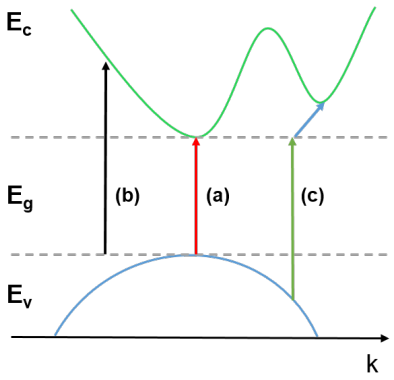

.

Figure C.4 Schematic bandgap transition representation. (a) allowed direct transition; (b)forbidden direct transition; (c) allowed indirect transition with the required assistance of a phonon. All these transition are possible only with a photon of energy $\geq E_g$. Adapted from [156]

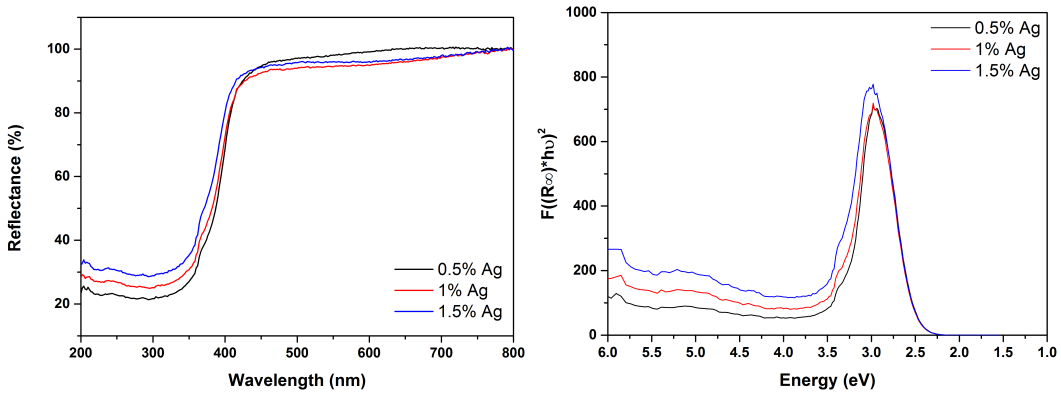

(a) **(b)**

Figure C.5 UV-Vis absorption profile (C.5a) for Ag/TiO_2 supported catalyst with different metal loadings and the corresponding Tauc plot (C.5b) in which only the LSPR can be observed

Appendix D

D.1 Cellobiose Oxidation Tables

D.2 2.8 mM Cellobiose Solutions

Table D.1 Cellobiose conversion, Product Distribution and Mass Balance values for the reactions run with a 2.8 mM cellobiose conversion under UVA light over 120 minutes of exposition using pure H_2O as reaction medium

Catalyst	Reaction Time (min)	Cellobiose Conversion (%)	Cellobionic Acid (%)	Cellobiosan (%)	$C_{11}H_{20}O_{10}$ (%)	Glucose (%)	Gluconic Acid (%)	Arabinose (%)	Erythrose + Glyceraldehyde (%)	Formic Acid (%)	Mass Balance (%)
Ag/TiO_2	30	6.40	63.71	4.25	32.05	-	-	-	-	-	100.66
	60	9.92	56.25	3.20	31.31	9.24	-	-	-	-	100.51
	90	14.12	55.97	3.77	32.13	8.13	-	-	-	-	100.57
	120	14.92	47.91	7.35	35.43	9.32	-	-	-	-	103.33
$Au_{0.05}Ag_{0.95}/TiO_2$	30	5.06	42.05	6.33	22.74	28.87	-	-	-	-	101.74
	60	12.99	50.99	4.97	26.82	17.22	-	-	-	-	98.99
	90	16.99	36.41	4.46	18.68	18.17	-	-	-	22.28	101.88
	120	22.52	43.62	1.99	20.50	10.67	-	-	-	23.22	99.53
$Au_{0.15}Ag_{0.85}/TiO_2$	30	7.47	48.93	8.73	26.50	15.85	-	-	-	-	100.39
	60	14.50	54.73	5.58	24.48	15.20	-	-	-	-	98.93
	90	16.16	46.93	6.56	32.13	14.38	-	-	-	-	101.27
	120	20.96	44.64	1.80	24.13	5.06	-	1.13	23.23	-	101.53
$Au_{0.50}Ag_{0.50}/TiO_2$	30	6.50	49.93	-	32.88	17.19	-	-	-	-	101.14
	60	13.17	53.15	2.81	29.15	14.89	-	-	-	-	99.27
	90	17.37	50.38	3.66	33.82	12.14	-	-	-	-	99.73
	120	23.66	42.63	3.55	24.71	9.27	-	-	-	19.84	101.28
$Au_{0.85}Ag_{0.15}/TiO_2$	30	11.33	54.03	4.66	29.19	12.13	-	-	-	-	98.99
	60	20.99	58.62	3.38	27.09	10.91	-	-	-	-	98.05
	90	26.61	48.28	4.33	25.68	11.40	10.32	-	-	-	102.14
	120	34.21	44.23	1.55	18.75	12.89	10.28	-	-	12.29	103.42
$Au_{0.95}Ag_{0.05}/TiO_2$	30	10.22	75.98	5.54	18.48	-	-	-	-	-	99.53
	60	14.10	74.92	4.01	21.08	-	-	-	-	-	99.44
	90	20.06	61.40	2.90	23.02	12.68	-	-	-	-	101.02
	120	24.82	63.39	3.27	22.98	10.36	-	-	-	-	100.99
Au/TiO_2	30	14.32	77.35	3.34	10.68	8.63	-	-	-	-	102.21
	60	22.02	73.02	5.65	12.23	9.10	-	-	-	-	103.47
	90	27.23	66.37	3.94	12.99	5.58	11.11	-	-	-	101.69
	120	29.11	61.75	5.79	15.94	6.32	10.20	-	-	-	101.63
TiO_2	30	14.54	66.36	1.21	21.05	11.38	-	-	-	-	101.20
	60	18.61	61.80	2.33	25.17	10.70	-	-	-	-	99.29
	90	22.26	58.34	2.44	28.77	10.45	-	-	-	-	98.56
	120	27.57	48.43	4.84	23.34	7.23	-	-	-	16.16	102.29

Table D.2 Cellobiose conversion, Product Distribution and Mass Balance values for the reactions run with a 2.8 mM cellobiose conversion under visible light over 120 minutes of exposition using pure H_2O as reaction medium

Catalyst	Reaction Time (min)	Cellobiose Conversion (%)	Cellobionic Acid (%)	Cellobiosan (%)	$C_{11}H_{20}O_{10}$ (%)	Glucose (%)	Gluconic Acid (%)	Arabinose (%)	Erythrose + Glyceraldehyde (%)	Formic Acid (%)	Mass Balance (%)
Ag/TiO_2	30	6.4	63.7	4.2	32.0	-	-	-	-	-	100.7
	60	9.9	56.3	3.2	31.3	9.2	-	-	-	-	100.5
	90	14.1	56.0	3.8	32.1	8.1	-	-	-	-	100.6
	120	14.9	47.9	7.3	35.4	9.3	-	-	-	-	103.3
$Au_{0.05}Ag_{0.95}/TiO_2$	30	5.1	42.0	6.3	22.7	28.9	-	-	-	-	101.7
	60	13.0	51.0	5.0	26.8	17.2	-	-	-	-	99.0
	90	17.0	36.4	4.5	18.7	18.2	-	-	-	22.3	101.9
	120	22.5	43.6	2.0	20.5	10.7	-	-	-	23.2	99.5
$Au_{0.15}Ag_{0.85}/TiO_2$	30	7.5	48.9	8.7	26.5	15.8	-	-	-	-	100.4
	60	14.5	54.7	5.6	24.5	15.2	-	-	-	-	98.9
	90	16.2	46.9	6.6	32.1	14.4	-	-	-	-	101.3
	120	21.0	44.6	1.8	24.1	5.1	-	1.1	23.2	-	101.5
$Au_{0.50}Ag_{0.50}/TiO_2$	30	6.5	49.9	-	32.9	17.2	-	-	-	-	101.1
	60	13.2	53.2	2.8	29.1	14.9	-	-	-	-	99.3
	90	17.4	50.4	3.7	33.8	12.1	-	-	-	-	99.7
	120	23.7	42.6	3.5	24.7	9.3	-	-	-	19.8	101.3
$Au_{0.85}Ag_{0.15}/TiO_2$	30	11.3	54.0	4.7	29.2	12.1	-	-	-	-	99.0
	60	21.0	58.6	3.4	27.1	10.9	-	-	-	-	98.1
	90	26.6	48.3	4.3	25.7	11.4	10.3	-	-	-	102.1
	120	34.2	44.2	1.6	18.8	12.9	10.3	-	-	12.3	103.4
$Au_{0.95}Ag_{0.05}/TiO_2$	30	10.2	76.0	5.5	18.5	0.0	-	-	-	-	99.5
	60	14.1	74.9	4.0	21.1	-	-	-	-	-	99.4
	90	20.1	61.4	2.9	23.0	12.7	-	-	-	-	101.0
	120	24.8	63.4	3.3	23.0	10.4	-	-	-	-	101.0
Au/TiO_2	30	14.3	77.4	3.3	10.7	8.6	-	-	-	-	102.2
	60	22.0	73.0	5.6	12.2	9.1	-	-	-	-	103.5
	90	27.2	66.4	3.9	13.0	5.6	11.1	-	-	-	101.7
	120	29.1	61.7	5.8	15.9	6.3	10.2	-	-	-	101.6
TiO_2	30	14.5	66.4	1.2	21.0	11.4	-	-	-	-	101.2
	60	18.6	61.8	2.3	25.2	10.7	-	-	-	-	99.3
	90	22.3	58.3	2.4	28.8	10.4	-	-	-	-	98.6
	120	27.6	48.4	4.8	23.3	7.2	-	-	-	16.2	102.3

Table D.3 Cellobiose conversion, Product Distribution and Mass Balance values for the reactions run with a 2.8 mM cellobiose conversion under visible light over 120 minutes of exposition using the 50/50 v/v H_2O/ACN mixture as reaction medium

Catalyst	Reaction Time (min)	Cellobiose Conversion (%)	Cellobionic Acid (%)	Cellobiosan (%)	$C_{11}H_{20}O_{10}$ (%)	Glucose (%)	Gluconic Acid (%)	Arabinose (%)	Erythrose + Glyceraldehyde (%)	Formic Acid (%)	Mass Balance (%)
Ag/TiO_2	30	9.5	58.9	3.8	25.4	11.9	-	-	-	-	100.5
	60	12.9	50.9	6.6	32.9	9.6	-	-	-	-	102.8
	90	18.8	38.2	3.7	24.4	4.6	-	-	-	29.1	102.7
	120	23.7	40.9	3.0	22.8	3.7	-	-	-	29.6	103.9
$Au_{0.05}Ag_{0.95}/TiO_2$	30	6.3	41.9	10.5	37.1	10.5	-	-	-	-	101.8
	60	14.6	51.2	6.5	35.1	7.2	-	-	-	-	100.9
	90	23.0	52.4	5.2	34.1	8.4	-	-	-	-	100.1
	120	27.9	44.8	2.0	29.0	5.1	-	-	-	19.1	101.4
$Au_{0.15}Ag_{0.85}/TiO_2$	30	8.0	55.6	8.5	27.5	8.4	-	-	-	-	102.2
	60	14.4	53.5	3.7	34.2	8.6	-	-	-	-	100.6
	90	19.8	40.9	4.8	28.4	5.3	-	-	-	20.6	102.4
	120	28.2	46.7	4.3	26.0	4.8	-	-	-	18.2	102.6
$Au_{0.50}Ag_{0.50}/TiO_2$	30	12.4	57.9	2.1	31.7	8.3	-	-	-	-	100.7
	60	22.8	42.5	5.2	27.2	4.5	-	-	-	20.7	103.0
	90	33.1	46.6	3.3	25.7	4.6	-	-	-	19.9	103.3
	120	39.2	43.1	3.8	26.4	3.4	-	-	-	23.4	103.0
$Au_{0.85}Ag_{0.15}/TiO_2$	30	15.0	58.1	4.0	32.4	5.6	-	-	-	-	100.8
	60	26.4	44.7	4.5	25.2	5.3	-	-	-	20.3	103.1
	90	35.1	44.3	3.2	24.8	4.3	-	-	-	23.4	103.5
	120	44.5	44.8	4.0	25.8	3.6	-	-	-	21.9	102.5
$Au_{0.95}Ag_{0.05}/TiO_2$	30	8.8	60.0	4.4	26.0	9.6	-	-	-	-	102.0
	60	17.6	63.3	3.4	26.4	6.9	-	-	-	-	102.6
	90	21.4	46.8	3.4	25.0	4.2	-	-	-	20.6	103.1
	120	28.3	50.1	3.4	25.1	3.5	-	-	-	17.9	103.2
Au/TiO_2	30	9.3	47.6	7.7	34.0	10.7	-	-	-	-	102.2
	60	19.2	41.9	4.1	26.2	5.8	-	-	-	22.0	103.7
	90	30.5	47.0	4.0	25.0	4.2	-	-	-	19.9	103.9
	120	37.6	43.7	4.0	24.1	5.5	-	-	-	22.8	104.9
TiO_2	30	9.8	53.2	4.0	33.3	9.5	-	-	-	-	102.2
	60	15.8	39.7	2.7	25.8	5.9	-	-	-	25.8	102.0
	90	22.8	39.5	3.1	23.5	4.5	-	-	-	29.6	102.9
	120	27.3	37.1	2.9	25.2	4.6	-	-	-	30.2	101.8

Table D.4 Cellobiose conversion, Product Distribution and Mass Balance values for the reactions run with a 2.8 mM cellobiose conversion under UVA light over 120 minutes of exposition using the 50/50 v/v H_2O/ACN mixture as reaction medium

Catalyst	Reaction Time (min)	Cellobiose Conversion (%)	Cellobionic Acid (%)	Cellobiosan (%)	$C_{11}H_{20}O_{10}$ (%)	Glucose (%)	Gluconic Acid (%)	Arabinose (%)	Erythrose + Glyceraldehyde (%)	Formic Acid (%)	Mass Balance (%)
Ag/TiO_2	30	20.1	59.2	3.2	24.4	13.2	-	-	-	-	104.2
	60	54.8	54.1	2.8	19.0	5.9	-	-	-	18.2	103.3
	90	77.2	56.5	3.9	18.1	6.5	-	-	-	15.0	100.7
	120	92.7	54.2	4.7	20.8	6.1	-	-	-	14.1	91.9
$Au_{0.05}Ag_{0.95}/TiO_2$	30	68.0	53.6	4.6	28.2	3.3	-	0.6	1.6	8.0	96.7
	60	87.0	45.8	7.9	29.9	3.6	-	1.3	2.1	9.3	93.2
	90	100.0	40.9	10.2	29.1	4.2	-	1.9	3.1	10.6	87.1
	120	100.0	37.1	12.1	25.1	3.2	-	3.1	3.7	15.7	92.5
$Au_{0.15}Ag_{0.85}/TiO_2$	30	53.5	52.7	3.1	25.5	4.4	-	0.0	3.0	11.5	101.3
	60	87.7	48.4	5.3	25.6	4.3	-	1.3	2.3	12.8	95.5
	90	100.0	44.8	9.0	26.4	4.4	-	1.6	3.2	10.7	92.6
	120	100.0	43.1	11.1	25.3	3.5	-	2.0	4.0	11.0	95.3
$Au_{0.50}Ag_{0.50}/TiO_2$	30	67.2	42.5	6.1	31.1	3.8	-	0.2	3.0	13.3	96.3
	60	91.1	35.3	7.7	30.9	3.5	-	0.8	2.5	19.3	89.8
	90	100.0	31.0	10.5	27.0	3.3	-	1.1	3.6	23.4	87.6
	120	100.0	23.1	14.0	24.1	3.3	-	2.6	6.0	26.9	83.6
$Au_{0.85}Ag_{0.15}/TiO_2$	30	64.6	40.1	5.2	32.8	3.5	-	-	-	18.4	95.0
	60	87.9	35.5	7.6	30.4	3.8	-	1.5	3.6	17.6	90.5
	90	98.6	29.6	9.7	28.3	3.8	-	1.8	4.3	22.5	85.5
	120	100.0	21.3	12.8	25.9	5.7	-	2.1	4.1	28.1	78.4
$Au_{0.95}Ag_{0.05}/TiO_2$	30	61.5	56.8	4.0	22.2	4.0	-	0.0	2.7	10.2	103.4
	60	83.9	52.7	5.1	24.8	4.9	-	0.3	2.9	9.3	96.2
	90	96.0	47.1	7.4	26.6	5.7	-	0.7	2.3	10.3	88.9
	120	100.0	41.5	9.2	26.8	7.3	-	1.1	3.4	10.6	85.6
Au/TiO_2	30	66.4	52.1	3.4	24.2	3.8	-	0.7	4.3	11.5	101.3
	60	88.5	47.8	5.1	25.7	3.3	-	0.6	3.2	14.3	94.4
	90	98.4	40.7	6.5	25.1	5.1	-	1.4	2.4	18.9	88.7
	120	100.0	36.6	9.6	23.0	5.7	-	2.4	3.5	19.3	88.6
TiO_2	30	36.1	46.2	3.8	23.0	6.4	-	-	-	20.6	104.5
	60	50.5	42.4	4.4	25.0	5.0	-	-	-	23.2	100.7
	90	63.6	42.4	4.4	25.8	5.6	-	0.2	-	21.6	99.9
	120	74.9	39.9	5.9	25.5	5.3	-	0.3	-	23.0	94.1

D.3 10 mM Cellobiose Solutions

Table D.5 Cellobiose conversion, Product Distribution and Mass Balance values for the reactions run with a 2.8 mM cellobiose conversion under UVA light over 120 minutes of exposition using the 50/50 v/v H_2O/ACN mixture as reaction medium

Catalyst	Reaction Time (min)	Cellobiose Conversion (%)	Cellobionic Acid (%)	Cellobiosan (%)	$C_{11}H_{20}O_{10}$ (%)	Glucose (%)	Gluconic Acid (%)	Arabinose (%)	Erythrose + Glyceraldehyde (%)	Formic Acid (%)	Mass Balance (%)
Ag/TiO_2	30	28.9	64.9	2.1	21.8	4.5	-	-	-	-	103.6
	60	44.1	62.3	2.6	22.3	4.2	2.1	-	-	-	103.9
	90	58.8	62.0	2.8	21.3	4.7	1.8	-	-	-	104.5
	120	69.8	59.9	3.4	21.9	4.5	2.6	-	-	7.6	103.1
$Au_{0.05}Ag_{0.95}/TiO_2$	30	32.6	59.2	3.2	26.5	4.5	-	-	-	6.6	104.1
	60	49.4	56.3	3.5	26.2	3.2	1.7	1.1	1.5	6.4	103.0
	90	63.6	53.5	4.1	26.1	3.6	2.4	1.4	1.7	7.0	105.1
	120	75.7	51.3	5.0	26.8	3.7	2.6	1.4	1.6	7.7	101.1
$Au_{0.15}Ag_{0.85}/TiO_2$	30	37.1	59.9	2.4	24.6	3.5	2.2	0.7	1.3	5.5	104.3
	60	55.4	54.8	4.1	25.1	3.7	2.3	0.8	2.6	6.5	107.1
	90	70.5	55.0	3.9	26.1	3.5	1.7	1.1	1.9	6.7	103.5
	120	84.1	52.4	4.5	25.8	3.9	2.7	1.3	1.7	7.6	103.4
$Au_{0.50}Ag_{0.50}/TiO_2$	30	29.6	61.5	3.1	25.2	4.0	-	-	-	6.1	102.5
	60	44.7	57.6	3.2	23.8	4.3	2.4	0.8	1.3	6.7	104.7
	90	57.0	56.8	3.5	24.9	3.8	1.9	0.9	1.3	6.8	104.6
	120	69.1	55.0	3.8	24.2	3.9	2.4	0.8	1.1	8.8	103.6
$Au_{0.85}Ag_{0.15}/TiO_2$	30	32.8	50.1	3.7	26.5	6.4	3.0	-	-	10.2	104.9
	60	53.0	49.4	3.8	26.1	4.6	2.5	0.9	1.9	10.7	105.2
	90	68.1	47.6	4.1	26.7	3.5	2.6	0.9	1.2	13.4	101.6
	120	78.4	43.3	5.0	25.7	4.6	2.1	1.3	2.7	15.2	101.0
$Au_{0.95}Ag_{0.05}/TiO_2$	30	28.1	62.6	3.2	22.0	4.3	-	-	-	7.9	104.3
	60	41.6	60.1	2.7	22.5	5.7	2.4	-	-	6.5	107.1
	90	56.1	59.0	3.2	22.7	3.7	2.2	0.3	1.4	7.6	105.9
	120	67.1	59.5	3.5	23.6	2.9	2.0	0.3	1.1	7.3	104.4
Au/TiO_2	30	29.0	61.1	2.4	21.6	4.1	2.6	0.3	1.4	6.5	103.6
	60	44.6	59.7	3.4	24.1	4.2	2.2	0.4	1.2	4.8	104.6
	90	56.5	59.5	3.1	24.3	4.4	2.1	0.5	1.0	5.2	104.0
	120	68.4	58.4	3.8	23.9	4.3	1.9	0.9	1.5	5.3	104.7
TiO_2	30	16.0	54.7	2.7	24.5	4.4	-	-	-	13.7	102.2
	60	27.7	50.0	3.1	23.8	6.3	-	-	-	16.8	103.9
	90	36.3	50.5	3.3	24.2	5.4	-	-	-	16.5	103.5
	120	46.5	50.8	3.2	23.6	4.9	-	-	-	17.6	103.2

Table D.6 Cellobiose conversion, Product Distribution and Mass Balance values for the reactions run with a 10 mM cellobiose conversion under visible light over 120 minutes of exposition using the 50/50 v/v H_2O/ACN mixture as reaction medium

Catalyst	Reaction Time (min)	Cellobiose Conversion (%)	Cellobionic Acid (%)	Cellobiosan (%)	$C_{11}H_{20}O_{10}$ (%)	Glucose (%)	Gluconic Acid (%)	Arabinose (%)	Erythrose + Glyceraldehyde (%)	Formic Acid (%)	Mass Balance (%)
Ag/TiO_2	30	3.5	57.7	3.5	25.6	13.1	-	-	-	-	101.2
	60	5.6	56.5	3.9	29.5	10.1	-	-	-	-	101.7
	90	8.2	60.0	4.1	27.8	8.1	-	-	-	-	102.3
	120	11.8	55.8	2.7	18.8	4.9	-	-	-	-	103.8
$Au_{0.95}Ag_{0.05}/TiO_2$	30	3.9	60.1	2.6	26.8	10.4	-	-	-	-	101.6
	60	8.0	61.2	4.1	28.1	6.6	-	-	-	-	102.3
	90	11.9	62.6	2.9	27.8	6.8	-	-	-	-	102.6
	120	16.5	54.7	3.2	25.0	5.9	-	-	-	11.2	103.7
$Au_{0.15}Ag_{0.85}/TiO_2$	30	2.7	60.6	3.3	22.9	13.3	-	-	-	-	101.6
	60	7.1	62.6	2.8	28.0	6.5	-	-	-	-	101.6
	90	11.2	55.9	3.9	23.7	4.9	-	-	-	11.6	103.4
	120	15.2	52.3	4.0	23.3	4.3	4.5	-	-	11.6	104.6
$Au_{0.50}Ag_{0.50}/TiO_2$	30	3.4	57.9	5.6	28.2	8.4	0.0	-	-	-	101.2
	60	7.1	61.6	6.4	26.2	5.8	0.0	-	-	-	102.1
	90	11.9	55.8	3.3	24.2	3.8	0.0	-	-	12.9	102.9
	120	15.5	51.8	2.3	23.6	3.1	5.0	-	-	14.2	103.4
$Au_{0.85}Ag_{0.15}/TiO_2$	30	7.2	58.4	5.8	27.9	8.0	0.0	-	-	-	102.4
	60	14.9	56.2	2.5	21.2	4.2	0.0	-	-	15.9	102.8
	90	22.1	55.1	2.2	22.5	3.8	4.4	-	-	12.0	104.7
	120	26.7	52.0	2.5	24.0	4.0	6.0	-	-	11.7	104.7
$Au_{0.95}Ag_{0.05}/TiO_2$	30	4.4	67.6	2.1	22.0	8.4	0.0	-	-	-	101.9
	60	9.2	69.8	1.9	24.1	4.2	0.0	-	-	-	102.1
	90	13.2	58.4	2.7	22.2	5.7	0.0	-	-	10.9	103.0
	120	16.2	55.5	2.6	21.8	4.4	3.9	-	-	11.8	104.5
Au/TiO_2	30	4.2	51.6	2.7	20.6	6.5	0.0	-	-	18.6	102.4
	60	8.9	49.0	3.7	24.2	5.1	0.0	-	-	17.9	103.4
	90	13.9	56.9	3.3	23.5	5.6	0.0	-	-	10.6	102.8
	120	17.7	54.0	2.7	22.4	3.2	4.5	-	-	13.3	104.2
TiO_2	30	2.2	44.9	9.8	25.1	20.2	-	-	-	-	102.7
	60	5.4	46.4	5.9	24.0	7.3	-	-	-	16.4	102.1
	90	8.1	50.3	1.9	23.0	6.6	-	-	-	18.2	102.0
	120	9.7	46.6	3.5	25.4	6.7	-	-	-	17.7	102.6

Table D.7 Cellobiose conversion, Product Distribution and Mass Balance values for the reactions run with a 10 mM cellobiose conversion under UVA light over 120 minutes of exposition using pure H_2O as reaction medium

Catalyst	Reaction Time (min)	Cellobiose Conversion (%)	Cellobionic Acid (%)	Cellobiosan (%)	$C_{11}H_{20}O_{10}$ (%)	Glucose (%)	Gluconic Acid (%)	Arabinose (%)	Erythrose + Glyceraldehyde (%)	Formic Acid (%)	Mass Balance (%)
Ag/TiO_2	30	10.0	60.9	2.4	21.3	7.85	-	-	-	7.5	100.6
	60	11.3	66.6	2.6	20.3	10.5	-	-	-	-	100.8
	90	13.8	64.1	3.0	22.9	10.0	-	-	-	-	100.6
	120	17.0	65.9	2.6	23.0	8.5	-	-	-	-	100.6
$Au_{0.05}Ag_{0.95}/TiO_2$	30	7.8	57.8	4.2	28.6	9.3	-	-	-	-	102.8
	60	15.2	61.9	4.4	28.3	5.4	-	-	-	-	102.4
	90	17.9	60.0	3.6	29.5	7.0	-	-	-	-	102.7
	120	23.0	58.7	4.0	27.3	6.0	-	2.1	1.9	-	103.1
$Au_{0.15}Ag_{0.85}/TiO_2$	30	16.3	59.6	2.2	26.3	11.9	-	-	-	-	97.3
	60	26.6	59.2	4.2	25.9	10.7	-	-	-	-	96.8
	90	30.5	57.6	3.7	25.8	8.3	3.5	1.0	-	-	97.5
	120	38.4	58.9	3.2	25.6	7.2	3.4	1.7	-	-	97.5
$Au_{0.50}Ag_{0.50}/TiO_2$	30	15.5	64.0	2.2	23.6	10.2	-	-	-	-	100.8
	60	22.4	60.5	2.2	26.8	6.8	3.8	-	-	-	101.0
	90	28.2	60.6	3.1	26.9	6.2	3.1	-	-	-	101.3
	120	34.1	59.1	3.5	27.4	6.8	3.3	-	-	-	101.1
$Au_{0.85}Ag_{0.15}/TiO_2$	30	15.0	52.0	3.8	36.6	7.6	-	-	-	-	100.5
	60	22.8	60.2	2.3	26.5	5.1	5.9	-	-	-	102.1
	90	30.4	44.7	4.6	33.9	5.1	2.7	1.1	2.7	5.2	100.4
	120	35.2	42.5	4.0	33.2	4.8	2.7	1.6	3.9	7.2	99.9
$Au_{0.95}Ag_{0.05}/TiO_2$	30	15.2	67.5	2.2	25.1	5.2	-	-	-	-	101.3
	60	24.9	50.1	4.1	36.0	6.0	3.7	-	-	-	99.4
	90	28.7	58.7	3.3	25.0	5.1	3.1	1.6	3.2	-	102.8
	120	33.6	57.4	3.0	24.6	5.1	2.4	2.4	5.2	-	102.9
Au/TiO_2	30	22.3	66.0	2.3	25.3	6.4	0.0	0.0	-	-	102.2
	60	33.9	62.0	2.7	23.1	5.4	2.5	0.0	-	4.5	102.7
	90	40.8	60.6	3.1	24.3	5.9	2.4	0.0	-	3.7	102.9
	120	47.5	61.2	3.1	23.0	5.3	3.1	1.0	-	3.3	102.5
TiO_2	30	5.9	57.2	4.4	26.1	12.3	-	-	-	-	101.7
	60	9.5	58.3	3.6	28.5	9.6	-	-	-	-	101.3
	90	12.6	60.0	3.2	29.1	7.8	-	-	-	-	101.0
	120	15.6	58.3	4.5	29.4	7.7	-	-	-	-	101.9

Table D.8 Cellobiose conversion, Product Distribution and Mass Balance values for the reactions run with a 10 mM cellobiose conversion under visible light over 120 minutes of exposition using pure H_2O as reaction medium

Catalyst	Reaction Time (min)	Cellobiose Conversion (%)	Cellobionic Acid (%)	Cellobiosan (%)	$C_{11}H_{20}O_{10}$ (%)	Glucose (%)	Gluconic Acid (%)	Arabinose (%)	Erythrose + Glyceraldehyde (%)	Formic Acid (%)	Mass Balance (%)
Ag/TiO_2	30	2.5	40.0	5.4	26.5	28.1	-	-	-	-	100.5
	60	4.3	51.4	3.6	25.9	19.1	-	-	-	-	100.1
	90	5.2	41.2	3.2	23.9	11.8	-	-	-	19.9	101.7
	120	7.6	42.8	3.6	24.8	9.5	-	-	-	19.2	100.7
$Au_{0.05}Ag_{0.95}/TiO_2$	30	3.0	39.3	6.0	29.3	25.4	-	-	-	-	100.6
	60	5.6	47.3	5.9	28.2	18.6	-	-	-	-	100.7
	90	8.2	53.5	3.2	27.8	15.5	-	-	-	-	100.4
	120	11.1	51.1	2.8	24.1	10.0	-	-	-	12.0	100.7
$Au_{0.15}Ag_{0.85}/TiO_2$	30	3.1	45.0	4.8	20.8	29.4	-	-	-	-	100.2
	60	5.6	56.6	5.3	27.5	10.6	-	-	-	-	100.8
	90	8.2	48.0	2.3	21.8	9.1	-	-	-	18.9	100.4
	120	13.2	54.5	2.2	18.6	8.3	7.5	-	-	8.8	103.0
$Au_{0.50}Ag_{0.50}/TiO_2$	30	3.1	44.3	6.9	30.6	18.3	-	-	-	-	100.7
	60	5.8	51.8	4.3	28.7	15.2	-	-	-	-	100.4
	90	8.7	45.7	2.9	27.8	9.3	-	-	-	14.3	100.1
	120	11.3	47.2	2.5	25.8	6.6	6.4	-	-	11.5	100.3
$Au_{0.85}Ag_{0.15}/TiO_2$	30	3.1	48.0	5.1	22.1	24.8	-	-	-	-	100.1
	60	5.6	53.5	5.0	26.0	15.5	-	-	-	-	101.0
	90	8.2	47.0	2.2	21.4	10.8	-	-	-	18.6	100.5
	120	13.2	54.5	2.2	18.6	8.3	7.5	-	-	8.8	103.0
$Au_{0.95}Ag_{0.05}/TiO_2$	30	3.6	54.2	5.7	22.2	17.9	-	-	-	-	100.8
	60	6.8	57.7	4.0	21.7	16.6	-	-	-	-	101.1
	90	8.6	61.0	3.3	22.2	13.6	-	-	-	-	101.1
	120	12.0	54.6	2.9	17.8	7.5	6.4	-	-	10.7	100.7
Au/TiO_2	30	7.0	71.5	2.8	12.2	13.6	-	-	-	-	101.2
	60	8.6	69.0	1.9	16.6	12.5	-	-	-	-	100.6
	90	10.8	59.4	4.8	18.3	9.4	8.2	-	-	-	101.3
	120	12.0	51.9	4.6	17.0	6.9	8.2	-	-	11.5	102.0
TiO_2	30	2.8	53.7	-	31.4	14.9	-	-	-	-	100.4
	60	3.9	44.1	-	27.6	28.3	-	-	-	-	101.1
	90	5.1	53.2	5.6	27.5	13.7	-	-	-	-	100.8
	120	6.3	43.3	3.6	26.1	10.2	-	-	-	16.9	101.2

Appendix E

E.1 Redispersion of Ag Nanoparticles on TiO_2

E.2 Fresh 1.5% Ag/TiO_2

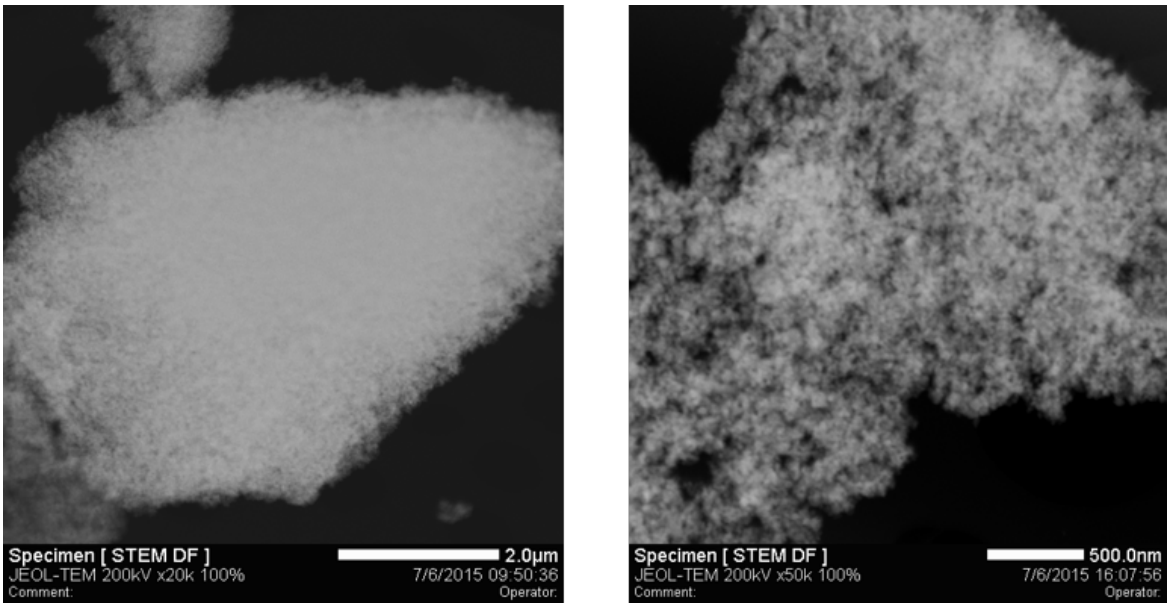

Figure E.1 STEM micrographs of the 1.5 wt% Ag/TiO_2 fresh catalyst which do not show the the presence of large metallic nanoparticles on the fresh material.

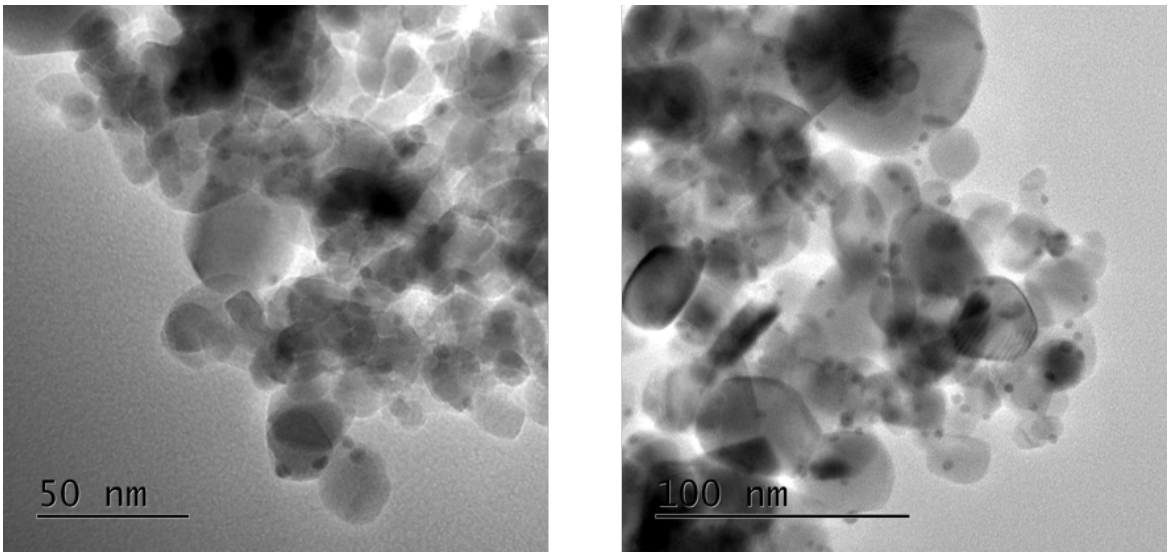

Figure E.2 TEM micrographs of the 1.5 wt% Ag/TiO_2 fresh catalyst.

E.3 Visible light - H_2O

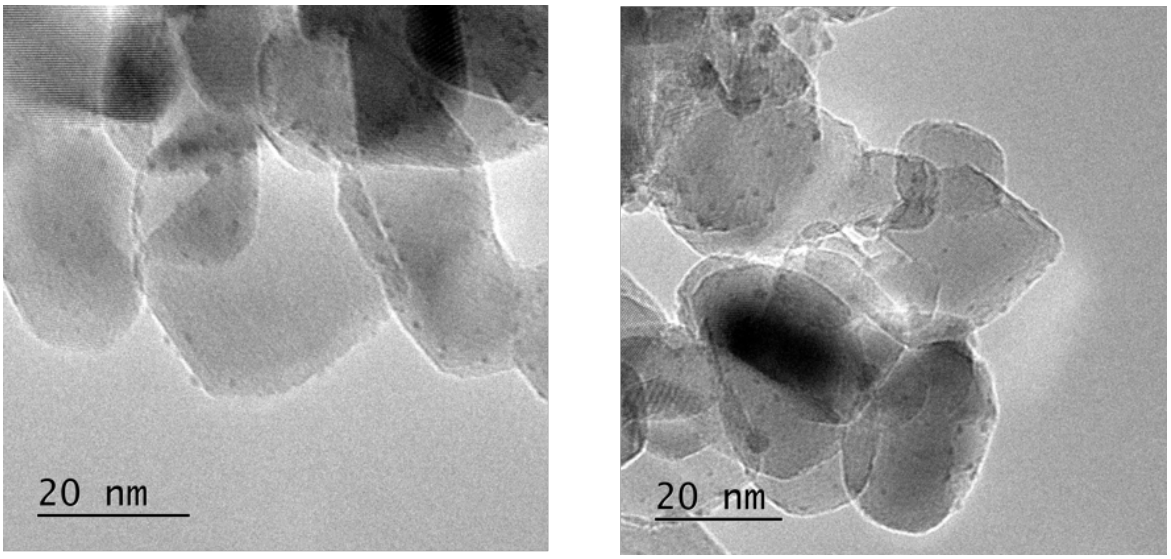

Figure E.3 TEM micrographs of the 1.5 wt% Ag/TiO_2 of the catalyst exposed to visible light in pure H_2O.

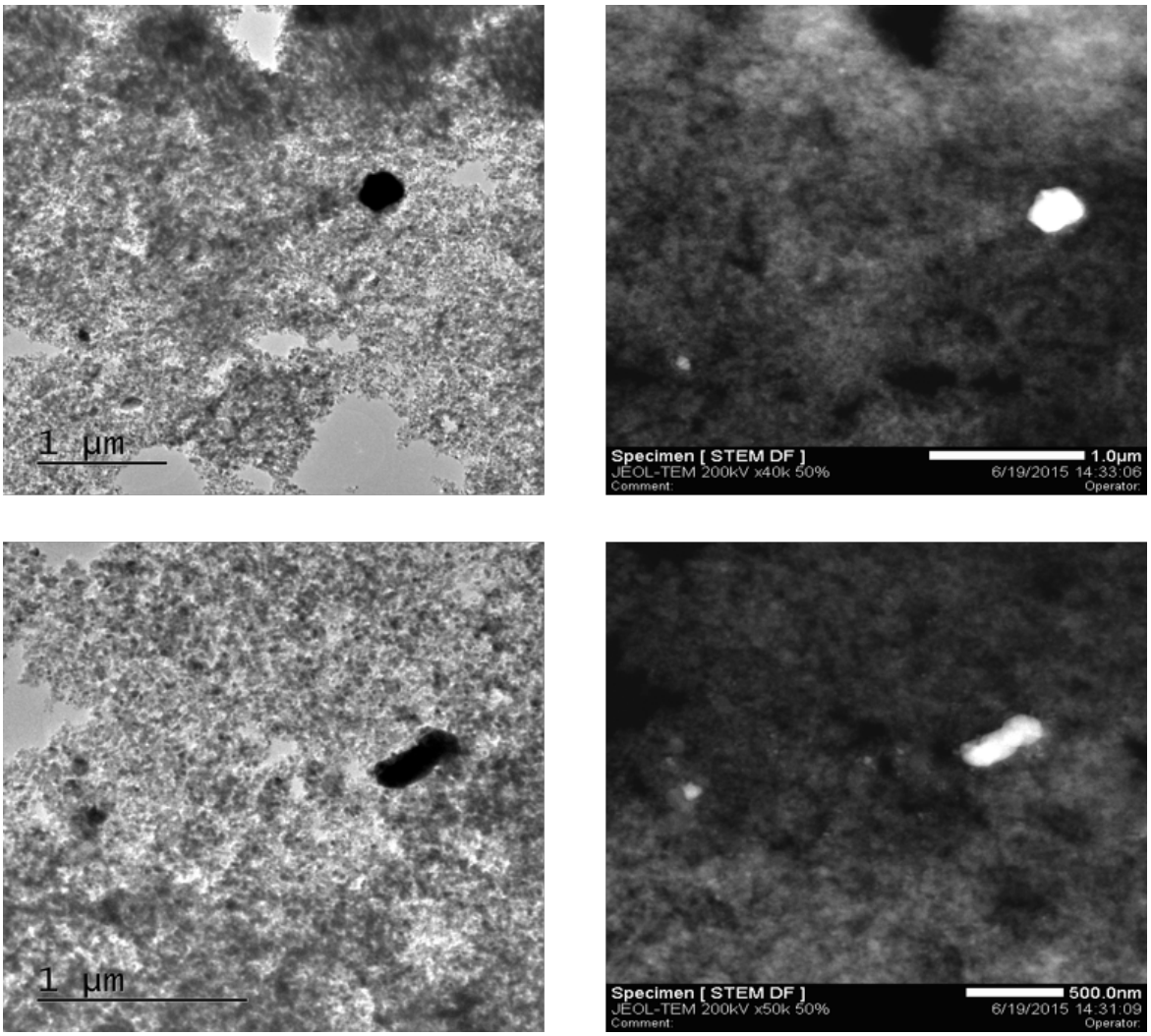

Figure E.4 STEM micrographs of the 1.5 wt% Ag/TiO_2 (left) and dark field images (right) of the catalyst exposed to visible light in pure H_2O.

E.4 Visible Light - MeCN/H_2O

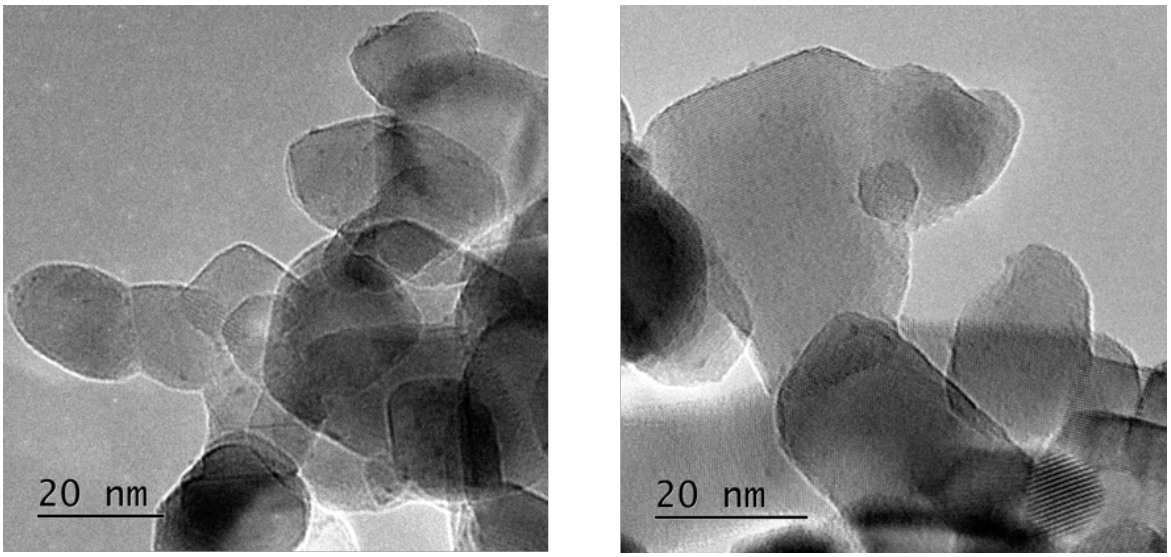

Figure E.5 TEM micrographs of the 1.5 wt% Ag/TiO_2 of the catalyst exposed to visible light in the 50/50 v/v $MeCN/H_2O$ mixture.

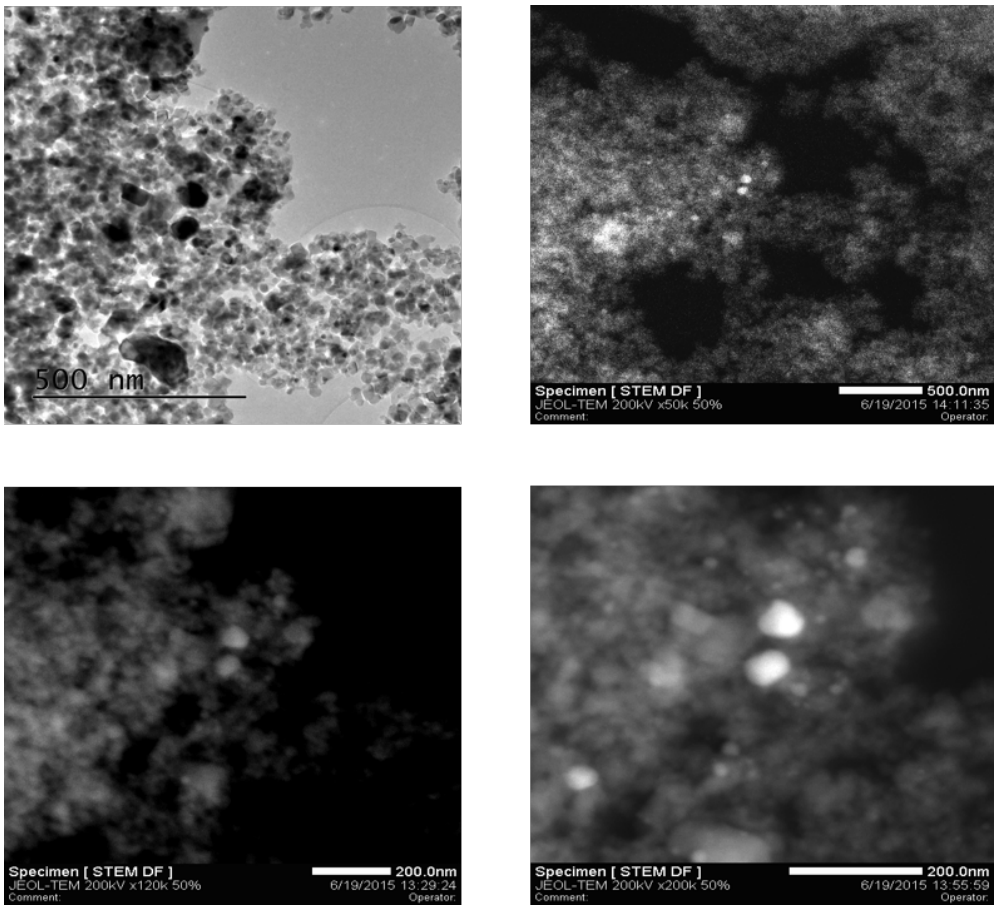

Figure E.6 STEM micrographs of the 1.5 wt% Ag/TiO_2 (left) and dark field images (right) of the catalyst exposed to visible light in the 50/50 v/v $MeCN/H_2O$ mixture.

E.5 UVA Light - H_2O

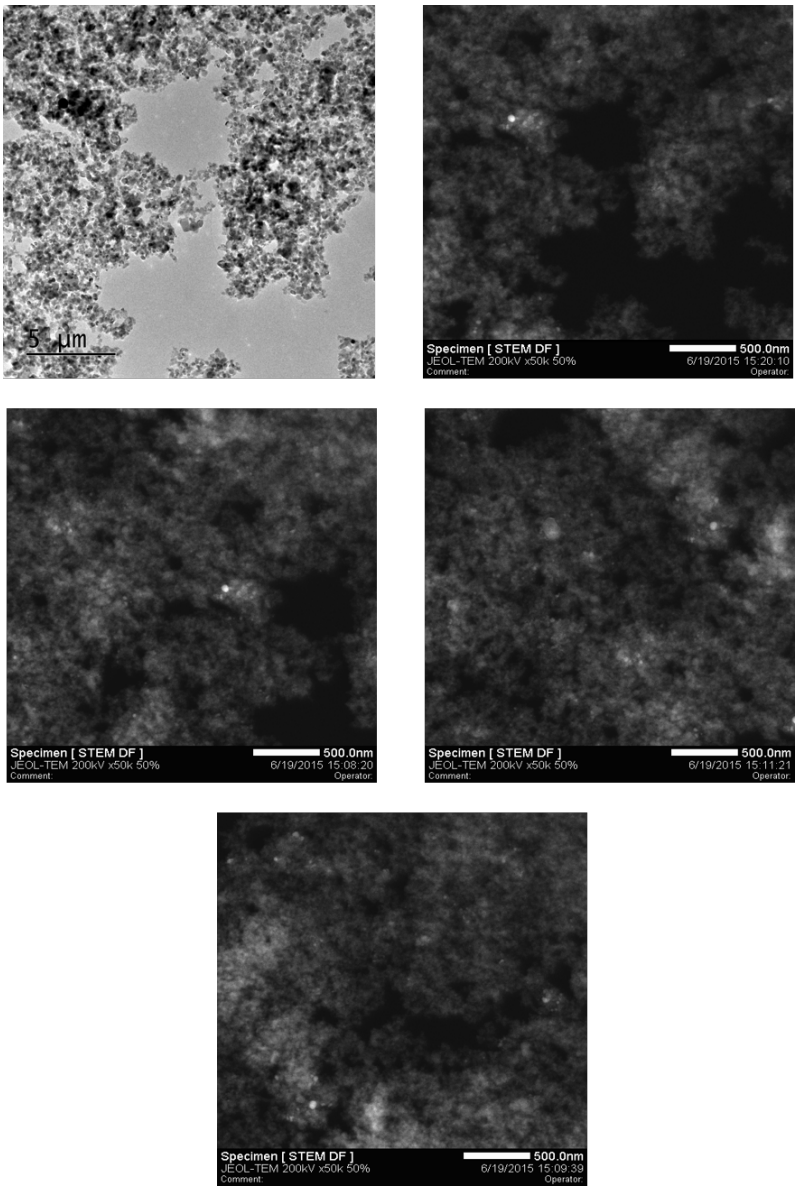

Figure E.7 STEM micrographs of the 1.5 wt% Ag/TiO_2 (left) and dark field images (right) of the catalyst exposed to UVA light in pure H_2O.

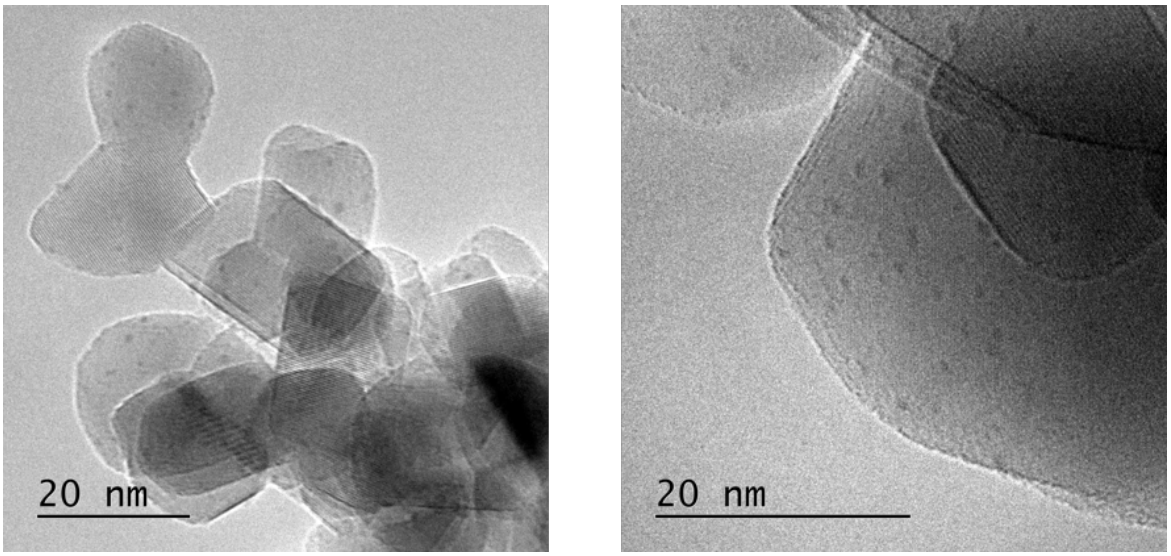

Figure E.8 TEM micrographs of the 1.5 wt% Ag/TiO_2 of the catalyst exposed to UVA light in pure H_2O.

E.6 UVA Light - MeCN/H_2O

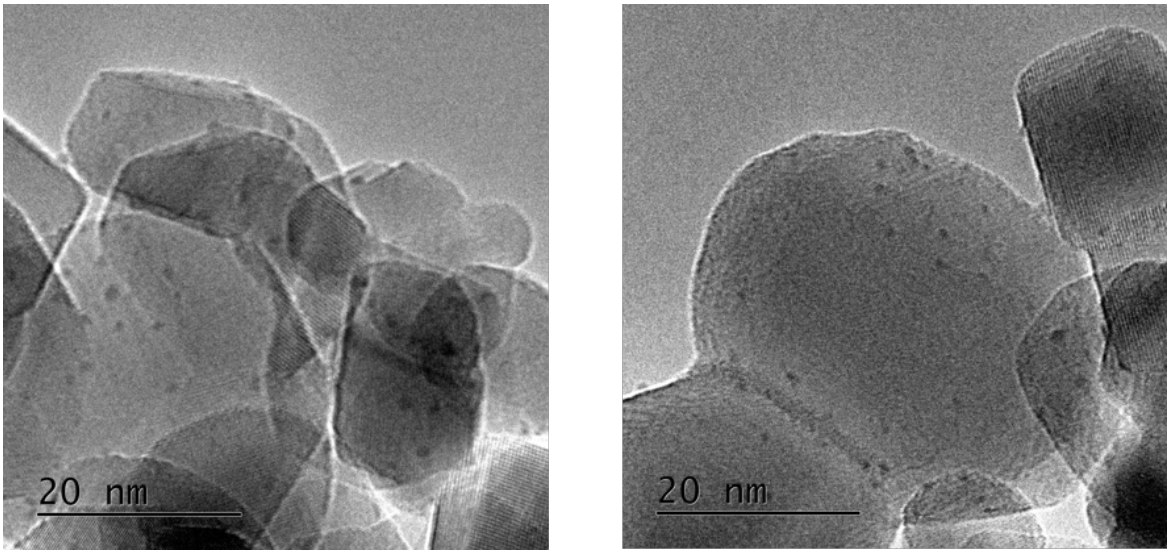

Figure E.9 TEM micrographs of the 1.5 wt% Ag/$TiO_2$of the catalyst exposed to UVA light in in the 50/50 v/v MeCN/H_2O mixture.

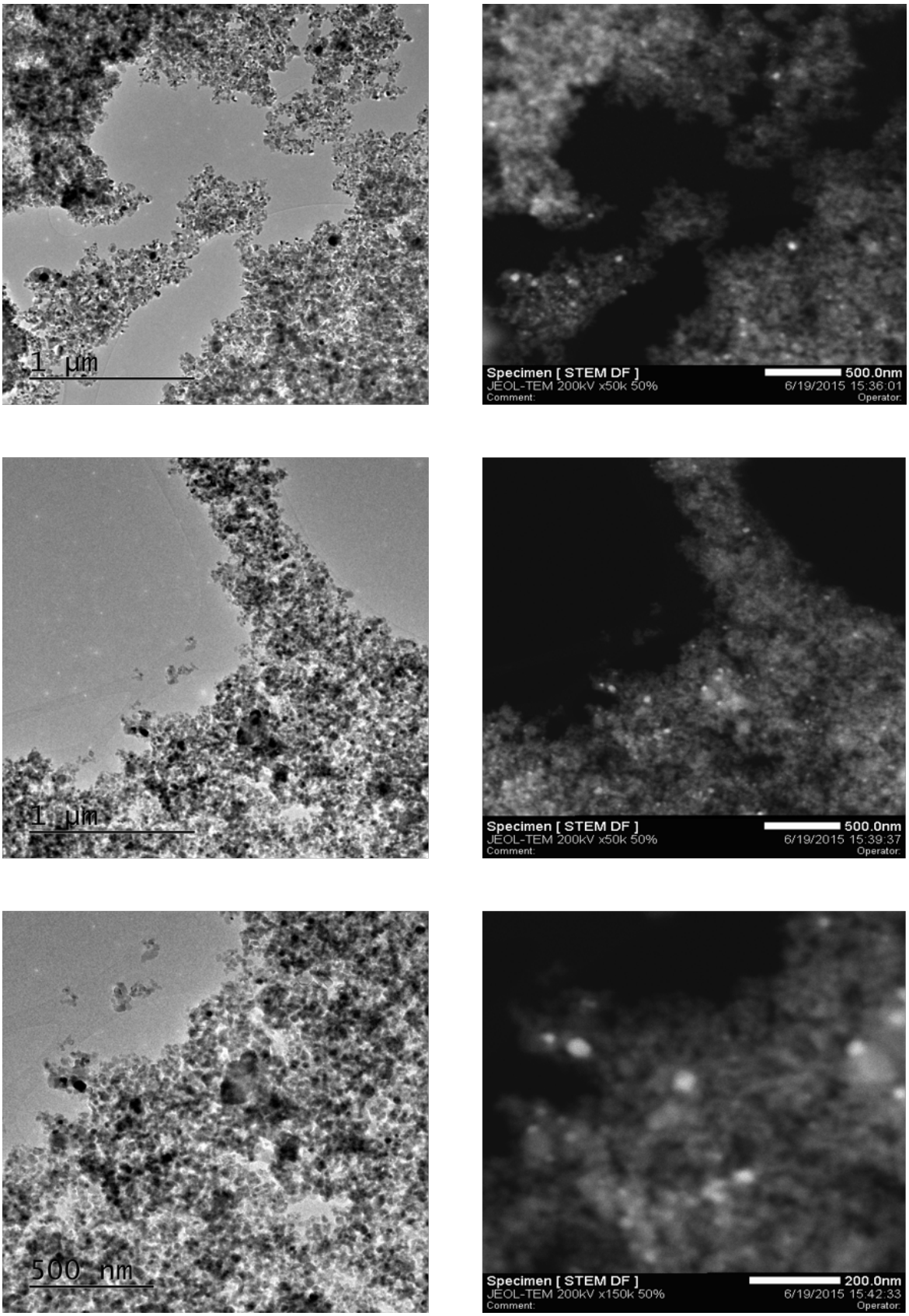

Figure E.10 STEM micrographs of the 1.5 wt% Ag/TiO_2 (left) and dark field images (right) of the catalyst exposed to UVA light in in the 50/50 v/v $MeCN/H_2O$ mixture.

Appendix F

F.1 Au_1Ag_{1-x}/TiO_2 TEM Micrographs

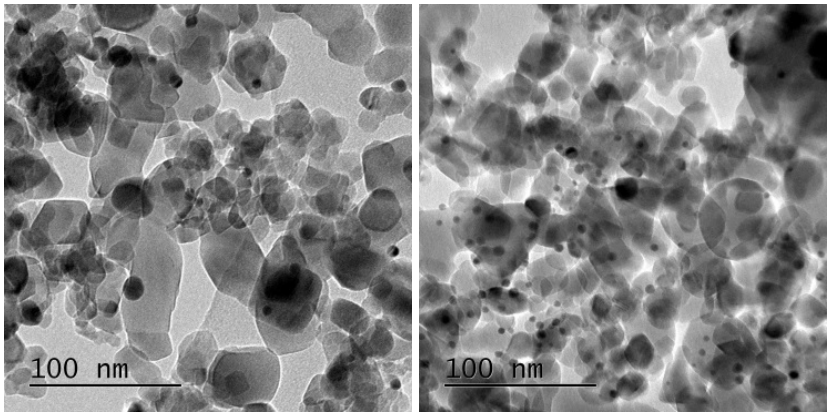

(a) Au/TiO_2 **(b)** $Au_{0.95}Ag_{0.05}/TiO_2$

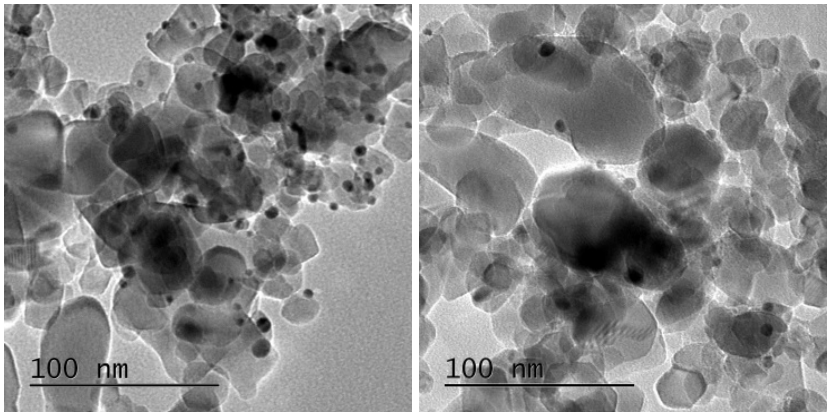

(c) $Au_{0.85}Ag_{0.15}/TiO_2$ **(d)** $Au_{0.50}Ag_{0.50}/TiO_2$

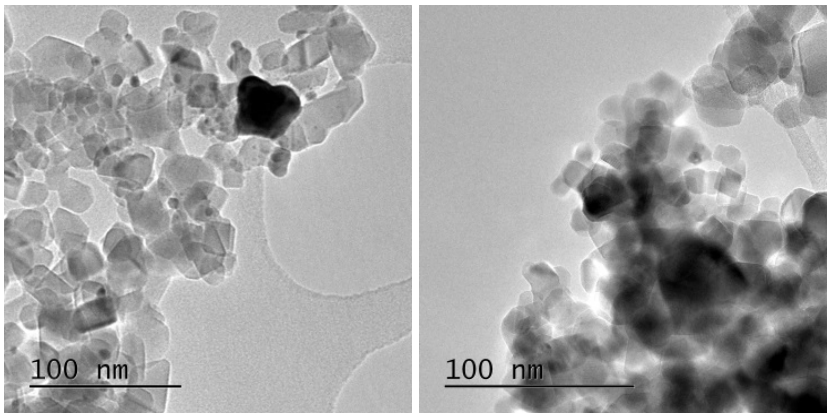

(e) $Au_{0.15}Ag_{0.85}/TiO_2$ **(f)** $Au_{0.05}Ag_{0.95}/TiO_2$

Figure F.1 TEM micrographs of the supported metal nanoparticles.

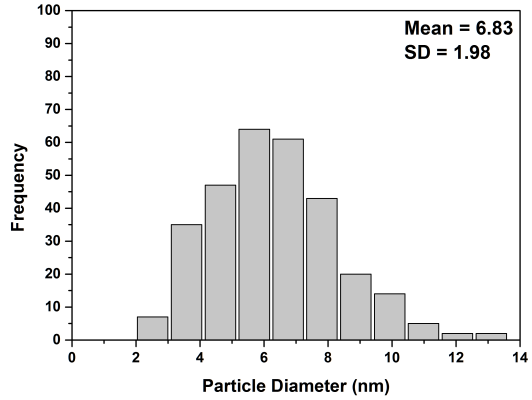

(a) Au/TiO_2

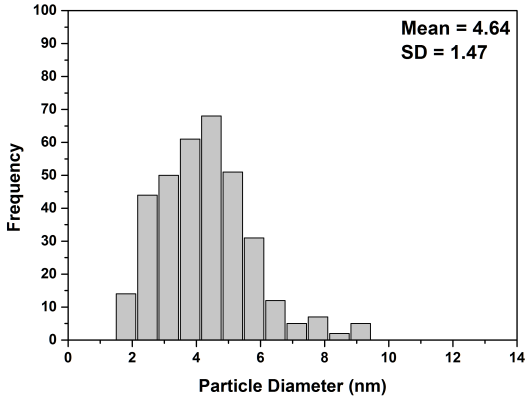

(b) $Au_{0.95}Ag_{0.05}/TiO_2$

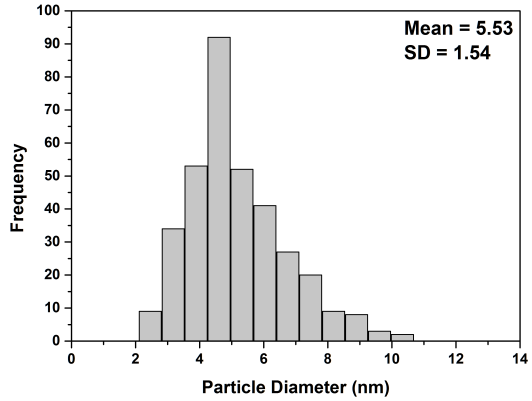

(c) $Au_{0.85}Ag_{0.15}/TiO_2$

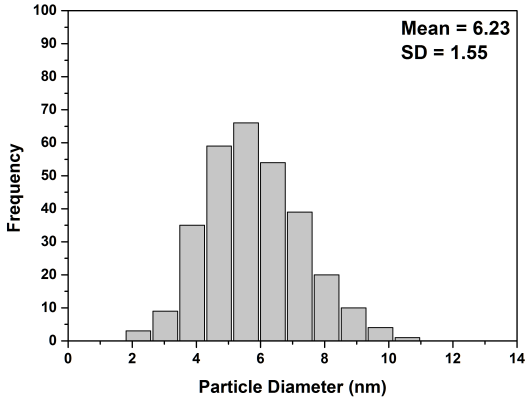

(d) $Au_{0.50}Ag_{0.50}/TiO_2$

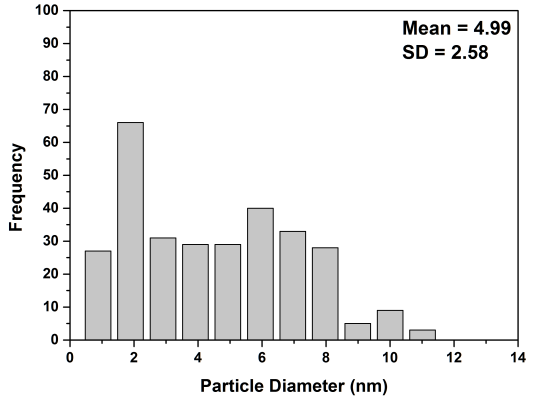

(e) $Au_{0.15}Ag_{0.85}/TiO_2$

Figure F.2 Particle size distribution of the supported metal nanoparticles. Unfortunately, it was not possible to obtain the PSD values for the $Au_{0.05}Ag_{0.95}/TiO_2$ and for the Ag/TiO_2.